

JUL -9

Final Report
on
**Liquid-Propellant Droplet Combustion and Cluster Behavior at
Supercritical Conditions**

for
AFOSR Contract/Grant F49620-98-1-0034

Prepared by

Vigor Yang
Propulsion Engineering Research Center
and
Department of Mechanical Engineering
The Pennsylvania State University
University Park, PA 16802

Submitted to:

Air Force Office of Scientific Research
801 N. Randolph Street, Room 732
Arlington, VA 22203-1977

May 2001

DISTRIBUTION STATEMENT A

Approved for Public Release
Distribution Unlimited

20010731 039

REPORT DOCUMENTATION PAGE

AFRL-SR-BL-TR-01-

Public reporting burden for this collection of information is estimated to average 1 hour per response, including the time for reviewing instructions data needed, and completing and reviewing this collection of information. Send comments regarding this burden estimate or any other aspect of this burden to Department of Defense, Washington Headquarters Services, Directorate for Information Operations and Reports (0704-0188), 121 4302. Respondents should be aware that notwithstanding any other provision of law, no person shall be subject to any penalty for failing to comply with a collection of information if it does not have a valid OMB control number. **PLEASE DO NOT RETURN YOUR FORM TO THE ABOVE ADDRESS.**

0422

| | | | | | |
|---------------------------------------------------------------------------------------------------------------------------------------------------------------------------------------------------------------------------------------------------------------------------------------------------------------------------------------------------------------------------------------------------------------------------------------------------------------------------------------------------------------------------------------------------------------------------------------------------------------------------------------------------------------------------------------------------------------------------------------------------------------------------------------------------------------------------------------------------------------------------------------------------------------------------------------------------------------------------------------------------------------------------------------------------------------------------------------------------------------------------------------------------------------------------------------------------------------------------------------------------------------------------------------------------------------------------------------------------------------------------------------------------------------------------------------------------------------------------------------------------------------------------------------------------------------------------------------------------------------------------------------------------------------------------------------------------------|------------------------------------|-------------------------------------------------|---------------------------------------------|----------------------------------------------------------------|------------------------------------------------------------------------|
| 1. REPORT DATE (DD-MM-YYYY) 01/05/2001 | | 2. REPORT TYPE Final Technical Report | | 3. DATES COVERED (From - To) ~ 01/11/1997-10/31/2000 | |
| 4. TITLE AND SUBTITLE Liquid-Propellant Droplet Combustion and Cluster Behavior at Supercritical Conditions | | | | 5a. CONTRACT NUMBER | |
| | | | | 5b. GRANT NUMBER F49620-98-1-0034 | |
| | | | | 5c. PROGRAM ELEMENT NUMBER | |
| 6. AUTHOR(S) Vigor Yang | | | | 5d. PROJECT NUMBER | |
| | | | | 5e. TASK NUMBER | |
| | | | | 5f. WORK UNIT NUMBER | |
| 7. PERFORMING ORGANIZATION NAME(S) AND ADDRESS(ES) The Pennsylvania State University 104 Research Building East University Park, PA 16802 | | | | 8. PERFORMING ORGANIZATION REPORT NUMBER | |
| 9. SPONSORING / MONITORING AGENCY NAME(S) AND ADDRESS(ES) Dr. Mitat A. Birkan Air Force Office of Scientific Research 801 N. Randolph Street, Room 732 Arlington, VA 22203-1977 | | | | 10. SPONSOR/MONITOR'S ACRONYM(S) AFOSR | |
| | | | | 11. SPONSOR/MONITOR'S REPORT NUMBER(S) | |
| 12. DISTRIBUTION / AVAILABILITY STATEMENT Approved for public release; distribution unlimited. | | | | | |
| 13. SUPPLEMENTARY NOTES | | | | | |
| 14. ABSTRACT A systematic investigation of supercritical droplet vaporization and cluster behavior has been conducted based on the complete conservation equations in both the gas and liquid phases. The research work addresses a variety of fundamental issues related to droplet vaporization and dynamics at realistic conditions typical of liquid-propellant rocket combustion devices. A unified treatment of real-fluid thermodynamics has been developed based on fundamental theories. Special attention was given to the thermodynamic non-ideality and transport anomaly in the transcritical regime. A series of calculations has been performed to examine the cluster behavior of liquid oxygen (LOX) droplets in both sub- and super-critical hydrogen environments. Results show that pressure has strong effect on droplet interactions, while the temperature effect is relatively minor at high pressures. The hydrogen density plays a decisive role in determining droplet interactions through its influence on the temperature and mass fraction gradients at the LOX droplet surface. The characteristics of LOX droplet vaporization in forced-convective environments has also been studied. A dimensionless parameter $We^{1/2}/Oh$, which represents the ratio of aerodynamic and viscous forces, is found to be the major factor determining the droplet deformation under supercritical conditions. Results of droplet lifetime are well correlated as a function of the initial droplet Reynolds number and pressure. Finally, the interactions between two droplets moving in tandem in supercritical convective environments were investigated in detail. | | | | | |
| 15. SUBJECT TERMS supercritical combustion, liquid rocket engines, droplet vaporization and combustion | | | | | |
| 16. SECURITY CLASSIFICATION OF: | | | 17. LIMITATION OF ABSTRACT UU | 18. NUMBER OF PAGES | 19a. NAME OF RESPONSIBLE PERSON 211 |
| a. REPORT unclassified | b. ABSTRACT unclassified | c. THIS PAGE unclassified | | | 19b. TELEPHONE NUMBER (include area code) (814) 863-1502 |

Abstract

A systematic investigation of supercritical droplet vaporization and cluster behavior has been conducted based on the complete conservation equations in both the gas and liquid phases. The research work addresses a variety of fundamental issues related to droplet vaporization and dynamics at realistic conditions typical of liquid-propellant rocket combustion devices.

A unified treatment of real-fluid thermodynamics has been developed based on fundamental theories. Special attention was given to the thermodynamic non-ideality and transport anomaly in the transcritical regime. A modified Soave-Redlich-Kwong (SRK) equation of state was utilized to derive all the thermodynamic correlations, which were then incorporated into the numerical scheme to enhance numerical efficiency and robustness. In addition, a preconditioning scheme with the dual time-stepping integration technique was implemented to render the numerical algorithm capable of treating fluid flows at low Mach numbers. The fluid thermal conductivity and viscosity were estimated by means of the extended corresponding states one-fluid principle, along with the Benedict-Webb-Rubin (BWR) equation of state. The pressure effect on binary mass diffusivity is corrected by the Takahashi method.

A series of calculations has been performed to examine the cluster behavior of liquid oxygen (LOX) droplets in both sub- and super-critical hydrogen environments. Results show that pressure has strong effect on droplet interactions, while the temperature effect is relatively minor at high pressures. The hydrogen density plays a decisive role in determining droplet interactions through its influence on the temperature and mass fraction gradients at the LOX droplet surface. In the later stage of the vaporization

process, droplet vaporization rate is dominated by the oxygen accumulation at the droplet surface, which leads to low thermal conductivity of the mixture and consequently reduces the heat transfer rate into the liquid droplet.

Much effort was expended to explore LOX droplet vaporization in forced-convection environments. A dimensionless parameter $We^{1/2}/Oh$, which represents the ratio of aerodynamic and viscous forces, is found to be the major factor determining the droplet deformation under supercritical conditions. Results of droplet lifetime are well correlated as a function of the initial Reynolds number and pressure. A linear relationship is generated for droplet velocity, and the droplet trajectories calculated from this linear relationship agree well with the results directly from numerical computation. The drag coefficient in the supercritical droplet vaporization process was found to decrease with time proportional to one-third power of the dimensionless droplet vaporization rate, which is due to the weak Reynolds number reduction.

The interactions with two droplets moving in tandem in supercritical convective environments have been investigated in detail. Results indicate that droplet dynamics exhibits characteristics distinct from that of an isolated droplet. No droplet collision was observed for all the cases studied herein. A forward bag break-up of the leading droplet, however, was found when the two droplets are initially positioned closely with a H/R ratio (the ratio of the initial droplet spacing to droplet radius) of 4 and a pressure of 100 atm. The presence of the trailing droplet slightly affects the lifetime and trajectory of the leading droplets. However, the lifetime of the trailing droplet is substantially elongated. Forward movement was observed for the trailing droplet at an H/R ratio of 4 and a pressure of 100atm. Increase of pressure weakens droplet interactions.

Table of Contents

| | |
|---------------------------------------------------------------------------------------------------|-------------|
| List of Tables | viii |
| List of Figures | ix |
| Nomenclature | xii |
| Acknowledgments | xix |
| 1 Introduction | 1 |
| 1.1 Literature Survey | 2 |
| 1.1.1 Droplet Vaporization in Quiescent Environments | 2 |
| 1.1.1.1 Single Droplet Vaporization | 2 |
| 1.1.1.2 Droplet Cluster Behavior | 10 |
| 1.1.2 Droplet Vaporization in Convective Environments | 14 |
| 1.1.2.1 Single Droplet Vaporization in Convective Environments | 16 |
| 1.1.2.2 Droplet Interactions in Convective Environments | 21 |
| 1.2 Research Objectives | 23 |
| 2 Theoretical Formulations of Supercritical Droplet Vaporization in Quiescent Environments | 26 |
| 2.1 Conservation Equations | 26 |
| 2.2 Boundary Conditions | 28 |
| 2.2.1 Initial Boundary Conditions | 28 |
| 2.2.2 Boundary Conditions at Droplet Center and Outside Field | 29 |
| 2.2.3 Boundary Conditions at Droplet Interface | 31 |
| 2.3 Irreversible Thermodynamic Phenomenon | 32 |
| 2.4 Equations of State | 34 |
| 2.4.1 Modified Soave-Redlich-Kwong (SRK) Equation of State | 34 |
| 2.4.2 Benedict-Webb-Rubin (BWR) Equation of State | 36 |
| 2.5 Thermodynamic Properties | 38 |
| 2.6 Transport Properties | 43 |
| 2.6.1 Corresponding States Theories | 43 |
| 2.6.2 Mixing Rules for Mixtures | 45 |
| 2.6.3 Viscosity of Mixtures | 46 |
| 2.6.4 Thermal Conductivity of Mixtures | 47 |
| 2.6.5 Binary Mass Diffusivity | 48 |
| 2.7 Numerical Method | 50 |
| 2.7.1 Grid Generation | 51 |
| 2.7.2 Independent Variables and Numerical Linearizations | 52 |
| 2.7.2.1 Linearization of Temperature | 53 |
| 2.7.2.2 Linearization of Pressure | 54 |
| 2.7.2.3 Linearization of Chemical Potential | 56 |

| | |
|-------------------------------------------------------------------------------------------------|------------|
| 2.7.3 Solution Procedures | 58 |
| 3 Droplet Cluster Behavior | 60 |
| 3.1 Problem Description | 60 |
| 3.2 Numerical Treatment | 63 |
| 3.3 Results and Discussions | 64 |
| 3.4 Summary of Results | 83 |
| 4 Unified Treatment of Real Fluid Mixtures and the Application to Preconditioning Scheme | 85 |
| 4.1 Preconditioning Scheme | 86 |
| 4.1.1 The Conservation Equations | 86 |
| 4.1.2 Preconditioning Method | 89 |
| 4.2 Numerical Derivations for Real Fluid Mixtures | 91 |
| 4.2.1 Important Thermodynamic Relationships | 91 |
| 4.2.2 Implicit Numerical Scheme and Jacobians | 97 |
| 4.2.3 Eigenvalues | 99 |
| 4.2.4 Selection of the Scaling Factor | 101 |
| 4.3 Thermophysical properties | 103 |
| 4.4 Numerical Solution | 104 |
| 5 Supercritical Oxygen Droplet Vaporizing in Convective Hydrogen Environments | 107 |
| 5.1 Problem Descriptions | 107 |
| 5.2 Numerical Treatment | 109 |
| 5.3 Results and Discussions | 110 |
| 5.3.1 Grid Independence Study | 111 |
| 5.3.2 Flow Patterns | 111 |
| 5.3.3 Temperature Contours and Droplet Deformations | 114 |
| 5.3.4 Mass Fraction Distributions | 117 |
| 5.3.5 Droplet Vaporization Times | 118 |
| 5.3.6 Droplet Dynamics | 123 |
| 5.4 Summary of Results | 129 |
| 6 Supercritical Vaporization of Two-Droplets-in-Tandem in Convective Environments | 142 |
| 6.1 Problem Description | 142 |
| 6.2 Numerical Treatment | 143 |
| 6.3 Results and Discussions | 144 |
| 6.3.1 Droplet Deformations and Temperature Fields | 144 |
| 6.3.2 Mass Fraction Fields | 146 |
| 6.3.3 Flow Field Developments | 148 |
| 6.3.4 Droplet Lifetimes | 151 |
| 6.3.5 Droplet Trajectories | 156 |
| 6.4 Summary of Results | 158 |

| | |
|---------------------------------------------------------------------------------------|------------|
| 7 Conclusions and Recommendations | 168 |
| References | 173 |
| Appendix A Thermodynamic Relationships | 181 |
| Appendix B Derivative Expressions in Soave-Redlich-Kwong Equation of State | 186 |
| Appendix C Numerical Jacobians in Preconditioning Scheme | 188 |
| Appendix D Numerical Model Validation | 192 |

List of Tables

| | | |
|------|---------------------------------------------------------------------------------------------|-----|
| 1.1 | Engine operation conditions and critical properties of fuels. | 1 |
| 2.1 | Coefficients of A_n . | 37 |
| 2.2 | Semi-empirical constants based on methane. | 37 |
| 2.3 | Coefficients for shape factor correlations. | 45 |
| 3.1a | Pressure effects on the properties of pure oxygen at 200K. | 74 |
| 3.1b | Pressure effects on the properties of pure hydrogen at 200K. | 74 |
| 3.1c | Pressure effects on the properties of oxygen and hydrogen at equal molar fractions at 200K. | 74 |
| 3.2 | Pressure effect on the density of oxygen and hydrogen. | 80 |
| 3.3 | Temperature effect on the density of hydrogen. | 81 |
| 5.1 | Droplet lifetimes at different numerical grids. | 111 |
| 5.2a | Pressure effects on thermophysical properties of hydrogen and oxygen. | 116 |
| 5.2b | Pressure effects on the combined parameters. | 116 |
| 5.3 | Properties of oxygen and hydrogen mixture at equal molar fractions and 200K. | 120 |
| 5.4 | Droplet lifetimes in a quiescent environment. | 120 |

List of Figures

| | | |
|------|----------------------------------------------------------------------------------------------------------------------------------------------------------------------------------------------------------------------|----|
| 2.1 | Boundary conditions at droplet surface (a) mass conservation; (b) species conservation; (c) energy conservation. | 30 |
| 2.2 | General phase diagrams of oxygen and hydrogen at different pressures. | 32 |
| 2.3 | Variations of the enthalpy of vaporization of oxygen at thermodynamic phase equilibrium states. | 40 |
| 2.4 | Illustration of numerical grids generated. | 51 |
| 3.1 | (a) Schematics of a droplet cluster and the inner region; (b) illustration of the numerical models. | 62 |
| 3.2 | Droplet lifetimes with an single droplet vaporization in an isolated impermeable bubble. | 63 |
| 3.3 | Droplet lifetimes with an isolated oxygen droplet vaporization in hydrogen environments at different pressures and temperatures. | 65 |
| 3.4 | Temporal variations of temperature at an ambient temperature of 1000 K and a pressure of 30 atm. | 66 |
| 3.5 | Temporal variations of oxygen mass fraction at an ambient temperature of 1000 K and a pressure of 30 atm. | 66 |
| 3.6 | Transient variations of dimensionless LOX droplet diameter squares at different interactive radius ratios with a pressure of 30atm and an ambient temperature of 1000K. | 68 |
| 3.7 | Transient variations of dimensionless LOX droplet diameter squares at different interactive radius ratios with a pressure of 100atm and an ambient temperature of 1000K. | 68 |
| 3.8 | Effect of droplet interactions on LOX droplet vaporization times at 1000K. | 70 |
| 3.9 | Effect of droplet interactions on LOX droplet vaporization times at 1500K. | 70 |
| 3.10 | Effect of droplet interactions on LOX droplet vaporization times at a pressure of 30atm. | 71 |
| 3.11 | Effect of droplet interactions on LOX droplet vaporization times at a pressure of 100atm. | 71 |
| 3.12 | Transient variations of droplet surface temperature at different pressures for both an isolated and an interacting LOX droplet. | 75 |
| 3.13 | Temperature distributions outside the droplets at a pressure of 30atm and an ambient temperature of 1000K for both an isolated and an interacting LOX droplet (1: 20%, 2: 40%, 3: 80% droplet mass vaporized). | 75 |
| 3.14 | Temperature distributions inside the droplets at a pressure of 30atm and an ambient temperature of 1000K for both an isolated and an interacting LOX droplet (1: 20%, 2: 40%, 3: 80% droplet mass vaporized). | 76 |
| 3.15 | Oxygen mass fraction distributions outside the droplets at a pressure of 30atm and an ambient temperature of 1000K for both an isolated and an interacting LOX droplet (1: 20%, 2: 40%, 3: 80% droplet mass | |

| | | |
|------|----------------------------------------------------------------------------------------------------------------------------------------------------------------------------------------------------------------------------------------------------------------------------------------------------------|-----|
| | vaporized). | 76 |
| 3.16 | Effects of ambient temperatures on temperature distributions outside an interacting LOX droplet at a pressure of 30atm when 80% droplet mass vaporized. | 78 |
| 3.17 | Effects of ambient temperatures on oxygen mass fraction distributions outside an interacting LOX droplet at a pressure of 30atm when 80% droplet mass vaporized. | 78 |
| 3.18 | Effects of pressures on temperature distributions outside an interacting LOX droplet at an ambient temperature of 1000K when 80% droplet mass vaporized. | 79 |
| 3.19 | Effects of pressures on oxygen mass fraction distributions outside an interacting LOX droplet at an ambient temperature of 1000K when 80% droplet mass vaporized. | 79 |
| 3.20 | Transient variations of bubble radii at different interactive radius ratios with a pressure of 30atm and an ambient temperature of 1000K. | 82 |
| 3.21 | Transient variations of bubble radii at different interactive radius ratios with a pressure of 100atm and an ambient temperature of 1000K. | 82 |
| 5.1 | Schematic of a supercritical droplet in a convective stream. | 108 |
| 5.2 | Part of the computational grids. | 109 |
| 5.3 | Transient developments of flow fields at $u=2.5\text{m/s}$, $p=100\text{atm}$ ($Re \approx 15$), at instants of $t=20, 100, 200, 400\mu\text{s}$, respectively. | 132 |
| 5.4 | Transient developments of flow fields at $u=5.0\text{m/s}$, $p=100\text{atm}$ ($Re \approx 30$), at instants of $t=12, 100, 150, 250\mu\text{s}$, respectively. | 133 |
| 5.5 | Transient developments of flow fields at $u=20.0\text{m/s}$, $p=100\text{atm}$ ($Re \approx 120$), at instants of $t=4, 20, 40, 60\mu\text{s}$, respectively. | 134 |
| 5.6 | Transient developments of flow fields at $u=5.0\text{m/s}$, $p=400\text{atm}$ ($Re \approx 120$), at instants of $t=10, 30, 60, 110\mu\text{s}$, respectively. | 135 |
| 5.7 | Vorticity distributions, (a) $u=2.5\text{m/s}$, $p=100\text{atm}$, $t=200\mu\text{s}$, (b) $u=5.0\text{m/s}$, $p=100\text{atm}$, $t=150\mu\text{s}$, (c) $u=20\text{m/s}$, $p=100\text{atm}$, $t=30\mu\text{s}$, (d) $u=5.0\text{m/s}$, $p=400\text{atm}$, $t=60\mu\text{s}$. | 136 |
| 5.8 | Transient developments of temperature contours at $u=2.5\text{m/s}$, $p=100\text{atm}$ ($Re \approx 15$), at instants of $t=20, 100, 200, 400\mu\text{s}$, respectively. | 137 |
| 5.9 | Transient developments of temperature contours at $u=5.0\text{m/s}$, $p=100\text{atm}$ ($Re \approx 30$), at instants of $t=12, 100, 150, 250\mu\text{s}$, respectively. | 138 |
| 5.10 | Transient developments of temperature contours at $u=20.0\text{m/s}$, $p=100\text{atm}$ ($Re \approx 120$), at instants of $t=4, 20, 40, 60\mu\text{s}$, respectively. | 139 |
| 5.11 | Transient developments of temperature contours at $u=5.0\text{m/s}$, $p=400\text{atm}$ ($Re \approx 120$), at instants of $t=10, 30, 60, 110\mu\text{s}$, respectively. | 140 |
| 5.12 | Distributions of oxygen mass fractions, (a) $u=2.5\text{m/s}$, $p=100\text{atm}$, $t=200\mu\text{s}$, (b) $u=5.0\text{m/s}$, $p=100\text{atm}$, $t=150\mu\text{s}$, (c) $u=20\text{m/s}$, $p=100\text{atm}$, $t=40\mu\text{s}$, (d) $u=5.0\text{m/s}$, $p=400\text{atm}$, $t=60\mu\text{s}$. | 141 |
| 5.13 | Effects of incoming velocities (Reynolds numbers) on the droplet vaporization rates at a pressure of 100atm. | 119 |
| 5.14 | Effects of incoming velocities (Reynolds numbers) on the droplet vaporization rates at a pressure of 400atm. | 119 |

| | | |
|------|-------------------------------------------------------------------------------------------------------------------------------------------------------------------------------------------------------|-----|
| 5.15 | Correlation of the dimensionless droplet lifetimes as a function of the Reynolds number and pressure. | 122 |
| 5.16 | Transient variations of droplet velocities and the linear relationships at a pressure of 100atm. | 124 |
| 5.17 | Transient variations of droplet velocities and the linear relationships at a Reynolds number of 60. | 124 |
| 5.18 | Correlation of the velocity coefficient b as a function of the Reynolds number and pressure. | 126 |
| 5.19 | Transient variations of droplet locations from both correlation and numerical computation at a pressure of 100atm. | 127 |
| 5.20 | Transient variations of droplet locations from both correlation and numerical computation at a Reynolds number of 60. | 127 |
| 6.1 | Two-droplets-in-tandem in a convective environment. | 142 |
| 6.2 | Part of the numerical grids for two-droplets-in-tandem. | 143 |
| 6.3 | Transient variations of temperature fields and droplet deformations at $p=100\text{atm}$, $u=10\text{m/s}$, and H/R ratio of 4 ($t=6, 60, 155$, and $200\mu\text{s}$, respectively). | 160 |
| 6.4 | Transient variations of temperature fields and droplet deformations at $p=100\text{atm}$, $u=10\text{m/s}$, and H/R ratio of 8 ($t=15, 145, 190$, and $225\mu\text{s}$, respectively). | 161 |
| 6.5 | Transient variations of temperature fields and droplet deformations at $p=100\text{atm}$, $u=10\text{m/s}$, and H/R ratio of 12 ($t=20, 60, 100$, and $150\mu\text{s}$, respectively). | 162 |
| 6.6 | Transient variations of oxygen mass fraction fields and droplet deformations at $p=100\text{atm}$, $u=10\text{m/s}$, and H/R ratio of 4 ($t=6, 60, 125$, and $200\mu\text{s}$, respectively). | 163 |
| 6.7 | Transient variations of oxygen mass fraction fields and droplet deformations at $p=100\text{atm}$, $u=10\text{m/s}$, and H/R ratio of 8 ($t=15, 60, 190$, and $225\mu\text{s}$, respectively). | 164 |
| 6.8 | Transient variations of flow fields at $p=100\text{atm}$, $u=20\text{m/s}$, and H/R ratio of 4 ($t=5, 40, 60, 85\mu\text{s}$, respectively). | 165 |
| 6.9 | Transient variations of flow fields at $p=100\text{atm}$, $u=20\text{m/s}$, and H/R ratio of 8 ($t=8, 40, 90, 110\mu\text{s}$, respectively). | 166 |
| 6.10 | Transient variations of flow fields at $p=100\text{atm}$, $u=20\text{m/s}$, and H/R ratio of 12 ($t=15, 40, 60, 80\mu\text{s}$, respectively). | 167 |
| 6.11 | Effects of incoming velocity and pressure on the flow fields, (a) $p=100\text{atm}$, $u=10\text{m/s}$, $t=145\mu\text{s}$, (b) $p=400\text{atm}$, $u=5\text{m/s}$, $t=115\mu\text{s}$. | 151 |
| 6.12 | Droplet vaporization rates at $p=100\text{atm}$, $u=20\text{m/s}$. | 153 |
| 6.13 | Droplet vaporization rates at $p=400\text{atm}$, $u=5\text{m/s}$. | 153 |
| 6.14 | Droplet lifetime ratios vs. H/R ratios at $p=100\text{atm}$. | 155 |
| 6.15 | Droplet lifetime ratios vs. H/R ratios at $p=400\text{atm}$. | 155 |
| 6.16 | Droplet trajectories for both the leading and trailing droplets at $p=100\text{atm}$, and $u=20\text{m/s}$. | 157 |
| 6.17 | Droplet trajectories for both the leading and trailing droplets at $p=400\text{atm}$, and $u=5\text{m/s}$. | 157 |

Nomenclature

| | |
|---------------|-------------------------------------------------|
| a | Constant in SRK equation of state |
| | Speed of sound |
| | Empirical parameter |
| A | Surface |
| | Thermodynamic expression |
| A_a | Control surface area |
| AR | Grid aspect ratio |
| b | Constant in SRK equation of state |
| | Empirical parameter |
| B | Thermodynamic expression |
| c | Empirical parameter |
| C_D | Drag coefficient |
| CFL | Courant-Friedrichs-Lewy Number |
| C_p | Constant-pressure heat capacity |
| C_v | Constant-volume heat capacity |
| D | Diameter |
| D_{ij} | Binary mass diffusion coefficient |
| D_{im} | Effective mass diffusion coefficient in mixture |
| e | Internal energy |
| \tilde{e}_i | Partial density internal energy of species i |
| e_t | Total internal energy |

| | |
|-------------|--------------------------------------------------------------------|
| E, F | Flux vector |
| f | Helmholtz potential |
| f_x | Equivalent substance temperature reduced ratio |
| F_η | Dimensional scaling factor in extended corresponding states theory |
| h | Enthalpy |
| \bar{h}_i | Partial mass enthalpy of species i |
| h_t | Total enthalpy |
| h_x | Equivalent substance volume reduced ratio |
| H | Droplet spacing |
| K_{vap} | Mass vaporization kinetic coefficient |
| Le | Lewis number |
| m | Mass |
| \dot{m} | Droplet mass vaporization rate |
| M_w | Molecular weight |
| \bar{n} | Outward unit normal surface vector |
| N | Total species number |
| Oh | Ohnesorge number |
| p | Pressure |
| p_g | Gauge Pressure |
| p_0 | Constant Pressure |
| P_i | Parachors of species i |

| | |
|-----------|----------------------------------------|
| Pr | Prandlt number |
| q_e | Thermal diffusion flux |
| q_i | Mass diffusion flux of species i |
| Q | Variable vector |
| r | Concentric sphere radius Coordinate |
| R | Droplet radius Viscous matrix |
| R_{bub} | Bubble radius |
| Re | Reynolds number |
| R_u | Universal gas constant |
| s | Entropy |
| S | Source term vector |
| Sc | Schmidt number |
| S_i | Parameter in SRK equation of state |
| t | Physical time |
| T | Temperature |
| u_x | Velocity in x-direction |
| u_r | Velocity in r-direction |
| v | Velocity |
| V | Volume |
| V_a | Control volume |

| | |
|--------------|------------------------------|
| VNN | von Neumann Number |
| w | Velocity at control surface |
| We | Weber number |
| x | x Coordinate |
| x_i | Mole fraction of species i |
| X | Correction factor |
| Y_i | Mass fraction of species i |
| T, A, B, D | Numerical Jacobians |

Greek Symbols

| | |
|---------------|-----------------------------------------------------|
| α | Soave temperature function in SRK equation of state |
| β | Scaling factor |
| γ | Strain-rate in BWR equation of state |
| ε | Numerical viscous coefficient |
| ξ | Coordinate quantity |
| λ | Thermal conductivity |
| | Eigenvalues |
| μ | Viscosity |
| | Chemical potential |
| ρ | Density |
| κ_{ij} | Binary interaction coefficient |
| l_{ij} | Binary interaction coefficient |

| | |
|------------------|-------------------------------------------|
| τ | Nondimensional Droplet lifetime |
| | Pseudo-time |
| Γ | Preconditioning matrix |
| $\dot{\omega}$ | Chemical reaction rate |
| ω | Acentric factor |
| ϵ | Energy shape factor |
| ϕ | Thermodynamic properties per unit mass |
| | Size shape factor |
| $\bar{\phi}_i$ | Partial mass properties of species i |
| $\tilde{\phi}_i$ | Partial density properties of species i |
| σ | Surface tension |

Subscripts

| | |
|-------|--------------------------------------|
| 0 | Initial quantity |
| | Ideal state |
| | Reference property |
| i | Species i |
| | Grid index i |
| in | Input quantity |
| + | Outside surface of droplet interface |
| - | Inside surface of droplet interface |
| bub | Bubble |

| | |
|--------|---------------------------------------------------|
| c | Critical state |
| d | Quantity of droplet |
| e | Energy |
| f | Fuel |
| g | Gas Phase |
| l | Liquid Phase |
| m | Mass |
| o | Oxidizer |
| p | Expression relative to pressure |
| r | Dimensionless Variable Quantity in r-direction |
| R | Dimensionless property Reference property |
| s | Quantity of surrounding fluid, hydrogen |
| T | Expression relative to temperature |
| v | Viscous term |
| x | Quantity in x coordinate |
| ρ | Expression relative to density |
| η | transport property |

Superscripts

| | |
|-----|---------------|
| g | Gaseous phase |
| l | Liquid phase |

| | |
|---------------|--------------------------------------------|
| r | In r coordinate |
| x | In x coordinate |
| \cdot | Time derivative |
| $-$ | Partial mass property |
| \rightarrow | Vector |
| \sim | Partial density property |
| \wedge | Vector variables in preconditioning scheme |

Chapter 1

INTRODUCTION

Spray combustion is an important phenomenon involved in various liquid-propellant combustion devices, including diesel engines, gas-turbine engines, liquid-propellant rocket engines, and oil-fired boilers. During spray injection, liquid fuel breaks up into small droplets through atomization, which then undergo a sequence of vaporization, mixing, and burning processes. The droplet vaporization rate has, therefore, great influence on the engine performance. In many practical liquid-fueled combustors, the chamber pressures and temperatures may well exceed the critical conditions of the injected fuels, as illustrated in Table 1.1. Therefore, droplet vaporization at high pressures has received considerable attention in the combustion community.

Table 1.1 Engine Operation Conditions and Critical Properties of Fuels

| Engines/Combustors | Fuels | Operation Conditions | Critical Properties of Fuel |
|---------------------------|--------------------|----------------------|------------------------------------|
| Space Shuttle Main Engine | Oxygen Hydrogen | 225 atm | 49.7 atm, 154.6K 13 atm, 33.2 K |
| Diesel Engine | Diesel Oil | > 50 atm | ~30 atm, ~650K |

High-pressure droplet vaporization exhibits many characteristics distinct from those of conventional low-pressure cases. The differences lie mainly in the following areas. First, high-pressure droplet vaporization is transient in nature, due mainly to the rapid droplet regression rate and the transient heating of the droplet interior. When the droplet surface reaches the critical mixing point, the sharp distinction between the liquid and gaseous phases diminishes, and the enthalpy of vaporization decreases down to zero, thereby leading to a high droplet vaporization rate. In addition, as gaseous properties are

strongly modified at high pressures, the diffusive velocity in the gaseous region becomes comparable to the droplet regressive motion, and the unsteadiness is further enhanced. With such a fast vaporization process, a uniform temperature distribution inside the droplet, which is commonly assumed for the quasi-steady case, may never be reached. The transient droplet heating may persist during the entire droplet lifetime, especially when supercritical conditions are reached. After that, there exists only one continuous fluid medium within which transient heat and mass transfer take place. Second, at high pressures, thermodynamic non-ideality becomes an important factor, which means the dissolution of ambient gas in the liquid droplet may not be neglected, and the partial molar enthalpies of both phases must be used to calculate the enthalpy of vaporization. The interfacial thermodynamic treatment must take into account these effects by means of an equation of state for real fluids, instead of the ideal equation of state. Finally, at high pressures, thermophysical properties become functions of temperature, pressure, and compositions. These include thermodynamic properties, such as enthalpy and the constant-pressure heat capacity, and transport properties, such as thermal conductivity and mass diffusivity. Furthermore, the property anomaly near the critical state becomes profound and must be treated properly.

1.1 Literature Survey

1.1.1 Droplet Vaporization in Quiescent Environments

1.1.1.1 Single Droplet Vaporization

The single droplet vaporization phenomenon has been studied since the 1950s. The earliest work is a one-dimensional low-pressure analytical solution by Godsave (1953), which was based on a few assumptions, including spherical symmetry, quasi-

steady state, constant and uniform pressure, etc. Spalding (1959) studied the combustion of a single fuel droplet at supercritical conditions, with an assumption that the droplet reaches the critical point immediately after being injected into the combustor. The droplet was further treated as a point source of mass. The analysis was later improved by Rosner (1967) to include a finite droplet mass. Both studies demonstrated the transient characteristics of droplet burning under supercritical conditions.

Wieber (1963) investigated a single droplet vaporizing in a convective environment using an empirical expression of the Nusselt number to calculate the heat transfer rate at the droplet surface. The liquid thermal conductivity was taken to be infinity by assuming rapid internal circulation within the droplet, which also implied a uniform distribution of temperature. Both heptane and oxygen droplets were studied with pressures up to 2000 psia. Results of temperature histories concluded that the droplet surface temperature could rise continuously and finally reach the critical point.

The similar problem was re-examined by a number of researchers (Brzustowski 1965, Chervinsky 1969, Polymeropoulos and Peskin 1972, Sanchez-Tarifa et al., 1972) in order to investigate the influences of convection, density variations, and finite-rate chemical kinetics. None of these early studies, however, provided faithful results, because many of the high-pressure characteristics, such as the thermodynamic nonideality and transport anomaly, were not taken into account.

A systematic investigation of high-pressure phenomena was first conducted by Manrique and Borman (1969). In their work, the concepts of non-ideal mixtures and transport property anomaly near the critical mixing point were introduced, while a quasi-steady vaporization model was employed to simplify the analysis. The droplet was

assumed to remain spherical symmetry with a uniform temperature distribution during the entire vaporization process, and the droplet regression rate was neglected. At the droplet surface, thermodynamic equilibrium was considered, with the dissolution of the ambient gas into the liquid phase confined within a thin layer near the droplet surface. It was demonstrated that the difference in the partial molar enthalpies of constituent species between the gaseous and liquid phases must be included in the energy equation to replace the latent heat of vaporization of the pure liquid species. The Redlich-Kwong equation of state was utilized to solve the two-component thermodynamic phase equilibrium problem, and to calculate the partial molar enthalpies. The carbon dioxide-nitrogen system was studied with ambient temperatures and pressures ranging from 500-1600K and 70-120 atm, respectively. The mass diffusivity was estimated from a corresponding-state chart, and the thermal conductivity was evaluated by using the Stiel and Thodos pure component correlation (1964), which treats the mixture as a hypothetical pure component with pseudocritical properties. The conclusion was that the thermodynamic non-ideality effects, such as the dissolution of ambient nitrogen in the liquid droplet and application of the partial molar enthalpies, and the transport property anomaly have significant influences at high pressures. Large errors may arise without considering them properly. For a given ambient temperature, steady-state vaporization may never be attained if the system pressure exceeds a threshold value. The droplet thus vaporizes unsteadily throughout its lifetime.

Following Manrique and Borman, Matlosz et al. (1972) studied n-hexane droplet vaporization in a stagnant environment of nitrogen and argon at pressures up to 102 atm, where the thermodynamic non-ideality effects on phase equilibrium and enthalpy of

vaporization were included. However, all the other thermophysical properties were taken to be constant. The transient behavior of droplet vaporization, such as surface regression, was taken into account, but the temperature inside the liquid droplet was still assumed to be uniform. The Redlich-Kwong equation of state was chosen to treat the high-pressure non-ideal mixture. Numerical results of the time histories of droplet temperature and radius were compared with experimental measurements. It was demonstrated that the non-ideal behavior of the gas phase, which includes the dissolution of gaseous species into the liquid droplet, is important at high pressures.

To clarify the systematic errors associated with the quasi-steady approximation in the droplet vaporization process when the droplet surface approaches its critical state, Rosner and Chang (1973) presented exact solutions for the transient vaporization of an isolated spherical droplet in a quiescent constant-property environment. Illustrative calculations were included for the case of a kerosene-like (n-dodecane) droplet evaporating into compression-heated air, similar to the conditions encountered in diesel engines. The non-ideality effects of gas dissolution in the droplet and the partial molar enthalpy were not considered, but it was indicated that the effects would not change the conclusion qualitatively. With pressures up to 2.96 times of the critical pressure, the quasi-steady theory would overestimate the droplet lifetimes by 47 percent, and the overestimation would reach 89 percent with the presence of an envelop flame. Results demonstrated that the evaporation process for an isolated fuel droplet near its critical condition could not be treated as quasi-steady.

These early works clearly show that high-pressure droplet vaporization is an unsteady process during which a droplet is continuously heated up, and the critical state

could eventually be reached. However, when a thermodynamic system transits from its subcritical to supercritical state, the singular behavior at critical state remains unclear. Umemura (1986) constructed an asymptotic analysis of the heat and mass transfer near the gas-liquid interface at the critical state of the mixture. He concluded that, within the range of validity of the so-called local equilibrium hypothesis and linear phenomenological relations, the mutual diffusion coefficient must vanish at the critical surface to ensure a finite evaporation rate in the critical condition.

In order to explore the natural convection effects on high-pressure droplet vaporization, Kadota and Hiroyasu (1976) investigated a single n-heptane droplet evaporating in high-pressure and high-temperature nitrogen environments. In this study, thermodynamic non-ideality was included, and thermophysical properties were calculated by fitted polynomials as functions of temperature and pressure. The effect of natural convection was treated using empirical relations of the Nusselt and Sherwood numbers. Jin and Borman (1986) applied a similar model to study the vaporization of multicomponent fuel droplets of pentane and octane in a nitrogen stream. The conclusion was that the difference of the evaporation rates between the two species decreases with increasing pressure, and the potential of micro-explosion is inhibited at high pressures.

Hsieh et al. (1991) conducted a comprehensive analysis of multicomponent fuel droplet vaporization at near critical conditions, based on transient conservation equations with a thorough treatment of property variations. Thermodynamic non-ideality effects on liquid dissolution and enthalpy of vaporization were modeled through the use of a modified Soave-Redlich-Kwong (SRK) equation of state, which was proved to be more accurate than the conventional Redlich-Kwong equation of state. A moving coordinate

system was employed to account for the droplet surface regression. Thermodynamic and transport properties, such as constant-pressure heat capacity and thermal conductivity, were treated as functions of temperature and pressure for each constituent species, and then evaluated for a mixture using appropriate mixing rules. Pressure effect on binary mass diffusivity was estimated using the Takahashi (1974) method. The analysis was used to study the vaporization process of single droplets containing either pure n-pentane or mixed n-pentane/n-octane in gaseous nitrogen at supercritical conditions. Calculations were carried out through either the end of droplet lifetime or the critical point. For multicomponent fuel systems, the droplet vaporization rate increases progressively with ambient pressure, and a droplet may reach its critical mixing state before the end of its lifetime for extreme cases.

Shuen et al. (1992) later extended the work by Hsieh et al. (1991) to study supercritical droplet combustion. In this analysis, complete conservation equations along with the consideration of bulk motion in the liquid phase were solved using the preconditioning dual-timing integration technique to overcome the numerical stiffness. Finite-rate chemical kinetics was accommodated for treating the gas-phase combustion. Once the droplet surface reached the critical mixing state, an isotherm line at the critical mixing temperature was employed to determine the gas-liquid interface, which allowed the model to compute entire droplet vaporization process. A n-paraffin fuel droplet burning in air was studied. Results for large droplets (e.g. 1000 μm in diameter) indicated that at subcritical conditions, the vaporization of liquid fuel dominates the burning characteristics of the droplet, while at supercritical conditions, the transient diffusion in the gas phase controls the combustion process. The combustion lifetime decreases with

increasing pressure, and reaches a minimum near the critical pressure of the liquid fuel. As pressure further increases, the combustion lifetime increases due to reduced mass diffusivity at high pressures, which is in qualitative agreement with the experimental observations of Faeth et al. (1969) and Sato et al. (1990).

This method was further extended by Yang et al. (1994) to treat liquid oxygen (LOX) droplet vaporization in a hydrogen environment. A modified Soave-Redlich-Kwong (SRK) equation of state was utilized with special attention focused on the quantum-gas behavior of hydrogen. Significant efforts were devoted to estimating the thermophysical properties as functions of pressure. The extended corresponding states model of Ely and Hanly (1981, 1983) was applied to evaluate thermal conductivity, heat capacity, and viscosity of real fluid mixtures. Various distinct high-pressure effects on droplet behavior were investigated in depth. Results indicated that droplet lifetime has strong pressure dependence, and can be well correlated with the square of the initial droplet diameter.

Lafon (1995) studied single droplet vaporization in a gaseous environment. Both cases of liquid oxygen (LOX) in hydrogen and hydrocarbon fuels in nitrogen were investigated. A unified treatment of thermodynamic properties and numerical algorithms for real fluid mixtures was carried out based on fundamental thermodynamic theories. The computational efficiency and robustness were significantly improved. A linear irreversible theory was formulated to calculate the mass vaporization rate at the droplet surface, which relates the vaporization rate to the difference of species chemical potential between the two phases. Extensive parametric studies were conducted, and results compared well with experimental measurements.

Haldenwang et al. (1996) also investigated the vaporization of liquid oxygen (LOX) droplet in a quiescent hydrogen environment. The transition from the subcritical to the supercritical vaporization regime was examined. After the droplet reached the supercritical vaporization regime, the droplet surface was defined based on the critical mixing mass fraction of oxygen, instead of the critical mixing temperature (Yang et al. 1994). A minimum of droplet lifetime at a pressure above the critical pressure of the fuel was revealed.

A few other researchers have conducted numerical analyses of high-pressure droplet vaporization in quiescent environments, notably Litchford and Jeng (1990), Curtis and Farrell (1992), Jia and Gogos (1993), Delplanque and Sirignano (1993), Umemura and Shimada (1996). The effect of ambient pressure oscillation on droplet behavior was also investigated (Lafon et al. 1995). Two recent review papers are available (Yang 2000, and Bellan 2000).

The research works mentioned above are all based on one conventional assumption that thermodynamic phase equilibrium prevails at the droplet surface, which is compatible with the local equilibrium hypothesis for defining local thermodynamic variables, such as temperature and density. Recently, an attempt was made to investigate this problem using non-equilibrium theory. Harstad and Bellan (1998) developed a model to study liquid oxygen (LOX) droplet vaporization in a hydrogen environment. The conservation equations were derived based on the fluctuation theory of Keizer (1987), which account for both Soret and Dufour effects in the calculation of heat and mass fluxes. A non-equilibrium evaporation law was incorporated to treat the mass vaporization flux at the droplet surface, which calculates the flux at the molecular level.

In this work, however, the non-equilibrium formulation played no role in the entire computation, because only supercritical conditions were investigated. The same model was applied to study n-heptane droplet vaporization in a nitrogen system (Harstad and Bellan, 1999). Because of the lack of methods to calculate the thermal diffusion factor at high pressures, this parameter was determined with arbitrariness. After the droplet surface reached critical condition, it was defined at the position of the maximum density gradient in order to be compared with optical measurements (Sato 1993, Nomura 1996, Morin 1999). Reasonably good agreements were obtained with microgravity experiments at low pressures (from 0.1-0.5 MPa), but obvious differences still exist at high pressures (1-2 MPa). Because these microgravity experiments were conducted with droplets suspended on a fiber in parabolic flights or drop tower, the effects of buoyancy and suspending fiber become more profound at high pressures (Vieille et al. 1996, Morin 1999). It is not clear what causes the differences between the simulation and experimental results.

Recently, limited success has also been achieved for exploring supercritical droplet vaporization using molecular dynamics (MD), which directly simulates the behavior of the molecules (Kaltz et al. 1998). A detailed description of this method is beyond the scope of this thesis. Additional information about the current progresses in this field is available in the review paper by Sirignano and Delplanque (1999).

1.1.1.2 Droplet Cluster Behavior

In practical spray combustors, there is no evidence that a droplet behaves in an isolated manner. In contrast, droplets normally vaporize and burn as a group (McCreath

and Chiger 1973). Because there are thousands of droplets involved in the problem, simplifications are required in numerical analyses.

Tishkoff (1979) studied the effect of droplet interactions by modeling the evaporation of a droplet inside a "bubble". The "droplet-in-bubble" concept was developed based on the cellular model of Zung (1967), and considerable improvement was achieved. The droplets were assumed to be monosized and distributed uniformly in a group. During the entire vaporization process, all the droplets, whether on the boundary or inside the cluster, remained a spherical shape and evaporated in a quiescent environment. The difference from the single droplet case is that a droplet is now evaporating in a finite space, a bubble. The heat and mass transfer between the droplet cluster and the outside environment were equally distributed to each bubble. Corresponding to different interactions between the droplet cluster and outside environment, the bubble could be impermeable or permeable to heat and mass transfer. The quasi-steady conservation equations of mass, species, and energy were solved within the bubble. Results show that saturation occurs before vaporization can be complete in small bubbles. Ambient pressure and temperature produce large effects on droplet interactions. An increase of either of them could cause a shift from incomplete to complete vaporization.

Bellan and Cuffel (1983) developed a theory of dense spray evaporation based on the scheme of single droplet vaporization in a finite sphere and the globe conservation equations for the two-phase mixture. Just like Tishkoff (1979), the monosized droplets were assumed to distribute uniformly inside the droplet cluster. Each droplet was surrounded in a finite space, called "sphere of influence", the radius of which is the half-

distance between the centers of two neighboring droplets. The interstitial regions among the spheres of influence possessed uniform time-dependent variables, which were obtained by solving the globe conservation equations. A method for solving single droplet vaporization was applied within the sphere of influences. The variables in the interstitial regions serve as the outside boundary conditions. Since the variables are uniform within the entire interstitial regions and each droplet evaporates in a same manner, the globe conservation equations for the droplet cluster could be simplified to include only the single droplet, its sphere of influence, and its related interstitial region. The only difference between this model and the model proposed by Tishkoff (1979) is the treatment of the interstitial region, which is considered as a separated space in this model, but incorporated into the bubble in the "droplet-in-bubble" model. Results obtained with an adiabatic n-decane droplet cluster evaporating in the air indicated that there are distinct characteristics that could not be described adequately in the single and dilute droplet vaporization theories. Bellan and Harstad (1987) further extended this dense droplet vaporization model to include convection effect. In the new method, a droplet still evaporated in a quiescent sphere of influence, while the convection effect on the vaporization rate was accounted for using an empirical correlation.

All these early investigations are related to low-pressure droplet cluster behavior. Jiang and Chiang (1994) studied the vaporization of a dense droplet cluster in both sub- and super-critical environments. Droplet interactions were accounted for using the "sphere of influence" concept (Bellan and Cuffel 1983). The transient conservation equations for both gas and liquid phases within the sphere of influence were solved with consideration of high-pressure effects, including thermodynamic nonideality and

transport anomaly, which followed the theoretical formulations of Hsieh et al. (1991) for the single droplet case. The boundary conditions at the edge of the sphere were determined by solving the globe conservation equations for the interstitial regions, where space-uniform variables were assumed. An adiabatic and impermeable cluster of n-pentane droplets vaporization in gaseous nitrogen was studied over a pressure range of 1-60 bar. The predictions for dilute sprays are in qualitative agreement with those of single droplet vaporization. Droplet lifetimes are significantly prolonged within a dense spray, and complete vaporization can not be achieved once a threshold value of the sphere of influence is reached. Droplet interaction effects decrease monotonically with the increase of ambient pressure.

The same authors (Jiang and Chiang 1996) improved their earlier method to include the interactions between the droplet cluster and the outside high-temperature environment. The sphere of influence was allowed to move (expansion or contraction) as a result of the constant-pressure condition. The variables in the interstitial regions were still assumed to be uniform in space, but varied temporally through interactions with both the sphere of influence and the outside gaseous environment. The outside gaseous field was assumed quiescent and spherically symmetric, where the variable distributions were determined by solving the one-dimensional conservation equations of mass, energy, and species. A dense cluster of n-pentane droplets vaporization in nitrogen environments was numerically investigated at two pressures of 5 and 60 bar. It was concluded that, at a supercritical condition (e.g., 60 bar), the surrounding temperature outside the droplet cluster has only limited effects on the heat-up of the droplet cluster. This is an important conclusion, because, in this study, the assumption was that the interstitial regions over the

entire droplet cluster were simultaneously heated up by the outside high-temperature gas environment. In practical situations, thermal penetration should take a longer time for the droplets in the inner region of the cluster to feel the influence. Therefore, heat transfer with the outside environment should not affect the droplet in the inner region of the droplet cluster.

Harstad and Bellan (1998) developed a numerical model to investigate the droplet behavior in a cluster, which is based on the “sphere of influence” concept (Bellan and Cuffel 1983) coupled with the high-pressure isolated droplet formulations (Harstad and Bellan 1998). Heat and mass transfer from the outside environment to the cluster are accounted for using an empirical correlation of the Nusselt number. A cluster of liquid oxygen (LOX) droplets vaporization in hydrogen environments at supercritical conditions was studied, with pressure ranging from 10 to 80 MPa. Because the value of the Nusselt number was chosen arbitrarily, sensitivity studies were conducted. Results indicated that droplet vaporization in the droplet cluster is insensitive to the value of Nusselt number over three orders of magnitude, which is consistent with the conclusion of Jiang and Chiang (1996) that outside heat transfer to the droplet cluster only presents minor effect.

1.1.2 Droplet Vaporization in Convective Environments

In practical combustion devices, droplets are generally moving relative to the gaseous environment. Therefore, the study of droplet vaporization in high-pressure convective environments is a very important research issue. Under convective conditions, a droplet may undergo severe deformation and even break-up. The droplet geometry becomes an unknown shape, which must be solved as part of the solution. In order to solve this problem, a numerical algorithm must have the ability to track an arbitrarily

shaped moving interface or discontinuity. For moving boundary problems, a few methods have been developed to track or capture the moving interface, which can be divided into two categories: the front-capturing, and front-tracking approaches. In the front-capturing method, the entire computational domain is discretized using a finite volume method, and artificial viscosity is possibly added to avoid oscillations. The enthalpy method (Voller and Prakash 1987) used in the material processing area belongs to this category. The other algorithms are the marker-in-cell (Harlow and Welch 1965), volume-of-fluid (VOF) (Hirt and Nichols 1981), and level-set (Sussman, Smereka, and Osher 1994) methods. In all these treatments, stationary Eulerian grids are utilized and the interface position and shape are reconstructed after each computational step by using markers, fractional volume, or a level-set function, which are advected with the local flow velocities. The disadvantage of these methods is that while merger and break-up of the interface can be well handled, they can not be treated with precision because the interface positions are not known explicitly. In the front-tracking methods, the discontinuous interface is represented by a set of connected points, which are tracked explicitly during the entire computational time. The other numerical grids can be either stationary, such as in the cut-cell method (Udaykumar 1994) and the immersed boundary technique (Tryggvason and Unverdi 1990, Unverdi and Tryggvason 1992), or in motion, such as in the arbitrary Lagrangian-Eulerian (ALE) method (Hirt, Amsden, and Cook 1974) and arbitrary moving mesh method (Welch 1993, Welch 1995). In the immersed boundary method, the interface is not kept sharp but rather given a finite thickness at the order of the mesh size. Thus, this method is not suitable for solving the high-pressure phase change problems. The cut-cell method is initially developed to treat solid-liquid

interfaces in the solidification problems. For the fluid-fluid interfaces, however, the method is proved to be sensitive to noise and is difficult to stabilize. Therefore, the current methods that are appropriate for solving high-pressure phase change problems are the arbitrary Eulerian-Lagrangian (ALE) method, which was applied for droplet deformation and vaporization by Deng and Jeng (1992), and the arbitrary moving mesh method. In both methods, there are explicit discontinuous interfaces where the boundary conditions regarding phase change can be applied.

1.1.2.1 Single Droplet Vaporization in Convective Environments

Welch (1993, 1995) studied a single-component liquid droplet vaporization in its own vapor. This is not a droplet vaporization case in spray combustors, but there are physical similarities between them, such as the treatment of the phase-changing interface and the interfacial thermodynamics. In this work, the interface was tracked explicitly by the computational nodes representing the liquid and vapor interfaces. Two nodes located in the same spatial position are needed to represent both phases. The interface motion is found by solving the interfacial boundary conditions and the bulk flow equations. The movements of the computational nodes in the bulk regions were designed to limit the amount of distortion of the mesh near the interface during deformation process. Their positions at the new time level were determined by interpolation between the movements of the outside boundary and the interface at the previous time level. Triangular meshes were utilized, which is more endurable in terms of the mesh distortion. Despite all these efforts, the fluid flows are still restricted to those in which the interfaces do not undergo significant distortions or change topological features.

Deng and Jeng (1992) studied n-heptane droplet vaporization in nitrogen gas at 40 atm, with the inflow gas temperature and velocity ranging from 500 to 1000 K, 2 m/s to 10 m/s, respectively. Special attention was devoted to droplet deformation and breakup using the Arbitrary Lagrangian-Eulerian (ALE) method. In this algorithm, the computational grids are first moving at local velocities. Then a rezone step, during which a new set of grids is generated and all the variables are updated, is utilized to avoid grid distortion. It is very expensive to generate a new set of grids and update variables at each time step. Despite of all these efforts, the scheme still could not handle flow situations after droplet break-up. Computation was terminated once the break-up occurred. Results indicated that the interfacial momentum exchange between gas and liquid not only moves the droplet downstream, but also deforms the droplet. Two types of droplet breakup, bag- and stripping-types, were found, which are sensitive to the gas phase velocity but insensitive to the gas temperature.

Because of the lack of reliable methods to track the phase changing interface with an unknown shape, the problem of forced-convection droplet vaporization is very difficult to handle. In order to avoid this difficulty, one common treatment is to assume the droplet remains a spherical shape during the entire vaporization process, which is valid only with the presence of extremely strong surface tension at low ambient pressures. A few works have been conducted for investigation of the vaporization of hydrocarbon fuels in convective environments.

Haywood et al. (1989) made a detailed examination of the evaporation of an n-heptane droplet in air at 800 K and 1 atm with an initial Reynolds number of 100. The effects of variable thermophysical properties, liquid phase motion and heating, regression

of droplet size, and transient variations of droplet velocity were considered in the numerical analysis. The droplet was assumed to maintain a spherical shape without deformation. Relationships were established for the transient variations of heat transfer rate (Nusselt number), mass transfer rate (Sherwood number), and drag coefficient.

The similar problem was also studied systematically by Chiang et al. (1992), where variable properties, regression of droplet size, transient droplet heating, and deceleration of the flow due to the drag action on the droplet were included. A spherical droplet was also assumed. Different fuel types, such as n-octane, n-decane, n-hexane, were considered, with the initial Reynolds numbers ranging from 50 to 150. Other parametric studies include initial droplet temperature and ambient temperature. Correlations regarding transient heat and mass transfer rates and droplet drag coefficient were established, which are different from those of Haywood et al. (1989) due to strong surface blowing. The conclusion was that the drag coefficient might increase or decrease over different portions of the droplet lifetime, while the Nusselt and Sherwood numbers follow a same gently decreasing trend.

For a supercritical droplet vaporizing in convective environments, a reasonable simplification is to assume the droplet reaches the critical mixing state immediately after being injected into the combustor. This is an approximation for most hydrocarbon fuels, but it is actually true for an oxygen droplet vaporizing in hydrogen environments at supercritical conditions, as demonstrated by the results regarding an isolated droplet vaporizing in a quiescent environment (Yang et al. 1994, Lafon 1995). Once the droplet reaches critical state, enthalpy of vaporization and surface tension vanish, and a continuous flow field is retained. A few research works have been conducted in this area.

Lee et al. (1990) analyzed the dispersion of a preheated fuel droplet that was suddenly set into motion in a gaseous environment at the same density. Temperature was assumed uniform in the entire flow field, and density and physical properties were treated as constants. The Schmidt number was taken to be unit. The initial droplet injection process was modeled by instantly imposing a harmonic vortex sheet at the droplet surface, which implies that the flow is totally induced by the vorticity. In this analysis, the transient axisymmetric stream function-vorticity and species equations were solved to determine the evolution of the vorticity distribution, species mixing, and droplet deformation. Two cases with the Reynolds numbers of 50 and 200 were studied. The study found that a mushroom-like droplet shape is formed due to strong droplet deformation, which is caused by the evolution of the vorticity and a formation of a ring vortex. The conclusion was that fuel vapor mixing is strongly produced by the vortex ring, and the fuel concentration gradient is higher around the axisymmetric axis, indicating an enhanced entrainment of ambient gas and mixing at the spiral tip. The effects are stronger at a higher Reynolds number.

Daou and Rogg (1998) investigated numerically the combustion of a supercritical fuel droplet suddenly set into motion in a high-temperature oxidizing environment. In this work, thermal conductivity, viscosity, the constant-pressure heat capacity, and the molecular weight of the gas mixture, as well as the product of density and mass diffusivity were taken as constants. The Burke-Schumann flame-sheet model was adopted, and the Lewis number was assumed as unit. Combustion was described using an irreversible one-step reaction mechanism. Density was further assumed to obey the ideal-gas equation of state. At a Reynolds number of 100, a large recirculating wake is formed

at the back of the droplet. The droplet experiences a substantial deformation, especially a stretching perpendicular to the symmetric axis, which was attributed to the combined effects of non-uniform pressure distribution and vorticity. The study was focused on the combustion time, which is defined as the time required to consume all the fuel mass. Due to deformation and straining of isoscalar surface, the dependence of combustion time on the magnitude of heat and mass diffusion decreases rapidly with the increase of the Reynolds number. Once the Reynolds number exceeds a few hundreds, the combustion time becomes independent of the diffusivity, and is proportional to the convective time multiplied by the square root of density ratio. The study concluded that the combustion time increases with increasing heat release as a result of gas expansion and the decrease of the scalar gradients. Droplet deformation becomes weaker at a higher heat release. Because of the simplicities regarding thermophysical properties, the results of supercritical droplet combustion and fuel mixing in these two works (Lee et al. 1990, Daou and Rogg 1998) should be used with caution.

In light of the apparent flaws with evaluations of thermophysical properties in the earlier works, Hsiao (1995) investigated systematically the problem of a supercritical oxygen droplet vaporization in convective hydrogen environments, where the pressure effects on thermophysical property evaluations have been carefully taken into account. In order to achieve high accuracy of density prediction, the Benedict-Webb-Rubin (BWR) equation of state was utilized with an extended corresponding state (EXCST) principal. The same principal was also adopted for evaluating all the thermodynamic properties, such as enthalpy and heat capacity. Thermal conductivity and viscosity were estimated by the corresponding states method proposed by Ely and Hanley (1981, 1983), and the

pressure effect on the binary mass diffusivity was calculated by the Takahashi (1974) scheme. Droplet deformation and droplet lifetimes at supercritical pressures were studied extensively. Results indicate that ambient flow strongly influences droplet evolution and changes the droplet vaporization rate and dynamic characteristics. Correlations of aerodynamic drag coefficient and droplet lifetime were established as functions of ambient pressure and the Reynolds number. Due to the complexity of the BWR equation of state, the pressure effects on the thermodynamic relationships in the numerical scheme were not considered properly in this work, which could cause inconsistency. In addition, the thermodynamic properties of a real fluid mixture, such as the partial mass or partial molar enthalpy, were not taken into account

1.1.2.2 Droplet Interactions in Convective Environments

In convective environments, droplet interactions present features distinct from those in a quiescent environment. Because of the complexity of droplet interactions in convective environments, numerical investigations are focused on the influences from the immediate neighboring droplets on droplet dynamics, such as drag coefficient and droplet collision/separation phenomenon.

Patnaik (1986) made an effort to investigate the interacting effects with two evaporating droplets moving in tandem with respect to the free stream. The complete set of conservation equations of mass, energy, and species were considered with full account of internal circulation and transient heating within the liquid phase, and variable density, but all the other thermophysical properties were taken as constants. Droplet deformations were neglected. The two droplets were treated separately, and the downstream solution of the leading droplet was used as the inflow conditions of the trailing droplet. In this way,

the influence of the leading droplet on the trailing droplet was studied, but the influence of the trailing droplet on the leading droplet was neglected. Moreover, the transient variations of the distance between the two droplets could not be investigated.

Raju and Sirignano (1990) examined the same problem, but allowed the two droplets moving relative to each other. Studies were conducted over a limited range of initial Reynolds numbers, interdrop spacings, and droplet radius ratios. Results indicated that when the interdrop spacing is sufficiently large, both droplets behave as an isolated droplet. Decreasing the interdrop spacing, the trailing droplet is fully covered by the wake of the leading droplet, resulting in the reduced drag coefficient and heat transfer rate for the trailing droplet. For equal sized droplets, collision occurs for all the Reynolds numbers and interdrop spacings studied. Decreasing the size of the trailing droplet to a certain limit, the two droplets never collide. The droplet radius ratio at this limit was termed bifurcation ratio.

Chiang (1990) extended the work by Raju and Sirignano (1990) to include the variable thermophysical properties due to the conclusion that the drag coefficient could be overestimated by at least 20% for the constant-property case. Extensive parametric studies were conducted regarding the effects of initial Reynolds numbers, interdrop spacings, droplet radius ratios, different fuel types, as well as ambient temperatures and initial droplet temperatures. The study concluded that the drag coefficient and Nusselt and Sherwood numbers of the trailing droplet are significantly lower than those of the leading droplet. The droplet spacing could increase or decrease with time, depending on the initial Reynolds number, initial interdrop spacing, and droplet radius ratio. Consistent with the earlier results (Raju and Sirignano 1990) at a given initial interdrop spacing,

there exists a critical droplet radius ratio (bifurcation ratio) below which droplet collision can not occur. Furthermore, the critical ratio increases when the initial Reynolds number decreases. Chiang (1990) also studied three-droplet-in-tandem vaporization in convective environments. Results indicated that the general conclusions drawn from two-droplet analysis could be applied to the two neighboring droplets in the three-droplet case.

All the studies above are regarding droplet interactions at low pressures. There is no investigation being conducted for the supercritical droplet interactions in convective environments.

1.2 Research Objectives

The physical and chemical mechanisms involved with high-pressure droplet vaporization and combustion are extremely complicated. Many intricate flow, transport, and combustion processes occur in various parts of the liquid and gaseous phase regions. In view of the inadequacy of existing theories and experimental techniques, especially for the liquid oxygen (LOX) vaporization in gaseous hydrogen case, a numerical investigation of the problem is conducted here. Special efforts are devoted to consider the pressure effects on thermophysical properties. Thermodynamic nonideality and transport anomaly will be treated properly. A robust all-fluid numerical algorithm is developed, in which the real fluid effects are treated consistently with full account of pressure effects. For droplet vaporization in convective environments, a small Mach-number region exists inside the droplet. Therefore, the preconditioning numerical algorithm with the dual time-stepping integration technique is applied to solve the unsteady flow field.

The overall objective of this work is to answer some of the fundamental questions regarding liquid-propellant droplet vaporization and combustion in high-pressure environments. Specific program objectives are:

1. to develop a robust all-fluid numerical algorithm, which is capable of treating the fluid fields over the entire thermodynamic regime, ranging from dense liquid to dilute gas. A unified treatment of the real fluids regarding both thermodynamic property evaluation and numerical relationship derivation is developed based on fundamental thermodynamic theories, which is valid for any equation of state. Full account is also taken for the pressure effects;
2. to study droplet cluster behavior at both sub- and super-critical conditions. In view of the complexity of the problem, the one-dimensional simplification is accepted, and the droplet interactions are treated by droplet vaporization in a "bubble". This represents the practical situation occurring in the inner region of a dense droplet cluster;
3. to investigate droplet vaporization in forced convective environments at supercritical conditions. A droplet will be assumed to reach the critical mixing state immediately after being injected into the combustor. The initial Reynolds number and pressure effects on droplet lifetimes, droplet deformations, and droplet dynamics will be explored in detail;
4. to examine droplet interactions in forced-convection environments at supercritical conditions. Two-droplet-in-tandem vaporization in convective environments is studied over a wide range of initial Reynolds numbers, pressures, and interdrop spacings. The effects of droplet interactions on

droplet lifetimes, droplet deformations, and droplet dynamics will be investigated.

The current numerical research represents a series of investigations into the behavior of liquid-propellant droplets at elevated pressures and temperatures. Results are extremely helpful for understanding the fundamental mechanisms of droplet vaporization and combustion. This thesis is arranged in the following manner. The theoretical formulations for an isolated droplet vaporization in a quiescent environment, including the conservation equations and thermophysical property evaluation methods, are described in Chapter 2. The numerical solution procedures are also described in detail. Chapter 3 presents the results regarding droplet cluster behavior. The studies are focused on the effects of ambient pressures and temperatures. In Chapter 4, a robust all-fluid numerical algorithm with the preconditioning technique is developed. Details of numerical derivations are presented. The numerical algorithm is applied to study supercritical droplet vaporization in convective environments in Chapter 5, where useful correlations of droplet lifetime and drag coefficient are established. Chapter 6 discusses droplet interactions with two-droplet-in-tandem vaporization in supercritical convective environments. Conclusions of the present research and recommendations for future works are summarized in Chapter 7.

Chapter 2

THEORETICAL FORMULATIONS OF SUPERCRITICAL DROPLET VAPORIZATION IN QUIESCENT ENVIRONMENTS

Based on the extensive literature survey, there are clearly distinct characteristics between high-pressure droplet vaporization and its low-pressure counterpart. In order to model supercritical droplet vaporization phenomenon accurately, the following features must be considered in the numerical treatment: 1) Transient conservation equations of mass, energy, and species for both the liquid and gaseous phases have to be established with the proper account of the droplet surface regression rate; 2) Thermodynamic non-ideality, including the pressure dependent gaseous dissolution in the liquid droplet and the partial molar enthalpy for calculating the enthalpy of vaporization, must be included; and 3) Pressure effects on the thermophysical properties must be taken into account with proper treatment of transport anomaly in the transcritical region. In this chapter, theoretical formulations of supercritical droplet vaporization in quiescent environments will be established.

2.1 Conservation Equations

A droplet is assumed to evaporate in a quiescent microgravity environment, and the flow field is thus spherically symmetric. The other reasonable simplifications are as follows:

- 1) Pressure remains constant during the entire vaporization process due to small flow velocity compared with the acoustic wave. This assumption has been justified by Jia and Gogos (1993);

- 2) The Soret and Dufour effects are neglected, which is justified by Curtis and Farrell (1992), and Lafon (1995);
- 3) Thermal radiation is neglected.

Based on these assumptions, the transient conservation equations are presented in the following forms:

- 1) Mass conservation

$$\frac{d}{dt} \int_{V_a(t)} \rho dV + \int_{A_a(t)} \rho(\bar{v} - \bar{w}) \cdot \bar{n} dA = 0 \quad (2.1)$$

- 2) Momentum conservation

$$\nabla p = 0 \quad (2.2)$$

- 3) Energy conservation

$$\frac{d}{dt} \int_{V_a(t)} \rho e_t dV + \int_{A_a(t)} \rho(\bar{v} - \bar{w}) e_t \cdot \bar{n} dA = - \int_{A_a(t)} \bar{q}_e \cdot \bar{n} dA - \int_{A_a(t)} p \bar{v} \cdot \bar{n} dA \quad (2.3)$$

- 4) Species conservation

$$\frac{d}{dt} \int_{V_a(t)} \rho Y_i dV + \int_{A_a(t)} \rho Y_i (\bar{v} - \bar{w}) \cdot \bar{n} dA = - \int_{A_a(t)} \bar{q}_i \cdot \bar{n} dA \quad (2.4)$$

where $i = 1, N-1$, and N is the total species number. Therefore, Eq. 2.4 represents $N-1$ species equations. The physical variables $\rho, \bar{v}, e_t, p, Y_i$ are density, velocity, specific total internal energy, pressure, and species concentration respectively. \bar{w} represents the moving velocity of the control surface. V_a, A_a are the volume and surface area of the control volume. \bar{n} is the unit vector normal to the control surface. The specific total internal energy is expressed as

$$e_t = e + \frac{\bar{v}^2}{2} \quad (2.5)$$

where e is the internal energy.

The diffusive flux terms \bar{q}_e, \bar{q}_i in Eqs. (2.3) and (2.4) are determined by Fourier's and Fick's Laws, respectively.

1) Species diffusion

$$\bar{q}_i = \rho Y_i (\bar{v}_i - \bar{v}) = -\rho D_{im} \nabla Y_i \quad (2.6)$$

where \bar{v}_i is the velocity of species i . D_{im} is the effective mass diffusivity of species i in the mixture, which is determined in terms of binary mass diffusivity D_{ij} (Bird et al. 1960),

$$D_{im} = (1 - x_i) / \sum_{i \neq j}^N (x_j / D_{ij}) \quad (2.7)$$

2) Energy diffusion

Energy diffusion consists of two parts. One is the thermal conduction term, and another term is related to mass diffusion.

$$\bar{q}_e = -\lambda \nabla T - \sum_{i=1}^N \bar{q}_i \bar{h}_i \quad (2.8)$$

where λ is thermal conductivity, and \bar{h}_i is the partial mass enthalpy of species i , which is defined later in this chapter.

2.2 Boundary Conditions

2.2.1 Initial Boundary Conditions

Inside the liquid droplet, initially a uniform temperature is prescribed, and there is no fluid flow and no gaseous species,

$$\begin{aligned}
T_{l,0} &= T_{l,in} \\
Y_{f,0} &= 1 \\
Y_{O,0} &= 0 \\
\bar{v}_{l,0} &= 0
\end{aligned} \tag{2.9}$$

where, $T_{l,0}, T_{l,in}$ are the initial liquid temperature and the prescribed liquid temperature respectively. $Y_{f,0}, Y_{O,0}$ are the initial fuel mass fraction and the mass fraction of the gaseous species. $\bar{v}_{l,0}$ is the initial liquid velocity.

The initial gaseous temperature is also assumed to be uniform, and there is no velocity and no fuel species in the gaseous phase,

$$\begin{aligned}
T_{g,0} &= T_{g,in} \\
Y_{f,0} &= 0 \\
Y_{O,0} &= 1 \\
\bar{v}_{g,0} &= 0
\end{aligned} \tag{2.10}$$

where the subscript g refers to the gaseous phase, and all the other nomenclatures are the same as those in the liquid phase, as defined above.

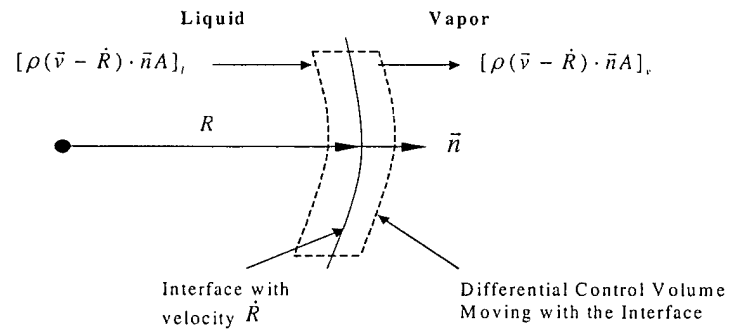
At droplet surface, the conventional assumption of thermodynamic phase equilibrium holds, resulting in the equality of temperature, pressure, and chemical potentials between the two phases. Accordingly, the equilibrium mass fractions in both sides can be calculated. The thermodynamic phase equilibrium boundary conditions will be established in detail later.

2.2.2 Boundary Conditions at Droplet Center and Outside Field

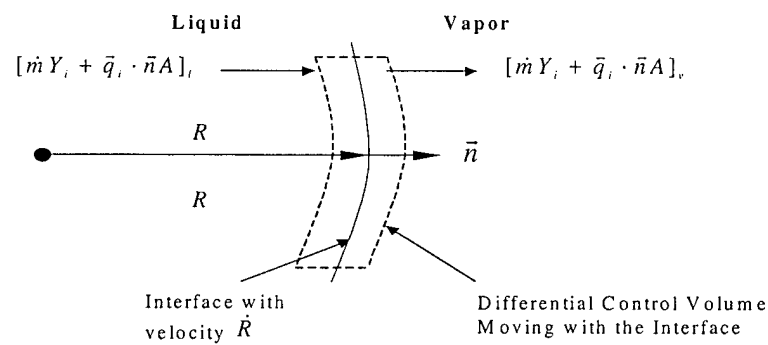
Spherical symmetry boundary conditions remain at the droplet center,

$$\begin{aligned}
\nabla T &= 0 \\
\nabla Y_i &= 0 \\
\bar{v} &= 0
\end{aligned} \tag{2.11}$$

(a)



(b)



(c)

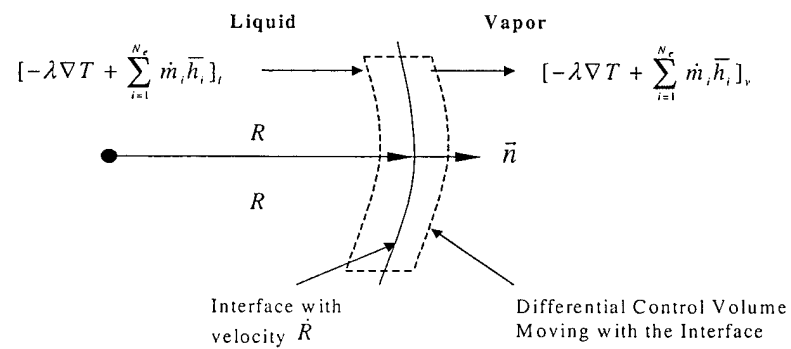


Fig. 2.1 Boundary conditions at droplet surface (a) mass conservation; (b) species conservation; (c) energy conservation

Outside boundary is maintained at a distance of 100 times of the droplet radius from the droplet center. All the variables there will not be affected by droplet vaporization and remain at their initial values.

2.2.3 Boundary Conditions at Droplet Interface

Phase change occurs at droplet surface, where undergo rapid heat and mass transfer. Mass, energy, and species across the surface must be conserved, as shown in Fig. 2.1. The conservation equations are

$$\dot{m} = \rho(\vec{v} - \dot{R}) \cdot \vec{n} A|_{r=R_+} = \rho(\vec{v} - \dot{R}) \cdot \vec{n} A|_{r=R_-} \quad (2.12)$$

$$\dot{m}_i = [\dot{m}Y_i + \vec{q}_i \cdot \vec{n} A]_{r=R_+} = [\dot{m}Y_i + \vec{q}_i \cdot \vec{n} A]_{r=R_-} \quad (2.13)$$

$$-\lambda \nabla T|_{r=R_-} = -\lambda \nabla T|_{r=R_+} + \sum_{i=1}^N \dot{m}_i (\bar{h}_i^g - \bar{h}_i^l) \quad (2.14)$$

where \dot{R} is the droplet regression rate, \dot{m} the mass vaporization rate, and \dot{m}_i the vaporization rate of species i .

Except for these conservation equations, thermodynamic phase equilibrium is also assumed at the droplet surface, which means temperatures, pressures, and chemical potentials at both sides of the surface must be equal (Callen 1985),

$$\begin{aligned} T^g &= T^l \\ p^g &= p^l \\ \mu_i^g &= \mu_i^l \end{aligned} \quad (2.15)$$

This general expression of thermodynamic phase equilibrium can naturally take into account the dissolution of gaseous species in the liquid droplet, which becomes extremely important with the increase of pressure. As a specific example, the phase diagrams of liquid oxygen (LOX) in gaseous hydrogen are illustrated in Fig. 2.2. In Fig.

2.2, the pressure dependent solubilities are clearly illustrated, where the critical mixing states are also shown to depend strongly on pressure.

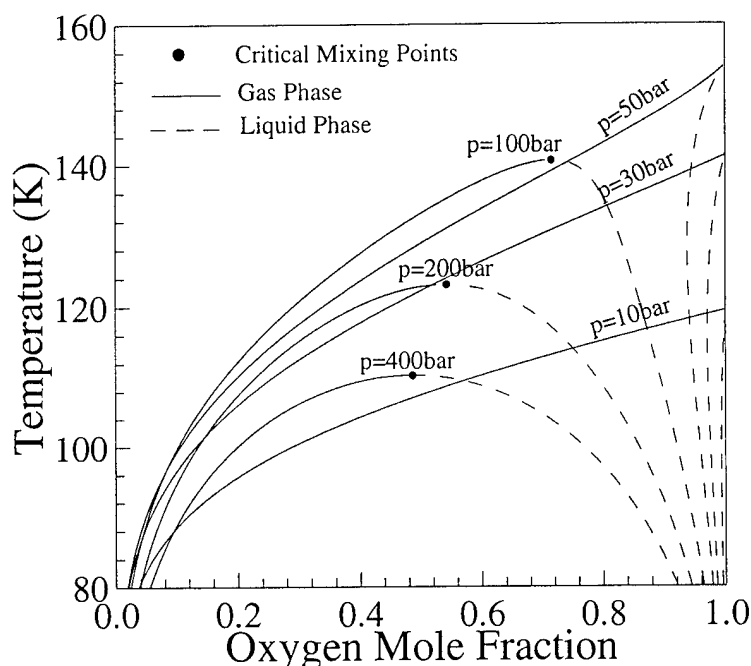


Fig. 2.2 General phase diagrams of oxygen and hydrogen at different pressures

2.3 Irreversible Thermodynamic Phenomenon

In this supercritical droplet vaporization problem, the internal boundary at the droplet surface renders numerical treatment very time-consuming. In fact, the boundary conditions established above are still not sufficient for solving this problem, and one more boundary condition is required. In the early works reviewed in Chapter 1, two methods are employed to handle this problem, which are directly related to the characteristics of spherical symmetry. One is to assume the velocity within the liquid droplet is zero. This is a reasonable assumption because the liquid velocity is indeed very small without internal circulation. Another one is to relate the interfacial regression rate to the total mass conservation in the liquid phase.

In this study, a more efficient method is utilized, which is initially proposed by Lafon (1995) based on irreversible thermodynamic theory. According to Onsager's irreversible theorem (Callen 1985), all the irreversible fluxes, including heat and mass fluxes, can be related to some generalized forces called affinities, which, in simple thermodynamic systems, include the differences of temperature, pressure, and chemical potential of each species. In this theorem, the dependence of a flux on the affinities is nonlinear. However, the high order terms are always found to be negligible. In fact, as Fourier's law indicates, heat flux is only strongly affected by temperature gradient, which is the driving force for heat transfer. Thermodynamics indicates that the driving force for species transfer is chemical potential. Moreover, thermodynamic phase equilibrium assumption requires extremely small differences of temperature and pressure at the droplet surface. Therefore, it is physically reasonable to neglect the effects of temperature and pressure on mass transfer, which leads to the following linear correlation:

$$\dot{m}_i = K_{vap,i}(\mu_i^l - \mu_i^g) \quad (2.16)$$

This relation is extremely useful for a simple interfacial boundary condition treatment. The only problem is how to determine the constant $K_{vap,i}$. In general, there is no specific formula available to determine this constant. However, because thermodynamic phase equilibrium is expected at the droplet surface, this constant can be simply chosen as a very large number to satisfy our requirement of small differences of chemical potentials. The accuracy of this method has been demonstrated by Lafon (1995) using results from an isolated droplet vaporization in quiescent environments.

2.4 Equations of State

In order to solve the thermodynamic phase equilibrium problem, as well as to evaluate thermophysical properties, an equation of state capable of handling real fluid behavior and high-pressure effect is required. The most common equation of state utilized for calculating high-pressure phase equilibrium is the cubic equations of state, which includes Redlich-Kwong, Peng-Robinson, and the modified Soave-Redlich-Kwong (SRK) equations of state. The modified SRK equation of state, which is capable of handling the quantum gas behavior of hydrogen, is adopted here for the treatment of thermodynamic phase equilibrium, calculation of thermodynamic properties, and derivation of numerical relationships. The consistent treatment of thermodynamic properties using one equation of state produces an efficient numerical algorithm. A more complicated Benedict-Webb-Rubin (BWR) equation of state, combined with the extended corresponding states theory, is utilized for estimating transport properties, as suggested by Ely and Hanly (1981, 1983). Both the modified SRK and the BWR equations of state are capable of representing liquid phase behavior. The BWR equation of state can be applied over broader temperature and pressure ranges, but the SRK equation of state is easier to apply, especially for deriving the thermodynamic differential relationships.

2.4.1 Modified Soave-Redlich-Kwong (SRK) Equation of State

The modified SRK equation of state is considered to be both simple and fairly accurate, which takes the following form (Graboski and Daubert 1978, 1979):

$$p = \frac{\rho R_u T}{(W - b\rho)} - \frac{a\alpha}{W} \frac{\rho^2}{(W + b\rho)} \quad (2.17)$$

where R_u is the universal gas constant. The parameters 'a' and 'b' account for the effects of the attractive and repulsive forces between molecules, respectively. ' α ' is the third parameter, which is a function of temperature and acentric factor. For mixtures, they are calculated from the following mixing rules:

$$\alpha a = \sum_{i=1}^N \sum_{j=1}^N x_i x_j \alpha_{ij} a_{ij} \quad (2.18)$$

$$b = \sum_{i=1}^N x_i b_i \quad (2.19)$$

The cross parameter $\alpha_{ij} a_{ij}$ in Eq. (2.18) is given by

$$\alpha_{ij} a_{ij} = \sum_{i=1}^N \sum_{j=1}^N \sqrt{\alpha_i \alpha_j a_i a_j} (1 - \kappa_{ij}) \quad (2.20)$$

where x_i is the mole fraction of species i. κ_{ij} is the binary interaction coefficient, which can be calculated from a known data set (Graboski and Daubert 1978). The constants a_i, b_i can be determined from the following universal relationships:

$$a_i = 0.42747 \frac{R_u^2 T_{ci}^2}{P_{ci}} \quad (2.21)$$

$$b_i = 0.08664 \frac{R_u T_{ci}}{P_{ci}} \quad (2.22)$$

The third parameter for species i is given as

$$\alpha_i = [1 + S_i (1 - \sqrt{T_{ri}})]^2 \quad (2.23)$$

where T_{ci} , P_{ci} , are the critical temperature and pressure for species i. T_{ri} is the reduced temperature for species i, and S_i is another variable. These parameters are given by the following formulas,

$$T_{ri} = \frac{T}{T_{ci}} \quad (2.24)$$

$$S_i = 0.48508 + 1.5517\omega_i - 0.15613\omega_i^2 \quad (2.25)$$

Equations (2.23) and (2.25) are not capable of accurately correlating hydrogen systems due to its quantum gas behavior. A modified expression of α for hydrogen is further established (Gradoski and Daubert 1979),

$$\alpha_{H_2} = 1.202 \exp(-0.30228T_r) \quad (2.26)$$

This correlation is expected to be accurate for hydrogen at reduced temperatures greater than about 2.5 (the critical temperature of hydrogen is 33.2K). No mixture of technical interests lies below this temperature. When Eq. (2.26) is used, the binary interaction coefficients κ_{ij} involving hydrogen species should be set to 0.

2.4.2 Benedict-Webb-Rubin (BWR) Equation of State

The BWR equation of state of methane is presented here, which is proposed by Jacobsen and Stewart (1973) based on very broad ranges of experimental data to ensure the proper extrapolation to low-temperature and high-pressure regions. Its expression is

$$p = \sum_{n=1}^9 A_n(T)\rho^n + \sum_{n=10}^{15} A_n(T)\rho^{2n-17} e^{-\gamma\rho^2} \quad (2.27)$$

where the 15 coefficients A_n are given in Table 2.1, which are functions of temperature.

The 32 semi-empirical Constants of Ns are list in Table 2.2. The units for pressure, density, and temperature are given in bar, mol/liter, and K. The stain-rate γ is 0.0096 (mol/liter)⁻².

Table 2.1 Coefficients of A_n

| | |
|-----------------------------------------------------|-------------------------------------------------|
| $A_1 = R_U T$ | $A_9 = N_{19}/T^2$ |
| $A_2 = N_1 T + N_2 T^{1/2} + N_3 + N_4/T + N_5/T^2$ | $A_{10} = N_{20}/T^2 + N_{21}/T^3$ |
| $A_3 = N_6 T + N_7 + N_8/T + N_9/T^2$ | $A_{11} = N_{22}/T^2 + N_{23}/T^4$ |
| $A_4 = N_{10} T + N_{11} + N_{12}/T$ | $A_{12} = N_{24}/T^2 + N_{25}/T^3$ |
| $A_5 = N_{13}$ | $A_{13} = N_{26}/T^2 + N_{27}/T^4$ |
| $A_6 = N_{14}/T + N_{15}/T^2$ | $A_{14} = N_{28}/T^2 + N_{29}/T^3$ |
| $A_7 = N_{16}/T$ | $A_{15} = N_{30}/T^2 + N_{31}/T^3 + N_{32}/T^4$ |
| $A_8 = N_{17}/T + N_{18}/T^2$ | |

Table 2.2 Semi-empirical Constants Based on Methane

| | |
|-------------------------------|-------------------------------|
| $N_1 = -1.184347314485E-2$ | $N_{17} = 1.071143181503E-5$ |
| $N_2 = 7.540377272657E-1$ | $N_{18} = -9.290851745353E-3$ |
| $N_3 = -1.225769717554E+1$ | $N_{19} = 1.610140169312E-4$ |
| $N_4 = 6.260681393432E+2$ | $N_{20} = 3.469830970789E+4$ |
| $N_5 = -3.490654409121E+4$ | $N_{21} = -1.370878559048E+6$ |
| $N_6 = 5.301046385532E-4$ | $N_{22} = 1.790105676252E+2$ |
| $N_7 = -2.875764479978E-1$ | $N_{23} = 1.615880743238E+6$ |
| $N_8 = 5.011947936427E+1$ | $N_{24} = 6.265306650288E-1$ |
| $N_9 = -2.821562800903E+4$ | $N_{25} = 1.820173769533E+1$ |
| $N_{10} = -2.064957753744E+5$ | $N_{26} = 1.449888505811E-3$ |
| $N_{11} = 1.285951844828E-2$ | $N_{27} = -3.159999123798E+1$ |
| $N_{12} = -1.106266656726E+0$ | $N_{28} = -5.290335668451E-6$ |
| $N_{13} = 3.060813353408E-4$ | $N_{29} = 1.694350244152E-3$ |
| $N_{14} = -3.174982181302E-3$ | $N_{30} = 8.612049038886E-9$ |
| $N_{15} = 5.191608004779E+0$ | $N_{31} = -2.598235689063E-6$ |
| $N_{16} = -3.074944210271E-4$ | $N_{32} = 3.153374374912E-5$ |

2.5 Thermodynamic Properties

In order to solve the conservation equations, additional thermodynamic relationships relating thermodynamic properties to temperature and, in high-pressure cases, pressure, are required. The thermodynamic properties to be evaluated are density, internal energy, enthalpy, entropy, partial molar enthalpy and chemical potential of each species. These properties can be derived directly from fundamental thermodynamic relationships,

$$e(T, \rho) = e_0(T) + \int_{\rho_0}^{\rho} \left[\frac{p}{\rho^2} - \frac{T}{\rho^2} \left(\frac{\partial p}{\partial T} \right)_{\rho} \right] d\rho \quad (2.28)$$

$$h(T, p) = h_0(T) + \int_{p_0}^p \left[\frac{1}{\rho} + \frac{T}{\rho^2} \left(\frac{\partial \rho}{\partial T} \right)_p \right] dp \quad (2.29)$$

$$s(T, \rho) = s_0(T, \rho_0) - \int_{\rho_0}^{\rho} \left[\frac{1}{\rho^2} \left(\frac{\partial p}{\partial T} \right)_{\rho} \right] d\rho \quad (2.30)$$

$$C_P(T, \rho) = C_{V0}(T) - \int_{\rho_0}^{\rho} \left[\frac{T}{\rho^2} \left(\frac{\partial^2 p}{\partial T^2} \right)_{\rho} \right] d\rho + \frac{T}{\rho^2} \left(\frac{\partial p}{\partial T} \right)_{\rho}^2 / \left(\frac{\partial p}{\partial \rho} \right)_T \quad (2.31)$$

where the e, h, s, C_P, C_V are internal energy, enthalpy, entropy, constant-pressure heat capacity, and constant-volume heat capacity, respectively. The subscript 0 refers to an ideal state at a low pressure. All the partial derivatives in these relations are calculated based on the Soave-Redlich-Kwong equation of state, and they are

$$\left(\frac{\partial p}{\partial T} \right)_{\rho_j} = \frac{\rho R_u}{(M_w - b\rho)} - \frac{1}{M_w} \left[\frac{\partial}{\partial T} (a\alpha) \right]_{\rho, Y_i} \frac{\rho^2}{(M_w + b\rho)} \quad (2.32)$$

$$\left(\frac{\partial p}{\partial \rho} \right)_{T, Y_i} = \frac{M_w R_u T}{(M_w - b\rho)^2} - \frac{a\alpha}{M_w} \frac{\rho(2M_w + b\rho)}{(M_w + b\rho)^2} \quad (2.33)$$

$$\begin{aligned}
\left(\frac{\partial p}{\partial \rho_i} \right)_{T, \rho_{j \neq i}} &= \frac{M_w R_u T}{M_{wi} (M_w - b\rho)^2} [M_w + \rho(b_i - b)] \\
&\quad - \frac{2\rho \sum_j x_j a_{ij} \alpha_{ij}}{M_{wi} (M_w + b\rho)} + \frac{a\alpha \rho^2 b_i}{M_{wi} (M_w + b\rho)^2}
\end{aligned} \tag{2.34}$$

where the derivative $\frac{\partial}{\partial T}(a\alpha)$ is given in Appendix B.

As being demonstrated in the early works (Manrique and Borman 1969, Hsieh et al. 1991), the properties of each component in a non-ideal mixture have to be defined by the partial molar or partial mass properties in order to find faithful results. According to thermodynamics, any thermodynamic property ϕ in a mixture is a function of temperature, pressure, and the masses of the constituent species,

$$m\phi = m\phi(T, p, m_i) \tag{2.35}$$

Therefore, the partial mass property is defined as

$$\bar{\phi}_i = \left(\frac{\partial m\phi}{\partial m_i} \right)_{T, p, m_{j \neq i}} \tag{2.36}$$

where $i, j = 1, \dots, N$, and ϕ refers to any proper thermodynamic property per unit mass of a mixture, such as enthalpy and internal energy. Figure 2.3 presents the variations of the enthalpy of vaporization of oxygen at thermodynamic phase equilibrium states, where the enthalpy of vaporization is calculated based on the partial mass enthalpy and shows strong dependence on both temperature and pressure.

In fluid mechanics, density is more convenient to use instead of mass. Therefore, it is better to define the mixture thermodynamic properties per unit volume,

$$\rho\phi = \rho\phi(T, \rho_i) \tag{2.37}$$

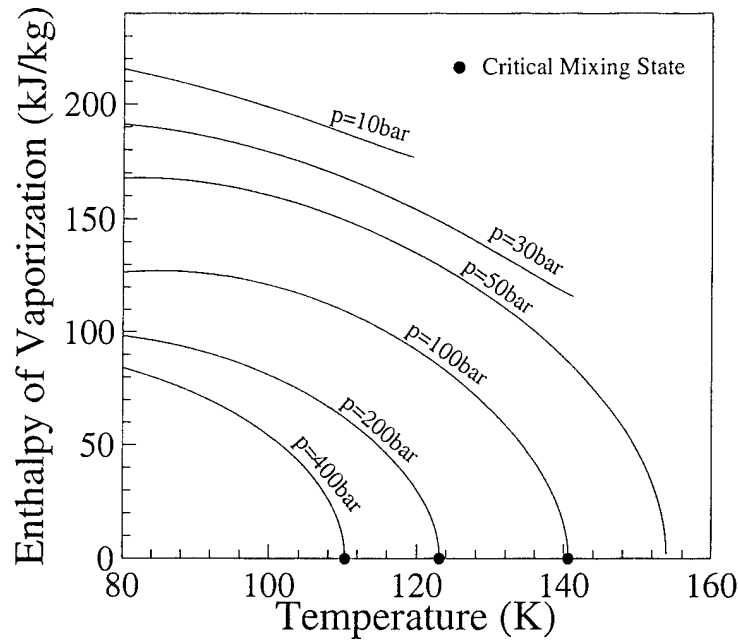


Figure 2.3 Variations of the enthalpy of vaporization of oxygen at thermodynamic phase equilibrium states.

This leads naturally to the definition of the partial density property $\tilde{\phi}_i$,

$$\tilde{\phi}_i = \left(\frac{\partial \rho \phi}{\partial \rho_i} \right)_{T, \rho_{j \neq i}} \quad (2.38)$$

According to this definition, the partial density internal energy, enthalpy, and entropy are expressed as

$$\tilde{e}_i = \left(\frac{\partial \rho e}{\partial \rho_i} \right)_{T, \rho_{j \neq i}} \quad (2.39)$$

$$\tilde{h}_i = \left(\frac{\partial \rho h}{\partial \rho_i} \right)_{T, \rho_{j \neq i}} \quad (2.40)$$

$$\tilde{s}_i = \left(\frac{\partial \rho s}{\partial \rho_i} \right)_{T, \rho_{j \neq i}} \quad (2.41)$$

where calculations of \tilde{e}_i , \tilde{h}_i , and \tilde{s}_i require the thermodynamic relations presented in Eqs. (2.28-2.30), and the SRK equation of state. In addition, a relationship between the partial density property and the partial mass property is derived as

$$\tilde{\phi}_i = \bar{\phi}_i + \rho \left(\frac{\partial \phi}{\partial p} \right)_{T, Y_j} \left(\frac{\partial p}{\partial \rho_i} \right)_{T, \rho_{j \neq i}} \quad (2.42)$$

Utilizing fundamental thermodynamic theories, including Euler equation and Gibbs-Duhem relation, the following relationship about chemical potential of each species, which is required for the treatment of thermodynamic phase equilibrium, can be derived:

$$\mu_i = \tilde{f}_i = \tilde{e}_i - T\tilde{s}_i \quad (2.43)$$

The details for calculating thermodynamic properties are presented in Appendix A. As a specific example, the partial density internal energy and enthalpy of species i , \tilde{e}_i and \tilde{h}_i , are derived here. According to the definition presented in Eq. (2.39), we first need to derive an expression for the internal energy e . Using Eq. (2.28) and the derivative expressions presented in Appendix A, the following relation is found:

$$e(T, \rho) = e_0(T) + \frac{T^2}{bM_w} \left(\frac{\partial a\alpha/T}{\partial T} \right)_{\rho, Y_i} \ln \left(1 + \frac{b\rho}{M_w} \right) \quad (2.44)$$

where the expression of $\frac{\partial a\alpha/T}{\partial T}$ is presented in Appendix B.

Based on the definition for the partial density property, the partial internal energy \tilde{e}_i can be expressed as

$$\begin{aligned}\tilde{e}_i = e_{i,0} + \frac{2}{bM_{wi}} \left[\sum_j x_j \left(T \frac{\partial}{\partial T} (a_{ij}\alpha_{ij}) - a_{ij}\alpha_{ij} \right) \right] \ln \left(1 + \frac{b\rho}{M_w} \right) \\ + \frac{b_i}{bM_{wi}} \left[T \frac{\partial}{\partial T} (a\alpha) - a\alpha \right] \left[\frac{\rho}{M_w + b\rho} - \frac{1}{b} \ln \left(1 + \frac{b\rho}{M_w} \right) \right]\end{aligned}\quad (2.45)$$

Utilizing Eq. (2.45), the expression for the internal energy, Eq. (2.44), can be related to the partial density internal energy,

$$e = \sum_i Y_i \tilde{e}_i - \frac{1}{M_w} \left[T \frac{\partial}{\partial T} (a\alpha) - a\alpha \right] \frac{\rho}{M_w + b\rho} \quad (2.46)$$

According to thermodynamics,

$$\rho h = \rho e + p \quad (2.47)$$

Following the definition for the partial density property, the following expression can be found by taking derivative of the partial density of species i at both sides of the Eq. (2.47) and keeping temperature and all the other partial densities constant:

$$\left(\frac{\partial \rho h}{\partial \rho_i} \right)_{T, \rho_{j \neq i}} = \left(\frac{\partial \rho e}{\partial \rho_i} \right)_{T, \rho_{j \neq i}} + \left(\frac{\partial p}{\partial \rho_i} \right)_{T, \rho_{j \neq i}} \quad (2.48a)$$

It is recognized that Eq. (2.48a) is equivalent to

$$\tilde{h}_i = \tilde{e}_i + \left(\frac{\partial p}{\partial \rho_i} \right)_{T, \rho_{j \neq i}} \quad (2.48b)$$

Substituting Eq. (2.42) into Eq. (2.48b), and taking use of the fundamental expressions of enthalpy, which are available in any thermodynamics textbook, the following relationship regarding the partial mass enthalpy, \bar{h}_i , can be derived:

$$\bar{h}_i = \tilde{e}_i + \frac{T \left(\frac{\partial p}{\partial T} \right)_{\rho_j}}{\rho \left(\frac{\partial p}{\partial \rho} \right)_{T, Y_j}} \left(\frac{\partial p}{\partial \rho_i} \right)_{T, \rho_{j \neq i}} \quad (2.49)$$

2.6 Transport Properties

Transport properties to be evaluated include viscosity, thermal conductivity and binary mass diffusivity. Accurate estimations of these properties are very important for high-pressure droplet vaporization computation, since they will determine the fluid field, as well as heat and mass transfer rates. As proved in the literature, pressure effects have to be taken into account to estimate these properties.

2.6.1 Corresponding States Theories

The law of corresponding state, which was originally proposed by van der Waals in 1873, expresses that the equilibrium properties of different fluids can be related to their critical properties in a universal way. For example, if pressure, temperature, and volume are related to their critical properties, the PVT function relating the reduced pressure, temperature, and volume becomes identical for all substances. The reduced property is defined as

$$p_r = p / p_c, T_r = T / T_c, V_r = V / V_c \quad (2.50)$$

The corresponding states theory also holds for other properties, including viscosity, and thermal conductivity. Via the corresponding states argument, a property of any fluid can be estimated by relating to its counterpart of a reference substance, whose property can be easily determined (Ely and Hanly 1981).

$$\eta_x(T, \rho) = \eta_0(T_0, \rho_0) F_\eta \quad (2.51)$$

where the subscript x refers to the fluid of interest, 0 to the reference fluid,

$$F_{\eta} = \left(\frac{Mw_x}{Mw_0} \right)^{1/2} f_{x,0}^{1/2} h_{x,0}^{-2/3} \quad (2.52)$$

and where Mw is the molecular weight. T_0 and ρ_0 of the reference fluid are calculated by

$$\begin{aligned} T_0 &= T / f_{x,0} \\ \rho_0 &= \rho h_{x,0} \end{aligned} \quad (2.53)$$

In general corresponding states theory, the parameters $f_{x,0}$ and $h_{x,0}$ is the ratio of the critical temperature and volume. However, the range of its applicability can be broadened considerably by introducing the extended corresponding states (EXCST) model, where the equivalent parameters of $f_{x,0}$ and $h_{x,0}$ become

$$f_{x,0} = (T_{c,x} / T_{c,0}) \theta(T_{r,x}, V_{r,x}, \omega_x) \quad (2.54)$$

$$h_{x,0} = (V_{c,x} / V_{c,0}) \phi(T_{r,x}, V_{r,x}, \omega_x) \quad (2.55)$$

In Eq. (2.54) and (2.55), θ and ϕ are the so-called shape factors, which are functions of Pitzer's acentric factor ω_x and the reduced temperature and volume. These functions can be calculated by the following correlations:

$$\theta(T_{r,x}, V_{r,x}, \omega_x) = 1 + (\omega_x - \omega_0) F(T_{r,x}, V_{r,x}) \quad (2.56)$$

$$\phi(T_{r,x}, V_{r,x}, \omega_x) = [1 + (\omega_x - \omega_0) G(T_{r,x}, V_{r,x})] Z_{c,0} / Z_{c,x} \quad (2.57)$$

where Z is the compressibility factor,

$$F(T_{r,x}, V_{r,x}) = a_1 + b_1 \ln T_x^+ + (c_1 + d_1 / T_x^+) (V_x^+ - 0.5) \quad (2.58)$$

$$G(T_{r,x}, V_{r,x}) = a_2 (V_x^+ + b_2) + c_2 (V_x^+ + d_2) \ln T_x^+ \quad (2.59)$$

and where

$$T_x^+ = \min[2, \max(T_{r,x}, 0.5)] \quad (2.60)$$

$$V_x^+ = \min[2, \max(V_{r,x}, 0.5)] \quad (2.61)$$

The coefficients in Eqs. (2.58) and (2.59) are list in Table 2.3.

| Table 2.3 Coefficients for Shape Factor Correlations | |
|------------------------------------------------------|----------------------------|
| Coefficients in Eq. (2.58) | Coefficients in Eq. (2.59) |
| $a_1=0.090569$ | $a_1=0.394901$ |
| $B_1=-0.862762$ | $b_1=-1.023545$ |
| $c_1=0.316636$ | $c_1=-0.932813$ |
| $D_1=-0.465684$ | $d_1=-0.754639$ |

The extended corresponding states theory will be utilized with appropriate mixing rules to estimate the transport properties of mixtures.

2.6.2 Mixing Rules for Mixtures

In order to apply the corresponding states theory to a mixture, the variables of that mixture have to be calculated from the corresponding parameters of its components using appropriate mixing rules. The following mixing rules are defined for calculating transport properties (Ely and Hanly 1981):

$$h_{x,0} = \sum_i \sum_j x_i x_j h_{ij,0} \quad (2.62)$$

$$f_{x,0} = h_{x,0}^{-1} \sum_i \sum_j x_i x_j f_{ij,0} h_{ij,0} \quad (2.63)$$

The molecular weight of the mixture can be found by

$$Mw_x^{1/2} = h_{x,0}^{-4/3} f_{x,0}^{-1/2} \sum_i \sum_j x_i x_j h_{ij,0}^{4/3} f_{ij,0}^{1/2} Mw_{ij,0}^{1/2} \quad (2.64)$$

where the indexes, i and j, represent the species components in the mixture. The following combining rules are chosen:

$$f_{ij,0} = (f_{i,0} f_{j,0})^{1/2} (1 - \kappa_{ij}) \quad (2.65)$$

$$h_{ij,0} = \frac{1}{8} (h_{i,0}^{1/3} + h_{j,0}^{1/3})^3 (1 - l_{ij}) \quad (2.66)$$

$$Mw_{ij} = 2Mw_iMw_j / (Mw_i + Mw_j) \quad (2.67)$$

where the variables, κ_{ij} , and l_{ij} , are the binary interaction parameters with values close to zero, which are set to zero for estimating transport properties.

2.6.3 Viscosity of Mixtures

The extended corresponding states one fluid model (Ely and Hanly 1981) is applied here for estimating the viscosity of a mixture. The basic idea is straightforward. First, it is assumed that the viscosity of a single-phase mixture is equated to that of a hypothetical pure fluid,

$$\mu_{mix}(T, \rho) = \mu_x(T, \rho) \quad (2.68)$$

where the subscripts, mix and x, refer to the mixture and the hypothetical pure fluid, respectively.

The corresponding states theory for transport properties is then used to evaluate the viscosity of the hypothetical pure fluid with respect to a given reference fluid,

$$\mu_x(T, \rho) = \mu_0(T_0, \rho_0)F_\mu \quad (2.69)$$

where the subscript, 0, refers to the reference fluid,

$$F_\mu = \left(\frac{Mw_x}{Mw_0} \right)^{1/2} f_{x,0}^{1/2} h_{x,0}^{-2/3} \quad (2.70)$$

The variables, $f_{x,0}$, $h_{x,0}$, and Mw_x are then evaluated by the extended corresponding states (EXCST) theory and the mixing rules.

Methane is chosen as the reference fluid, because of the existence of its PVT and viscosity data over the entire range of fluid states. The date fitted methane viscosity correlation is

$$\mu_0(\rho_0, T_0) = \mu_0^{(1)}(T_0) + \mu_0^{(2)}(T_0)\rho_0 + \Delta\mu_0(\rho_0, T_0)X_\mu \quad (2.71)$$

where the first two terms represent the dilute gas and first density correction, respectively, while the last term is a remainder which dominates in high-density region. The factor, X_μ , is a correction of the possible non-correspondence of viscosity. The details about this correlation can be found in the paper of Ely and Hanly (1981).

2.6.4 Thermal Conductivity of Mixtures

Estimating the thermal conductivity of a mixture is more complicated, since it is affected by two factors, one arising from the transfer of energy from pure collision or translation effect, λ' , and another from the transfer of energy via the internal degree of freedom, λ'' (Ely and Hanly 1983). The latter term is, in general, independent of density. Therefore, only the collision or translation part is evaluated using the extended corresponding states one fluid model, which takes the same procedure as that for estimating the viscosity of a mixture. First, the thermal conductivity of a mixture is equated to that of a hypothetical pure fluid as

$$\lambda'_{mix}(\rho, T) = \lambda'_x(\rho, T) \quad (2.72)$$

The corresponding states theory is then applied to calculate the thermal conductivity of the hypothetical pure fluid via

$$\lambda'_x(T, \rho) = \lambda'_0(T_0, \rho_0)F_\lambda X_\lambda \quad (2.73)$$

where F_λ takes the same form as in Eq. (2.70), whose calculation requires the extended corresponding states theory and the mixing rules, and X_λ is the correction term for non-correspondence.

Finally, the thermal conductivity of a mixture can be expressed as

$$\lambda_{mix}(\rho, T) = \lambda'_0(\rho_0, T_0) F_\lambda X_\lambda + \lambda''_{mix}(T) \quad (2.74)$$

In Eq. (2.74) the thermal conductivity of the reference fluid, methane, is evaluated via an empirical correlation. The second term in Eq. (2.74), which is related to internal degree of freedom, can be calculated via the modified Eucken correlation with mixing rules (Ely and Hanly 1983), which are

$$\frac{\lambda''_i M_{wi}}{\mu_i^g} = 1.32 \left(C_{p,i}^g - \frac{5R_u}{2} \right) \quad (2.75)$$

and,

$$\lambda''_{mix}(T) = \sum_i \sum_j x_i x_j \lambda''_{ij} \quad (2.76)$$

$$(\lambda''_{ij})^{-1} = 2[(\lambda''_i)^{-1} + (\lambda''_j)^{-1}] \quad (2.77)$$

where the indexes, *i* and *j*, refer to the components in the mixture, μ_i^g is the dilute gas viscosity of component *i*, $C_{p,i}^g$ is the ideal gas heat capacity of component *i*, and R_u is the universal gas constant.

2.6.5 Binary Mass Diffusivity

Binary mass diffusivity presents more challenge than viscosity and thermal conductivity because of the following two reasons. 1. There are only limited experimental data existent for binary mass diffusivity at high pressures, which results in few estimation methods. 2. There is no satisfactory liquid state theory available for calculating binary mass diffusivity in the liquid phase.

In this work, the binary mass diffusivity in gaseous phase at low pressure is evaluated using empirical correlation of Fuller et al., which is recommended by Reid et al. (1987). It takes the following form:

$$D_{ij} = \frac{0.00143T^{1.75}}{pMw_{ij}^{1/2}[(\Sigma_v)_i^{1/3} + (\Sigma_v)_j^{1/3}]^2} \quad (2.78)$$

where D_{ij} is binary mass diffusivity, cm^2/s

T is temperature, K

p is pressure, bar

Mw_{ij} is the combined molecular weight, as expressed in Eq. (2.67)

and Σ_v is found for each component by summing atomic diffusion volumes, which is tabulated in Reid et al. (1987, Table 11-1).

High-pressure effect on binary mass diffusivity is evaluated by the method proposed by Takahashi (1974), which is based on a simple corresponding state method,

$$\frac{D_{ij}p}{(D_{ij}p)^+} = f(T_r, p_r) \quad (2.79)$$

where the superscript + indicates the low-pressure values given by Eq. (2.78). The function $f(T_r, P_r)$ represents a scaling factor of pressure based on the reduced temperature and pressure, which is tabulated by Takahashi and also shown in Reid et al. (1987, Fig. 11-3). In order to calculate the reduced parameters, the following combining rules for pseudocritical properties of a mixture are used:

$$T_c = x_i T_{c,i} + x_j T_{c,j} \quad (2.80)$$

$$P_c = x_i P_{c,i} + x_j P_{c,j} \quad (2.81)$$

The binary mass diffusivities in liquids are evaluated by the method of Tyn and Calus, as recommended by Reid et al. (1987). For a binary mixture of solute i in solvent j , it is

$$D_{ij} = 8.93 \times 10^{-8} \left(\frac{V_i}{V_j^2} \right)^{1/6} \left(\frac{P_j}{P_i} \right)^{0.6} \frac{T}{\mu_j} \quad (2.82)$$

where V is the molar volume at the normal boiling temperature, cm^3/mol

T is temperature, K

μ_j is the viscosity of solvent, cP

P_i and P_j are parachors for the solute and solvent, and the calculation method is given in Reid et al. (1987).

There is no correlation currently available for estimating the pressure effect on binary mass diffusivity in liquid phase.

2.7 Numerical Method

An implicit finite volume scheme is used in this study to solve the problem of supercritical droplet vaporization in a quiescent environment. The implicit scheme is used because there is no numerical convergence restriction for time steps, which allows us to choose them purely from the physical consideration, leading to large time steps and reduced total computational time. The numerical methods are presented in detail in this section.

2.7.1 Grid Generation

Because two phases have to be treated simultaneously, finite volumes will be generated for each phase, namely liquid oxygen and gaseous hydrogen phases, separately. The control surfaces are concentric spheres with the droplet center as the sphere center. Because the gradients near the droplet interface are expected to be very steep, the grids are clustered around it, which is determined by a grid generation function given later in Eq. (2.83). The grids are shown in Fig. 2.4.

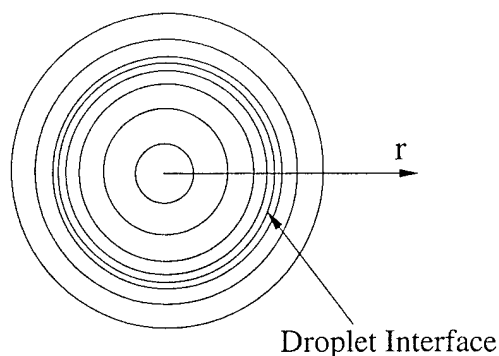


Figure 2.4 Illustration of numerical grids generated

When the droplet vaporizes, its radius generally decreases with time. In order to implement the interfacial boundary conditions, we need to track the interface during the entire computational time. In this work, all the control surfaces are kept moving with the droplet surface during the vaporization process. The movement of these surfaces is defined by the following equation:

$$r(\xi, t) = R(t)f(\xi) \quad (2.83)$$

where ξ is the transformed grid coordinate quantity whose semi-integer values correspond to the positions of the control surfaces. r is the radius of the control surface, which is a function of both position and time. R is the radius of the droplet interface, which only varies with time. $f(\xi)$ is the function used to generate the grid. Using Eq. (2.83), all the control surfaces are moving with the droplet interface, and fine grids are always kept around the interface, as determined by the function $f(\xi)$.

2.7.2 Independent Variables and Numerical Linearizations

The independent variables in this work are defined as

$$Q = (\rho V, \rho v_r A, \rho e V, \rho Y_i V, V)^T \quad (2.84)$$

where V is the control volume, A the area of the control surface, and v_r the velocity in the r direction. The volume V is chosen to be a variable since in the present moving boundary problem, it varies with time. Its movement is governed by the following equation:

$$\frac{d}{dt} \int_{V_d(t)} dV - \int_{A_d(t)} \vec{w} \cdot \vec{n} dA = 0 \quad (2.85)$$

where \vec{w} is the velocity of control surfaces. For this one-dimensional problem, the control volume can be expressed as

$$V(\xi) = \frac{4}{3} \pi r^3 |_{\xi+1/2} - \frac{4}{3} \pi r^3 |_{\xi-1/2} = [f^3(\xi + 1/2) - f^3(\xi - 1/2)] V_d \quad (2.86)$$

or,

$$\frac{dV(\xi)}{dt} = [f^3(\xi + 1/2) - f^3(\xi - 1/2)] \frac{dV_d}{dt} \quad (2.87)$$

where V_d is the volume of the droplet.

Equation (2.87) clearly indicates that all the control volumes can be related to the droplet volume, which is determined by the interfacial boundary conditions.

The following relation can be further developed for the moving velocity of a control surface, which is required in the expression of the surface fluxes:

$$w_r A|_{\xi+1/2} = \frac{dr}{dt} \cdot 4\pi r^2 = \frac{d\left(\frac{4}{3}\pi r^3|_{\xi+1/2}\right)}{dt} = f^3(\xi + 1/2) \frac{dV_d}{dt} \quad (2.88)$$

For application of the implicit scheme, all the variables in the discretized governing equations need to be linearized and related to the independent variables shown in Eq. (2.84). This linearization processes lead to the numerical Jacobians. Combining Eqs. (2.87) and (2.88), the flux terms resulting from grid movement in the conservation equations can be related to one independent variable, the control volume. The linearization processes with temperature, pressure, and chemical potential of each species are given in detail in the following subsections.

2.7.2.1 Linearization of Temperature

For this linearization process, a thermodynamic relation between temperature and the independent variables are required. First we begin with the following thermodynamic relation:

$$\rho e = \rho e(T, \rho_i) \quad (2.89)$$

where $i = 1, \dots, N$.

Its differential form is

$$d\rho e = \left(\frac{\partial \rho e}{\partial T} \right)_{\rho_j} dT + \sum_{j=1}^N \tilde{e}_j d\rho_j = \rho C_V dT + \sum_{j=1}^N \tilde{e}_j d\rho_j \quad (2.90)$$

where \tilde{e}_j is the partial density internal energy as defined earlier in this chapter. It is very easy to find

$$d\rho eV = Vd\rho e + \rho e dV \quad (2.91)$$

After substituting Eq. (2.90) into Eq. (2.91) and a little manipulation, the following relationship is established:

$$d\rho eV = \rho VC_V dT + \sum_{j=1}^{N_e} \tilde{e}_j d\rho_j V + (\rho e - \sum_{j=1}^{N_e} \tilde{e}_j \rho_j) dV \quad (2.92)$$

This is still not what we need since the independent variable, $\rho Y_i V$ in Eq. (2.84), only ranges from 1 to (N-1). Equation (2.92) is further manipulated to take into account of this difference,

$$d\rho eV = \rho VC_V dT + \tilde{e}_N d\rho V + \sum_{j=1}^{N-1} (\tilde{e}_j - \tilde{e}_N) d\rho Y_i V + (\rho e - \sum_{j=1}^N \tilde{e}_j \rho_j) dV \quad (2.93)$$

Basing on Eq. (2.93), the following Jacobian matrix is obtained:

$$\frac{dT}{dQ} = \frac{1}{\rho VC_V} \left[-\tilde{e}_N, 0, 1, \tilde{e}_N - \tilde{e}_1, \dots, \tilde{e}_N - \tilde{e}_{N-1}, \sum_{j=1}^N \tilde{e}_j \rho_j - \rho e \right] \quad (2.94)$$

Therefore, the temperature T at a new time step n+1 can be expressed as

$$T^{n+1} = T^n + \left(\frac{dT}{dQ} \right) \Delta Q = T^n + \left(\frac{dT}{dQ} \right) (Q^{n+1} - Q^n) \quad (2.95)$$

2.7.2.2 Linearization of Pressure

According to fundamental thermodynamic theory, the following relationship holds:

$$p = p(T, \rho_i) \quad (2.96)$$

Its differential form can written as

$$dp = \left(\frac{\partial p}{\partial T} \right)_{\rho_j} dT + \sum_{i=1}^N \left(\frac{\partial p}{\partial \rho_i} \right)_{T, j \neq i} d\rho_i \quad (2.97)$$

where $i, j = 1, \dots, N$. This relation can be related to the independent variables Q as

$$dp = \left(\frac{\partial p}{\partial T} \right)_{\rho_j} dT + \sum_{i=1}^N \left(\frac{\partial p}{\partial \rho_i} \right)_{T, \rho_{j \neq i}} \frac{1}{V} d\rho_i V - \frac{1}{V} \sum_{i=1}^N \rho_i \left(\frac{\partial p}{\partial \rho_i} \right)_{T, \rho_{j \neq i}} dV \quad (2.98)$$

The third term in Eq. (2.98) can be further simplified based on

$$\sum_{i=1}^N \rho_i \left(\frac{\partial p}{\partial \rho_i} \right)_{T, \rho_{j \neq i}} = \rho \left(\frac{\partial p}{\partial \rho} \right)_{T, Y_j} \quad (2.99)$$

Substituting Eq. (2.99) into Eq. (2.98), and changing the range of i in the second term in Eq. (2.98) as 1 to $(N-1)$, we have

$$dp = \left(\frac{\partial p}{\partial T} \right)_{\rho_j} dT + \sum_{i=1}^{N-1} \left(\frac{\partial p}{\partial \rho_i} \right)_{T, \rho_{j \neq i}} \frac{1}{V} d\rho_i V + \left(\frac{\partial p}{\partial \rho_N} \right)_{T, \rho_{j \neq N}} \frac{1}{V} d\rho_N V - \frac{1}{V} \rho \left(\frac{\partial p}{\partial \rho} \right)_{T, Y_j} dV \quad (2.100)$$

We then need to do a little manipulation about the third term in Eq. (2.100) according to

$$d\rho_N V = d\left(\rho - \sum_{i=1}^{N-1} \rho_i\right)V = d\rho V - \sum_{i=1}^{N-1} d\rho_i V \quad (2.101)$$

Substituting Eq. (2.101) into Eq. (2.100),

$$\begin{aligned}
dp = & \left(\frac{\partial p}{\partial T} \right)_{\rho_j} dT + \sum_{i=1}^{N-1} \left[\left(\frac{\partial p}{\partial \rho_i} \right)_{T, \rho_{j \neq i}} - \left(\frac{\partial p}{\partial \rho_N} \right)_{T, \rho_{j \neq N}} \right] \frac{1}{V} d\rho_i V \\
& + \left(\frac{\partial p}{\partial \rho_N} \right)_{T, \rho_{j \neq N}} \frac{1}{V} d\rho V - \frac{1}{V} \rho \left(\frac{\partial p}{\partial \rho} \right)_{T, Y_j} dV
\end{aligned} \quad (2.102)$$

Therefore,

$$\begin{aligned}
\frac{dp}{dQ} = & \left(\frac{\partial p}{\partial T} \right)_{\rho_j} \frac{dT}{dQ} + \\
& \frac{1}{V} \left[\left(\frac{\partial p}{\partial \rho_N} \right)_{T, \rho_{j \neq N}}, 0, 0, \left(\frac{\partial p}{\partial \rho_1} \right)_{T, \rho_{j \neq 1}} - \left(\frac{\partial p}{\partial \rho_N} \right)_{T, \rho_{j \neq N}}, \dots, \right. \\
& \left. \left(\frac{\partial p}{\partial \rho_{N-1}} \right)_{T, \rho_{j \neq N-1}} - \left(\frac{\partial p}{\partial \rho_N} \right)_{T, \rho_{j \neq N}}, -\rho \left(\frac{\partial p}{\partial \rho} \right)_{T, Y_j} \right]
\end{aligned} \quad (2.103)$$

where the $\frac{dT}{dQ}$ term can be found from Eq. (2.94).

2.7.2.3 Linearization of Chemical Potential

In this numerical study, the chemical potential of each species is required for treating thermodynamic phase equilibrium at the droplet surface and calculating the droplet vaporization rate in the irreversible thermodynamic relationship expressed in Eq. (2.16). We begin with the following thermodynamic relation:

$$\mu_i = \mu_i(T, p, Y_j) \quad (2.104)$$

where $i = 1, N, j = 1, \dots, N-1$.

Its differential form is

$$d\mu_i = \left(\frac{\partial \mu_i}{\partial T} \right)_{P, Y_j} dT + \left(\frac{\partial \mu_i}{\partial p} \right)_{T, Y_j} dp + \sum_{j=1}^{N-1} \left(\frac{\partial \mu_i}{\partial Y_j} \right)_{T, P, Y_{k \neq j}} dY_j \quad (2.105)$$

where $k = 1, \dots, N - 1$.

We then need to express Y_j in terms of the independent variables Q ,

$$\begin{aligned} dY_j &= d\left(\frac{\rho Y_j V}{\rho V}\right) = \frac{1}{\rho V} d\rho Y_j V - \frac{\rho Y_j V}{(\rho V)^2} d\rho V \\ &= \frac{1}{\rho V} d\rho Y_j V - \frac{Y_j}{\rho V} d\rho V \end{aligned} \quad (2.106)$$

Substituting Eq. (2.106) into Eq. (2.105), we obtain

$$\begin{aligned} d\mu_i &= \left(\frac{\partial \mu_i}{\partial T}\right)_{P, Y_j} dT + \left(\frac{\partial \mu_i}{\partial p}\right)_{T, Y_j} dp + \sum_{j=1}^{N-1} \frac{1}{\rho V} \left(\frac{\partial \mu_i}{\partial Y_j}\right)_{T, P, Y_{k \neq j}} d\rho Y_j V \\ &\quad - \sum_{j=1}^{N-1} \frac{Y_j}{\rho V} \left(\frac{\partial \mu_i}{\partial Y_j}\right)_{T, P, Y_{k \neq j}} d\rho V \end{aligned} \quad (2.107)$$

From Eq. (2.107), the Jacobian matrix for the chemical potential is obtained as

$$\begin{aligned} \frac{d\mu_i}{dQ} &= \left(\frac{\partial \mu_i}{\partial T}\right)_{P, Y_j} \frac{dT}{dQ} + \left(\frac{\partial \mu_i}{\partial P}\right)_{T, Y_j} \frac{dP}{dQ} + \\ &\quad \left[0, 0, 0, \frac{1}{\rho V} \left(\frac{\partial \mu_i}{\partial Y_1}\right)_{T, P, Y_{k \neq 1}}, \dots, \frac{1}{\rho V} \left(\frac{\partial \mu_i}{\partial Y_{N-1}}\right)_{T, P, Y_{k \neq N-1}}, - \sum_{j=1}^{N-1} \frac{Y_j}{\rho V} \left(\frac{\partial \mu_i}{\partial Y_j}\right)_{T, P, Y_{k \neq j}} \right] \end{aligned} \quad (2.108)$$

where the first two terms can be obtained in Eqs. (2.94) and (2.103), respectively. The

terms associated with $\left(\frac{\partial \mu_i}{\partial Y_j}\right)_{T, P, Y_{k \neq j}}$ can be calculated by using Eq. (2.43). All the

expressions used in the linearization processes are presented in Appendix A in detail.

2.7.3 Solution Procedures

In this work, a new method based on the irreversible thermodynamic phenomenon for treating interfacial boundary conditions is utilized, as shown in equation (2.16), where species vaporization is related to the difference of chemical potential. This equation is used in the species conservation equation for the two interfacial grid cells, and the vaporization constant $K_{vap,i}$ is taken to be a very large number ($\sim 10^5$). Therefore, the chemical potential difference at the interface can be kept as small as needed, which leads to automatic satisfaction of the thermodynamic phase equilibrium conditions regarding chemical potentials. This method is possible because of the implicit numerical algorithm utilized.

Similarly, when the heat flux at the droplet interface is computed in the energy conservation equation, the thermal conductivity at the droplet surface will also be taken as a large number, leading to the equality of temperature at both sides of the droplet. Based on the assumption that the pressure is a constant in the entire flow field, no special effort is necessary for its treatment. Following this strategy, numerical iteration is no longer required for solving the interfacial boundary equations.

An upwind scheme is applied in the numerical treatment of the convection terms in order to avoid numerical oscillations, especially at the droplet surface, where a large density gradient may exist.

Using the linearization processes described earlier, a set of discretized equations is obtained with the independent variables shown in Eq. (2.84) as the only unknowns. For the implicit numerical treatment, an efficient numerical solver is employed to solve the

resulting block tri-diagonal matrix (Douglas and Gunn 1964, Briley and McDonald 1977).

During the computational process, when the relative difference between species mass fractions in the two interfacial cells becomes sufficiently small (less than $5 \cdot 10^{-3}$), a assumption is made that the critical mixing state is reached. Afterwards, the droplet becomes a pocket of dense fluid, and the flow field is, therefore, in a single phase. The droplet interface is defined as an isotherm line at the critical mixing temperature.

Chapter 3

DROPLET CLUSTER BEHAVIOR

3.1 Problem Description

It has been commonly accepted that droplets evaporate and burn in a group in practical spray combustion devices. Therefore, there is increasing interests in studying droplet cluster behavior in the combustion community. This problem is so complicated that some necessary assumptions are inevitable. In the literature, there are two numerical models for studying droplet interactions in a cluster. One is the “droplet-in-bubble” model (Tishkoff 1979); another is the “sphere of influence” concept (Bellan and Cuffel 1983). The two models are very similar in the fact that they both take the following assumptions: 1) The monosize spherical droplets distribute uniformly in a droplet cluster; 2) There is a finite quiescent surrounding environment for each droplet (a “bubble” or “sphere of influence”), within which a numerical method developed for an isolated droplet vaporization in a quiescent environment is still valid. The only difference between the two methods is the treatment of the interstitial regions, which serve as the outside boundary conditions for those finite quiescent bubbles or spheres. In the “droplet-in-bubble” model, the interstitial regions are incorporated into each bubble, while they are treated separately in the “sphere of influence” concept, which assumes uniform variables in the interstitial regions. These variables are then solved using the global conservation equations. The assumption of uniform variables in the interstitial regions means that the effects of energy and mass exchanges between the droplet cluster and its

outside environment instantly spread over the entire interstitial regions. This assumption is strictly valid at the outer region of a droplet cluster.

Although the assumptions in the two numerical models can not be totally justified for the practical situations, they serve to simplify the droplet cluster problem and make numerical solutions possible. Results can enhance our deep understanding of the physics in droplet interactions.

Recently, a few researchers applied the "sphere of influence" concept to study droplet interactions at high pressures (Jiang and Chiang 1994, 1996, Harstad and Bellan 1998). Jiang and Chiang (1994, 1996) considered n-pentane droplets vaporization in nitrogen, and Harstad and Bellan (1998) investigated oxygen droplet vaporization in supercritical hydrogen environments. Some interesting results, which show the characteristics of droplet interactions distinct from that of an isolated droplet, were presented. However, considering the complexity of the problem and the simplifications accepted, these results are not complete and conclusive. Further studies based on different views of the problem are absolutely necessary and are expected to complement the current results.

In this chapter, a cluster of liquid oxygen (LOX) droplets vaporization in hydrogen environments at both sub- and super-critical conditions is numerically studied. Figure 3.1 shows the schematics of the problem, where monosized spherical droplets are uniformly distributed in a droplet cluster. Since the assumption of uniform variables in the interstitial regions in the early works is valid in the outer region of a droplet cluster, this study is focused on droplet interactions in the inner region, as shown in Fig. 3.1a. In this study, an isolated impermeable bubble is assumed to surround each droplet in the

inner region of a droplet cluster, and there is no heat and mass transfer across the bubble surface. This is a reasonable assumption because it really takes very long time, compared with the droplet lifetime, for the outside thermal wave to penetrate into the droplet cluster. Mass transfer is also weak when far from the outside boundary (Annamalai and Ryan 1992). For example, with an oxygen droplet cluster of 1cm in diameter vaporization in a hydrogen environment, the thermal penetration time is of the order of 1000 ms, while the lifetime of a droplet at 100 μm in diameter is only around 10 ms at high pressures. Just like Tishkoff's model, the interstitial regions are uniformly incorporated into each bubble, as shown in Fig. 3.1b, where the bubble size is a little larger than that of a "sphere of influence", whose radius is the half distance between two neighboring droplets (Bellan and Cuffel 1983). Within each bubble, the environment is considered as quiescent. The bubble size represents the intensity of droplet cluster effect. For example, a small bubble size means more droplets in a droplet cluster, which leads to stronger droplet interactions. Results from this study are expected to complement those from the early research works (Jiang and Chiang 1996, Harstad and Bellan 1998).

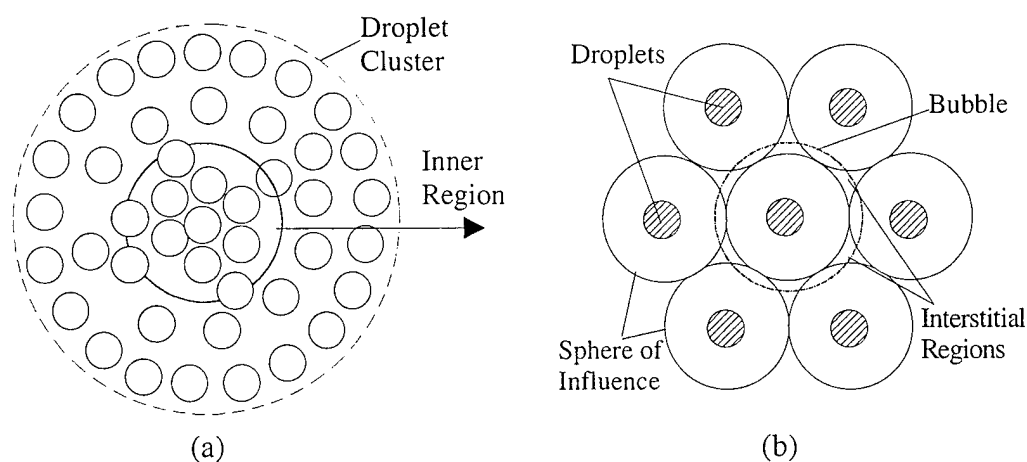


Fig. 3.1 (a) Schematics of a droplet cluster and the inner region;
(b) Illustration of the numerical models

3.2 Numerical Treatment

Droplet cluster behavior with liquid oxygen (LOX) droplets vaporization in hydrogen environments at both sub- and super-critical conditions are systematically investigated using the numerical algorithm developed in Chapter 2. The high-pressure effects, including thermodynamic nonideality and transport property anomaly, are fully considered. The computational domain is shown in Fig. 3.2, where a droplet is evaporating in an isolated impermeable bubble.

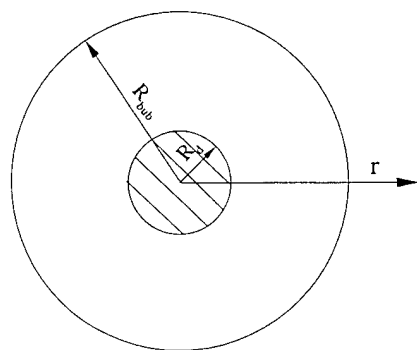


Fig. 3.2 Single droplet vaporization in an isolated impermeable bubble.

The bubble size, which indicates the intensity of droplet interactions, is initially prescribed, but it will change during the vaporization process, depending on the conservation equations of mass, energy, and the equation of state. The boundary conditions for this elastic, isolated, and impermeable bubble are defined as

$$\begin{aligned} \nabla T &= 0 \\ \nabla Y_i &= 0 \\ \vec{v} &= \vec{w} \end{aligned} \tag{3.1}$$

As described in Chapter 2, all the control surfaces are moving with the droplet surface during numerical computation, and the movements are generally inward because of droplet vaporization. Since the movement of the control surface next to the bubble

surface is faster than that of the bubble surface, grids become increasingly coarser in that region. New grids have to be added in order to ensure computational accuracy, and a simple linear interpolation method, which proves to be efficient and accurate, is adopted for calculating the new variables.

3.3 Results and Discussions

Droplet cluster behavior at both sub- and super-critical conditions is studied numerically with liquid oxygen (LOX) droplet vaporization within a bubble of gaseous hydrogen, as shown in Fig. 3.2. The initial temperature and diameter of the liquid oxygen (LOX) droplet are 100K and 100 μ m, respectively, while the initial ambient temperature of hydrogen ranges from 700K to 1500K. Ambient pressures at 10, 30 and 100 atms, among which the first two cases represent subcritical states while the last one is at supercritical condition (see Fig. 2.2), are considered. Computation goes on until all the droplet mass is evaporated. Complete vaporization is considered to be impossible once the saturation conditions are reached. These are defined as mass fraction ratio $(Y_{O_2, \text{int}} - Y_{O_2, \text{bub}}) / Y_{O_2, \text{int}}$ less than 2% or the temperature at the bubble surface minus the temperature at the droplet interface lower than 5K. In the above definitions, $Y_{O_2, \text{int}}$ is the mass fraction of oxygen at the droplet interface on the gaseous side, and $Y_{O_2, \text{bub}}$ is the mass fraction of oxygen at the bubble surface. This research work is focused on the effects of pressure and temperature on droplet interactions.

For the purpose of comparison, droplet lifetimes of an isolated oxygen droplet vaporization in quiescent hydrogen environments at different pressures and temperatures are first presented. Figure 3.3 clearly indicates that droplet lifetimes decrease monotonically with the increase of pressures or temperatures.

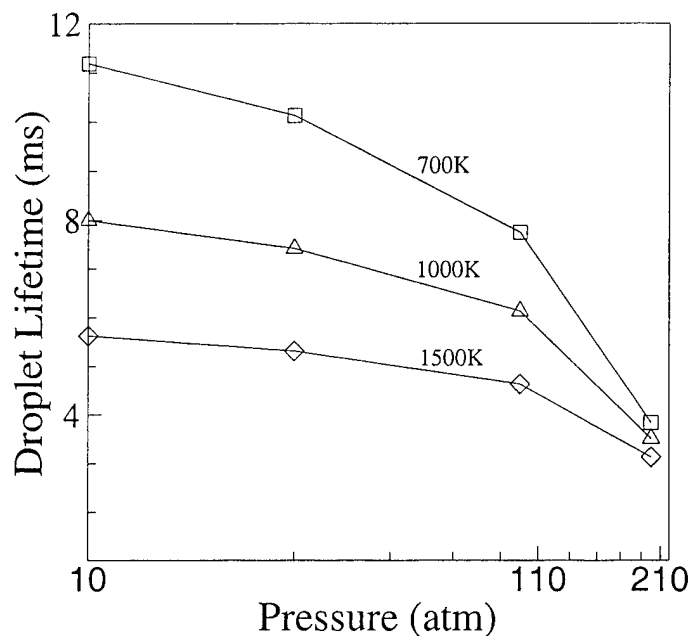


Fig. 3.3 Droplet lifetimes with an isolated oxygen droplet vaporization in hydrogen environments at different pressures and temperatures

In this study, a droplet is assumed to vaporize as an isolated droplet when the initial radius of the outside bubble reaches 100 times of that of the droplet. The validity of the assumption is demonstrated in Figs. 3.4 and 3.5, where the initial temperature and pressure are 1000 K and 30 atm, respectively. Figure 3.4 illustrates the temporal variations of temperature outside the droplet at three instants when 20%, 40 %, and 80% of the droplet mass are vaporized. Results indicate that the temperature gradients approach zero within a computational domain whose radius is less than 50 times of the initial droplet radius. The same conclusion can be drawn from the distributions of oxygen mass fraction, as shown in Fig. 3.5

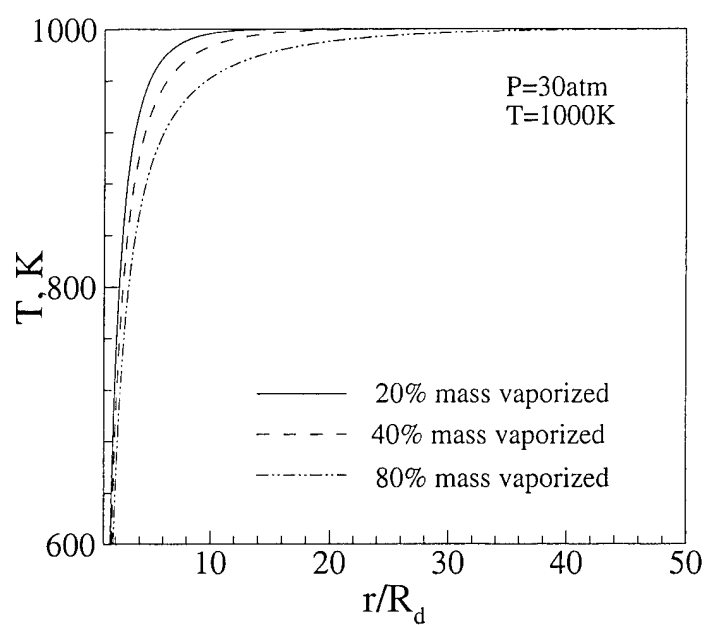


Fig. 3.4 Temporal variations of temperature at an ambient temperature of 1000 K and a pressure of 30 atm

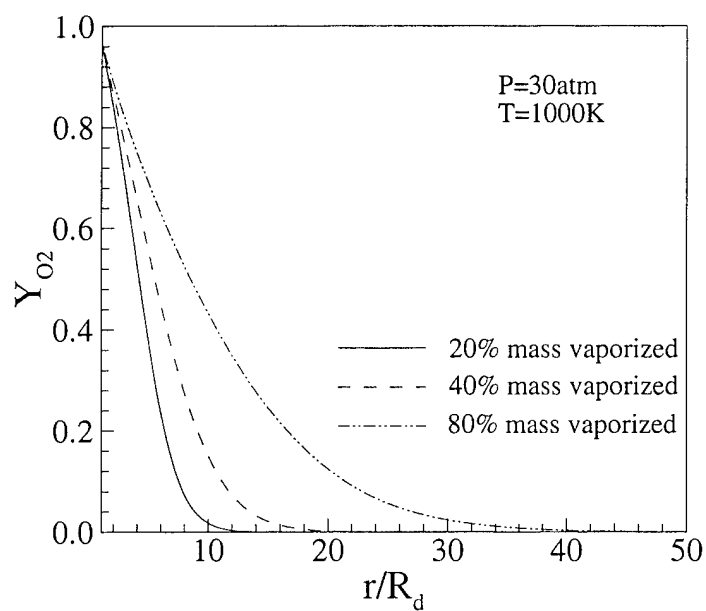


Fig. 3.5 Temporal variations of oxygen mass fraction at an ambient temperature of 1000 K and a pressure of 30 atm.

The effects of droplet interactions on droplet lifetimes at two different pressures, namely 30 and 100 atms, are presented in Fig. 3.6 and 3.7, respectively, where the temporal variations of nondimensional droplet diameter, D^2/D_0^2 , are illustrated. In each case, droplet vaporization rates at different ratios of initial bubble to droplet radius, which is called interactive radius ratios, $(R_{\text{bub}}/R_d)_0$, are compared. Fig. 3.6 indicates that at a pressure of 30atm, the effect of droplet interactions on droplet vaporization rate is weak, once the interactive radius ratio reaches 10. A droplet behaves exactly like an isolated droplet and follows the traditional D^2 law. With the decrease of the interactive radius ratio, droplet vaporization rates change dramatically. At a lower interactive radius ratio, or in a denser droplet cluster, the droplet vaporization rate follows that of an isolated droplet only at the short beginning period. Afterwards, the vaporization rate slows down. As illustrated in Fig. 3.6, there is a significant decrease of vaporization rate at an interactive radius ratio of 5, as time increases.

The pressure effect on droplet cluster behavior is further illustrated in Fig. 3.7, where pressure is increased to 100atm. Figure 3.7 shows very weak droplet interactions for all the interactive radius ratios (e.g., from 5-10).

Further studies of pressure effects on droplet lifetimes are thoroughly conducted, and the results are presented in Figs. 3.8 and 3.9, which correspond to two different ambient temperatures at 1000K and 1500K, respectively. A dimensionless droplet vaporization time is defined as

$$\tau = \frac{\text{vaporization time of an isolated droplet}}{\text{droplet lifetime at a interactive radius ratio}} \quad (3.2)$$

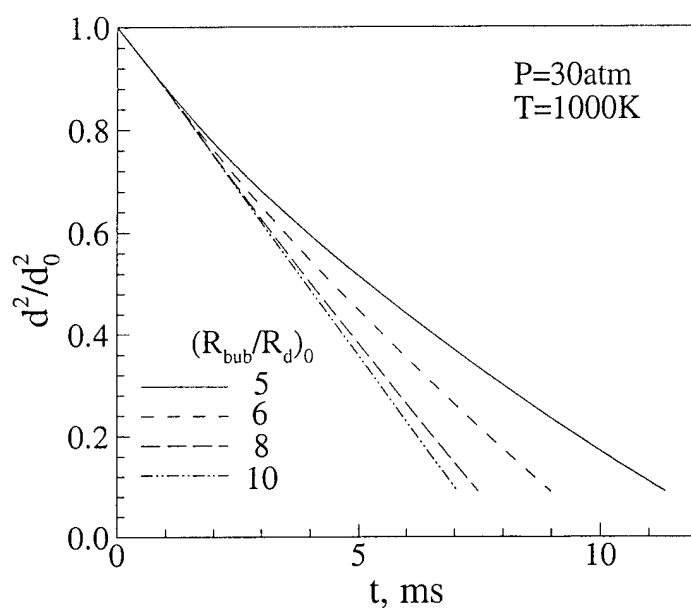


Fig. 3.6 Transient variations of dimensionless LOX droplet diameter squares at different interactive radius ratios with a pressure of 30atm and an ambient temperature of 1000K

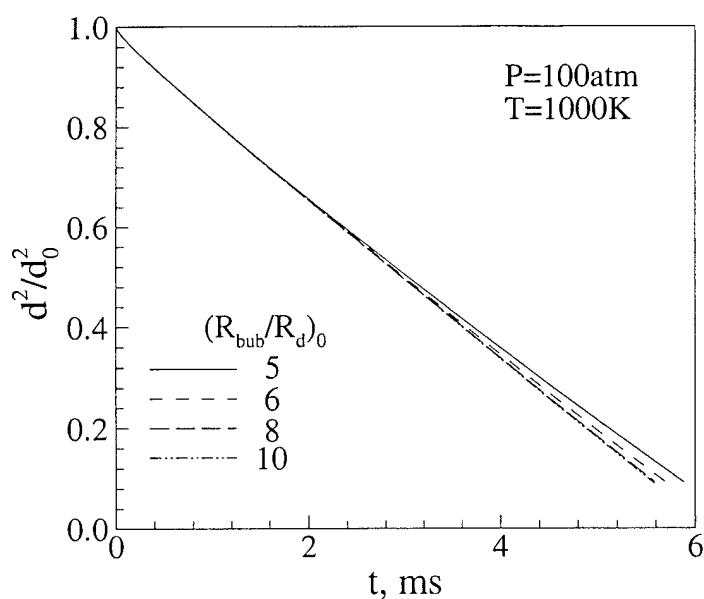


Fig. 3.7 Transient variations of dimensionless LOX droplet diameter squares at different interactive radius ratios with a pressure of 100atm and an ambient temperature of 1000K

Results in these two figures indicate similar trends at both temperatures, which strongly suggest that the ambient pressure presents a significant effect on droplet interactions. At a lower pressure, droplet interactions become stronger. For example, at a given R_{bub}/R_0 , τ is smaller at a lower pressure, since the droplet lifetime is significantly prolonged compared with that of an isolated droplet. In addition, the critical interactive radius ratio, $(R_{\text{bub}}/R_0)_{\text{crit}}$, at which the complete droplet vaporization cannot be reached, decreases significantly with increasing pressure. At both ambient temperatures, the critical radius ratios at 100atm are only around 2.5, but the corresponding values at 10atm are larger than 6.

Increase of ambient temperature produces slightly stronger droplet interactions, as shown in Figs. 3.10 and 3.11. At a given pressure, although the lifetime of an isolated droplet is shorter at a higher ambient temperature, as shown in Fig. 3.3, the droplet in the inner region of a dense droplet cluster experiences more lifetime prolongation, which could compromise the benefit resulting from high ambient temperature. The effect of ambient temperature on droplet lifetime is, however, significantly weaker than that of pressure, as clearly supported by the results in Figs. 3.8-3.11. With the increase of pressure, the effect of ambient temperature is further decreased. As illustrated in Fig. 3.11, the differences between the results at 700K and 1000K is negligible.

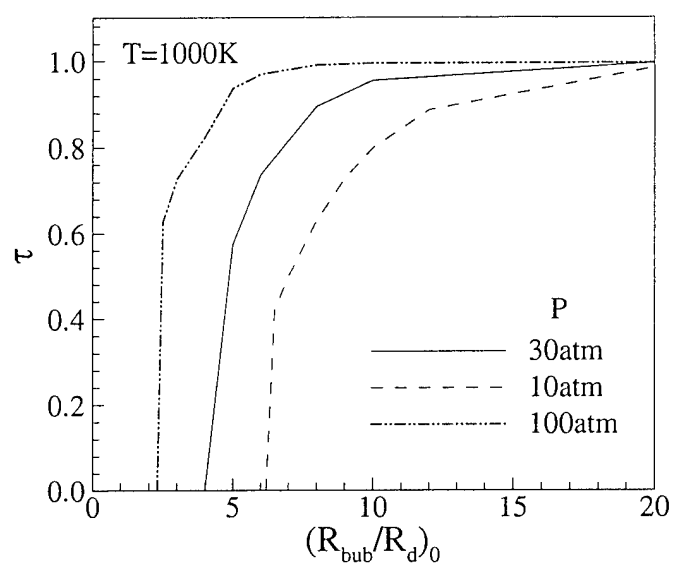


Fig. 3.8 Effect of droplet interactions on LOX droplet vaporization times at 1000K.

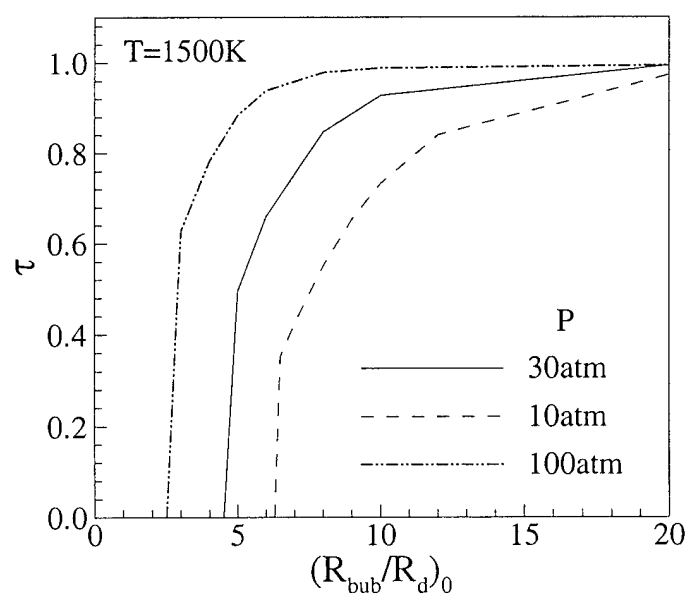


Fig. 3.9 Effect of droplet interactions on LOX droplet vaporization times at 1500K.

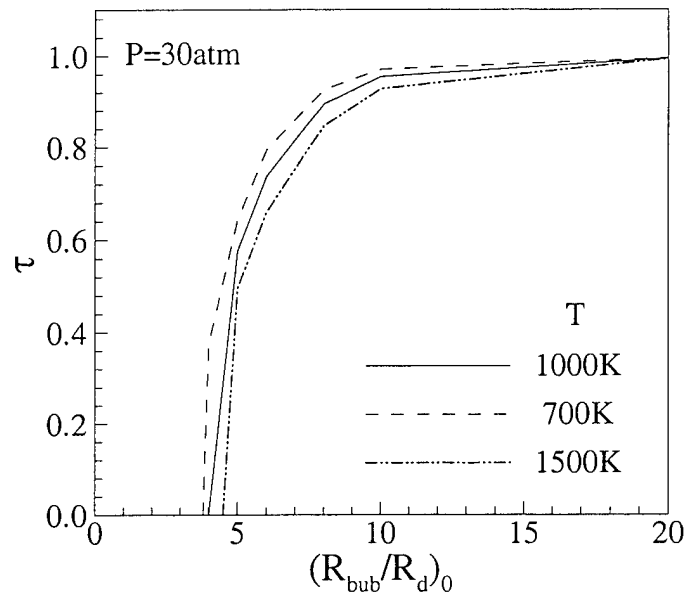


Fig. 3.10 Effect of droplet interactions on LOX droplet vaporization times at a pressure of 30atm.

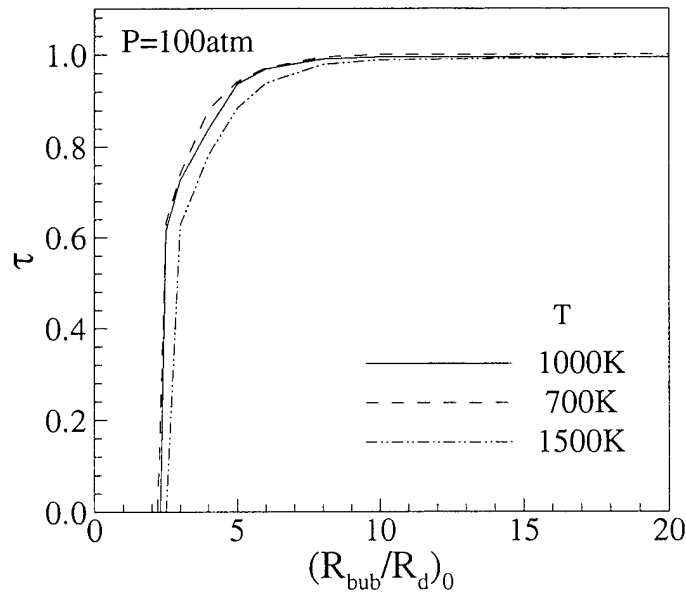


Fig. 3.11 Effect of droplet interactions on LOX droplet vaporization times at a pressure of 100atm.

The effect of droplet interactions on the transient development of droplet surface temperature at different pressures is presented in Fig. 3.12. At a pressure of 100atm, the droplet interactions produce no effect on the attainability of the critical mixing state, which is reached after a very short time for both cases of an isolated droplet and a droplet at a interactive radius ratio of 3. At a pressure of 30atm, the temporal variations of surface temperature are presented for both an isolated droplet and a droplet at an interactive radius ratio of 5. Surface temperatures for both cases increase continuously, indicating unsteady droplet vaporization processes. The increase rate of the interacting droplet is slower, but eventually the surface temperature reaches the same value as that of the isolated droplet at the end of the vaporization process. The situations at a pressure of 10atm are similar to those at 30atm, except that the transient variations of surface temperatures are weaker, and quasi-steady state surface temperatures are attained.

The effect of droplet interactions on temperature distributions outside of the droplet is compared in Fig. 3.13, where results are presented at three instants, when 20%, 40%, and 80% of droplet mass are evaporated. At an interactive radius ratio of 5, temperature outside of the droplet decreases faster than that of an isolated droplet. At all three times, the temperature gradients at droplet surface are smaller for the interacting droplet. This conclusion is consistent with the result of the slower increase of droplet surface temperature. Temperature decreases uniformly within the bubble due to the large thermal diffusivity of hydrogen.

Figure 3.14 presents the temperature distributions inside the droplet at the same three instants as those in Fig. 3.13. The transient heating of the liquid phase is clearly illustrated for both the isolated and the interacting droplets. With the increase of time, differences of temperature distributions of the two cases increase dramatically. For a droplet in a dense droplet cluster, more energy, which is transferred from the outside high-temperature environment into the droplet, is spent for heating the liquid phase. This leads to less temperature difference inside the droplet.

Figure 3.15 compares the distributions of oxygen mass fractions outside the droplet for the same two cases as those in Fig. 3.14. With more oxygen mass evaporated, the oxygen mass fraction increases dramatically for the interacting droplet case. At the instant when 80% of droplet mass is evaporated, the differences of the oxygen mass fractions at droplet and bubble surfaces become extremely close to the saturation condition. With the decrease of mass fraction gradient at the droplet surface as time increases, the slow mass transfer rate at the droplet surface results in more oxygen mass accumulation. Because the thermal conductivity of oxygen is much smaller than that of hydrogen, more oxygen mole fraction at the droplet surface also means a slower heat transfer rate. Some properties of pure oxygen, pure hydrogen, and oxygen and hydrogen mixture at equal molar fractions are given in Table 3.1, where a temperature of 200K is chosen as the characteristic temperature near the droplet surface.

Table 3.1a Pressure Effects on the Properties of Pure Oxygen at 200K

| P (atm) | ρ (kg/m ³) | C_p (J/kg/K) | λ (W/m/K) | D_{ij} (m ² /s) |
|---------|-----------------------------|----------------|-------------------|------------------------------|
| 10 | 20.12 | 958.8 | 0.201E-01 | 0.393E-05 |
| 30 | 64.53 | 1079.9 | 0.222E-01 | 0.123E-05 |
| 100 | 274.43 | 1874.8 | 0.331E-01 | 0.284E-06 |
| 200 | 550.42 | 1996.5 | 0.547E-01 | 0.136E-06 |

Table 3.1b Pressure Effects on the Properties of Pure Hydrogen at 200K

| P (atm) | ρ (kg/m ³) | C_p (J/kg/K) | λ (W/m/K) | D_{ij} (m ² /s) |
|---------|-----------------------------|----------------|-------------------|------------------------------|
| 10 | 1.22 | 13901.5 | 0.138 | 0.408E-05 |
| 30 | 3.58 | 14020.3 | 0.141 | 0.138E-05 |
| 100 | 11.18 | 14350.8 | 0.151 | 0.430E-06 |
| 200 | 20.41 | 14660.6 | 0.164 | 0.215E-06 |

Table 3.1c Pressure Effects on the Properties of Oxygen and Hydrogen at Equal Molar Fractions at 200K

| P (atm) | ρ (kg/m ³) | C_p (J/kg/K) | λ (W/m/K) | D_{ij} (m ² /s) |
|---------|-----------------------------|----------------|-------------------|------------------------------|
| 10 | 10.40 | 1713.2 | 0.401E-01 | 0.402E-05 |
| 30 | 31.33 | 1784.2 | 0.431E-01 | 0.133E-05 |
| 100 | 103.8 | 2006.0 | 0.538E-01 | 0.388E-06 |
| 200 | 195.6 | 2192.2 | 0.696E-01 | 0.198E-06 |

Further comparisons of temperature and oxygen mass fraction distributions outside a droplet at different temperatures are presented in Figs. 3.16-3.17 for an interacting droplet with an interactive radius ratio of 5, when 80% of the droplet mass is evaporated. Fig. 3.16 shows different temperature gradients at the droplet surface, where a larger temperature gradient maintains for an initially higher ambient temperature. This is inconsistent with the former conclusion of slightly stronger droplet interaction at a higher ambient temperature. In contrast, Fig. 3.17 indicates an opposite trend for oxygen mass fraction distributions, where the mass fraction gradient at the droplet surface is smaller for a higher ambient temperature. This results in more oxygen accumulation. Therefore, the slightly stronger droplet interactions at a higher ambient temperature is solely due to oxygen mass accumulation at the droplet surface, which decreases the heat

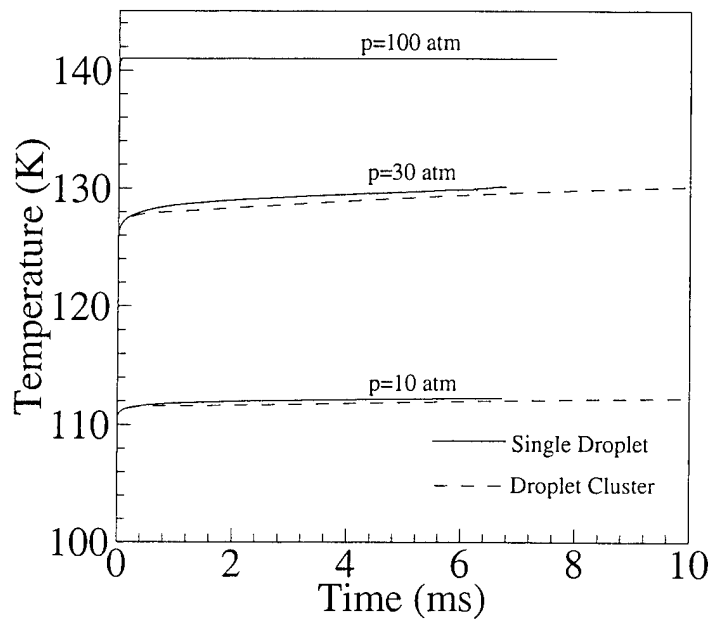


Fig. 3.12 Transient variations of droplet surface temperatures at different pressures for both an isolated and an interacting LOX droplet.

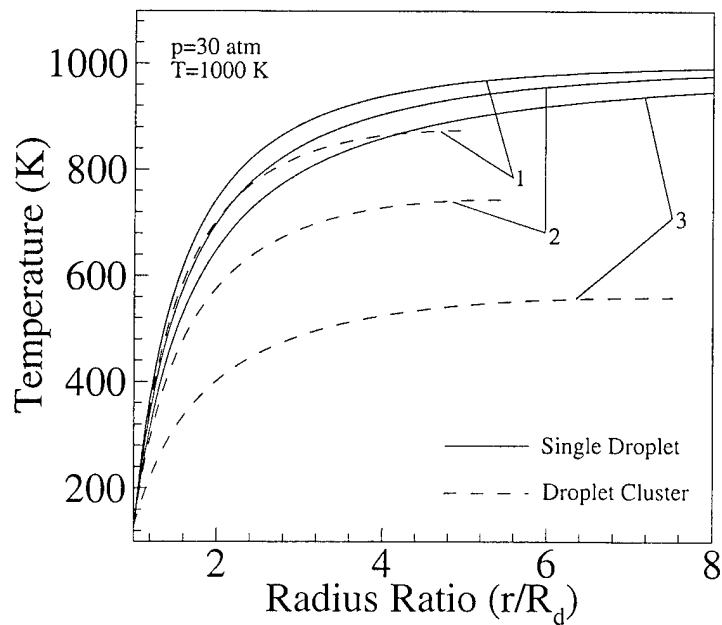


Fig. 3.13 Temperature distributions outside the droplets at a pressure of 30atm and an ambient temperature of 1000K for both an isolated and an interacting LOX droplet (1: 20%, 2: 40%, 3: 80% droplet mass vaporized)

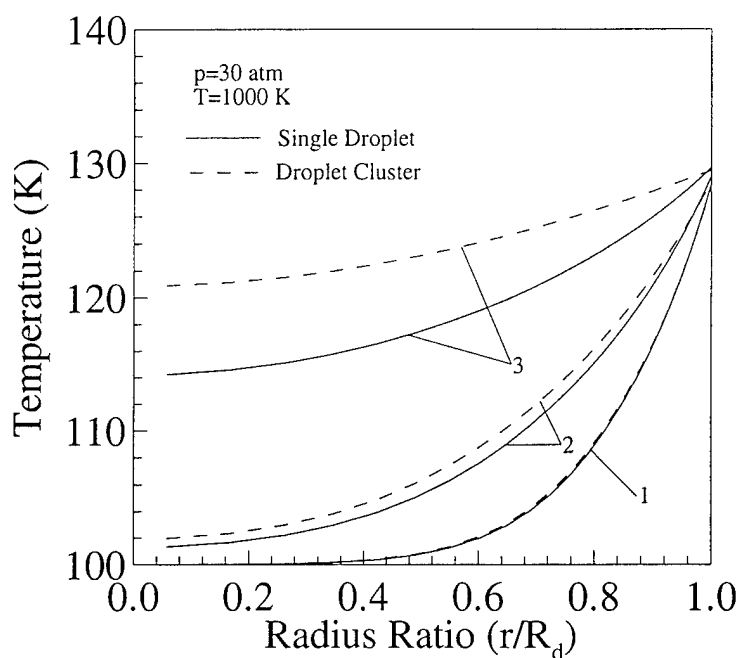


Fig. 3.14 Temperature distributions inside the droplets at a pressure of 30atm and a ambient temperature of 1000K for both an isolated and an interacting LOX droplet (1: 20%, 2: 40%, 3: 80% droplet mass vaporized)

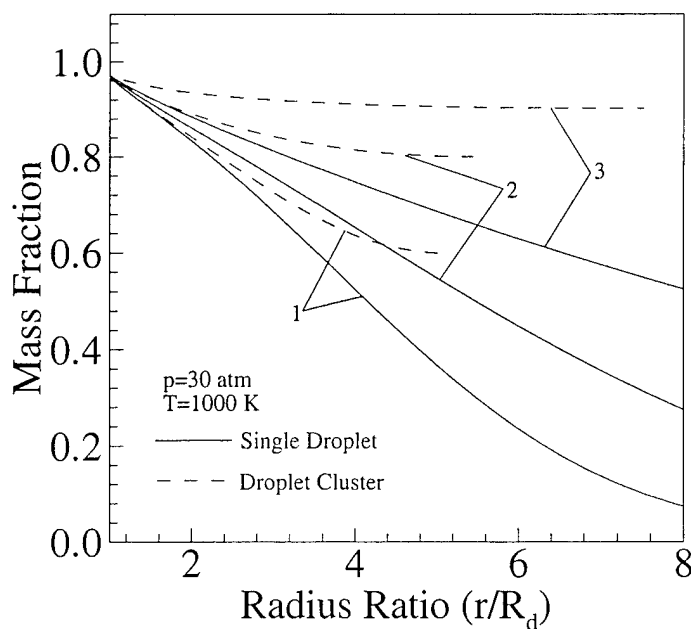


Fig. 3.15 Oxygen mass fraction distributions outside the droplets at a pressure of 30atm and a ambient temperature of 1000K for both an isolated and an interacting LOX droplet (1: 20%, 2: 40%, 3: 80% droplet mass vaporized)

transfer rate into the liquid droplet by decreasing the thermal conductivity of the mixture. This phenomenon is so strong that it totally counteracted the effect of the high temperature gradient.

Pressure effects on temperature and oxygen mass fraction distributions are presented in Fig. 3.18-3.19 for an interacting droplet at an interactive radius ratio of 5. Both the temperature and oxygen mass fraction gradients at the droplet surfaces are in favor of the high-pressure case. This result clearly explains the weaker droplet interactions at a higher pressure.

Summarizing the early results, droplet interactions in the inner region of a droplet cluster results in significantly prolongation of droplet lifetimes, especially at a small interactive radius ratio. Lifetime prolongation is mainly caused by the following reasons: 1) The rapid decrease of the bulk temperature in the bubble results in decreased temperature gradients at the droplet surface during the droplet vaporization process, and consequently the slow heat transfer rate to the droplet; 2) More energy is transferred inside the droplet for liquid heating for an interacting droplet; and 3) At the later stage of the droplet vaporization process, low oxygen mass fraction gradient at the droplet surface leads to oxygen accumulation and consequently low thermal conductivity of the mixture. The last reason is the major one for low droplet vaporization rate, or strong droplet interactions, at the later stage of the vaporization process.

In the inner region of a droplet cluster, there is no outside energy and hydrogen supply during the entire droplet vaporization process. This conclusion leads to the assumption of an isolated and impermeable bubble. The decrease of bulk temperature and

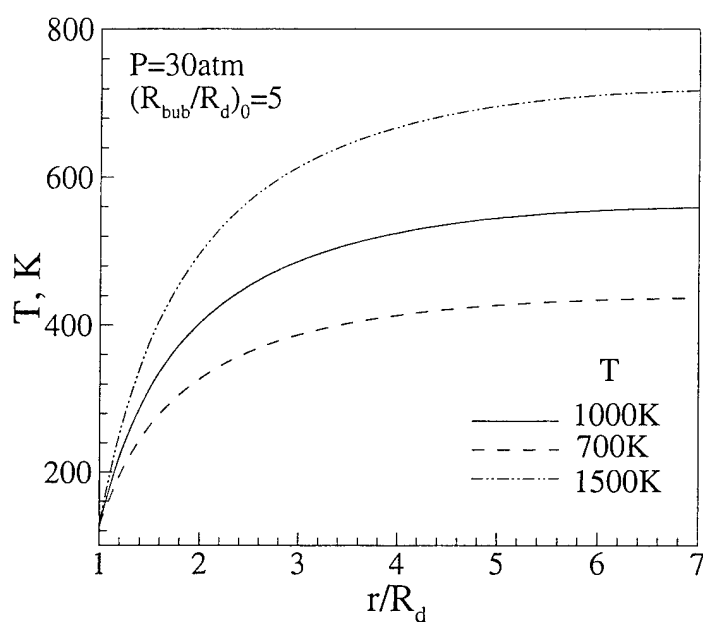


Fig 3.16 Effects of ambient temperatures on temperature distributions outside an interacting LOX droplet at a pressure of 30atm when 80% droplet mass vaporized.

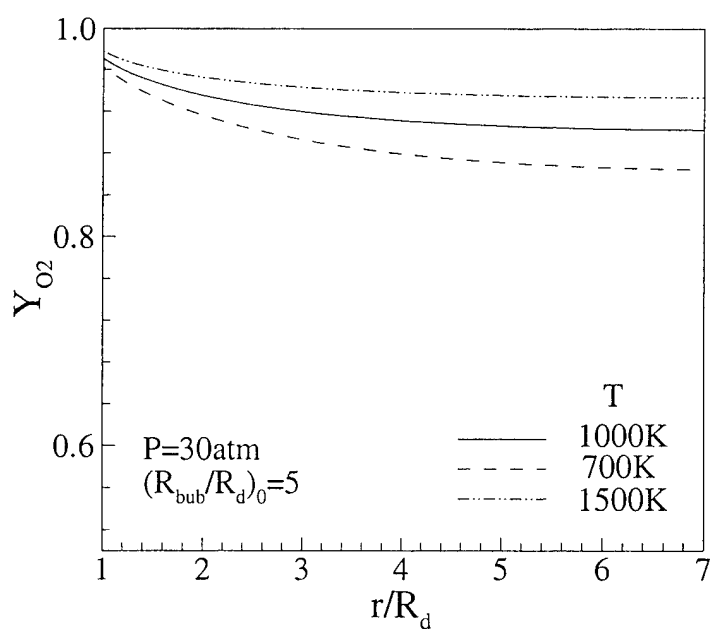


Fig 3.17 Effects of ambient temperatures on oxygen mass fraction distributions outside an interacting LOX droplet at a pressure of 30atm when 80% droplet mass vaporized.

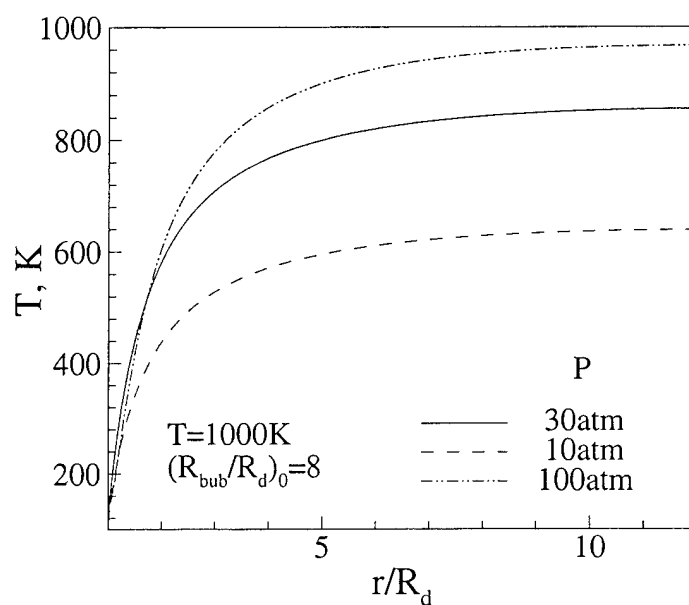


Fig 3.18 Effects of pressures on temperature distributions outside an interacting LOX droplet at an ambient temperature of 1000K when 80% droplet mass vaporized.

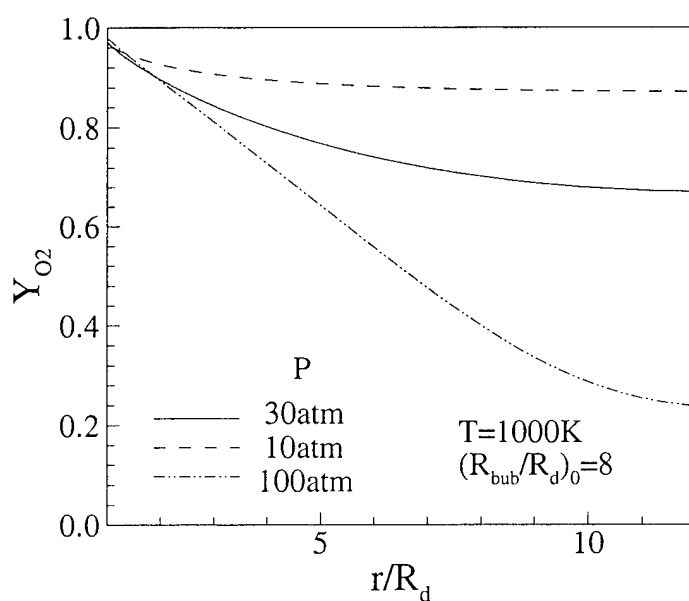


Fig 3.19 Effects of pressures on oxygen mass fraction distributions outside an interacting LOX droplet at an ambient temperature of 1000K when 80% droplet mass vaporized.

the increase of oxygen mass fraction are decided by the initial total energy and hydrogen mass quantity within the bubble. The initial total energy depends on initial hydrogen temperature, as well as the initial hydrogen mass quantity. At a given interactive radius ratio or bubble size, temperature and pressure effects on the hydrogen density play a decisive role for droplet cluster behavior. Pressure effect on the densities of initial gaseous hydrogen (e.g., at 1000K) and liquid oxygen (e.g., at 100K) are presented in Table 3.2, where pressure presents only slight influence on the density of liquid oxygen but strong effect on the density of hydrogen. With the increase of pressure, the hydrogen density increases almost linearly. Therefore, at a higher pressure, more hydrogen mass, as well as more total energy, strongly slow down the decrease rate of bulk temperature and the increase rates of oxygen accumulation.

The temperature effect on the hydrogen density is shown in Table 3.3, where the hydrogen density increases with the decrease of temperature. However, because of the narrow ranges of temperature variations, its effect on hydrogen density is much weaker than that of pressure, and the increase of hydrogen density is not capable of changing the total energy sufficiently, as indicated in Fig. 3.16. However, the variation of temperature can dramatically change the oxygen mass fraction distribution at the later stage of the vaporization process, and the oxygen accumulation is the major reason for determining droplet vaporization rate. This provides the explanation for the slightly weaker droplet interactions at a lower ambient temperature.

Table 3.2. Pressure Effect on the Density of Oxygen and Hydrogen

| Pressure (atm) | Density of H ₂ at 1000K (kg/m ³) | Density of O ₂ at 100K (kg/m ³) |
|----------------|---------------------------------------------------------|--------------------------------------------------------|
| 10 | 0.240 | 1087.2 |
| 30 | 0.717 | 1094.8 |
| 100 | 2.355 | 1118.0 |

Table 3.3. Temperature Effect on the Density of Hydrogen

| Temperature (K) | Density of H ₂ at 30atm (kg/m ³) |
|-----------------|---------------------------------------------------------|
| 700 | 1.022 |
| 1000 | 0.717 |
| 1500 | 0.479 |

Finally, the temporal variations of the bubble radius at different conditions, which represent the possible expansion or contraction of the droplet cluster in its inner region, are studied in detail. The bubble radius variations are illustrated in Figs. 3.20 and 3.21, which correspond to two different pressures of 30atm and 100atm, respectively. The bubble radius variation is due to two factors: the decrease of hydrogen temperature and the gasification of oxygen species. The first factor tends to decrease the bubble radius, while the second one increases it.

At a pressure of 30atm, as shown in Fig. 3.20, the bubble radii decrease at all the interactive radius ratios studied herein. This result indicates that the inner region of a droplet cluster is contracting during the entire vaporization process. The decrease of bubble radius is stronger at a lower interactive radius ratio, or denser droplet cluster. When pressure is increased to 100atm, the phenomenon of bubble contraction still exists, but the contraction becomes much weaker compared with that at 30atm. Results indicate that decrease of hydrogen temperature dominates this contraction process.

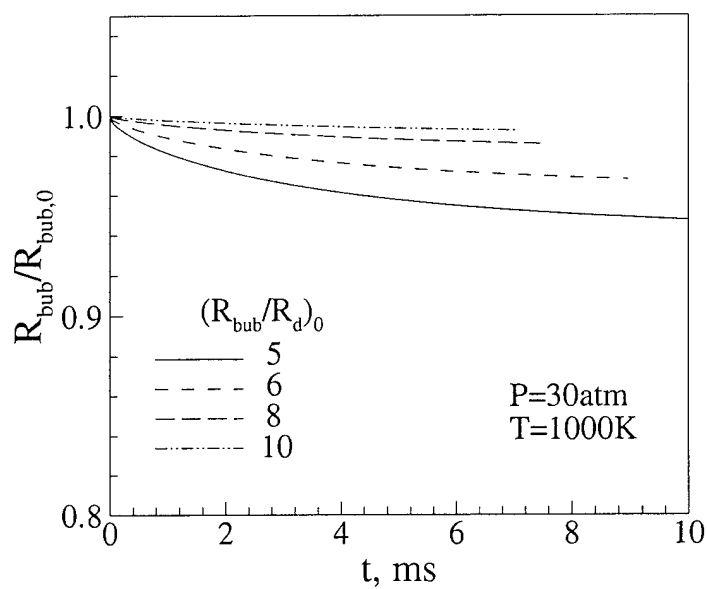


Fig. 3.20 Transient variations of bubble radii at different interactive radius ratios with a pressure of 30atm and an ambient temperature of 1000K.

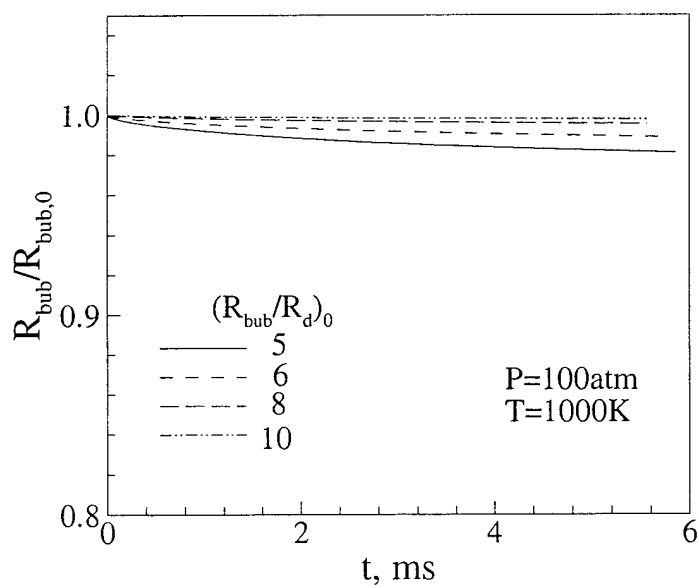


Fig. 3.21 Transient variations of bubble radii at different interactive radius ratios with a pressure of 100atm and an ambient temperature of 1000K.

3.4 Summary of Results

Droplet cluster behavior with liquid oxygen (LOX) droplets vaporization in gaseous hydrogen environments at both sub- and super-critical conditions is numerically investigated in this chapter. A high-pressure droplet vaporization model is applied with full account of thermodynamic nonideality and transport anomaly. Droplet interactions in the inner region of a droplet cluster are modeled by assuming an isolated and impermeable bubble surrounding each droplet. This research work is focused on the effects of ambient pressure and temperature on droplet interactions. The following conclusions are found important:

- 1) Pressure has strong effect on droplet interactions, while temperature presents only a minor effect, especially at a high pressure. With the increase of pressure, the effect of droplet interactions on droplet lifetime decreases.
- 2) Detailed analyses indicate that the prolongation of droplet lifetime in a dense droplet cluster is mainly caused by three reasons. First, the decrease of bulk temperature leads to a lower temperature gradient at droplet surface and, consequently, the lower heat transfer rate into the droplet. Second, more energy is transferred inside the droplet for liquid heating for an interacting droplet. Finally, at the later stage of the vaporization process, the lower gradient of oxygen mass fraction at the droplet surface causes more oxygen accumulation and lower thermal conductivity of the mixture at that region. The third factor dominates at the later stage of the droplet vaporization process.
- 3) The effects of the initial ambient pressure and temperature on hydrogen density play a decisive role in determining the initial hydrogen mass quantity and total energy in the

isolated and impermeable bubble, and ultimately decided the decrease rates of temperature and mass fraction gradients at the droplet surface.

- 4) The inner region of a droplet cluster presents continuous contraction during the entire droplet vaporization process, and the phenomenon is stronger at a lower pressure.

The results of this study complement those from the early researches (Jiang and Chiang 1996, Harstad and Bellan 1998), and give us a complete physical understanding of droplet cluster behavior.

Chapter 4

UNIFIED TREATMENT OF REAL FLUID MIXTURES AND THE APPLICATION TO PRECONDITIONING SCHEME

In practical spray combustion devices, droplets generally evaporate in convective environments. A unified numerical algorithm capable of treating the real fluid behavior ranging from dense liquid to dilute gas has to be developed. All the high-pressure characteristics, including thermodynamic nonideality and transport anomaly, must be properly taken into account. In addition, the numerical algorithm must be able to handle small-Mach number fluid flows in the dense liquid region.

In this chapter, a unified treatment of real fluid behavior is developed, and is applied to the preconditioning scheme. The unique features in this numerical algorithm are as following. First, definitions of the partial mass and partial density properties are introduced to take into account of the thermodynamic properties in real fluid mixtures. Second, thermodynamic properties are derived using fundamental thermodynamic theories, and they can be calculated based on any equation of state to naturally take into account of the pressure effect. Finally, the development is applied to the preconditioning scheme, which renders the numerical algorithm capable of solving small-Mach number fluid flows. With the combinations of the consistent thermodynamic treatments of real fluid behavior and the preconditioning scheme, an efficient and robust numerical algorithm is developed in this chapter for solving all-Mach number fluid flows at any fluid state.

4.1 Preconditioning Scheme

4.1.1 Conservation Equations

The transient conservation equations of mass, momentum, energy, and species are compactly expressed as

$$\frac{\partial rQ}{\partial t} + \frac{\partial r(E - E_v)}{\partial x} + \frac{\partial r(F - F_v)}{\partial r} = S \quad (4.1)$$

where the equations are established in an axisymmetric coordinate system in order to be consistent with the computations in the next two chapters.

The conserved variable vector Q is defined as

$$Q = [\rho \quad \rho u_x \quad \rho u_r \quad \rho e_t \quad \rho Y_i]^T \quad (4.2)$$

The convective flux vectors in the axial and radial directions, E and F , take the following forms:

$$E = \begin{bmatrix} \rho u_x \\ \rho u_x^2 + p \\ \rho u_x u_r \\ (\rho e_t + p)u_x \\ \rho u_x Y_i \end{bmatrix} \quad (4.3)$$

$$F = \begin{bmatrix} \rho u_r \\ \rho u_x u_r \\ \rho u_r^2 + p \\ (\rho e_t + p)u_r \\ \rho u_r Y_i \end{bmatrix} \quad (4.4)$$

The source vector S , which includes the terms associated with the axisymmetric geometry, viscous diffusion, and chemical reaction, is expressed in the following form:

$$S = \begin{bmatrix} 0 \\ -\frac{\partial}{\partial x} \left(\frac{2}{3} \mu u_r \right) \\ p - \frac{4}{3} \frac{\mu u_r}{r} + \frac{2}{3} \mu \frac{\partial u_x}{\partial x} - \frac{2}{3} u_r \frac{\partial \mu}{\partial r} \\ -\frac{\partial}{\partial x} \left(\frac{2}{3} \mu u_r u_x \right) - \frac{\partial}{\partial r} \left(\frac{2}{3} \mu u_r^2 \right) \\ r \dot{\omega}_i \end{bmatrix} \quad (4.5)$$

where $i = 1, \dots, N$, and the variable N is the total number of species involved in the problem.

The corresponding viscous flux vectors, E_v and F_v , can be written as second-order terms. In order to do this, a viscous vector Q_v is first defined as

$$Q_v = [p, u_x, u_r, T, Y_i]^T \quad (4.6)$$

The viscous flux vectors are then expressed as

$$E_v = R_{xx} \frac{\partial Q_v}{\partial x} + R_{xr} \frac{\partial Q_v}{\partial r} \quad (4.7)$$

$$F_v = R_{rx} \frac{\partial Q_v}{\partial x} + R_{rr} \frac{\partial Q_v}{\partial r} \quad (4.8)$$

where the viscous coefficient matrixes are

$$R_{xx} = \begin{bmatrix} 0 & 0 & 0 & 0 & 0 & \dots & 0 \\ 0 & \frac{4}{3}\mu & 0 & 0 & 0 & \dots & 0 \\ 0 & 0 & \mu & 0 & 0 & \dots & 0 \\ 0 & \frac{4}{3}\mu u_x & \mu u_r & \lambda & \rho(\bar{h}_1 D_{1m} - \bar{h}_N D_{Nm}) & \dots & \rho(\bar{h}_{(N-1)} D_{(N-1)m} - \bar{h}_N D_{Nm}) \\ 0 & 0 & 0 & 0 & \rho D_{1m} & \dots & 0 \\ \vdots & \vdots & \vdots & \vdots & \vdots & \ddots & \vdots \\ 0 & 0 & 0 & 0 & 0 & \dots & \rho D_{(N-1)m} \end{bmatrix} \quad (4.9a)$$

$$R_{xr} = \begin{bmatrix} 0 & 0 & 0 & 0 & 0 & \dots & 0 \\ 0 & 0 & -\frac{2}{3}\mu & 0 & 0 & \dots & 0 \\ 0 & \mu & 0 & 0 & 0 & \dots & 0 \\ 0 & \mu u_r & -\frac{2}{3}\mu u_x & 0 & 0 & \dots & 0 \\ 0 & 0 & 0 & 0 & 0 & \dots & 0 \\ \vdots & \vdots & \vdots & \vdots & \vdots & \ddots & \vdots \\ 0 & 0 & 0 & 0 & 0 & \dots & 0 \end{bmatrix} \quad (4.9b)$$

$$R_{rx} = \begin{bmatrix} 0 & 0 & 0 & 0 & 0 & \cdots & 0 \\ 0 & 0 & \mu & 0 & 0 & \cdots & 0 \\ 0 & -\frac{2}{3}\mu & 0 & 0 & 0 & \cdots & 0 \\ 0 & -\frac{2}{3}\mu u_r & \mu u_x & 0 & 0 & \cdots & 0 \\ 0 & 0 & 0 & 0 & 0 & \cdots & 0 \\ \vdots & \vdots & \vdots & \vdots & \vdots & \ddots & \vdots \\ 0 & 0 & 0 & 0 & 0 & \cdots & 0 \end{bmatrix} \quad (4.9c)$$

$$R_{rr} = \begin{bmatrix} 0 & 0 & 0 & 0 & 0 & \cdots & 0 \\ 0 & \mu & 0 & 0 & 0 & \cdots & 0 \\ 0 & 0 & \frac{4}{3}\mu & 0 & 0 & \cdots & 0 \\ 0 & \mu u_x & \frac{4}{3}\mu u_r & \lambda & \rho(\bar{h}_1 D_{1m} - \bar{h}_N D_{Nm}) & \cdots & \rho(\bar{h}_{(N-1)} D_{(N-1)m} - \bar{h}_N D_{Nm}) \\ 0 & 0 & 0 & 0 & \rho D_{1m} & \cdots & 0 \\ \vdots & \vdots & \vdots & \vdots & \vdots & \ddots & \vdots \\ 0 & 0 & 0 & 0 & 0 & \cdots & \rho D_{(N-1)m} \end{bmatrix} \quad (4.9d)$$

The standard variables are used in Eqs. (4.6-4.9), including density ρ , velocity components in x- and r- directions u_x and u_r , pressure p , temperature T , the total energy per unit mass e_t , mass fraction of species i Y_i , viscosity μ , conductivity λ , mass diffusivity in the mixture D_{im} , and the chemical reaction rate of species i $\dot{\omega}_i$. There is only one special variable, the partial mass enthalpy of species i \bar{h}_i , which is defined in Chapter 2.

4.1.2 Preconditioning Method

It is well known that time-marching algorithms are extremely efficient for solving the transonic, supersonic, and hypersonic compressible flow problems, but they encounter convergence difficulties for small-Mach number flows. Two major reasons account for this: the machine round-off errors arising from the calculation of the pressure gradients and the stiffness of the eigenvalues in the numerical system.

The first problem can be circumvented easily by introducing pressure decomposition (Choi and Merkle 1993, Shuen et al. 1993),

$$p = p_0 + p_g \quad (4.10)$$

where p_0 is a constant, which is generally chosen as the major part of the pressure. The gauge pressure p_g is the dynamic part, responsible for the velocity-pressure coupling in the momentum equations, and it is the driving force for fluid flows.

After pressure decomposition, the total pressure in the momentum equations is replaced by the gauge pressure p_g . We then have the following new inviscid flux and source terms:

$$E = \begin{bmatrix} \rho u_x \\ \rho u_x^2 + p_g \\ \rho u_x u_r \\ (\rho e_t + p)u_x \\ \rho u_x Y_i \end{bmatrix} \quad (4.11)$$

$$F = \begin{bmatrix} \rho u_r \\ \rho u_x u_r \\ \rho u_r^2 + p_g \\ (\rho e_t + p)u_r \\ \rho u_r Y_i \end{bmatrix} \quad (4.12)$$

$$S = \begin{bmatrix} 0 \\ -\frac{\partial}{\partial x} \left(\frac{2}{3} \mu u_r \right) \\ p_g - \frac{4}{3} \frac{\mu u_r}{r} + \frac{2}{3} \mu \frac{\partial u_x}{\partial x} - \frac{2}{3} u_r \frac{\partial \mu}{\partial r} \\ -\frac{\partial}{\partial x} \left(\frac{2}{3} \mu u_r u_x \right) - \frac{\partial}{\partial r} \left(\frac{2}{3} \mu u_r^2 \right) \\ r \dot{\omega}_i \end{bmatrix} \quad (4.13)$$

The new viscous variable vector is also redefined as

$$Q_v = [p_g, u_x, u_r, T, Y_i]^T \quad (4.14)$$

All the other terms in the conservation equations are not affected by pressure decomposition.

In order to circumvent the difficulty of eigenvalue stiffness, we need to add in a preconditioning term $\Gamma \frac{\partial r \hat{Q}}{\partial \tau}$, where the variable τ represents the pseudo-time. The

preconditioning matrix Γ , and the variable vector \hat{Q} are chosen as (Shuen et al. 1993)

$$\Gamma = \begin{bmatrix} 1/\beta & 0 & 0 & 0 & 0 & \cdots & 0 \\ u_x/\beta & \rho & 0 & 0 & 0 & \cdots & 0 \\ u_r/\beta & 0 & \rho & 0 & 0 & \cdots & 0 \\ h_t/\beta - 1 & \rho u_x & \rho u_r & \rho & 0 & \cdots & 0 \\ Y_1/\beta & 0 & 0 & 0 & \rho & \cdots & 0 \\ \vdots & \vdots & \vdots & \vdots & \vdots & \ddots & 0 \\ Y_{N_e-1}/\beta & 0 & 0 & 0 & 0 & \cdots & \rho \end{bmatrix} \quad (4.15)$$

and,

$$\hat{Q} = [p_g, u_x, u_r, h, Y_i]^T \quad (4.16)$$

where the variables are enthalpy h , the total enthalpy per unit mass h_t , and a scaling parameter β .

The conservation equations with the pseudo-time derivative terms are expressed as

$$\Gamma \frac{\partial r\hat{Q}}{\partial \tau} + \frac{\partial rQ}{\partial t} + \frac{\partial rE}{\partial x} + \frac{\partial rF}{\partial r} - \frac{\partial}{\partial x} \left[rR_{xx} \frac{\partial Q_v}{\partial x} + rR_{xr} \frac{\partial Q_v}{\partial r} \right] - \frac{\partial}{\partial r} \left[rR_{rx} \frac{\partial Q_v}{\partial x} + rR_{rr} \frac{\partial Q_v}{\partial r} \right] = S \quad (4.17)$$

Proof of the appropriateness of the chosen preconditioning term for a real fluid mixture is presented in the following sections, where the scaling factor β is also defined.

4.2. Numerical Derivations for Real Fluid Mixtures

All the relationships required in the numerical algorithm are derived using fundamental thermodynamic theories. They can be calculated based on any equation of state. The partial mass and partial density properties of a real fluid mixture, as defined in Chapter 2, are also utilized in the derivations.

4.2.1 Important Thermodynamic Relationships

Some important thermodynamic relationships are needed for the derivations of numerical Jacobians and eigenvalues in the following sections. We will derive these relationships here.

First, a thermodynamic relationship correlating enthalpy as a function of pressure, density, and mass fractions are derived. According to thermodynamics, each intensive property will depend on $N + 1$ other intensive variables in the mixture. We begin with the following relation:

$$\rho e = \rho e(T, \rho_i) \quad (4.18)$$

where $i = 1, \dots, N$, and e is the internal energy per unit mass.

We are only interested in its differential form, which can be expressed as

$$d\rho e = \rho \left(\frac{\partial e}{\partial T} \right)_{\rho_i} dT + \sum_{i=1}^N \left(\frac{\partial \rho e}{\partial \rho_i} \right)_{T, \rho_{j \neq i}} d\rho_i \quad (4.19)$$

Based on the definition of partial density properties, it is recognized

$$\tilde{e}_i = \left(\frac{\partial \rho e}{\partial \rho_i} \right)_{T, \rho_{j \neq i}}$$

which is the partial density internal energy of species i in the mixture. The first derivative in Eq. (4.19) is the constant volume heat capacity C_v . Substituting these variables into Eq. (4.19) leads to the following expression:

$$d\rho e = \rho C_v dT + \sum_{i=1}^N \tilde{e}_i d\rho_i \quad (4.20)$$

We then want to correlate temperature T as a function of pressure p and the partial density ρ_i . According to thermodynamics, the following relation exists:

$$p = p(T, \rho_i) \quad (4.21)$$

where $i = 1, \dots, N$.

Its differential form is expressed as

$$dp = \left(\frac{\partial p}{\partial T} \right)_{\rho_i} dT + \sum_{i=1}^N \left(\frac{\partial p}{\partial \rho_i} \right)_{T, \rho_{j \neq i}} d\rho_i \quad (4.22)$$

In this equation, the summation in the second term is first changed to be $1, \dots, N-1$. Some simple manipulations will then lead to the following relation:

$$dT = \frac{dp - \sum_{i=1}^{N-1} \left[\left(\frac{\partial p}{\partial \rho_i} \right)_{T, \rho_{j \neq i}} - \left(\frac{\partial p}{\partial \rho_N} \right)_{T, \rho_{j \neq N}} \right] d\rho_i - \left(\frac{\partial p}{\partial \rho_N} \right)_{T, \rho_{j \neq N}} d\rho}{\left(\frac{\partial p}{\partial T} \right)_{\rho_i}} \quad (4.23)$$

Substituting Eq. (4.23) into Eq. (4.20), the following expression is easily derived:

$$\begin{aligned} d\rho e = & \rho C_v \left(\frac{\partial T}{\partial p} \right)_{\rho_i} dp + \sum_{i=1}^N \tilde{e}_i d\rho_i - \rho C_v \left(\frac{\partial T}{\partial p} \right)_{\rho_i} \left(\frac{\partial p}{\partial \rho_N} \right)_{T, \rho_{j \neq N}} d\rho \\ & - \rho C_v \left(\frac{\partial T}{\partial p} \right)_{\rho_i} \sum_{i=1}^{N-1} \left[\left(\frac{\partial p}{\partial \rho_i} \right)_{T, \rho_{j \neq i}} - \left(\frac{\partial p}{\partial \rho_N} \right)_{T, \rho_{j \neq N}} \right] d\rho_i \end{aligned} \quad (4.24)$$

The left hand-side term is further rewritten as

$$d\rho e = \rho de + e d\rho \quad (4.25)$$

Substituting Eq. (4.25) into Eq. (4.24), the following relation is established after the reorganization:

$$\begin{aligned} de = & C_v \left(\frac{\partial T}{\partial p} \right)_{\rho_i} dp - C_v \left(\frac{\partial T}{\partial p} \right)_{\rho_i} \left(\frac{\partial p}{\partial \rho_N} \right)_{T, \rho_{j \neq N}} d\rho \\ & - C_v \left(\frac{\partial T}{\partial p} \right)_{\rho_i} \sum_{i=1}^{N-1} \left[\left(\frac{\partial p}{\partial \rho_i} \right)_{T, \rho_{j \neq i}} - \left(\frac{\partial p}{\partial \rho_N} \right)_{T, \rho_{j \neq N}} \right] d\rho_i \\ & + \frac{1}{\rho} \sum_{i=1}^{N-1} (\tilde{e}_i - \tilde{e}_N) d\rho_i + \frac{\tilde{e}_N}{\rho} d\rho - \frac{e}{\rho} d\rho \end{aligned} \quad (4.26)$$

Based on fundamental thermodynamic theories, the following relation can be easily obtained:

$$dh = de + \frac{1}{\rho} dp - \frac{p}{\rho^2} d\rho \quad (4.27)$$

Substituting Eqs. (4.26) into Eq. (4.27), the following expression can be obtained after some straightforward manipulations:

$$\begin{aligned} dh = & \left[C_v \left(\frac{\partial T}{\partial p} \right)_{\rho_i} + \frac{1}{\rho} \right] dp \\ & + \left[-C_v \left(\frac{\partial T}{\partial p} \right)_{\rho_i} \left(\frac{\partial p}{\partial \rho} \right)_{T, Y_i} + \frac{1}{\rho} \sum_{i=1}^N Y_i \tilde{e}_i - \frac{e}{\rho} - \frac{p}{\rho^2} \right] d\rho \\ & + \sum_{i=1}^{N-1} \left\{ -\rho C_v \left(\frac{\partial T}{\partial p} \right)_{\rho_i} \left[\left(\frac{\partial p}{\partial \rho_i} \right)_{T, \rho_{j \neq i}} - \left(\frac{\partial p}{\partial \rho_N} \right)_{T, \rho_{j \neq N}} \right] + (\tilde{e}_i - \tilde{e}_N) \right\} dY_i \end{aligned} \quad (4.28a)$$

This relation will be used frequently for the derivation of the numerical Jacobians.

The following compact notations are, therefore, defined:

$$A_p = C_v \left(\frac{\partial T}{\partial p} \right)_{\rho_i} + \frac{1}{\rho} \quad (4.28b)$$

$$A_\rho = -C_v \left(\frac{\partial T}{\partial p} \right)_{\rho_i} \left(\frac{\partial p}{\partial \rho} \right)_{T, Y_i} + \frac{1}{\rho} \sum_{i=1}^N Y_i \tilde{e}_i - \frac{e}{\rho} - \frac{p}{\rho^2} \quad (4.28c)$$

$$A_{Y_i} = -\rho C_v \left(\frac{\partial T}{\partial p} \right)_{\rho_i} \left[\left(\frac{\partial p}{\partial \rho_i} \right)_{T, \rho_{j \neq i}} - \left(\frac{\partial p}{\partial \rho_N} \right)_{T, \rho_{j \neq N}} \right] + (\tilde{e}_i - \tilde{e}_N) \quad (4.28d)$$

Equation (4.28a) is finally expressed in the following form:

$$dh = A_p dp + A_\rho d\rho + \sum_{i=1}^{N-1} A_{Y_i} dY_i \quad (4.28e)$$

Equation (4.28e) is one of the thermodynamic relationships we are looking for.

Next, another relationship, which correlates enthalpy as a function of pressure, temperature, and mass fractions, will be developed. We start with the following relation:

$$d\rho_i = \rho dY_i + Y_i d\rho \quad (4.29)$$

Using Eq. (4.29), Eq. (4.20) can be rewritten as

$$d\rho e = \rho C_v dT + \sum_{i=1}^N \rho \tilde{e}_i dY_i + \sum_{i=1}^N Y_i \tilde{e}_i d\rho \quad (4.30)$$

Using Eq. (4.25), Eq. (4.30) can be further derived as

$$de = C_v dT + \sum_{i=1}^{N-1} (\tilde{e}_i - \tilde{e}_N) dY_i + \frac{1}{\rho} \left(\sum_{i=1}^N Y_i \tilde{e}_i - e \right) d\rho \quad (4.31)$$

Based on Eqs. (4.25) and (4.29), a differential relationship correlating density as a function of temperature, pressure, and the mass fractions can be expressed as

$$d\rho = \frac{dp - \left(\frac{\partial p}{\partial T} \right)_{\rho_i} dT - \sum_{i=1}^{N-1} \rho \left[\left(\frac{\partial p}{\partial \rho_i} \right)_{T, \rho_{j \neq i}} - \left(\frac{\partial p}{\partial \rho_N} \right)_{T, \rho_{j \neq N}} \right] dY_i}{\left(\frac{\partial p}{\partial \rho} \right)_{T, Y_i}} \quad (4.32)$$

Substituting Eqs. (4.27) and (4.32) into Eq. (4.31), another important differential thermodynamic relationship is established

$$dh = B_T dT + B_p dp + \sum_{i=1}^{N-1} B_{Y_i} dY_i \quad (4.33a)$$

where the coefficients B_T , B_p , and B_{Y_i} are defined as

$$B_T = C_v - \frac{1}{\rho} \left(\frac{\partial p}{\partial T} \right)_{\rho_i} \left(\frac{\partial \rho}{\partial p} \right)_{T, Y_i} \left(\sum_{i=1}^N Y_i \tilde{e}_i - e - \frac{p}{\rho} \right) \quad (4.33b)$$

$$B_p = \frac{1}{\rho} + \frac{1}{\rho} \left(\frac{\partial \rho}{\partial p} \right)_{T, Y_i} \left(\sum_{i=1}^N Y_i \tilde{e}_i - e - \frac{p}{\rho} \right) \quad (4.33c)$$

$$B_{Y_i} = (\tilde{e}_i - \tilde{e}_N) - \left(\frac{\partial \rho}{\partial p} \right)_{T, Y_i} \left(\sum_{i=1}^N Y_i \tilde{e}_i - e - \frac{p}{\rho} \right) \left[\left(\frac{\partial p}{\partial \rho_i} \right)_{T, \rho_{j \neq i}} - \left(\frac{\partial p}{\partial \rho_N} \right)_{T, \rho_{j \neq N}} \right] \quad (4.33d)$$

According to the definition in thermodynamics, we recognize that the coefficient B_T is equal to the constant pressure heat capacity C_p of a mixture,

$$C_p = B_T = C_v - \frac{1}{\rho} \left(\frac{\partial p}{\partial T} \right)_{\rho_i} \left(\frac{\partial \rho}{\partial p} \right)_{T, Y_i} \left(\sum_{i=1}^N Y_i \tilde{e}_i - e - \frac{p}{\rho} \right) \quad (4.34)$$

Finally a relationship regarding the speed of sound in the mixture is derived.

According to the definition of the speed of sound,

$$a^2 = \left(\frac{\partial p}{\partial \rho} \right)_{s, Y_i} \quad (4.35)$$

Based on Eqs. (4.25) and (4.29), the following relationship is derived:

$$dp = \left(\frac{\partial p}{\partial T} \right)_{\rho_i} dT + \sum_{i=1}^{N-1} \rho \left[\left(\frac{\partial p}{\partial \rho_i} \right)_{T, \rho_{j \neq i}} - \left(\frac{\partial p}{\partial \rho_N} \right)_{T, \rho_{j \neq N}} \right] dY_i + \left(\frac{\partial p}{\partial \rho} \right)_{T, Y_i} d\rho \quad (4.36)$$

Based on Eq. (4.36), the following expression is obtained in a straightforward manner:

$$\left(\frac{\partial p}{\partial \rho} \right)_{s, Y_i} = \left(\frac{\partial p}{\partial T} \right)_{\rho_i} \left(\frac{\partial T}{\partial \rho} \right)_{s, Y_i} + \left(\frac{\partial p}{\partial \rho} \right)_{T, Y_i} \quad (4.37)$$

In thermodynamics, the following relationship exists:

$$s = s(T, \rho, Y_i) \quad (4.38)$$

where $i = 1, \dots, N-1$.

After utilizing some fundamental thermodynamic relationships, the following differential form of Eq. (4.38) can be obtained:

$$ds = \frac{C_v}{T} dT - \frac{1}{\rho^2} \left(\frac{\partial p}{\partial T} \right)_{\rho_i} d\rho + \sum_{i=1}^{N-1} \left(\frac{\partial s}{\partial Y_i} \right)_{T, \rho, Y_{j \neq i}} dY_i \quad (4.39)$$

Based on Eq. (4.39), the following expression is further derived:

$$\left(\frac{\partial T}{\partial \rho} \right)_{s, Y_i} = \frac{T}{\rho^2} \left(\frac{\partial p}{\partial T} \right)_{\rho_i} / C_v \quad (4.40)$$

Substituting Eq. (4.40) into Eq. (4.37), a general expression of the speed of sound in a mixture is established as

$$a^2 = \left(\frac{\partial p}{\partial \rho} \right)_{s, Y_i} = \frac{C_p}{C_v} \left(\frac{\partial p}{\partial \rho} \right)_{T, Y_i} \quad (4.41)$$

Equations (4.28), (4.33), (4.34), and (4.41) are the important thermodynamic relationships required in the numerical derivations below.

4.2.2 Implicit Numerical Scheme and Jacobians

The preconditioned transient conservation equations are solved using the implicit scheme with the dual time-stepping integration technique. The discretized equations are

$$\begin{aligned} & \left[\Gamma - \frac{\Delta \tau}{r} D + \frac{a_1 \Delta \tau}{\Delta t} T + \Delta \tau \frac{\partial}{\partial x} A + \Delta \tau \frac{\partial}{\partial r} B - \Delta \tau \frac{\partial}{\partial x} \left(r \hat{R}_{xx} \frac{\partial}{\partial x} \left(\frac{1}{r} \cdot \right) \right) \right] \Delta r \hat{Q} \\ & - \Delta \tau \frac{\partial}{\partial r} \left(r \hat{R}_{rr} \frac{\partial}{\partial r} \left(\frac{1}{r} \cdot \right) \right) \\ & = \Delta \tau \left(S^p - \frac{a_1 r Q^p + a_2 r Q^n + a_3 r Q^{n-1}}{\Delta t} - \frac{\partial r(E - E_v)^p}{\partial x} + \frac{\partial r(F - F_v)^p}{\partial r} \right) \end{aligned} \quad (4.42)$$

where T, D, A, B, \hat{R}_{xx} , and \hat{R}_{rr} are the numerical Jacobians defined in the linearization process:

$$T = \frac{\partial Q}{\partial \hat{Q}} \quad (4.43) \quad A = \frac{\partial E}{\partial \hat{Q}} \quad (4.44) \quad B = \frac{\partial F}{\partial \hat{Q}} \quad (4.45)$$

$$D = \frac{\partial S}{\partial \hat{Q}} \quad (4.46) \quad \hat{R}_{xx} = R_{xx} \frac{\partial Q_v}{\partial \hat{Q}} \quad (4.47) \quad \hat{R}_{rr} = R_{rr} \frac{\partial Q_v}{\partial \hat{Q}} \quad (4.48)$$

The coefficients a_1, a_2 , and a_3 are chosen based on the requirement of the time accuracy. In the case that time steps are uniform and the second-order time accuracy is required, they can be chosen as

$$a_1 = \frac{3}{2}, a_2 = -2, a_3 = \frac{1}{2} \quad (4.49)$$

The left hand-side of Eq. (4.42) is evaluated in the pseudo-time step p . The superscripts $n+1, n$, and $n-1$ in the right hand-side represent the variables in the new, current, and old physical time steps, respectively. Once steady state solution is reached through pseudo-time iterations, the new solution in the physical time step $n+1$ is obtained.

The thermodynamic relationships derived in the section above will be utilized to find the numerical Jacobians. Only the Jacobian A is presented here as an illustrative example, all the other Jacobians are given in Appendix C.

During the derivation of the numerical Jacobian A , a relationship correlating enthalpy as a function of density, pressure, and mass fractions is obviously required. Based on the thermodynamic relationships shown in Eqs. (4.28b)-(4.28e), the numerical Jacobian A takes the following form:

$$A = \begin{bmatrix} -u_x \frac{A_p}{A_\rho} & \rho & 0 & \frac{u_x}{A_\rho} & -u_x \frac{A_{Y1}}{A_\rho} & \cdots & -u_x \frac{A_{Y_{N-1}}}{A_\rho} \\ -u_x^2 \frac{A_p}{A_\rho} + 1 & 2\rho u_x & 0 & \frac{u_x^2}{A_\rho} & -u_x^2 \frac{A_{Y1}}{A_\rho} & \cdots & -u_x^2 \frac{A_{Y_{N-1}}}{A_\rho} \\ -u_x u_r \frac{A_p}{A_\rho} & \rho u_r & \rho u_x & \frac{u_x u_r}{A_\rho} & -u_x u_r \frac{A_{Y1}}{A_\rho} & \cdots & -u_x u_r \frac{A_{Y_{N-1}}}{A_\rho} \\ -u_x h_t \frac{A_p}{A_\rho} & \begin{bmatrix} \rho u_x^2 \\ + \rho h_t \end{bmatrix} & \rho u_x u_r & \begin{bmatrix} \rho u_x + \\ \frac{u_x h_t}{A_\rho} \end{bmatrix} & -u_x h_t \frac{A_{Y1}}{A_\rho} & \cdots & -u_x h_t \frac{A_{Y_{N-1}}}{A_\rho} \\ -u_x Y_1 \frac{A_p}{A_\rho} & \rho Y_1 & 0 & \frac{u_x Y_1}{A_\rho} & \begin{bmatrix} -u_x Y_1 \frac{A_{Y1}}{A_\rho} \\ + \rho u_x \end{bmatrix} & \cdots & -u_x Y_1 \frac{A_{Y_{N-1}}}{A_\rho} \\ \vdots & \vdots & \vdots & \vdots & \vdots & \ddots & \vdots \\ -u_x Y_{N-1} \frac{A_p}{A_\rho} & \rho Y_{N-1} & 0 & \frac{u_x Y_{N-1}}{A_\rho} & -u_x Y_{N-1} \frac{A_{Y1}}{A_\rho} & \cdots & \begin{bmatrix} -u_x Y_{N-1} \frac{A_{Y_{N-1}}}{A_\rho} \\ + \rho u_x \end{bmatrix} \end{bmatrix} \quad (4.50)$$

4.2.3 Eigenvalues

For the preconditioned conservation equations, the eigenvalues in the x-direction are obtained in the matrix $\Gamma^{-1}A$. The calculation is straightforward, and the eigenvalues are

$$\lambda_A = u_x, \frac{1}{2} \left[u_x \left(1 + \frac{\beta}{a_c^2} \right) \pm \sqrt{u_x^2 \left(1 - \frac{\beta}{a_c^2} \right)^2 + 4\beta} \right], u_x, u_x, \dots, u_x \quad (4.51)$$

where

$$a_c^2 = \frac{A_\rho}{\frac{1}{\rho} - A_p} \quad (4.52)$$

We will prove that the variable a_c is indeed equal to the speed of sound a in a mixture. The variable A_ρ is first reorganized as

$$\begin{aligned}
A_\rho &= -C_v \left(\frac{\partial T}{\partial p} \right)_{\rho_i} \left(\frac{\partial p}{\partial \rho} \right)_{T, Y_i} + \frac{1}{\rho} \sum_{i=1}^N Y_i \tilde{e}_i - \frac{e}{\rho} - \frac{p}{\rho^2} \\
&= - \left(\frac{\partial T}{\partial p} \right)_{\rho_i} \left(\frac{\partial p}{\partial \rho} \right)_{T, Y_i} \left[C_v - \frac{1}{\rho} \left(\frac{\partial p}{\partial T} \right)_{\rho_i} \left(\frac{\partial \rho}{\partial p} \right)_{T, Y_i} \left(\sum_{i=1}^N Y_i \tilde{e}_i - e - \frac{p}{\rho} \right) \right] \quad (4.53a)
\end{aligned}$$

It is recognized that the term in the brackets is equal to the constant heat capacity C_p (e.g., referring to Eq. (4.34)). Therefore, the following relation is derived:

$$A_\rho = - \left(\frac{\partial T}{\partial p} \right)_{\rho_i} \left(\frac{\partial p}{\partial \rho} \right)_{T, Y_i} C_p \quad (4.53b)$$

Utilizing Eq. (4.28b), it then gives

$$\frac{1}{\rho} - A_p = -C_v \left(\frac{\partial T}{\partial p} \right)_{\rho_i} \quad (4.54)$$

Substituting Eqs. (4.53b) and (4.54) into Eq. (4.52), a final relation is derived as

$$a_c^2 = \frac{- \left(\frac{\partial T}{\partial p} \right)_{\rho_i} \left(\frac{\partial p}{\partial \rho} \right)_{T, Y_i} C_p}{- C_v \left(\frac{\partial T}{\partial p} \right)_{\rho_i}} = \frac{C_p}{C_v} \left(\frac{\partial p}{\partial \rho} \right)_{T, Y_i} = a^2 \quad (4.55)$$

The eigenvalues in x-direction can now be expressed as

$$\lambda_A = u_x, \frac{1}{2} \left[u_x \left(1 + \frac{\beta}{a^2} \right) \pm \sqrt{u_x^2 \left(1 - \frac{\beta}{a^2} \right)^2 + 4\beta} \right], u_x, u_x, \dots, u_x \quad (4.56)$$

This result is extremely important since it indicates the eigenvalues of the preconditioned conservation equations of real fluid mixtures are in the same form as those of the ideal gas mixtures (Shuen et al. 1993, Buelow, 1995). This result also demonstrates that our choice of the preconditioning matrix Γ and main variables \hat{Q} are appropriate. The derivations are independent of any equation of state.

Based on the eigenvalues in Eq. (4.56), another important conclusion is that the scaling factor β can be chosen exactly as that derived in an ideal gas mixture. Since the eigenvalues remain the same forms, the same scaling factor will definitely work for both cases to overcome the eigenvalue stiffness problem.

4.2.4 Selection of the Scaling Factor

For inviscid flows, in order to get the well-conditioned eigenvalues, the scaling factor can be taken as (Choi and Merkle 1993, Shuen et al. 1993, Hsieh and Yang 1997)

$$\beta_{inv} = \begin{cases} u_R^2 & \text{if } u^2 < u_R^2 \\ u^2 & \text{if } u_R^2 < u^2 < a^2 \\ a^2 & \text{if } u^2 > a^2 \end{cases} \quad (4.57)$$

where the variable u_R is a reference velocity. Generally a very small number is chosen to maintain the reference Mach number at the order of 10^{-5} .

Referring to the eigenvalue expressions in Eq. (4.56), we found that this choice of scaling factor indeed maintains all the eigenvalues at the same order for inviscid all-Mach number flows. Moreover, all the eigenvalues remain as real numbers, and the preconditioned conservation equations are still of hyperbolic nature.

In some viscous flow regions, since the flow Reynolds number Re can become far smaller than 1, the viscous diffusions becomes dominant compared with the convection terms. Under these circumstances, the scaling factor must also be able to control the viscous damping rates. Therefore, an appropriate scaling factor for Navier-Stokes equations should be able to simultaneously control both the Courant-Friedrichs-Lewy (CFL) and the von Neumann (VNN) numbers. This can be accomplished by choosing the scaling factor as (Choi and Merkle 1993, Buelow 1995)

$$\beta = \min(1, \max(\beta_{inv}, \beta_{vis})) \quad (4.58)$$

where the inviscid scaling factor β_{inv} is given in Eq. (4.57). The viscous scaling factor β_{vis} will have to consider the grid aspect ratio effect, which is an important factor for viscous flow computation. For the 2-D and axisymmetric flows, the viscous scaling factor is chosen as (Buelow 1995)

$$\beta_{vis} = \max(\beta_{vis}^x, \beta_{vis}^r) \quad (4.59a)$$

where the two scaling factors in both x- and r- directions are defined as

$$\beta_{vis}^x = \frac{\sigma_x(\sigma_x - 1)u_x^2}{1 + \frac{u_x^2}{a^2}(\sigma_x - 1)} \quad (4.59b)$$

$$\beta_{vis}^r = \frac{\sigma_r(\sigma_r - 1)u_r^2}{1 + \frac{u_r^2}{a^2}(\sigma_r - 1)} \quad (4.59c)$$

The variables σ_x, σ_r are

$$\sigma_x = \frac{AR^2 \cdot CFL}{VNN \cdot \text{Re}_{\Delta x}} \quad (4.59d)$$

$$\sigma_r = \frac{CFL}{AR^2 \cdot VNN \cdot \text{Re}_{\Delta r}} \quad (4.59e)$$

The other variables are Courant-Friedrichs-Lewy (CFL) number, the von Neumann (VNN) number, the grid aspect ratio AR , and the cell Reynolds numbers in x- and r- directions $\text{Re}_{\Delta x}, \text{Re}_{\Delta r}$, respectively. The definitions of these variables are

$$CFL = \frac{|\lambda|_{\max} \Delta \tau}{\Delta x} \quad (4.59f)$$

$$VNN = \max\left(\frac{\mu}{\rho}, \frac{k}{\rho C_p}, D_{im}\right) \cdot \Delta\tau / \Delta x^2 \quad (4.59g)$$

$$AR = \frac{\Delta x}{\Delta r} \quad (4.59h)$$

$$Re_{\Delta x} = \frac{\rho u_x \Delta x}{\mu} \quad (4.59i)$$

$$Re_{\Delta r} = \frac{\rho u_r \Delta r}{\mu} \quad (4.59j)$$

The scaling factor of the preconditioned conservation equations, which is valid for both inviscid and viscous flows, is now completely established.

4.3 Thermophysical Properties

The Soave-Redlich-Kwong (SRK) equation of state, as presented in Chapter 2, is utilized for calculating all the thermodynamic properties with full account of thermodynamic nonideality. Some relationships have already been derived in Chapter 2, and more details are presented in Appendix A.

The transport properties to be evaluated herein are thermal conductivity, viscosity and mass diffusivity. These properties are evaluated for a real fluid mixture with proper consideration of transport anomaly. To evaluate thermal conductivity and viscosity, the extended corresponding states one-fluid model is used (Ely and Hanly 1981, 1983). The binary mass diffusivities at high pressures are evaluated by the method proposed by Takahashi (1974), which is a very simple corresponding state method. The details can be found in Chapter 2.

4.4 Numerical Solution

The preconditioned conservation equations are discretized by central-differencing in space. With an oxygen droplet vaporization in supercritical hydrogen environments, a contact discontinuity with a very large density gradient exists between the oxygen and hydrogen interface. Therefore, artificial viscous dissipation terms are required. In this numerical treatment, the second-order and fourth-order explicit artificial viscous terms are used. An implicit second-order artificial viscous term is also added in the left hand-side in order to make the scheme stable. With these artificial viscous terms, the discretized governing equations become

$$\left[\Gamma - \frac{\Delta\tau}{r} D + \frac{a_1 \Delta\tau}{\Delta t} T + \Delta\tau \frac{\partial}{\partial x} A \cdot + \Delta\tau \frac{\partial}{\partial r} B \cdot - \Delta\tau \frac{\partial}{\partial x} \left(r \hat{R}_{xx} \frac{\partial}{\partial x} \left(\frac{1}{r} \cdot \right) \right) \right] \Delta \hat{Q} \\ - \Delta\tau \frac{\partial}{\partial r} \left(r \hat{R}_{rr} \frac{\partial}{\partial r} \left(\frac{1}{r} \cdot \right) \right) - \Delta\tau D_i^{(2)} \right] \\ = \Delta\tau \left(\frac{S^p - \frac{a_1 r Q^p + a_2 r Q^n + a_3 r Q^{n-1}}{\Delta t} - \frac{\partial r(E - E_v)^p}{\partial x} + \frac{\partial r(F - F_v)^p}{\partial r}}{+ D_e^{(2)} - D_e^{(4)}} \right) \quad (4.60)$$

where $D_i^{(2)}$ represents the implicit second-order artificial viscous terms, and $D_e^{(2)}, D_e^{(4)}$ represent the explicit second-order and fourth-order artificial viscous terms, respectively.

The implicit second-order artificial viscous terms can be further expressed as

$$D_i^{(2)} = D_{ix}^{(2)} + D_{ir}^{(2)} \quad (4.61)$$

where the term in the x-direction is

$$D_{ix}^{(2)} = \Gamma \nabla_x \left(\epsilon_{ix}^{(2)} |\lambda_A| r \right) \Delta_x \left(\frac{1}{r} \cdot \right) \quad (4.62)$$

In Eq. (4.62), Δ_x , and ∇_x are the standard forward and backward difference operators in x-direction, and $\varepsilon_{ix}^{(2)}$ is the viscous coefficient, which will be defined later in this section.

The term in the r-direction can be expressed similarly.

The explicit second-order artificial viscous terms can be expressed as

$$D_e^{(2)} = D_{ex}^{(2)} + D_{er}^{(2)} \quad (4.63)$$

where the term in the x-direction is given as

$$D_{ex}^{(2)} = \Gamma \nabla_x \left(\varepsilon_{ex}^{(2)} |\lambda_A| r \right) \Delta_x (\hat{Q}) \quad (4.64)$$

The coefficient $\varepsilon_{ex}^{(2)}{}_{i+1/2,j}$ is defined as

$$\begin{aligned} \varepsilon_{ex}^{(2)}{}_{i+1/2,j} &= K^{(2)} \psi_{i+1/2,j}^{(x)} \\ &= K^{(2)} \max(\psi_{i,j}^{(x)}, \psi_{i+1,j}^{(x)}) \end{aligned} \quad (4.65)$$

where $K^{(2)} = 0.5$.

To make the scheme TVD, the following flux limiter function, $\psi_{i,j}^{(x)}$, is defined as

(Swanson and Turkel 1992, Jorgenson and Turkel 1993):

$$\psi_{i,j}^{(x)} = \frac{|\rho_{i+1,j} - 2\rho_{i,j} + \rho_{i-1,j}|}{(1-\omega)(|\rho_{i+1,j} - \rho_{i,j}| + |\rho_{i,j} - \rho_{i-1,j}|) + \omega(\rho_{i+1,j} + 2\rho_{i,j} + \rho_{i-1,j})} \quad (4.66)$$

where $\omega = 0.01$ is chosen in this research work. Density is chosen as the controlling parameter in Eq. (4.66) since contact discontinuity exists in this problem.

The terms relating to r-direction can be expressed similarly.

The explicit fourth-order artificial viscous terms can be expressed as

$$D_e^{(4)} = D_{ex}^{(4)} + D_{er}^{(4)} \quad (4.67)$$

where the term in the x-direction is defined as

$$D_{ex}^{(4)} = \Gamma \nabla_x \left(\varepsilon_{ex}^{(4)} |\lambda_A| r \right) \Delta_x \nabla_x \Delta_x (\hat{Q}) \quad (4.68)$$

The coefficient $\varepsilon_{ex\ i+1/2,j}^{(4)}$ is defined as

$$\varepsilon_{ex\ i+1/2,j}^{(4)} = \max \left(0, K^{(4)} - \varepsilon_{ex\ i+1/2,j}^{(2)} \right) \quad (4.69)$$

The parameter $K^{(4)}$ is a constant, which is taken as $\frac{1}{32}$ in this numerical algorithm.

In order to make the scheme stable, the coefficient $\varepsilon_{ix}^{(2)}$ in the implicit second-order artificial viscous terms is chosen as

$$\varepsilon_{ix\ i+1/2,j}^{(2)} = \max \left(\varepsilon_{ex\ i+1/2,j}^{(2)}, 2\varepsilon_{ex\ i+1/2,j}^{(4)} \right) \quad (4.70)$$

The central-difference TVD scheme for the preconditioning numerical scheme is completely defined. The discretized equations are solved by the modified strongly implicit procedure (MSIP) originally developed by Schneider and Zedan (1981).

Chapter 5

SUPERCRITICAL OXYGEN DROPLET VAPORIZING IN CONVECTIVE HYDROGEN ENVIRONMENTS

5.1 Problem Description

In practical spray combustion devices, such as diesel engines, high-performance gas turbine engines, and liquid-propellant rocket engines, droplets are vaporizing in supercritical convective environments. During the vaporization process, a droplet may deform and even break up. Therefore, a practical requirement is to study the convection effect on supercritical droplet vaporization processes.

In this chapter, an oxygen droplet vaporizing in convective hydrogen environments at supercritical conditions is numerically studied. The oxygen droplet is assumed to reach its critical state immediately after being injected into the combustor. Therefore, it becomes a problem of supercritical fluid flow with heat and mass transfer. To numerically analyze this problem, several difficulties have to be circumvented. First, the oxygen droplet is injected into the combustion chamber at an approximate temperature of 100K, which is lower than the critical temperature of oxygen (e.g., 154.6K). Therefore, at supercritical conditions, the oxygen droplet and the oxygen-hydrogen mixture in the region near the droplet can not be assumed as an ideal gas mixture. A consistent and efficient numerical algorithm has to be developed to handle the real fluid behavior. Second, in a droplet vaporization and combustion problem, density variation is significant due to the change of mass fractions of the species. The numerical algorithm for solving compressible fluid flows is a natural choice. However, in the dense oxygen droplet region, the flow velocity is generally very small. A numerical method

capable of solving small-Mach number flows is a prerequisite for this study. Third, for this supercritical droplet vaporization case, a very large density gradient exists between the dense oxygen and the surrounding hydrogen. For example, the oxygen density is about 1200kg/m^3 at 100atm and 100K, while the hydrogen density is approximately 2.4kg/m^3 at the same pressure and 1000K. In this case, the density ratio reaches 500 to 1. An appropriate numerical method should be utilized to treat the large density gradient. Finally, accurate evaluations of thermophysical properties always present a great challenge for solving supercritical droplet vaporization problems.

A supercritical droplet vaporization in a convective environment is illustrated in Fig. 5.1. The following assumptions are taken in this study:

1. The flow is laminar and axisymmetric;
2. The oxygen droplet reaches the critical point immediately after being injected into the combustion chamber. This is an approximation for most of the hydrocarbon fuels, but it is true for this oxygen-hydrogen case (Yang et al. 1994, Lafon, 1995, Handenwang et al. 1996).

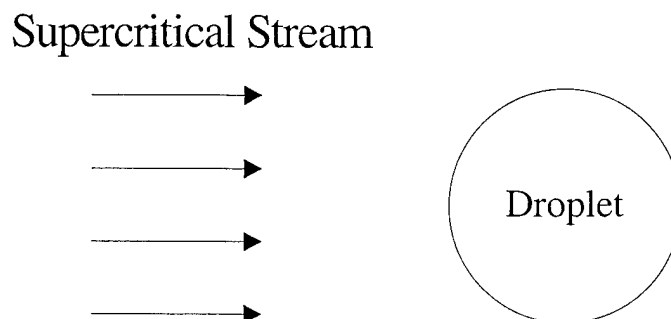


Fig. 5.1 Schematic of a supercritical droplet in a convective stream.

5.2 Numerical Treatment

A preconditioning numerical algorithm with a unified treatment of real fluid mixture, which is developed in Chapter 4, is utilized to solve the current supercritical droplet vaporization problem. A central-difference TVD method is applied to handle the large density gradient (Swanson and Turkel 1992, Jorgenson and Turkel 1993). The state-of-the-art techniques are taken for thermophysical property evaluations, as presented in Chapter 2.

During the vaporization process, a droplet will move and experience strong deformation. There is no advantage to generate grids that are initially conforming to the droplet surface. Therefore, a grid system shown in Fig. 5.2 is used in this numerical study. The mesh in the region around the droplet is refined for computational accuracy. The distances of the outside boundaries from the droplet are at least 15 times of the droplet radius to avoid the far field effect.

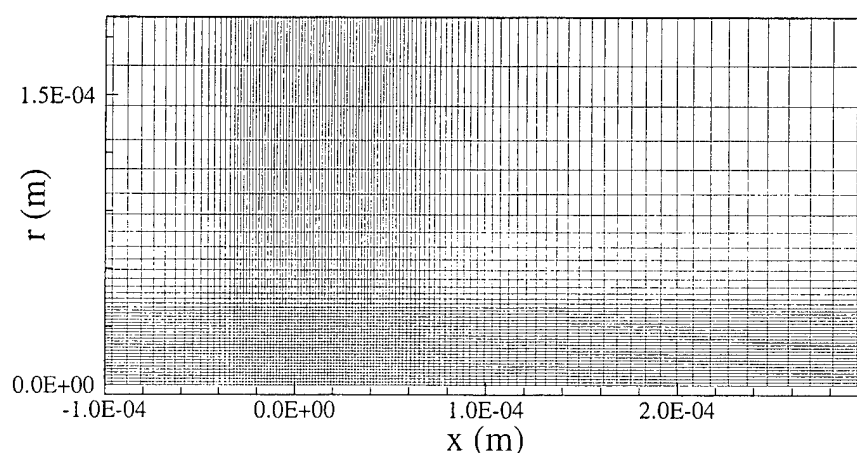


Fig. 5.2 Part of the computational grids.

5.3 Results and Discussions

An oxygen droplet vaporizing in convective hydrogen environments at supercritical conditions is shown in Fig. 5.1. In this research work, the droplet is 50 μm in diameter. Initially, the droplet is at a uniform temperature of 100K, while the inflow hydrogen is at 1000K. Pressures range from 100 to 400 atm. The flows studied herein are restricted to those with the Reynolds number (Re) less than 240. The Reynolds number (Re) is defined based on the initial droplet diameter d_0 , the inflow hydrogen velocity u_0 , and the hydrogen properties ρ_s, μ_s ($\text{Re} = \rho_s u_0 d_0 / \mu_s$). The Reynolds number limit is based on the result of an incompressible viscous fluid flow past a stationary sphere, in which a steady axisymmetric flow can only be maintained with the Reynolds number up to 200 (Nakamura 1976, Johnson and Patel 1999). For this supercritical droplet vaporization case, at the present time, no experimental or 3-D numerical results are available to validate the upper limit of the Reynolds number for the axisymmetric assumption.

For this supercritical droplet vaporization case, although the droplet has already been assumed to reach critical mixing state, its core region with low temperatures still possesses liquid-like density and characteristics. Since the droplet becomes a dense fluid, it leaves us the freedom to define the droplet surface. In the early works regarding an isolated droplet vaporizing in a quiescent environment (Yang et al. 1994, Lafon, 1995), an isothermal line at the critical mixing temperature of the oxygen-hydrogen mixture, as indicated by the phase diagrams in Fig. 2.2, is generally defined as the surface of the oxygen droplet. Fig. 2.2 clearly illustrates that, at a given pressure, a critical mixing state is not only corresponding to a critical mixing temperature, but also to the critical mixing

mass fractions. Therefore, instead of the critical mixing temperature, a critical mixing mass fraction can also be used to define the droplet surface (Hadenwang et al. 1996). Furthermore, a critical mixing state in Fig. 2.2 exists only at the states with thermodynamic phase equilibrium. Without phase equilibrium, the critical temperature and critical mass fractions are not located at the same position, rendering the critical mixing state meaningless. This is actually the case after the droplet reaches the critical mixing state as a result of different heat and mass transfer rates. Therefore, the droplet surface is defined as an isothermal line at the critical temperature of oxygen (154.6K) in this work, which is a physically meaningful and unique state.

5.3.1 Grid Independence Study

The computational domain in this study is chosen as $2000 \times 400 \mu m$. Three different sets of grids have been tested to determine an appropriate computational mesh. The droplet lifetimes based on these grids are compared, as shown in Table 5.1, where the incoming hydrogen velocity is 20m/s at pressure of 100atm. Results based on the last two sets of grids are very close, with a relative error about 4%. Therefore, the second set of grids, 201×71 , is considered sufficient for this numerical study.

Table 5.1. Droplet Lifetimes at Different Numerical Grids

| Grids | 169×47 | 201×71 | 253×99 |
|-------------------------------|--------|--------|--------|
| Droplet Lifetimes (μs) | 59 | 70 | 73 |
| Relative Error | N/A | 18.6% | 4.3% |

5.3.2 Flow Patterns

The flow fields are illustrated in Figs. 5.3-5.6, where the reference frame is moving with the droplet at the mass-weighted droplet velocity. Figs. 5.3-5.5 present results corresponding to a pressure of 100 atm, and Figs. 5.5-5.6 represent flows with a same Reynolds number ($Re \approx 120$), but different pressures. In all these figures,

streamlines are presented with temperature contours, which is used to indicate the location of the droplet. It should be emphasized that in the unsteady fluid flows, the streamlines could only represent the instant velocity directions. Figure 5.3 illustrates the transient variations of the flow fields at an incoming velocity of 2.5 m/s and a pressure of 100atm with the corresponding Reynolds number (Re) about 15. In this low Reynolds number case, there is no recirculating wake behind the droplet, and the incoming flow is redirected and passes the droplet smoothly. Because of the droplet vaporization, there is a stagnant point in front of the droplet, which exists in the entire droplet lifetime. With the incoming velocity increasing to 5.0 m/s and Reynolds number to 30 as shown in Fig. 5.4, the flow patterns change dramatically. A recirculating eddy appears, and its center moves downstream during the vaporization process. When compared with Fig 5.3, the stagnation point in front of the droplet moves closer to the droplet surface because of stronger incoming aerodynamic force. Figure 5.5 corresponding to a velocity of 20 m/s at 100 atm ($Re \approx 120$), where a recirculating eddy behind the droplet is visible just shortly after the droplet is injected. The eddy is moving away from the droplet, and it is growing bigger. Results in Figs. 5.3-5.5 clearly demonstrate that the Reynolds number presents strong effect on the supercritical fluid flows at a same pressure of 100 atm.

In Fig. 5.6, pressure is increased to 400 atm. With the decrease of the incoming velocity to 5 m/s, the corresponding Reynolds number is about the same as that in Fig. 5.5 ($Re \approx 120$). At different incoming velocities, the same Reynolds number is maintained mainly by the increase of the hydrogen density with pressure as shown in Table 5.2a, where the pressure effects on thermodynamic properties are presented. For example, the hydrogen density is 2.4kg/m^3 at 100atm and 1000K, but it becomes slightly

above 9kg/m^3 at the same temperature but 400atm. At the same Reynolds number but different pressures, the streamlines in Fig. 5.6 look similar to those in Fig. 5.5, but the recirculating eddy becomes smaller. Results in Figs 5.5-5.6 demonstrate the significant effect of pressure on flow fields.

In fluid mechanics literature, there are two distinct explanations about the formation of recirculating wakes behind bluff bodies (Dandy and Leal 1986, Leal 1989): vorticity accumulation and boundary-layer separation. Leal (1989) argues that the recirculating wake behind a bluff body with a smooth slip surface is created by vorticity accumulation. The flow detachment occurs when the maximum surface vorticity reaches a critical value about 5.25 (which should be 10.5 corresponding to the definition of the dimensionless vorticity in this work, $\omega' = \omega \cdot d_0 / u_0$). Figure 5.7 presents the vorticity distributions corresponding to the four cases discussed earlier. The maximum vorticities in all these cases are far less than 10.5, especially for the second case at $\text{Re} = 30$. The formation of the recirculating wake in this supercritical droplet vaporization case is caused by flow separation, which is enhanced by droplet deformation and surface blowing. The streamlines in Figs. 5.3-5.6 clearly illustrate that the flow, resulting from vaporization, divides the flow field into the inner and outer regions, and the surface blowing results in flow separation from the droplet surface. When the incoming flow is strong, a recirculating eddy appears. The further stretching of the droplet perpendicular to the flow direction enhances the flow separation, and helps the recirculating eddy grow bigger.

In Figs. 5.3-5.6, the flow fields inside the droplet regions clearly illustrate the trend of droplet deformation, which will be discussed shortly.

5.3.3 Temperature Contours and Droplet Deformations

Under supercritical conditions, an oxygen droplet becomes a dense fluid, and the droplet surface is defined as an isothermal line at the oxygen critical temperature. Therefore, study of the temperature fields will reveal the droplet deformation and the possible secondary break-up phenomena, which are closely related to the fuel vapor distributions and mixing in the combustion devices. Many research works were conducted about droplet deformations and secondary break-ups at low pressures without heat transfer (Hinze 1955, Range and Nicholls 1969, Wierzbna and Takayama 1988, Pilch and Erdman 1987, Hsiang and Faeth 1992). The studies have determined that droplet deformation and break-up patterns in a forced convection flow are affected by two dimensionless parameters: the Weber number and the Ohnesorge number. The Weber number, $We = \rho_s d_0 u_0^2 / \sigma$, represents the ratio of aerodynamic force to the surface tension, and the Ohnesorge number, $Oh = \mu_d / \sqrt{\rho_d d_0 \sigma}$, is the ratio of viscous force to surface tension. Here σ is surface tension, d_0 is the initial droplet diameter, and the subscripts s and d refer to hydrogen and oxygen, respectively. Because the oxygen droplet is assumed to reach critical mixing state immediately after being injected into the combustion chamber, there is no surface tension in this case. One reasonable way is to define another dimensionless parameter in this supercritical droplet deformation case to represent the ratio of aerodynamic to viscous forces.

$$We^{1/2} / Oh = \frac{\sqrt{\rho_s u_0^2 d_0 / \sigma}}{\mu_d / \sqrt{\rho_d d_0 \sigma}} = \frac{\rho_s u_0 d_0}{\mu_s} \frac{\mu_s}{\sqrt{\rho_s}} \frac{\sqrt{\rho_d}}{\mu_d} = Re \frac{\mu_s}{\mu_d} \sqrt{\frac{\rho_d}{\rho_s}} \quad (5.1)$$

This dimensionless parameter is related to Reynolds number, hydrogen and oxygen viscosity ratio, and square root of density ratio, which are the crucial factors affecting droplet deformations at supercritical conditions.

To illustrate the oxygen droplet deformation and the effects of the dimensionless parameter $Re \frac{\mu_s}{\mu_d} \sqrt{\frac{\rho_d}{\rho_s}}$, the temperature contours under different conditions are presented in Figs. 5.8-5.11, where the transient developments are illustrated.

Figures 5.8-5.10, where the Reynolds numbers are the same as those in Figs. 5.3-5.5, illustrate the Reynolds number effects at 100atm. Figure 5.8 presents the temperature contours in an incoming hydrogen flow at a low velocity, $u=2.5\text{m/s}$ ($Re=15$). The droplet slightly extends in the cross-flow direction and becomes an oblate. When the incoming velocity increases to 5m/s ($Re=30$), the droplet deformation becomes stronger in Fig. 5.9. The droplet first becomes an oblate. With the back further flattened up, the droplet begins to look like a 'mushroom'. The stripping effect at the tip of the droplet appears during the vaporization process. As the Reynolds number increases to about 120 in Fig. 5.10, the strong stripping effect is clearly illustrated, and a sharp tip is stretched out. The droplet is further extended in the cross-flow direction and becomes slender. Afterwards, it is easily bent backward, and remains a crescent shape near the end of the vaporization process.

The pressure effect on the droplet deformations is studied in Figs. 5.10-5.11, corresponding to a same Reynolds number ($Re \approx 120$) but with two different pressures of 100atm and 400atm, respectively. As expressed in Eq. (5.1), pressure affects the droplet deformation by changing ratios of viscosity and the square root of density. As shown in Table 5.2b, the values of $\frac{\mu_s}{\mu_d} \sqrt{\frac{\rho_d}{\rho_s}}$ decrease with the increase of pressure. This indicates

the droplet deformation will become weaker at a higher pressure. The results in Figs. 5.10-5.11 confirm this conclusion. With the increase in pressure, the stripping effect at the tip of the droplet, as well as the extension in the cross-flow direction, obviously weaken. Fig. 5.11 shows no stripping effect.

Table 5.2a. Pressure Effects on Thermophysical Properties of Hydrogen and Oxygen

| Pressures (atm) | Hydrogen at 1000K | | Oxygen at 100K | |
|--------------------|----------------------------------|------------------------------------------|----------------------------------|------------------------------------------|
| | Density ρ_s (kg/m^3) | Viscosity μ_s ($N \cdot s/m^2$) | Density ρ_s (kg/m^3) | Viscosity μ_s ($N \cdot s/m^2$) |
| 100 | 2.4 | 1.968e-05 | 1118.2 | 1.721e-04 |
| 200 | 4.7 | 1.972e-05 | 1144.9 | 1.884e-04 |
| 400 | 9.0 | 1.982e-05 | 1184.3 | 2.187e-04 |

Table 5.2b. Pressure effects on the Combined Parameters

| Pressure (atm) | $\frac{\mu_s}{\mu_d} \sqrt{\frac{\rho_d}{\rho_s}}$ | $\frac{\rho_d}{\rho_s} \left(\frac{v_R}{v_s} \right)^2 p_R^{-1.164}$ |
|----------------|----------------------------------------------------|-----------------------------------------------------------------------|
| 100 | 2.47 | 206.7 |
| 200 | 1.63 | 184.2 |
| 400 | 1.04 | 161.2 |

The analysis above demonstrates that the ratio of aerodynamic and viscous forces, as defined by the dimensionless parameter $We^{1/2}/Oh$ ($= Re \frac{\mu_s}{\mu_d} \sqrt{\frac{\rho_d}{\rho_s}}$), is the major factor determining the droplet deformation under supercritical conditions. At a given pressure, the variations of incoming velocity affect the droplet deformation by changing the Reynolds number. At a given Reynolds number, pressure will affect the droplet deformation by changing the value of $\frac{\mu_s}{\mu_d} \sqrt{\frac{\rho_d}{\rho_s}}$.

From these figures, what is also clear is that the droplet shape is closely related to the formation of the recirculating wake behind the droplet, as shown in Figs. 5.3-5.6. With the forward flow close to the axisymmetric axis, the temperature gradient becomes very steep in that region.

5.3.4 Mass Fraction Distributions

The mass fraction distributions of the oxygen species are shown in Fig. 5.12, where the same cases with both the Reynolds number and pressure effects, as shown in Figs. 5.3-5.6, are presented. In this figure, the vaporized oxygen species are strongly advected downstream and mixed with hydrogen by the incoming flow. The forward diffusion is limited within a very thin boundary layer, and the diffusion in the cross-flow direction is also restricted by the flow.

Comparing to the figures of temperature contours, the core region of the oxygen species deforms in the same patterns with the strong stripping at the tip and extension in the cross-flow direction at larger values of $We^{1/2}/Oh$. In fact, the conclusions can also be applied to the droplet region defined by density contours. This similarity demonstrates that, no matter how we define the droplet surface, the droplet deformation is mainly determined by the dimensionless parameter $We^{1/2}/Oh$ in the supercritical droplet vaporization processes.

It should be mentioned that, there is no secondary droplet break-up observed in this study because of the lack of surface tension. This is in consistency with the low-pressure droplet break-up results (Pilch and Erdman 1987, Hsiang and Faeth 1992), which indicate that break-up seems impossible when the Ohnesorge number

($Oh = \mu_d / \sqrt{\rho_d d_0 \sigma}$) approaches infinity. This is exactly the case here with no surface tension.

5.3.5 Droplet Vaporization Times

In spray combustion models, the droplet vaporization rate and droplet lifetime must be determined. The droplet vaporization rates at supercritical conditions are presented in Figs. 5.13-5.15, where both the pressure and Reynolds number effects are illustrated. In these figures, the definition of the droplet mass ratio is

$$\text{Droplet Mass Ratio} = \frac{\text{The Remaining Droplet Mass (m)}}{\text{The Initial Droplet Mass (m}_0\text{)}} \quad (5.2)$$

Figure 5.13 shows the results at a pressure of 100atm with velocities ranging from 2.5-20m/s, which correspond to the Reynolds numbers (Re) from 15-120. At the beginning of all the droplet vaporization processes, there are rapid droplet vaporization periods, because droplets (at 100K) are suddenly encountering the high-temperature environments (at 1000K). After very short times, vaporization rates slow down, and droplets at different Reynolds numbers begin to evaporate at different rates. The droplet facing a higher incoming velocity (Reynolds number) begins the transition earlier because of the stronger convection effect. Figure 5.14 represents the same situations at 400atm, where the differences among the transition times are smaller, because of the relative higher Reynolds numbers (60-230) compared with the cases at the same velocities in Fig. 5.13. The results in these two figures clearly demonstrate the strong effects of Reynolds numbers on the droplet vaporization rates and droplet lifetimes. Droplets evaporate much faster and result in much shorter lifetimes at higher Reynolds numbers.

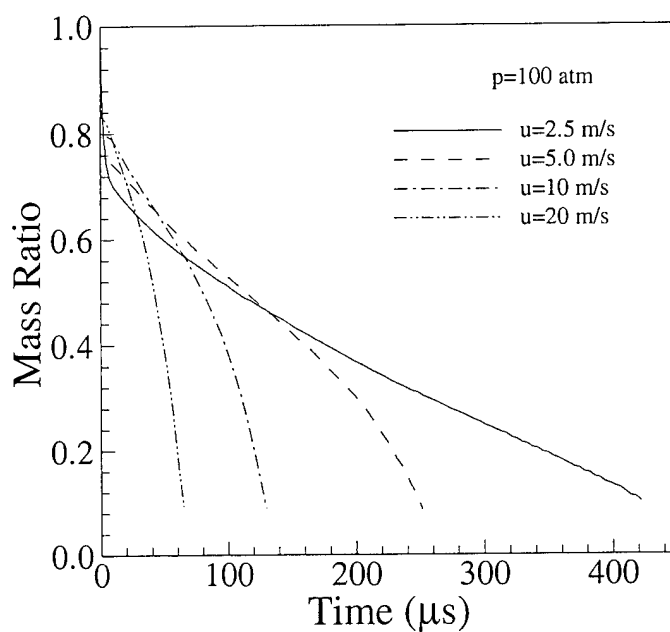


Fig. 5.13 Effects of incoming velocities (Reynolds numbers) on the droplet vaporization rates at a pressure of 100atm.

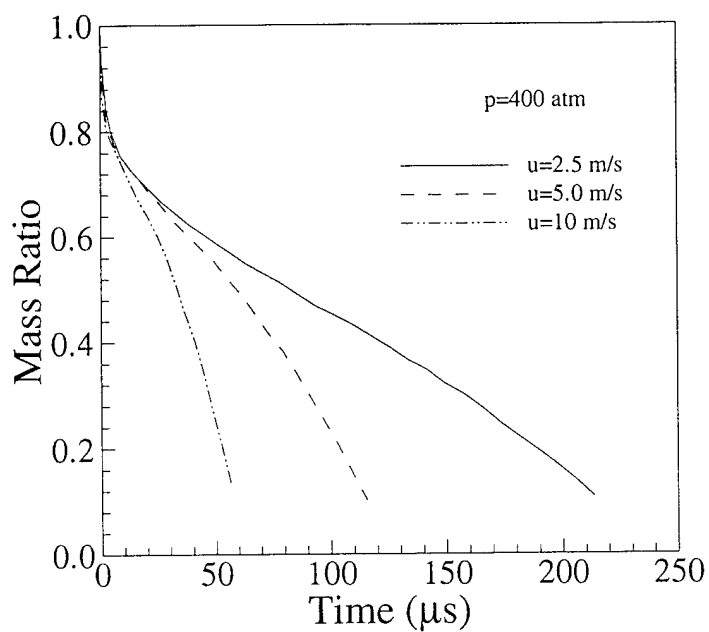


Fig. 5.14 Effects of incoming velocities (Reynolds numbers) on the droplet vaporization rates at a pressure of 400atm.

At a given Reynolds number, the transition to convective vaporization starts earlier, and the droplet lifetime is shorter at a lower pressure case. Pressure affects the droplet lifetimes by changing the Prandlt and Schmidt numbers of the oxygen-hydrogen mixture, as shown in Table 5.3, where the properties of the oxygen and hydrogen mixture at a temperature of 200K and equal molar fractions are presented as a representative case at the near-droplet regions. The Schmidt number Sc increases significantly with pressures, but the Prandlt number Pr decreases slightly. Therefore, the droplet lifetimes are proportional to the Schmidt number ($\sim Sc$), and inversely proportional to the Prandlt number ($\sim 1/Pr$).

Table 5.3. Properties of Oxygen and Hydrogen Mixture
at Equal Molar Fractions and 200K

| p (atm) | ρ (kg/m ³) | C_p (J/kg-K) | K (W/m-K) | $\mu \cdot 10^4$ (N-s/m ²) | $D_{ij} \cdot 10^6$ (m ² /s) | Pr | Sc | Le |
|---------|--------------------------------|-------------------|----------------|-------------------------------------------|--------------------------------------------|-------|-------|-------|
| 100 | 103.76 | 2006.04 | 0.054 | 0.1489 | 0.3877 | 0.555 | 0.370 | 0.667 |
| 200 | 195.64 | 2192.15 | 0.070 | 0.1728 | 0.1984 | 0.544 | 0.445 | 0.818 |
| 400 | 325.81 | 2270.10 | 0.098 | 0.2250 | 0.0992 | 0.523 | 0.696 | 1.331 |

Table 5.4. Droplet Lifetimes in a Quiescent Environment

| Pressure (atm) | 100 | 200 | 400 |
|-----------------|------|-----|-----|
| Time (μ s) | 1497 | 853 | 486 |

Results in Figs. 5.13-5.14 demonstrate that droplet lifetime is a function of Reynolds number (Re) and pressure at a supercritical condition. Before attempting any effort to find the possible relationship, the variables of droplet lifetime (t) and pressure are first non-dimensionalized. An apparent choice of the reference pressure is the critical pressure of oxygen ($p_{c,O_2} = 49.74 atm$). The reference time (t_0) is chosen to be the droplet lifetime, with an isolated droplet vaporizing in a quiescent environment at a given pressure, as presented in Table 5.4. Droplet lifetimes in Table 5.4 are calculated from the method presented in Chapter 2.

Utilizing the dimensionless parameters, the following relationship is what we are searching for:

$$\frac{t}{t_0} = f(Re, p_R) \quad (5.3)$$

where p_R is the dimensionless pressure, $p_R = p/p_{c,O_2}$.

At given pressures, the following formula is a natural choice following the popular Ranz and Marshall correlation:

$$\frac{t}{t_0} = \frac{1}{1 + c Re^a} \quad (5.4)$$

Equation (5.4) naturally set the time ratio to 1 with no convection ($Re = 0$).

Data Analysis reveals that the coefficient a is approximately a constant of 1.26 at different pressures. This leads to the conclusion that the coefficient c must be a function of pressure. The following relation is proposed:

$$c = bp_R^d \quad (5.5)$$

Equation (5.5) does not change the unique characteristics of Eq. (5.4)

$$\left(\frac{t}{t_0} = 1, \text{ at } \text{Re} = 0\right).$$

Based on the available numerical data, the following coefficients are obtained:

$$a = 1.26, d = -1.58, b = 0.1549 \quad (5.6)$$

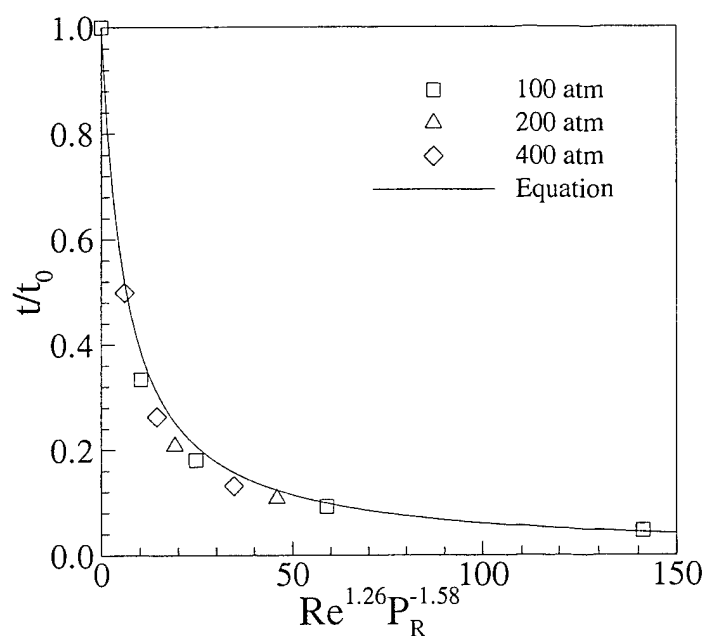


Fig. 5.15 Correlation of the dimensionless droplet lifetime as a function of the Reynolds number and pressure

Finally, a relationship for calculating droplet lifetimes becomes

$$\frac{t}{t_0} = \frac{1}{1 + 0.1549 \text{Re}^{1.26} p_R^{-1.58}} \quad (15 < \text{Re} < 240, 2 < p_R < 8) \quad (5.7)$$

The results from both numerical computations and Eq. (5.7) are compared in Fig. 5.15, where excellent agreement is reached.

5.3.6 Droplet Dynamics

In this section, droplet drag coefficient during vaporization process is studied. In a convective environment, a droplet constantly deforms. In this study, the droplet location is defined as its center of mass. Because of the axisymmetry, droplet locations always lie in the axis and are moving downstream. The droplet velocity is calculated by the transient variations of droplet locations based on the same method used by the experimentalists (Yuen and Chen 1976). Figures. 5.16-5.17 present the temporal variations of droplet velocities, and the effects of both Reynolds number and pressure are clearly illustrated. Velocities of the droplets increase with time in both figures. At a given pressure of 100atm in Fig. 5.16, a droplet moves faster with a higher incoming velocity (higher Reynolds number). At a given Reynolds number of 60 in Fig. 5.17, a droplet moves faster at a lower pressure because of the faster incoming velocity. However, there are oscillations in both figures, especially at the beginning and near the end of the vaporization processes. These oscillations are caused by both droplet deformation and surface blowing.

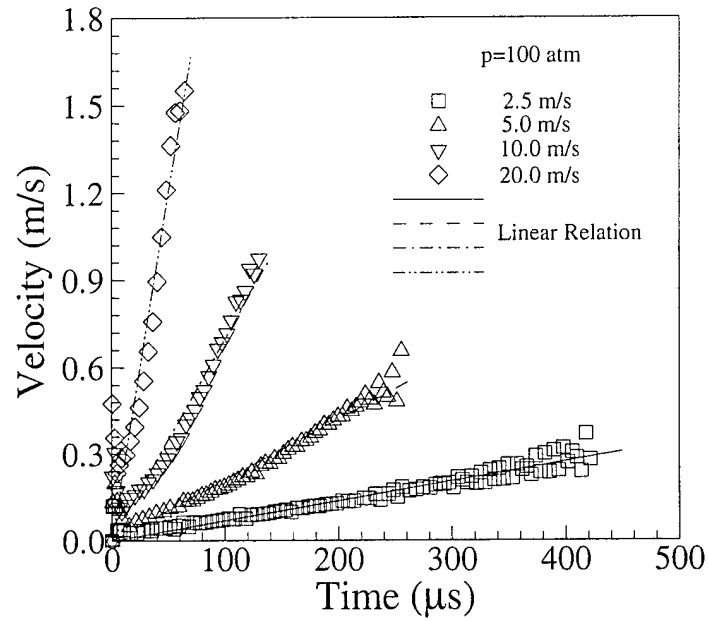


Fig. 5.16 Transient variations of droplet velocities and the linear relationships at a pressure of 100atm.

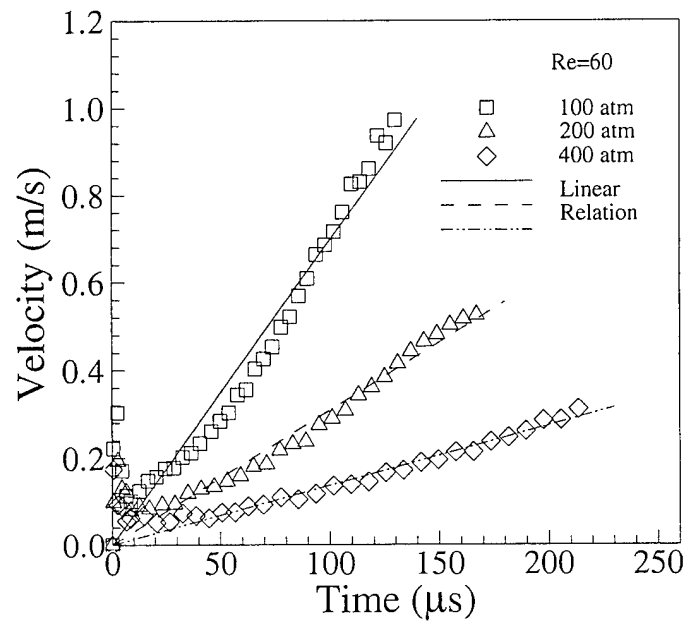


Fig. 5.17 Transient variations of droplet velocities and the linear relationships at a Reynolds number of 60.

Due to the sudden injection of a droplet into a uniform flow field, the time required for the flow field to relax can be estimated as $\Delta t_{relax} = d_0 / u_0$. Careful inspection of the transient variations of droplet velocities indicates simple linear relations, except within the relaxation times when the nonlinear effects are trivial because of the relative slow velocities and short times. Therefore, the transient variations of droplet velocities are correlated as

$$v = bt \quad (5.8)$$

It should be kept in mind that the coefficient b has a dimension of m/s^2 . The following relationship of the velocity coefficient b , which is a function of Reynolds number and pressure, is assumed:

$$b = c \text{Re}^a p_R^d \quad (5.9)$$

In Eq. (5.9), when the Reynolds number is set to 0, a zero value of coefficient b will naturally lead to a stationary droplet, as physically required.

All the parameters in Eq. (5.9) can be easily determined by simple linear regression. Analyzing the available data at given pressures indicates that the coefficient a is a constant of 1.76. At given Reynolds numbers, the coefficient d also approaches a constant. Finally, with the known coefficients a and d , the coefficient c can be easily found out. These coefficients are

$$a = 1.76, d = -1.164, c = 12 \quad (5.10)$$

where the dimension of parameter c is m/s^2 . Substituting these numbers into Eq. (5.9), the relationship for the velocity coefficient b is expressed as

$$b = 12 \text{Re}^{1.76} p_R^{-1.164} \quad (15 < \text{Re} < 240, 2 < P_R < 8) \quad (5.11)$$

Figure 5.18 shows a very good agreement between the numerical results and those from Eq. (5.11).

The correlation in Eq. (5.11) is employed to calculate the transient variations of droplet locations, as illustrated in Figs. 5.19-5.20. The droplet location S is calculated as

$$S = \frac{1}{2}bt^2 \quad (4.12)$$

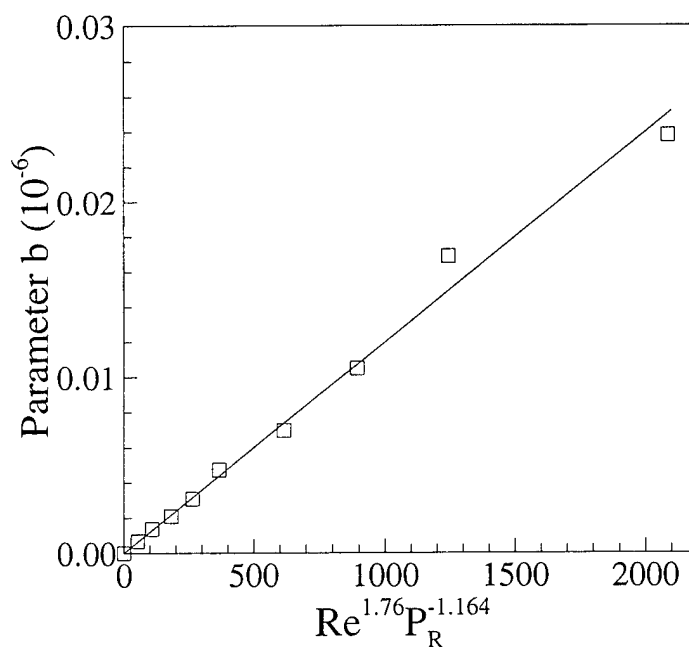


Fig. 5.18 Correlation of the velocity coefficient b as a function of the Reynolds number and pressure.

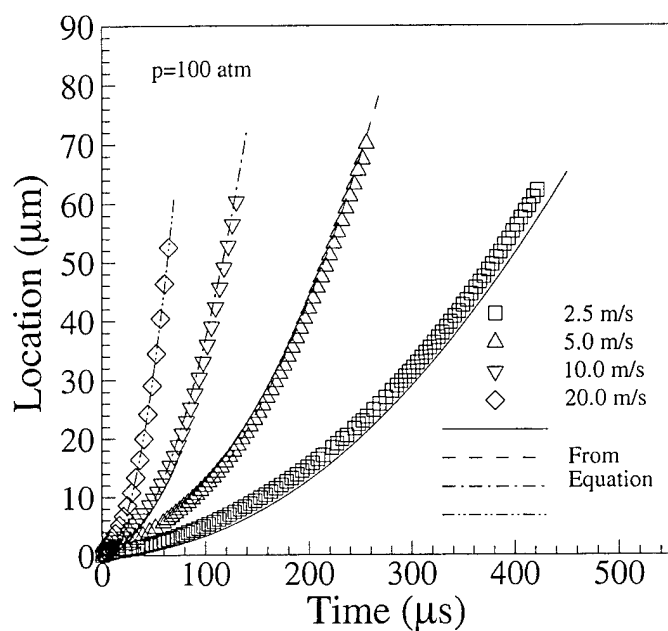


Fig. 5.19 Transient variations of droplet locations from both correlation and numerical computations at a pressure of 100atm.

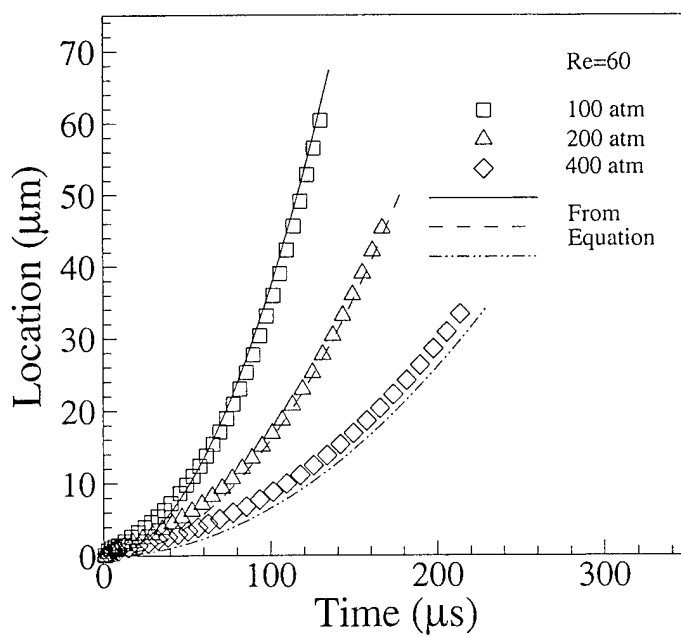


Fig. 5.20 Transient variations of droplet locations from both correlation and numerical computations at a Reynolds number of 60.

Figures 5.19-5.20 represent two cases at $p = 100\text{atm}$ and $\text{Re} = 60$, respectively. In these figures, droplet locations calculated from Eq. (5.12) are compared with those directly from numerical computations. Good agreements are clearly demonstrated.

Based on Eq. (5.8), it is easy to find the droplet acceleration a_c ,

$$a_c = b \quad (5.13)$$

The drag force acting on the droplet can be approximately expressed as

$$F_D = ma_c \quad (5.14)$$

The drag coefficient is defined as

$$C_D = \frac{F_D}{1/2 \rho u_0^2 \pi r_m^2} \quad (5.15)$$

Because of the droplet deformation, the droplet radius r_m is defined as the radius of a mass-equivalent droplet sphere with a uniform density at its initial value,

$$r_m = \left(\frac{3m}{4\rho_d \pi} \right)^{1/3} \quad (5.16)$$

where m is the droplet mass at any instant.

Substituting Eqs. (5.14), (5.16) and (5.11) into the drag coefficient expression (5.15), the following relationship can be established:

$$C_D = \frac{\frac{4}{3} \left(\frac{m}{m_0} \right)^{1/3} \frac{\rho_d}{\rho_s} \left(\frac{\nu_R}{\nu_s} \right)^2 \left(\frac{cd_0^3}{\nu_R^2} \right)}{\text{Re}^{0.24} p_R^{1.164}} \quad (15 < \text{Re} < 240, 2 < P_R < 8) \quad (5.17)$$

where ν_R is defined as the reference kinematic viscosity of hydrogen at 1000K and 100atm.

Equation (5.17) clearly indicates that the drag coefficient always decreases with time ($\sim \left(\frac{m}{m_0}\right)^{1/3}$) in the supercritical vaporization case. This trend is different from that of the low-pressure droplet vaporization case without droplet deformation (Chiang et al. 1992). Results from Chiang et al. (1992) indicate that the drag coefficient could increase or decrease with time during different portions of the droplet lifetime. At the end of the vaporization process, it generally increases with time as a result of the reduction in the Reynolds number, which is defined using the relative velocity between the incoming stream and the droplet. In the supercritical droplet vaporization case, the moving velocities of the droplets are relatively small compared with the incoming velocity, as shown in Figs. 5.16-5.17. Therefore, the Reynolds number reduction is not strong enough to increase the drag coefficient.

At a given Reynolds number, pressure influences the drag coefficient by changing the product of $\frac{\rho_d}{\rho_s} \left(\frac{v_R}{v_s}\right)^2 p_R^{-1.164}$, as illustrated in Table 5.2b. Results in Table 5.2b clearly demonstrate that the drag coefficient has a slight decrease with the increase of pressure at a given Reynolds number. It should be kept in mind that pressure could also affect the Reynolds number in this supercritical droplet vaporization case.

5.4 Summary of Results

In this paper, an oxygen droplet vaporizing in convective hydrogen environments at supercritical conditions are numerically investigated. A consistent and efficient numerical algorithm is utilized, with full account of real fluid behavior. Thermodynamic relationships are derived using fundamental theories and can be calculated based on any

equation of state. A preconditioning numerical scheme is employed to handle small-Mach-number fluid flows. The details of the numerical and thermodynamic treatments can be found in Chapter 4. The transport properties are estimated by the state-of-the-art techniques with proper consideration of high-pressure effects.

An oxygen droplet is assumed to reach the critical mixing state immediately after being injected into the combustion chamber. Therefore, this is a problem of supercritical fluid flow with strong heat and mass transfer. An isothermal line at the critical temperature of oxygen is defined as the droplet surface. The transient developments of temperature, oxygen mass fraction, and flow fields are presented. The effects of incoming velocity (or Reynolds number) and pressure on droplet deformations are explored in detail. The major factor determining the droplet deformations under supercritical conditions is a dimensionless parameter $We^{1/2}/Oh$ ($= Re \frac{\mu_s}{\mu_d} \sqrt{\frac{\rho_d}{\rho_s}}$), which represents the ratio of aerodynamic and viscous forces. Both Reynolds number and pressure perform their effects by changing this parameter.

The droplet vaporization rates and droplet lifetimes are studied. Droplet lifetimes are affected strongly by the incoming hydrogen velocity (or Reynolds number) and pressure. At a given pressure, a droplet evaporates more rapidly at a higher Reynolds number. The droplet lifetime is significantly shortened at a lower pressure and a given Reynolds number. A relationship is established to calculate droplet lifetimes accurately.

The transient variations of droplet velocities and drag coefficients during droplet vaporization processes are illustrated. A linear relationship is reasonably assumed for droplet velocity, and the linear velocity coefficient b is found to be proportional to

$\text{Re}^{1.76} p_R^{-1.164}$. Droplet positions calculated from this linear relationship agree well with those directly from numerical computations. The drag coefficient always decreases with time ($\sim \left(\frac{m}{m_0}\right)^{1/3}$) as a result of the weak Reynolds number reduction in this supercritical vaporization case. At a given Reynolds number, pressure influences the drag coefficients by changing the product of $\frac{\rho_d}{\rho_s} \left(\frac{\nu_R}{\nu_s}\right)^2 p_R^{-1.164}$, and the drag coefficient decreases slightly with the increase of pressure.

Results in this study give a deeper understanding of the supercritical droplet vaporization process. The correlations regarding droplet lifetime and drag coefficient can be directly applied to the numerical modeling of supercritical spray combustion.

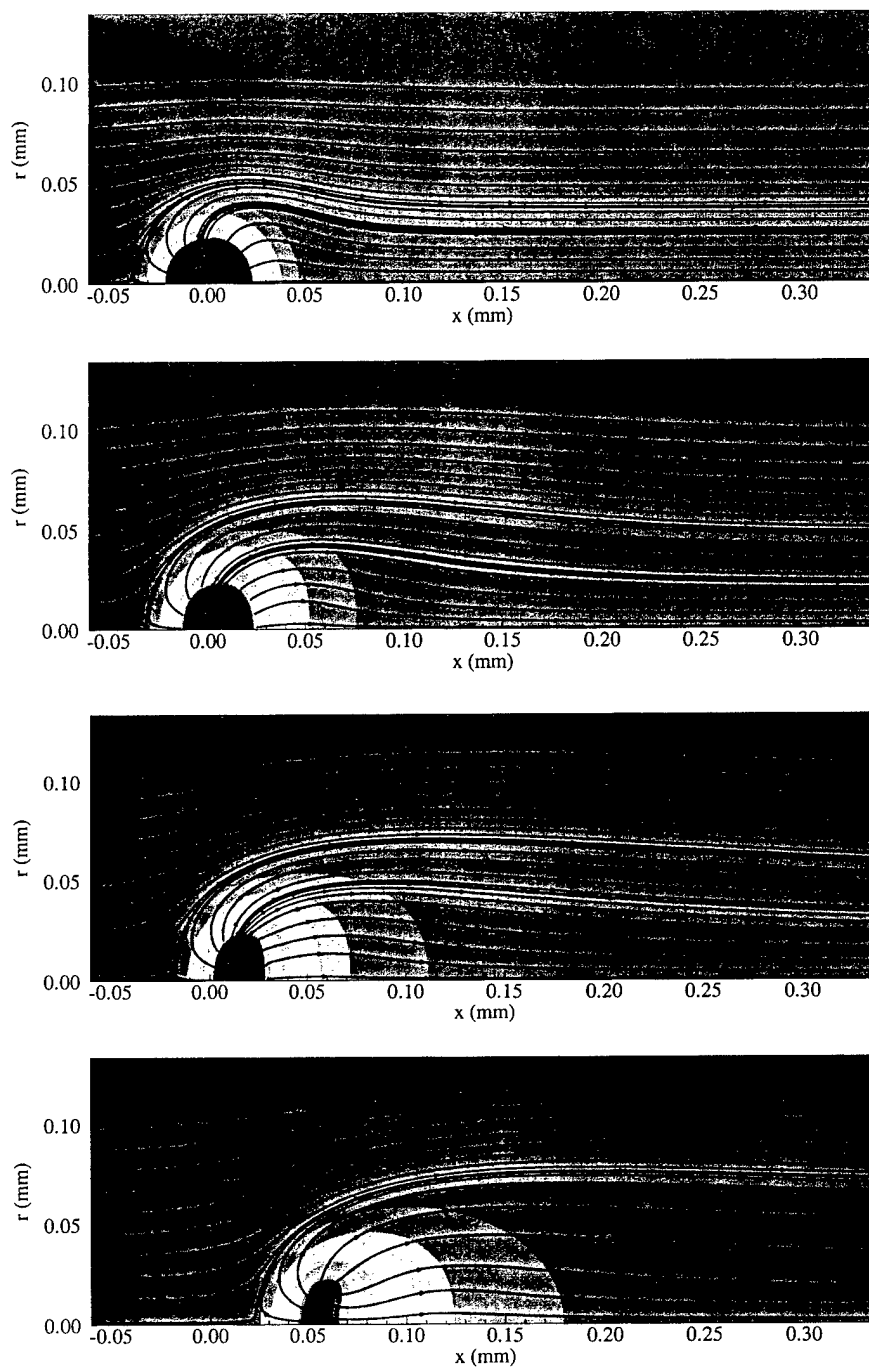


Fig. 5.3 Transient developments of flow fields at $u=2.5\text{m/s}$, $p=100\text{atm}$ ($Re \approx 15$), at instants of $t=20, 100, 200, 400 \mu\text{s}$, respectively.

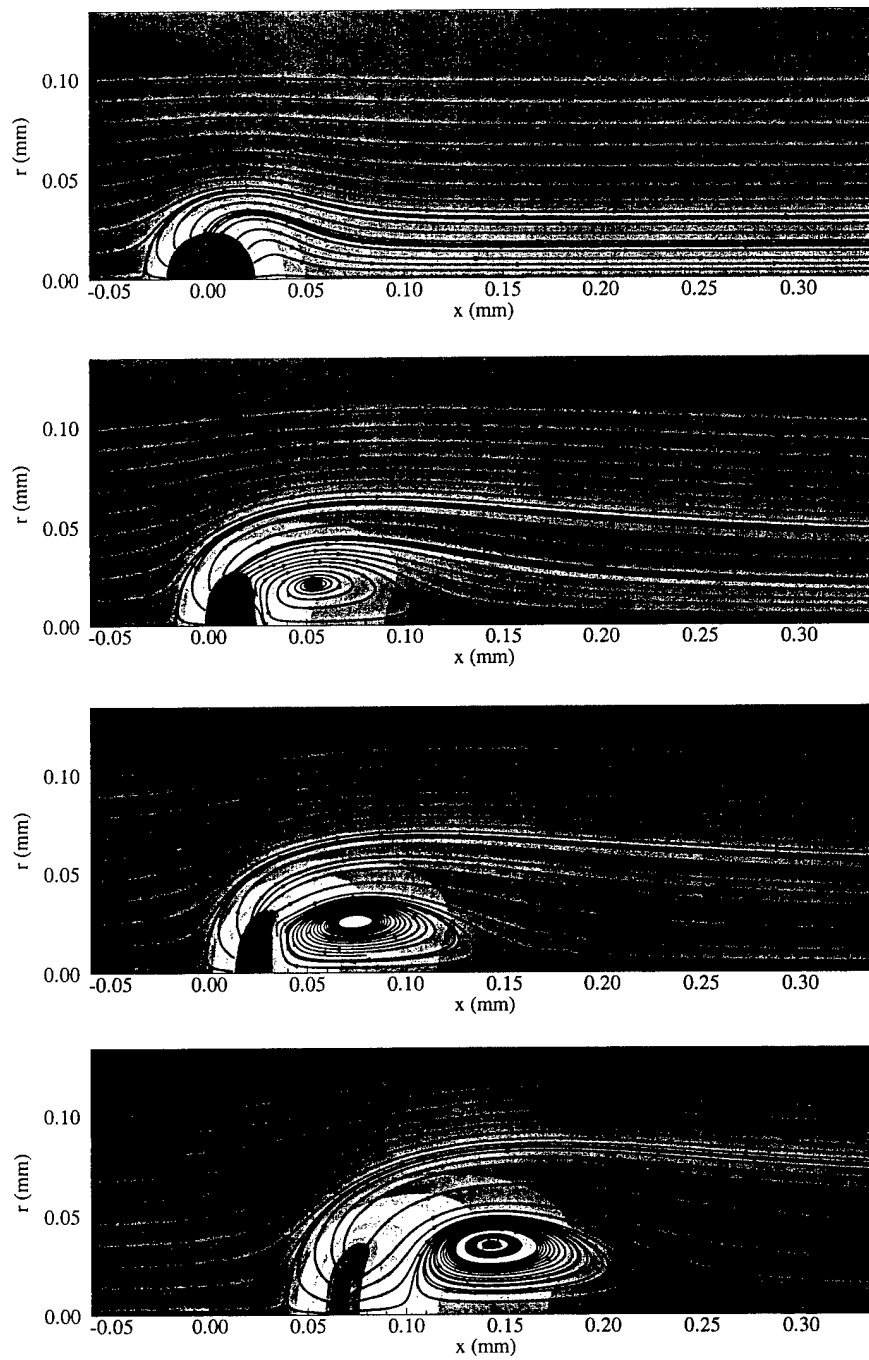


Fig. 5.4 Transient developments of flow fields at $u=5.0\text{m/s}$, $p=100\text{atm}$ ($\text{Re} \approx 30$), at instants of $t=12, 100, 150, 250\mu\text{s}$, respectively.

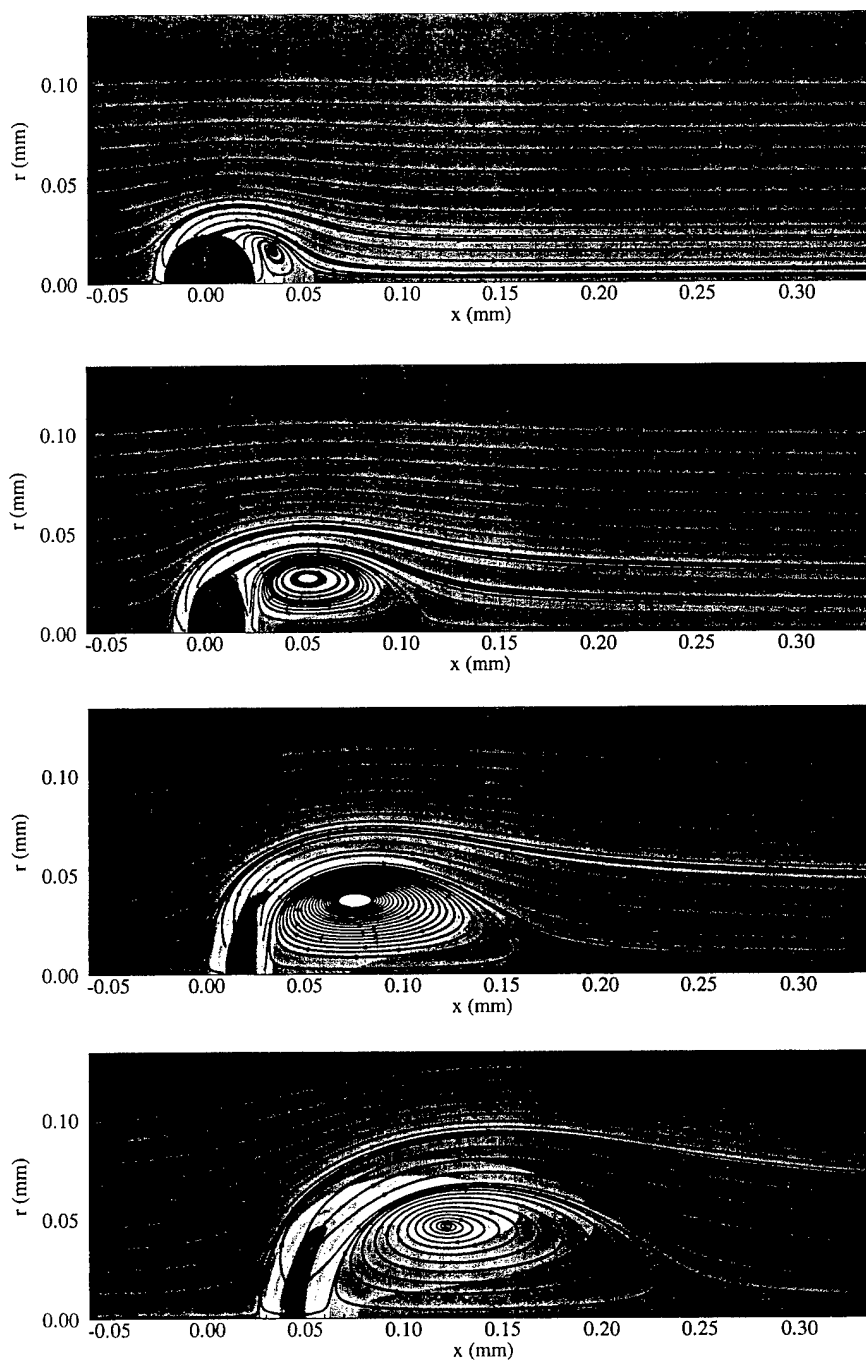


Fig. 5.5 Transient developments of flow fields at $u=20.0\text{m/s}$, $p=100\text{atm}$ ($Re \approx 120$), at instants of $t=4, 20, 40, 60\mu\text{s}$, respectively.

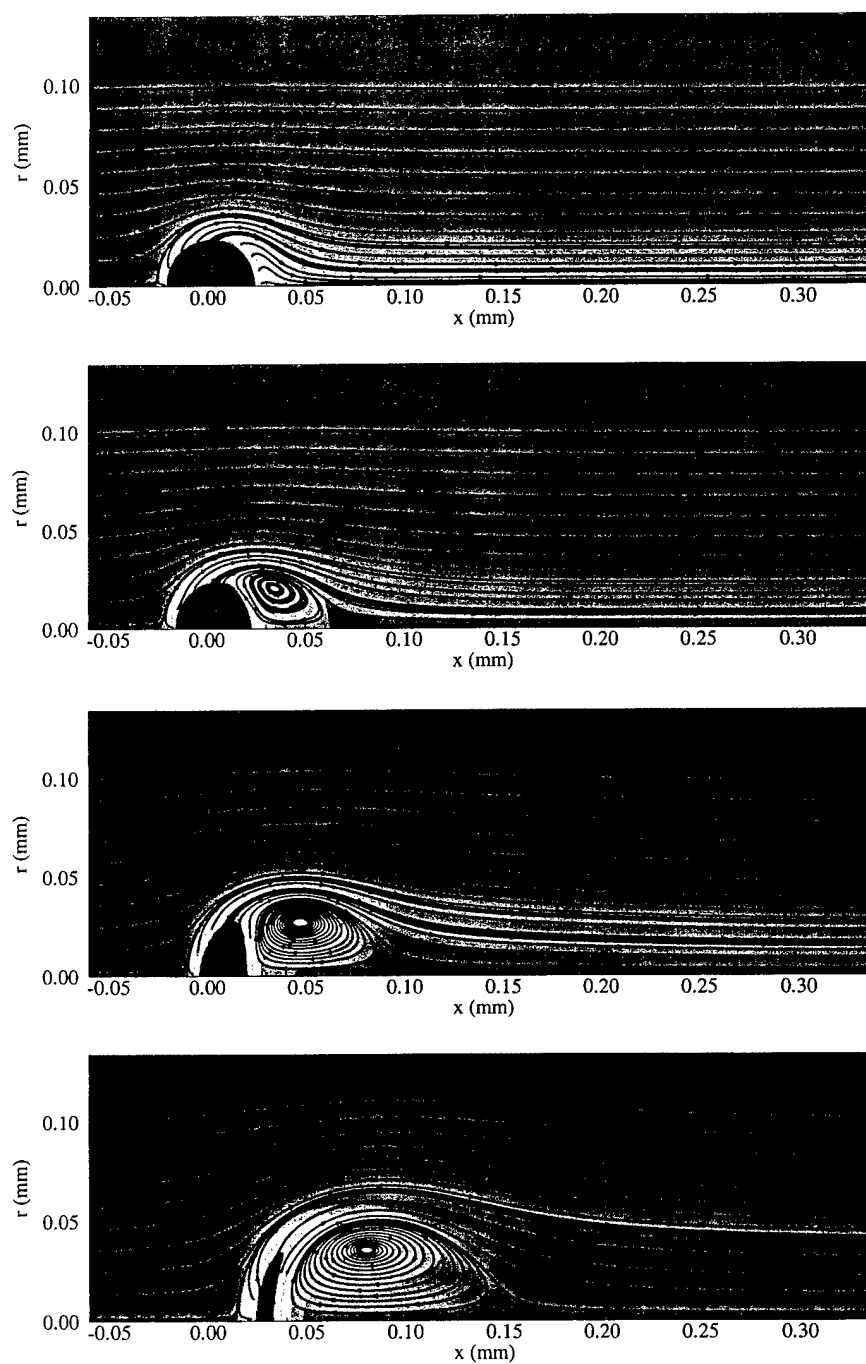


Fig. 5.6 Transient developments of flow fields at $u=5.0\text{m/s}$, $p=400\text{atm}$ ($\text{Re} \approx 120$), at instants of $t=10, 30, 60, 110 \mu\text{s}$, respectively.

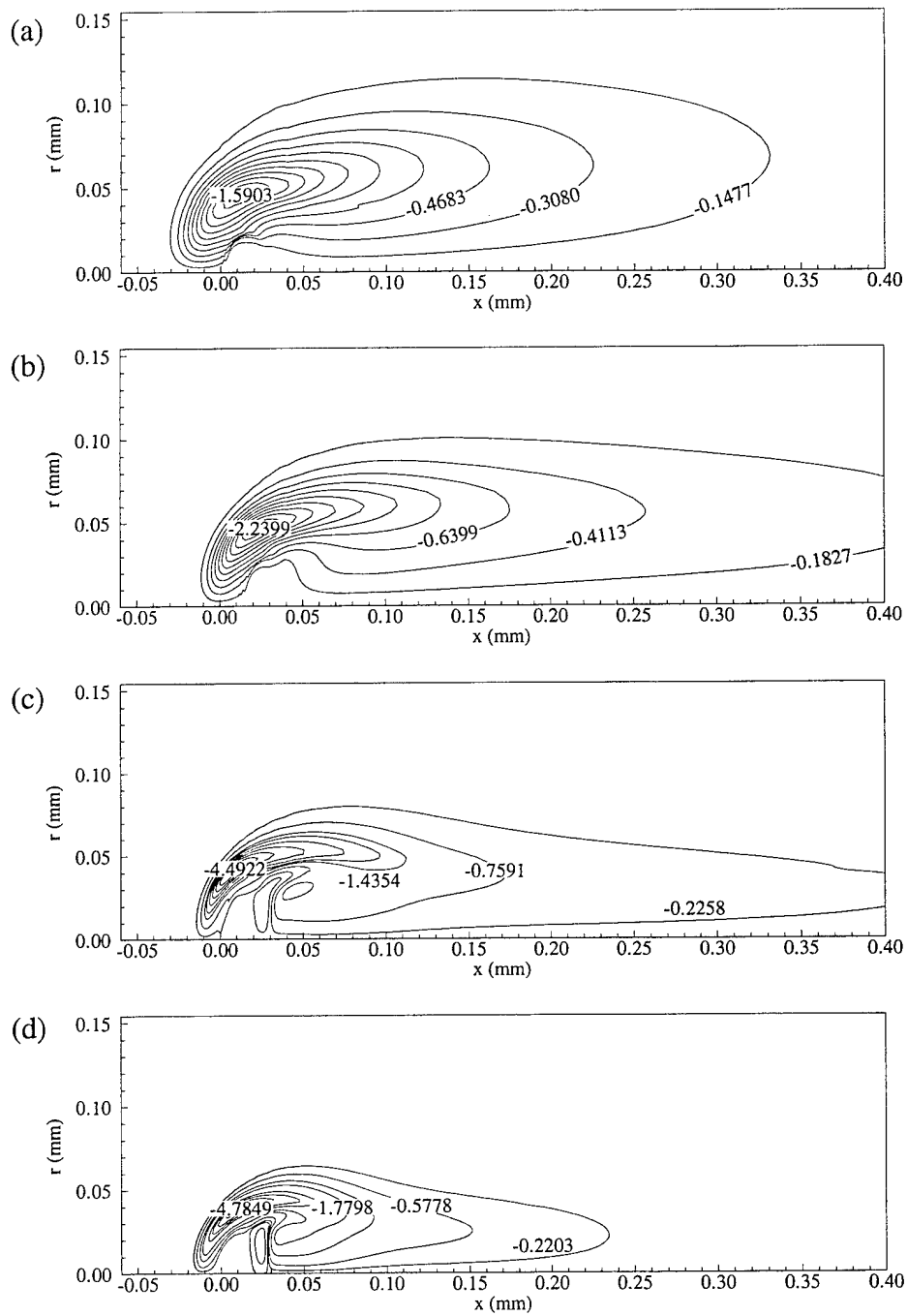


Fig. 5.7 Vorticity distributions, (a) $u=2.5\text{m/s}$, $p=100\text{atm}$, $t=200\mu\text{s}$, (b) $u=5.0\text{m/s}$, $p=100\text{atm}$, $t=150\mu\text{s}$, (c) $u=20\text{m/s}$, $p=100\text{atm}$, $t=30\mu\text{s}$, (d) $u=5.0\text{m/s}$, $p=400\text{atm}$, $t=60\mu\text{s}$.

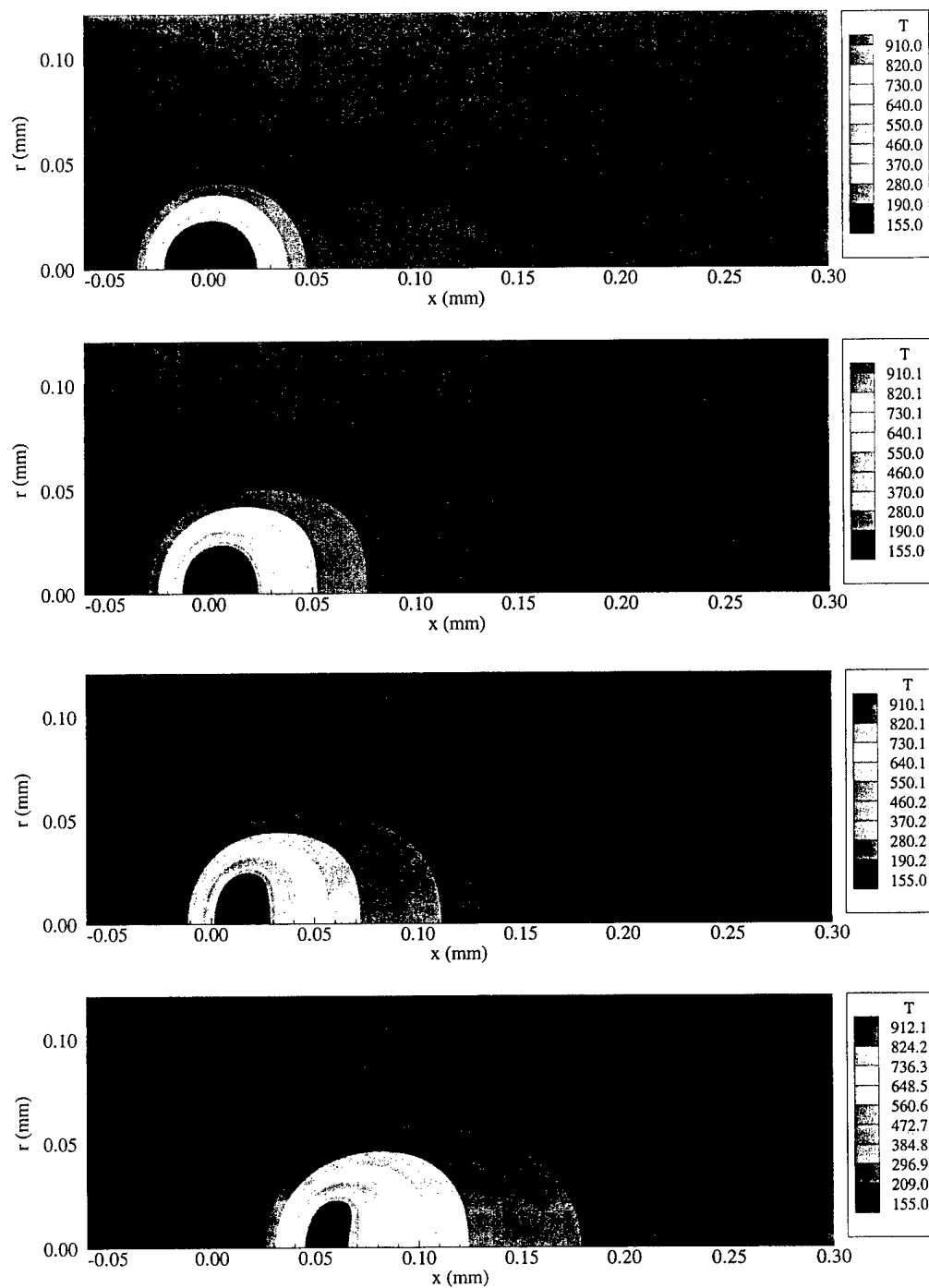


Fig. 5.8 Transient developments of temperature contours at $u=2.5\text{m/s}$, $p=100\text{atm}$, ($Re \approx 15$), at instants of 20, 100, 200, 400 μs , respectively.

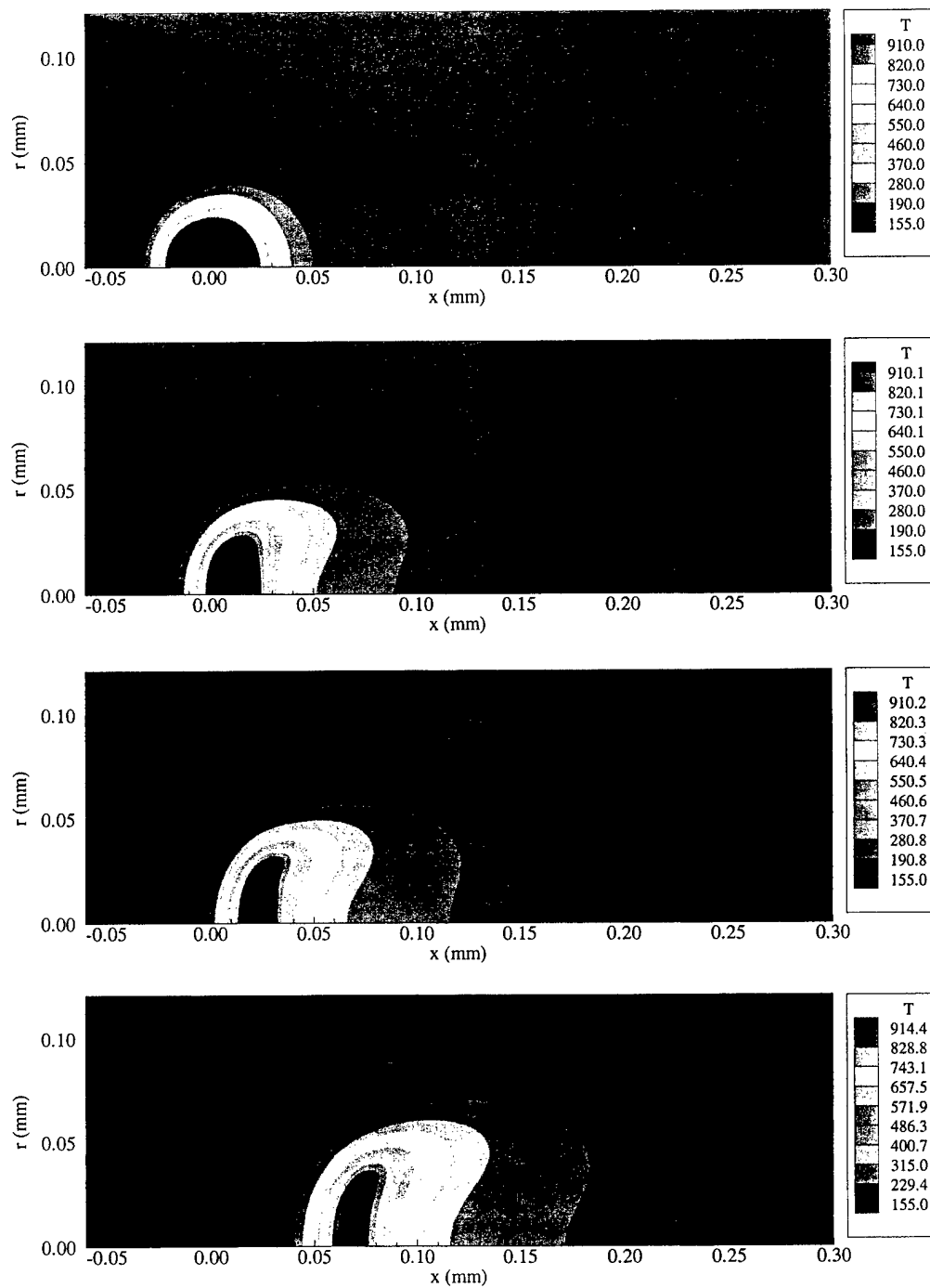


Fig. 5.9 Transient developments of temperature contours at $u=5.0\text{m/s}$, $p=100\text{atm}$, ($\text{Re} \approx 30$), at instants of 12, 100, 150, 250 μs , respectively.

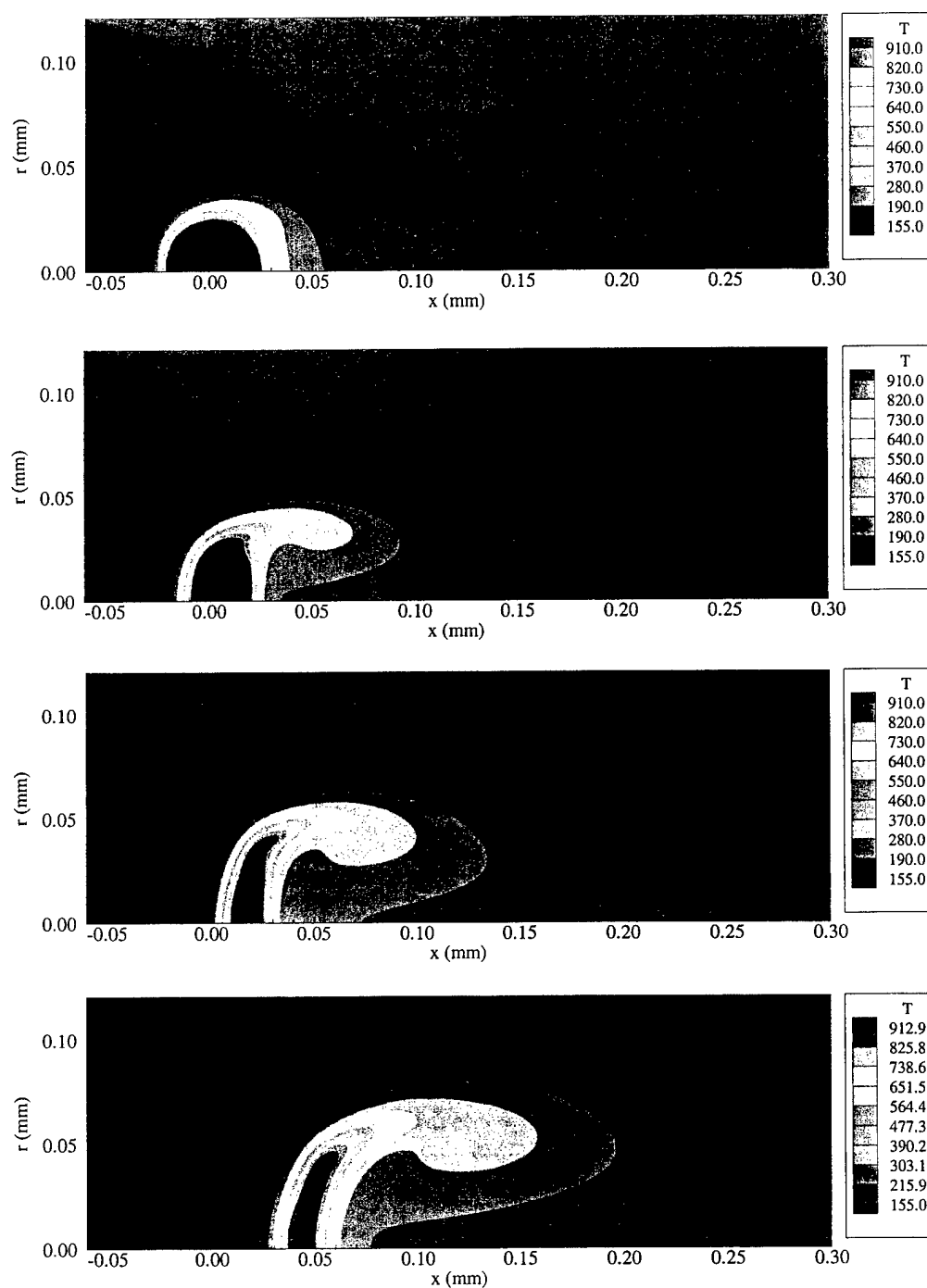


Fig. 5.10 Transient developments of temperature contours at $u=20.0\text{m/s}$, $p=100\text{atm}$, ($Re \approx 120$), at instants of 4, 20, 40, 60 μs , respectively.

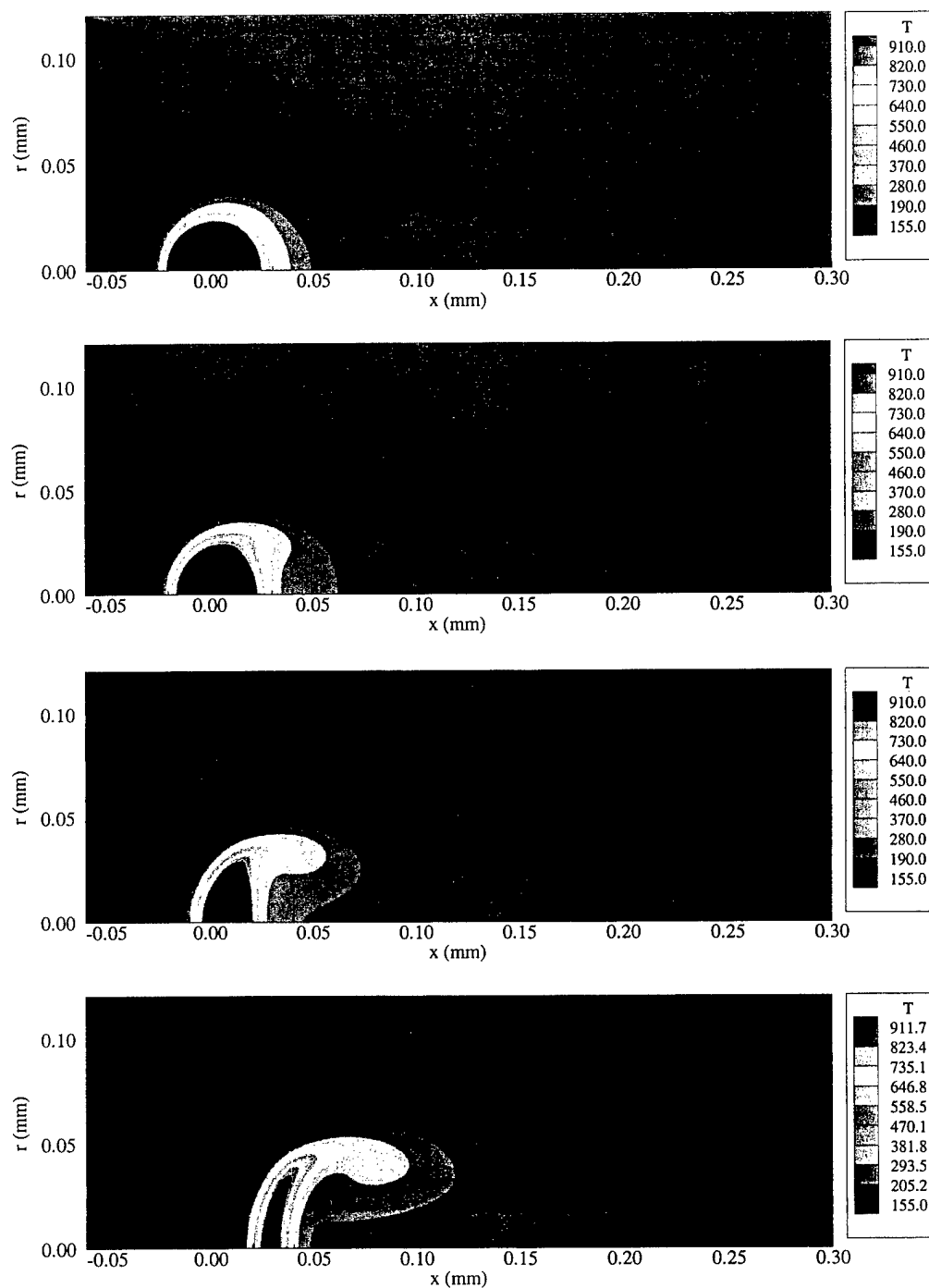


Fig. 5.11 Transient developments of temperature contours at $u=5.0\text{m/s}$, $p=400\text{atm}$, ($\text{Re} \approx 120$), at instants of 10, 30, 60, 110 μs , respectively.

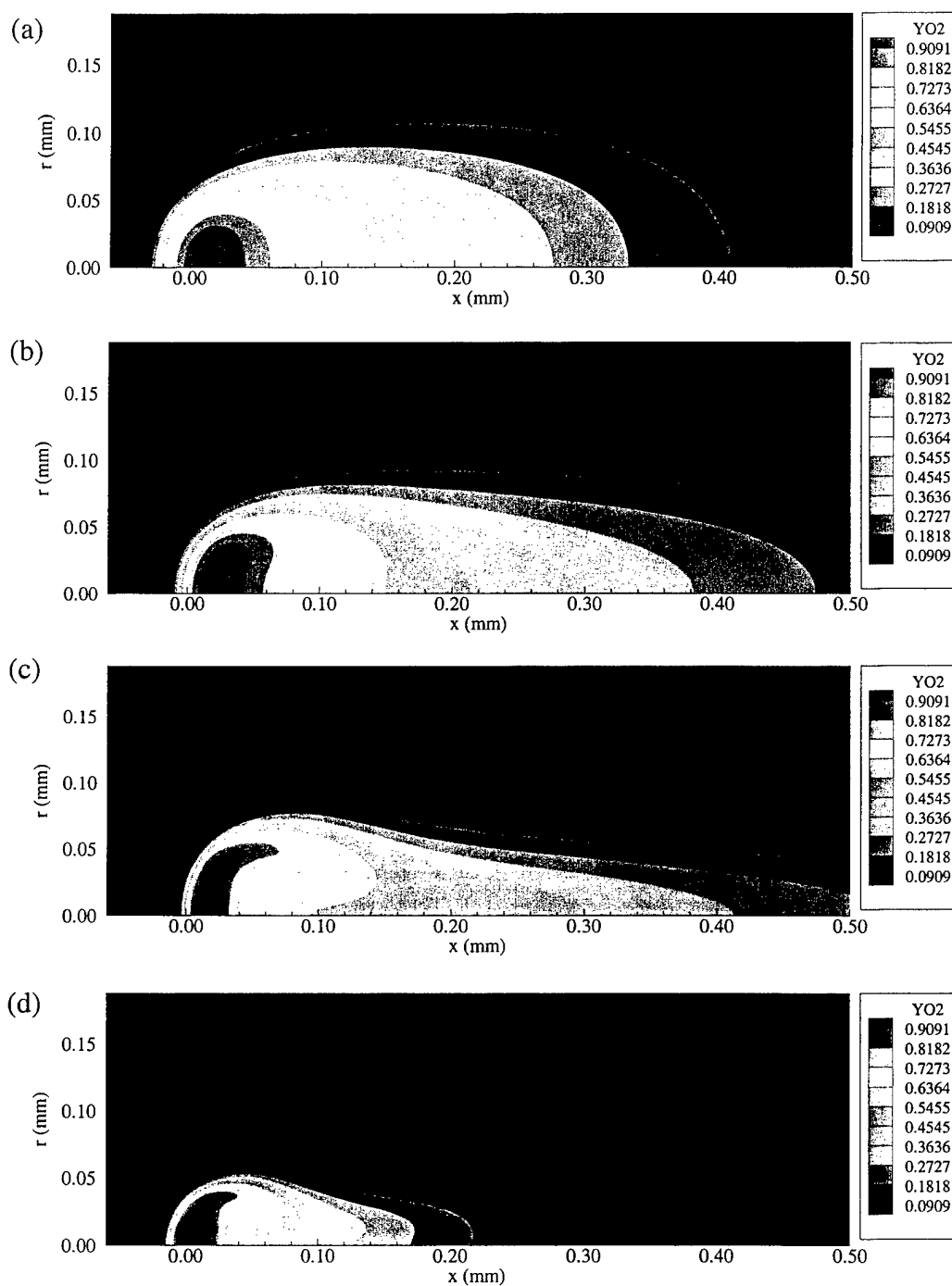


Fig. 5.12 Distributions of oxygen mass fractions, (a) $u=2.5\text{m/s}$, $p=100\text{atm}$, $t=200\mu\text{s}$, (b) $u=5.0\text{m/s}$, $p=100\text{atm}$, $t=150\mu\text{s}$, (c) $u=20.0\text{m/s}$, $p=100\text{atm}$, $t=40\mu\text{s}$, (d) $u=5.0\text{m/s}$, $p=400\text{atm}$, $t=60\mu\text{s}$

Chapter 6

SUPERCritical VAPORIZATION OF TWO-DROPLETS-IN-TANDEM IN CONVECTIVE ENVIRONMENTS

6.1 Problem Description

The effects of droplet interactions on droplet lifetimes at high pressures have been studied in Chapter 3, where the droplet cluster behavior in a quiescent environment is extensively examined. However, convection effect could easily change the results. Since it is still not a reality for current computational capacity to investigate numerically a group of droplet vaporizing in a convective environment, oxygen droplet interactions in convective hydrogen environments are studied in this chapter by setting up a simple configuration of two droplets moving in tandem. The goal is to identify the detailed vaporization characteristics with two neighboring droplets interacting with each other, and the study is focused on the influences from the immediate neighboring droplet on droplet lifetimes and dynamics, such as droplet collision/separation phenomenon. The configuration is sketched in Fig. 6.1, where the initial droplet spacing is prescribed (H). The ratio of the initial droplet spacing and droplet radius, H/R , is defined to indicate the intensity of droplet interactions.

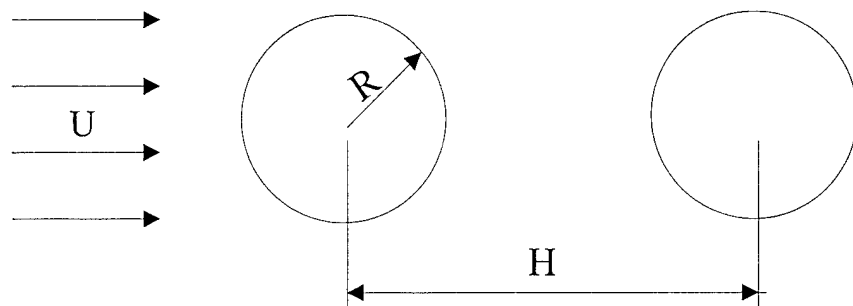


Fig.6.1. Two-droplets-in-tandem in a convective environment.

The following assumptions are taken in this study:

- 1) The flow is laminar and axisymmetric;
- 2) The two droplets reach the critical mixing state immediately after being injected into the combustion chamber;
- 3) The droplet boundary is defined as the isothermal line at the critical temperature of oxygen species (154.6 K).

6.2 Numerical Treatment

The preconditioning numerical algorithm with a unified treatment of real fluid behavior, as developed in Chapter 4, is utilized to solve the current problem. The methods presented in Chapter 2 are applied to evaluate the transport properties, with full account of pressure effect. Non-uniform grids are generated in the same manner as that in the single droplet case so that no extra effort is needed for grid independence study. Part of the grids is illustrated in Fig. 6.2, where meshes around the two droplets are significantly refined for numerical accuracy.

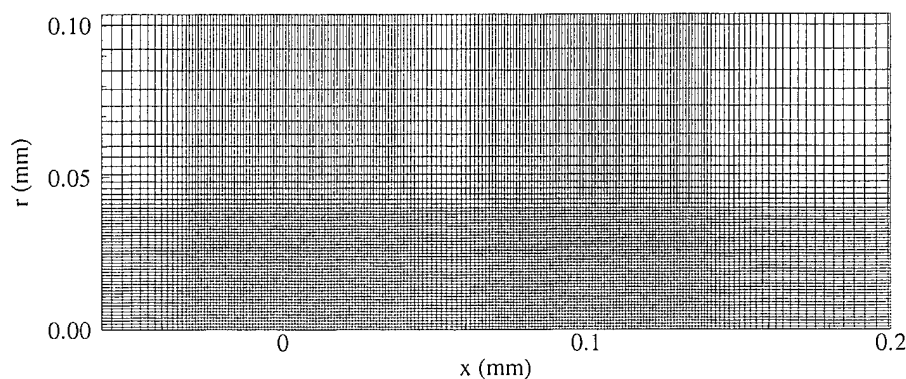


Fig. 6.2. Part of the Numerical Grids for Two-Droplets-in-Tandem.

6.3 Results and Discussions

Supercritical vaporization of two-droplets-in-tandem is illustrated in Fig. 6.1, where two oxygen droplets are suddenly injected into a uniform hydrogen flow field. Initially, the two droplets are at the same size of $50\mu\text{m}$ in diameter. The oxygen droplet and the hydrogen fluid are at the uniform temperatures of 100 K and 1000K, respectively. Pressures range from 100 to 400 atm. As for the single droplet case, the flow is sustained as laminar and axisymmetric by limiting the Reynolds Number (Re) to be less than 240. The Reynolds number is defined based on the initial droplet diameter and the inflow hydrogen velocity, density, and viscosity.

6.3.1 Droplet Deformations and Temperature Fields

As in the single droplet vaporization case, the droplet boundary is defined as an isothermal line at the critical temperature of the oxygen species (154.6 K) in the numerical investigation. Therefore, the temperature fields will illustrate the droplet deformation characteristics.

Figures 6.3-6.5 present the typical droplet deformation features at a pressure of 100atm, an incoming velocity of 10m/s ($Re \approx 60$), but different H/R ratios of 4, 8, and 12. Figure 6.3 shows the transient developments of temperature fields at a H/R ratio of 4. Initially, the two droplets evaporate independently. With the increase of time, the convection effect begins to dominate the vaporization process, and the temperature fields around the two droplet merges. At the time of $t = 60 \mu\text{s}$, the two droplets deform in completely different patterns. The leading droplet confronting stronger incoming flow behaves more like an isolated droplet and deforms perpendicular to the flow direction. Its backside becomes flat, while the front side retains a round shape. The deformation of the

trailing droplet, due to much weaker incoming fluid flow, is dominated by diffusion. The phenomenon is especially profound near the axisymmetric axis, where the temperature contours significantly diffuse outward, resulting in relatively small temperature gradient. The boundary layer theory is obviously invalid in this region. Near the axisymmetric axis, the trailing droplet strongly expands along the flow direction and presents the characteristics of deformation distinct from the leading droplet. When time is increased to $155 \mu s$, the leading droplet moves very close to the trailing droplet, but there is no droplet collision based on temperature contours. At this instant, the leading droplet is clearly breaking up at the axisymmetric axis. With most of mass moving toward the edge of the droplet, the break-up is categorized as the typical forward bag break-up. The mass ring resulted from the bag break-up is transported downstream by moving over the surface of the trailing droplet and disappears shortly after the break-up. Meantime, there is apparent stretching at the tip of the trailing droplet. The outside temperature fields behave as if they are surrounding a large isolated droplet. After the leading droplet disappears, the remaining trailing droplet begins to deform like an isolated droplet, except that the outside temperature contours experience stronger expansion perpendicular to the flow direction. Because the trailing droplet now has to confront incoming flow directly, strong stretching of the droplet is clearly illustrated.

Droplet deformations at a H/R ratio of 8 present features distinct from that at a H/R ratio of 4. At the time of $t = 145 \mu s$, the leading droplet is forced to expand strongly perpendicular to the axisymmetric axis and retains a slightly convexed disk shape. Meantime, the expansion of the trailing droplet along the flow direction is significantly weakened compared with that at a H/R ratio of 4, although it is still dominated by

diffusion near the axisymmetric axis. The trailing droplet is strongly bent downstream and shows a skirt-like shape. Before the low-temperature core regions of the two droplets contact each other, the leading droplet has already been completely evaporated, as illustrated at the instant of $t=190 \mu s$. At the same time, the trailing droplet is further stretched. There is no droplet break-up occurring for the leading droplet during its entire vaporization process. By the end of the vaporization process, only one highly stretched trailing droplet is remaining in the flow field.

Droplet deformations at a H/R ratio of 12 are presented in Fig. 6.5. During the entire droplet lifetimes, the two droplets both behave in similar patterns as an isolated droplet, with the droplet expansions perpendicular to the axisymmetric axis and crescent shapes remaining at the end of the vaporization process.

Increasing the incoming velocity to 20 m/s ($Re \approx 120$), the two droplets still deform in the same features as those illustrated in Figs. 6.3-6.5. At a higher pressure, droplet interactions become weaker. When pressure increases to 400 atm, the two droplets begin to deform like two isolated droplets at a H/R ratio of 8, while the same situation only occurs at a H/R ratio of 12 at a pressure of 100 atm.

6.3.2 Mass Fraction Fields

The typical mass fraction fields are presented in Figs. 6.6-6.7, which correspond to the same initial conditions as those in Figs. 6.3-6.4. At a H/R ratio of 4, the mass fraction contours around the two droplets begin to merge even at the very beginning of the vaporization process, as shown in Fig. 6.6. When time increases to $60 \mu s$, the deformations of the two droplets illustrated by the mass fraction contours are similar to those represented by temperature contours shown in Fig. 6.3. At this instant, the leading

droplet becomes an oblate with a flat back, while the trailing droplet maintains a prolate shape with indentation at its backside. The difference between the fields of mass fraction and temperature is that species diffuse much faster than thermal diffusion does, and there is consequently stronger downstream transport of the oxygen species. In Fig. 6.6, as time further increases to $125 \mu s$, the two droplets collided according to the mass fraction field, and a complete mushroom-like shape is produced. This feature is significantly different from that in the corresponding temperature field. In addition, there is no forward bag break-up observed for the leading droplet in the mass fraction field. At the end of the vaporization process, the two droplets completely merge together, and begin to behave like an isolated droplet.

Fig 6.7 presents the developments of mass fraction fields at a H/R ratio of 8. No droplet interaction is illustrated with the vaporization time up to $16 \mu s$. As time reaches $60 \mu s$, the oxygen species from the leading droplet is connected with those from the trailing droplet due to strong convective transport. However, at this time, the effect of interactions on both droplets is trivial, and the two droplets still perform similar deformations. With time increase to $190 \mu s$, the dense oxygen regions of the two droplets merge together, and the effect of droplet interactions becomes significant. The leading droplet expands strongly perpendicular to the flow direction, while the trailing droplet is mainly stretched along the flow direction. However, there still remains the oxygen-rich region for the leading droplet, in contrast to its disappearance in the temperature field. Finally, the two droplets collide and form one droplet, which is slightly stretched at the tip. The stretched deformation of the merged droplet is different from that

of an isolated droplet, which maintains a crescent shape at the end of the vaporization process.

The effect of droplet interactions on the deformations of the two droplets becomes extremely weak at a H/R ratio of 12. Both droplets deform like an isolated droplet and remain crescent shapes at the end of the vaporization process. Increase of the incoming velocity from 10 m/s to 20 m/s does not change the deformation characteristics. In contrast, increase of pressure from 100 atm to 400 atm will weaken the droplet interactions just like the situations demonstrated in temperature fields. Only minor effect of droplet interactions on both droplets is illustrated once the H/R ratio reaches 8.

6.3.3 Flow Field Developments

With two droplets confronting the forced incoming flow in tandem, the flow fields around the leading and trailing droplets are extremely different. The characteristics distinct from those of an isolated droplet are also displayed.

Figures 6.8-6.10 present the flow fields at the same initial pressure and incoming velocity of 100 atm and 20 m/s ($Re \approx 120$) but different H/R ratios. A stationary reference frame is maintained in these three figures. Streamlines are utilized to illustrate the instant flow fields with temperature fields displayed to indicate the droplet locations. Figure 6.8 illustrates the transient flow developments at a H/R ratio of 4. At the beginning of the vaporization process, the flow fields around the two droplets are similar in the fact that a recirculating eddy is developed in the wake of each droplet. Because the leading droplet faces stronger incoming flow than the trailing droplet does, flow separation around it occurs earlier, resulting in a slightly larger recirculating region in its wake. At the time of $t = 40 \mu s$, as the leading droplet retains a disk-like shape, flow

separation is further enhanced, resulting in a larger recirculating eddy. Since the trailing droplet diffuses significantly in the upstream direction, it pushes the first recirculating eddy slightly upward. The second recirculating eddy also grows during the vaporization process, but it is relatively smaller compared with the first one. The reason is that, with the trailing droplet deforming mainly along the flow direction, flow separation around it is weaker than that around the leading droplet. When the leading droplet moves further close to the trailing droplet (at $t = 65 \mu s$), the first recirculating eddy is pushed upward and located at the top of the trailing droplet. Because the presence of the trailing droplet restricts the possible recirculating space for the first eddy, its size becomes smaller. With the first eddy pushed on top of the trailing droplet, an interesting phenomenon appears. Since flow is now redirected by the first eddy and separated behind it instead of the trailing droplet, the original second recirculating eddy disappears. Instead, another recirculating eddy is created behind the first one. These two eddies locate very close to each other. At the time of $t = 85 \mu s$, the two droplets move so close to each other that their effect on the flow fields become similar to that of an isolated droplet. Meantime, the first eddy and the new eddy behind it merge together, resulting in one large recirculating region.

The flow fields at a H/R ratio of 8 is different from that at a $H/R = 4$, as shown in Fig. 6.9. Initially, there are two eddies independently developing behind the two droplets. With the increase of time, the two eddies both grow in size. However, the first eddy is much larger than the second one because of two reasons. The first reason is related to the deformation of the leading droplet, which enhances flow separation. The second reason is that, since the two droplets form a close region between them, it helps entraining vorticity

and maintaining a strong recirculating flow there. Once the leading droplet moves closer to the trailing droplet, the first recirculating eddy is pushed upwards and decreases in size. The size of the second eddy also decreases. This is partially due to the deformation of the second droplet, and partially caused by the position of the first eddy, which significantly changes the flow field. Since the leading droplet completely disappears at the time of $t = 110 \mu s$, the result is the disappearance of the first eddy. However, the second eddy is maintained during the entire vaporization process.

The flow fields corresponding to a H/R ratio of 12 is illustrated in Fig. 6.10, where the interactions between the two droplets are extremely weak. The first recirculating eddy remains growing in the entire vaporization process because of the existence of the closed region between the two droplets and its entraining of vorticity. The second recirculating eddy increases in size at the beginning of the process, but its size decreases gradually at the later stage, because the deformation of the trailing droplet eases flow separation.

To demonstrate the effects of incoming velocity and pressure on flow field developments, Fig. 6.11 shows the flow fields at a H/R ratio of 8 for two different initial conditions. Fig 6.11a corresponds to the flow field at a pressure of 100 atm and an incoming velocity of 10m/s ($Re \approx 60$), while Fig 6.11b represents the flow fields at a pressure of 400 atm and an incoming velocity of $u = 5 \text{ m/s}$ ($Re \approx 120$). The flow field in Fig. 6.11a indicates that the second recirculating eddy disappears without creation of a new recirculating region, because incoming flow is not sufficiently strong to maintain a second eddy. Figure 6.11b corresponds to a same Reynolds number ($Re \approx 120$) as Fig. 6.9 does, but its flow field is completely different from the former one in the fact that

there are two independent recirculating eddies existing at the end of the vaporization process. Comparison of the flow fields, as shown in both Fig.6.9 and 6.11b, indicates that droplet interaction becomes significantly weaker at a higher pressure of 400 atm. This conclusion is consistent with those drawn from both the temperature and mass fraction fields.

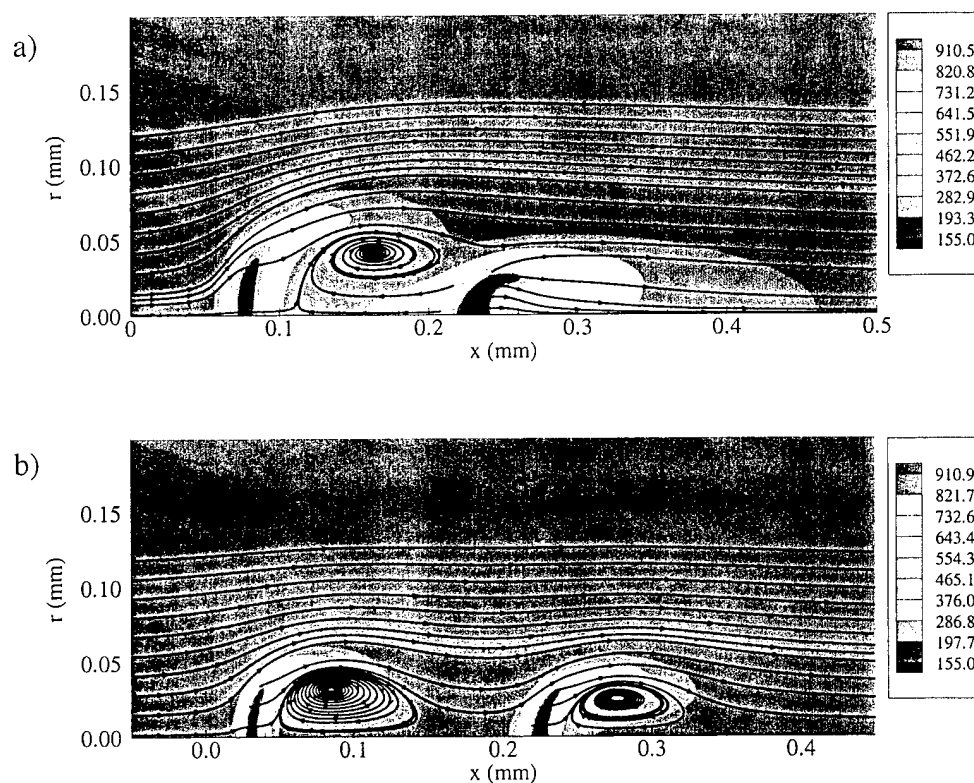


Fig. 6.11 Effects of Incoming Velocity and Pressure on the Flow Fields, a) $p=100$ atm, $u=10$ m/s, $t=145 \mu\text{s}$, b) $p=400$ atm, $u=5$ m/s, $t=115 \mu\text{s}$.

6.3.4 Droplet Lifetimes

With two droplets moving in tandem, the droplet vaporization rates and droplet lifetimes for the leading and trailing droplets show significantly different characteristics. Figures 6.12-6.13 illustrate the vaporization rates for the two droplets at different H/R ratios. Figure 6.12 represents the cases at an initial pressure and velocity of 100 atm and

20 m/s ($Re \approx 120$), respectively. These figures clearly demonstrate that the droplet interactions at different H/R ratios present only minor effects on the leading droplets, but effects on the trailing droplets are much stronger. The trailing droplet evaporates at the same rates as the leading droplet only at the beginning of the vaporization process. Once the two droplets start to interact with each other, the vaporization rates of the trailing droplets begin to deviate significantly from those of the leading droplets. The exact deviation times depend on the H/R ratios. At a H/R ratio of 4, the vaporization rate of the trailing droplet slows down only shortly after the beginning of the vaporization process. During the times around 90-100 μs , there is another sudden change of the vaporization rate. During this second transition period, the leading droplet breaks up. The mass ring resulted from the break-up is transported over the surface of the trailing droplet and causes the low-temperature oxygen-rich region of the leading droplet to merge with the trailing droplet. There is no obvious transition period existing in the other two cases at the H/R ratios of 8 and 12, since the low-temperature regions of the leading droplets have already disappeared before they could contact the trailing droplets.

At a pressure of 400 atm and an incoming velocity of 5 m/s ($Re \approx 120$), droplet interaction effects on droplet vaporization rates become extremely weak as demonstrated in Fig. 6.13. Significant change of droplet vaporization rates of the trailing droplet only occurs when the two droplets are very close to each other at a H/R ratio of 4.

To further clarify the effect of droplet interactions on droplet lifetimes, the droplet lifetimes of both the leading and trailing droplets are compared with that of an isolated droplet, while all the other flow conditions are maintained as the same. A droplet lifetime ratio τ is defined as

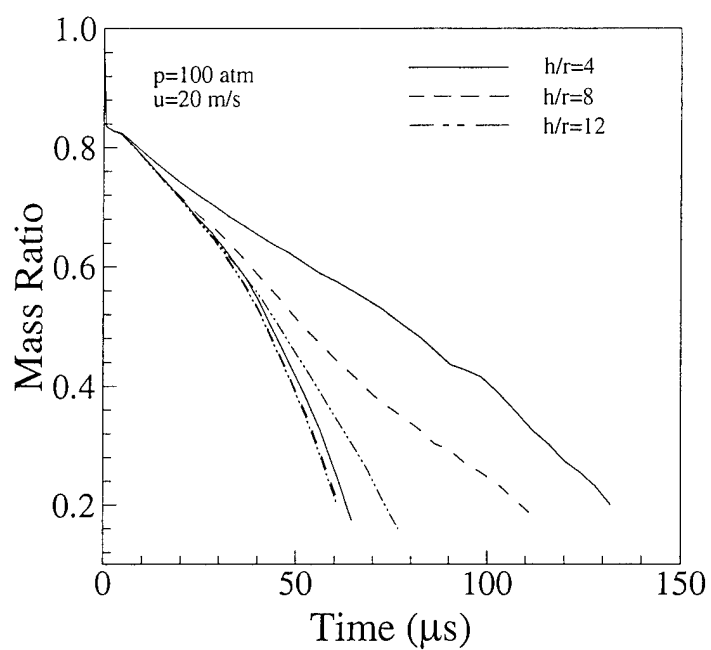


Fig. 6.12. Droplet vaporization rates at $p=100$ atm, $u=20$ m/s.

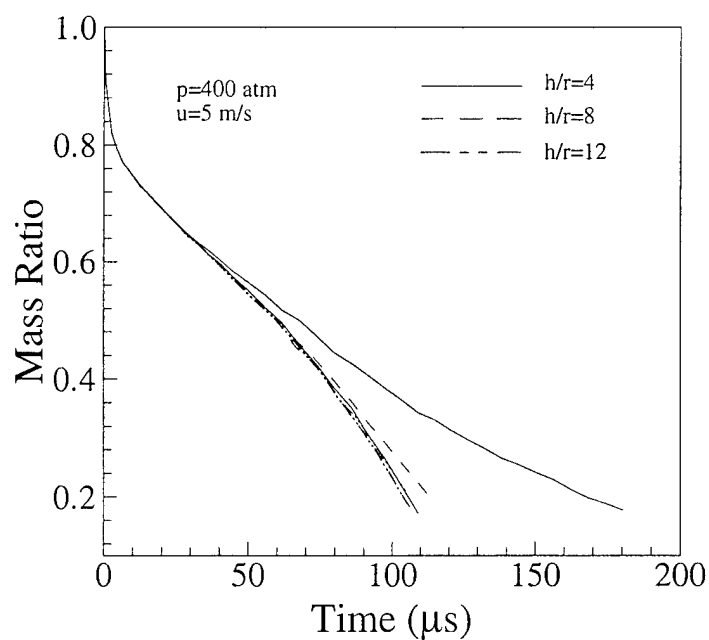


Fig. 6.13. Droplet vaporization rates at $p=400$ atm, and $u=5$ m/s.

$$\tau = \frac{\text{Lifetime of an isolated droplet}}{\text{Lifetime of the leading/trailing Droplet}} \quad (6.1)$$

Figure 6.14-6.15 present the variations of droplet lifetime ratios at two pressures of 100 and 400 atm and two incoming velocities of 10 and 20m/s. At a pressure of 100 atm, there is only slight interaction effect on the droplet lifetimes of the leading droplet at a H/R ratio of 4, at which the droplet lifetime ratios τ are around 0.8 for both incoming flow velocities. The lifetimes of the trailing droplets are dramatically elongated due to the weak convection effect caused by the existence of the leading droplet. The droplet lifetime ratios are about the same (around 0.5) for the trailing droplets at both H/R ratios of 4 and 8, although their initial vaporization rates are different. At a H/R ratio of 4, the trailing droplet initially evaporates at a slower rate, but the leading droplet in this case disappears in relatively shorter time than that at a H/R ratio of 8. After the disappearance of the leading droplet, the trailing droplet begins to evaporate like an isolated droplet, and its vaporization rate consequently becomes faster than before.

Figure 6.14 clearly indicates that there are only slight effects of incoming velocities on droplet lifetime ratios. The maximum difference, which occurs for the leading droplet between the droplet lifetime ratios at two velocities at a H/R ratio of 4, is less than 0.1. The same situation applies to the cases at a pressure of 400 atm, as shown in Fig. 6.15.

At a higher pressure of 400atm, droplet interaction effect becomes much weaker, as already discussed above. In Fig. 6.15, the droplet lifetime ratios of the leading droplets are all above 0.9 because of negligible interaction effect. For the trailing droplet, the droplet lifetime ratios at a H/R ratio of 8 becomes larger than 0.8, which is significantly higher than its counterparts at a pressure of 100 atm (e.g., ~ 0.5).

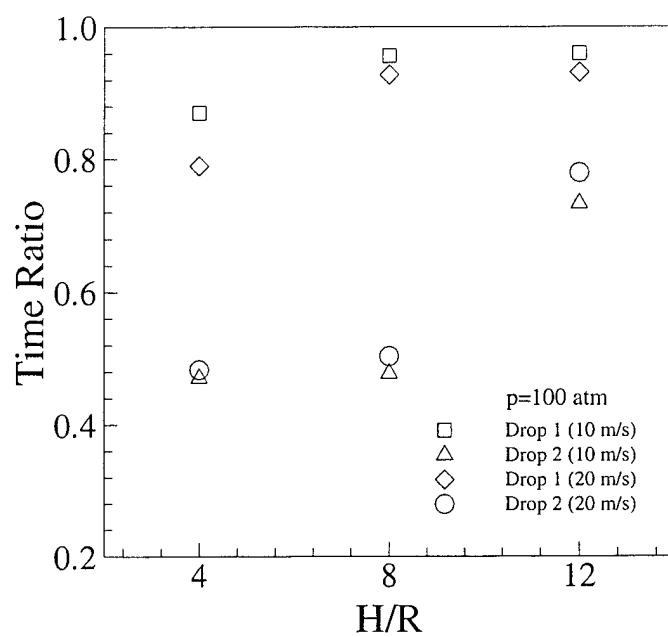


Fig. 6.14. Droplet lifetime ratios vs. H/R ratios at p=100 atm

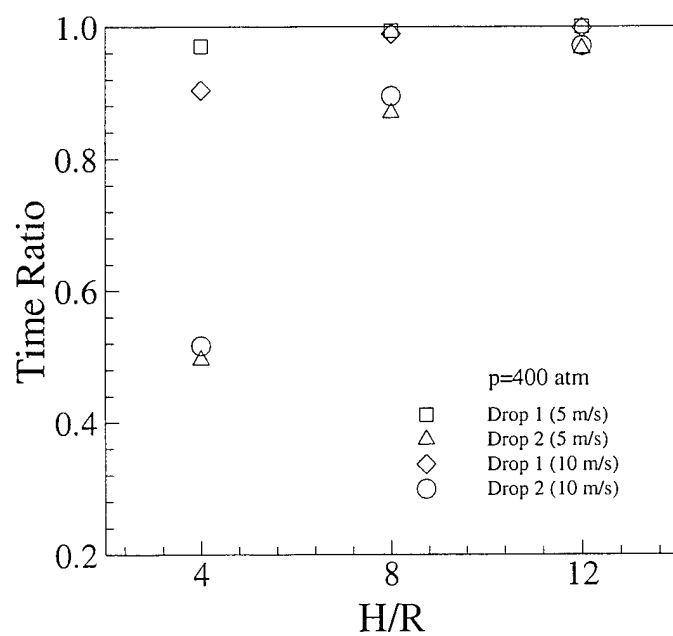


Fig. 6.15. Droplet lifetime ratios vs. H/R ratios at p=400 atm

6.3.5 Droplet Trajectories

For the droplet vaporization case, the total drag force acting on a droplet consists of three components: the friction drag, the pressure drag, and the thrust drag. The thrust drag results from the surface blowing. With two droplets moving in tandem, the moving trajectories for the leading and trailing droplets are significantly different, especially at low H/R ratios. Fig 6.16 presents the droplet moving trajectories at the same pressure and incoming velocity of 100 am and 20 m/s but different H/R ratios. The presence of the trailing droplet performs only a minor effect on the motion of the leading droplet, whose trajectory generally follows that of an isolated droplet. The situation for the trailing droplet at a H/R ratio of 4 is dramatically different. The trajectory of the trailing droplet deviates from that of the leading droplet after a short time. After that, the droplet moves extremely slowly. From 50 μs on, the droplet even begins a slightly forward movement, corresponding to a forward drag force dominated by the pressure drag. After reaching about 85 μs when the leading droplet undergoes break-up and is blown over the top of it, the trailing droplet begins to move like an isolated droplet as expected.

At a H/R ratio of 8, there is also a transition time when the movement of the trailing droplet tremendously slows down, but there is no forward movement observed. After the transition time, the leading droplet disappears, resulting in a lone second droplet moving at much faster speeds.

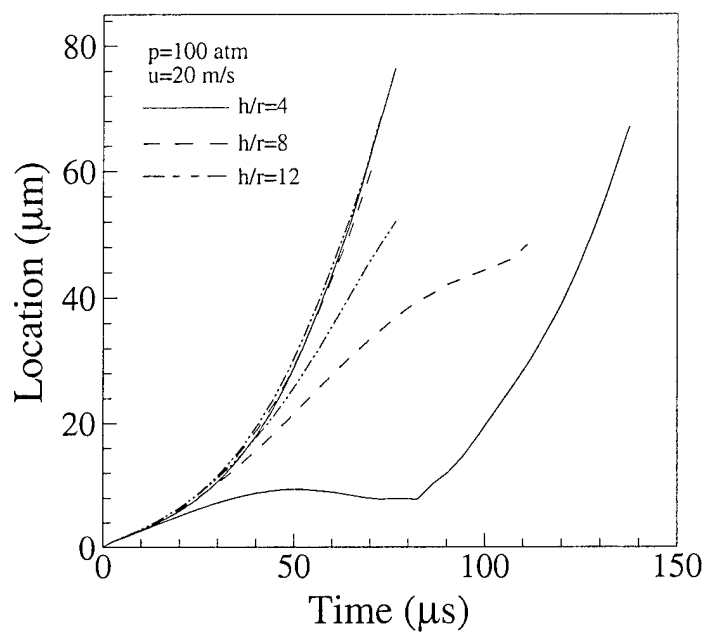


Fig. 6.16. Droplet trajectories for both the leading and trailing droplets at $p=100$ atm, and $u=20$ m/s.

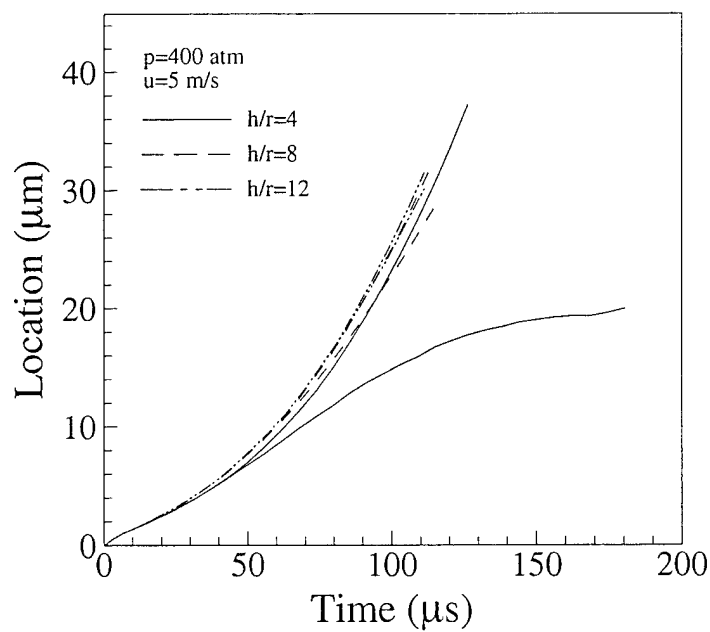


Fig. 6.17. Droplet trajectories for both the leading and trailing droplets at $p=400$ atm, and $u=5$ m/s.

Pressure effect on droplet trajectories are illustrated in Fig. 6.17, which presents droplet movements at a pressure and an incoming velocity of 400 atm and 5 m/s ($Re \approx 120$), respectively. In Fig. 6.17, the only difference between the droplet trajectories of the leading and trailing droplets occurs at a H/R ratio of 4. This result further proves the conclusion that pressure renders weak droplet interactions. At a H/R ratio of 4, the transition time for the trailing droplet begins at about $100 \mu s$, after which point the movement of the trailing droplet decelerates through the end of the vaporization process. There is no forward droplet movement observed for all the cases shown in Fig. 6.17.

6.4 Summary of Results

Supercritical vaporization of two oxygen droplets moving in tandem in convective hydrogen environments is numerically investigated. The influences of the immediate neighboring droplet on droplet lifetimes, deformations, and trajectories are studied in detail.

Based on the definition of the droplet surface at an isothermal line of oxygen critical temperature (154.6K), there is no droplet collision observed for all the cases studied herein. However, a forward bag break-up of the leading droplet is found when the two droplets are initially positioned closely at a H/R ratio of 4 and a pressure of 100 atm. According to mass fraction fields, droplet collisions do happen at two initial H/R ratios of 4 and 8.

Deformations of the two droplets display distinct characteristics. The leading droplet confronting strong incoming flow expands perpendicular to the flow direction, while the trailing droplet mainly deforms along the flow direction.

Initially there are two recirculating eddies developed independently in the wakes of the two droplets. With an incoming velocity of 10 m/s and an initial H/R ratio of 4, the second eddy disappears before the end of the vaporization process, but a new eddy is created behind the first one. Increasing the initial H/R ratio to 8, however, changes the flow fields dramatically. In the later case, the first eddy disappears, after the leading droplet is completely evaporated. The second eddy remains during the entire vaporization process.

The existence of the trailing droplet produces only minor effects on the lifetimes and trajectories of the leading droplets. At a pressure of 100 atm and the initial H/R ratios of 4 and 8, the lifetimes of the trailing droplet are strongly elongated. There is forward movement observed for the trailing droplet at a H/R ratio of 4 and a pressure of 100 atm.

Increase of pressure weakens droplet interactions, and this conclusion is consistently verified in the studies of temperature fields, flow fields, droplet lifetimes, and droplet trajectories.

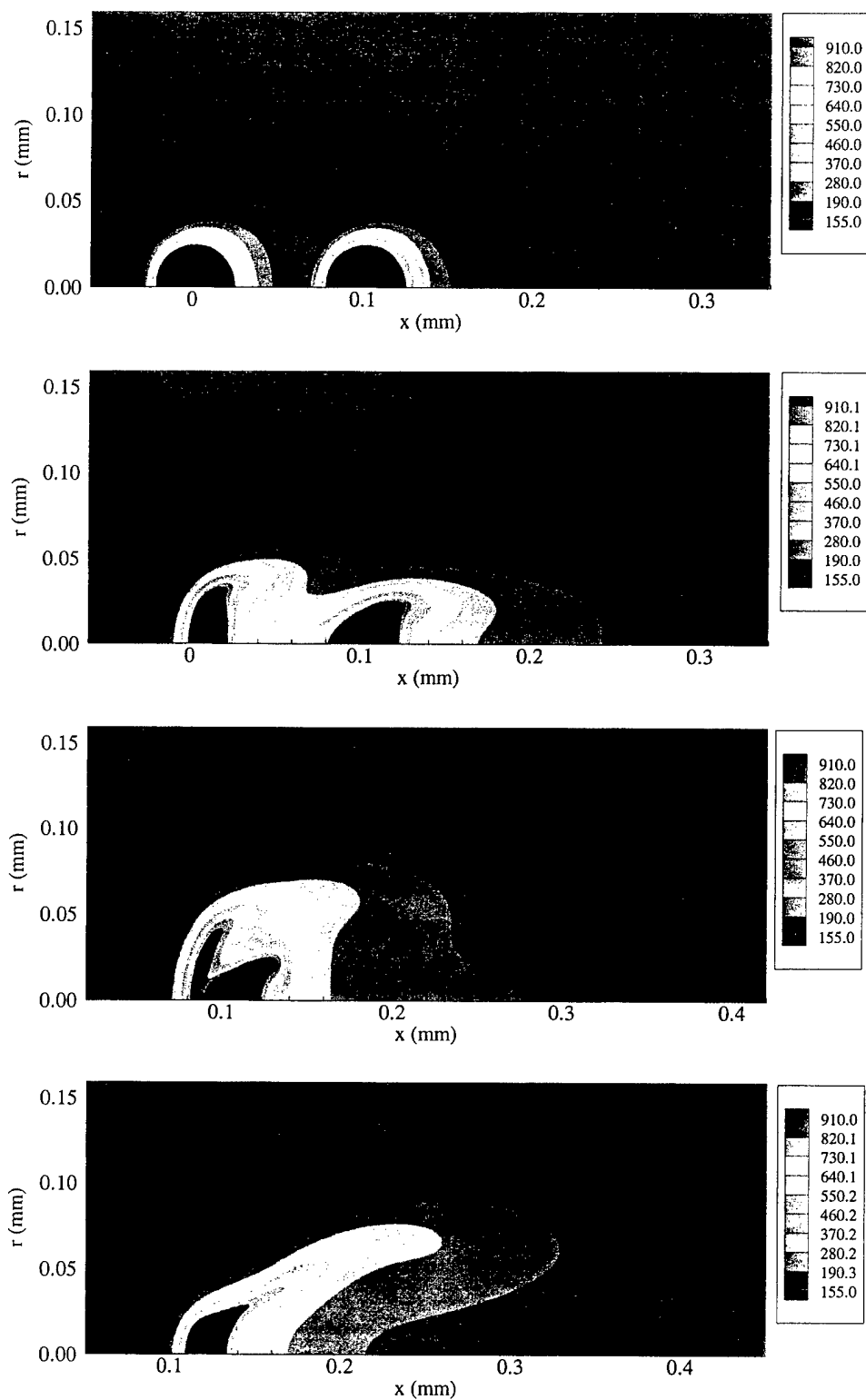


Fig. 6.3. Transient variations of temperature fields and droplet deformations at $p=100$ atm, $u=10$ m/s, and H/R ratio of 4 ($t=6, 60, 155$, and $200 \mu\text{s}$, respectively).

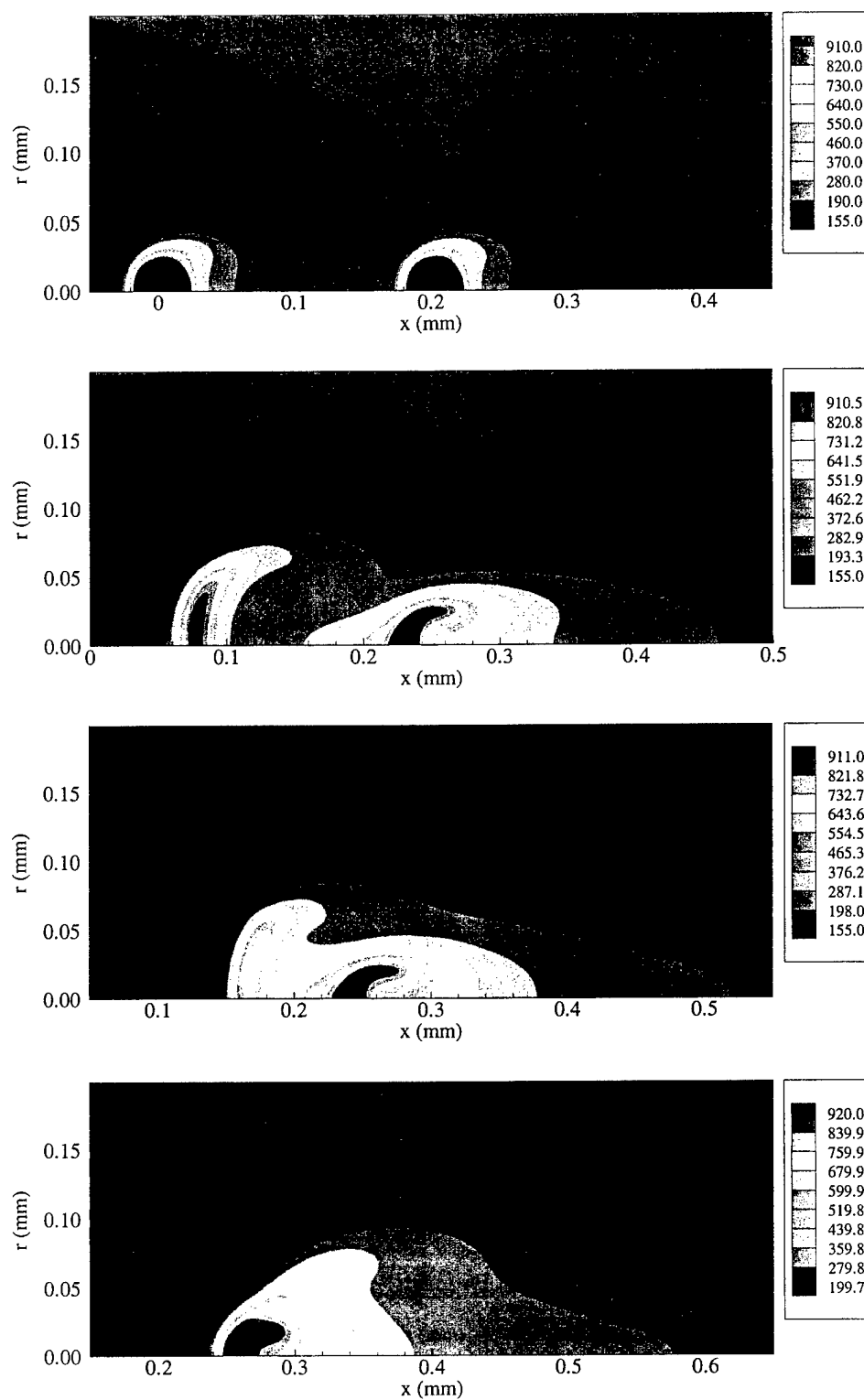


Fig. 6.4. Transient variations of temperature fields and droplet deformations at $p=100$ atm, $u=10$ m/s, and H/R ratio of 8 ($t=15, 145, 190$, and $225 \mu s$, respectively).

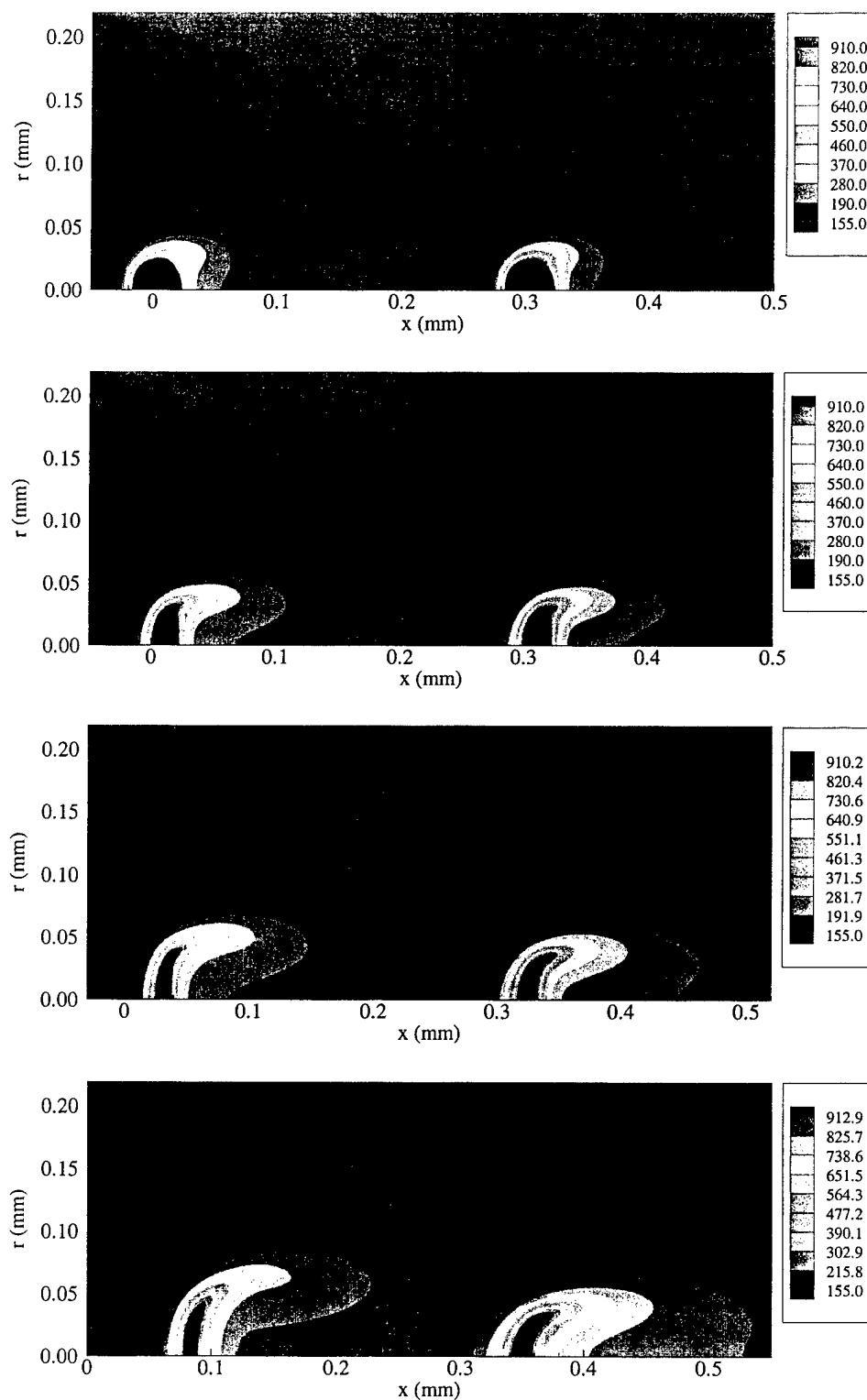


Fig. 6.5. Transient variations of temperature fields and droplet deformations at $p=100$ atm, $u=10$ m/s, and H/R ratio of 12 ($t=20, 60, 100,$ and $150 \mu s$, respectively).

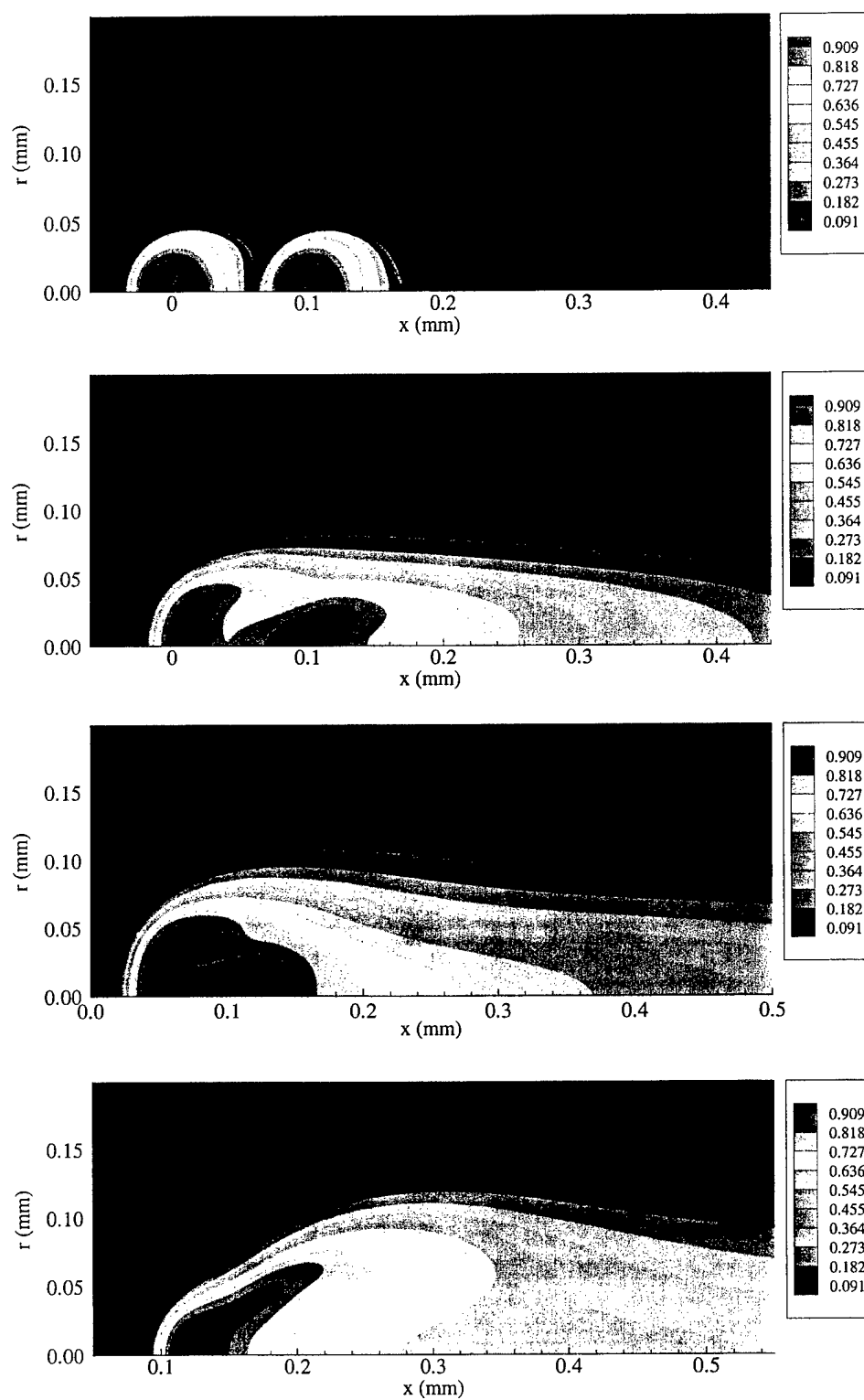


Fig. 6.6. Transient variations of oxygen mass fraction fields at $p=100$ atm, $u=10$ m/s, and H/R ratio of 4 ($t=6, 60, 125$, and $200 \mu\text{s}$, respectively).

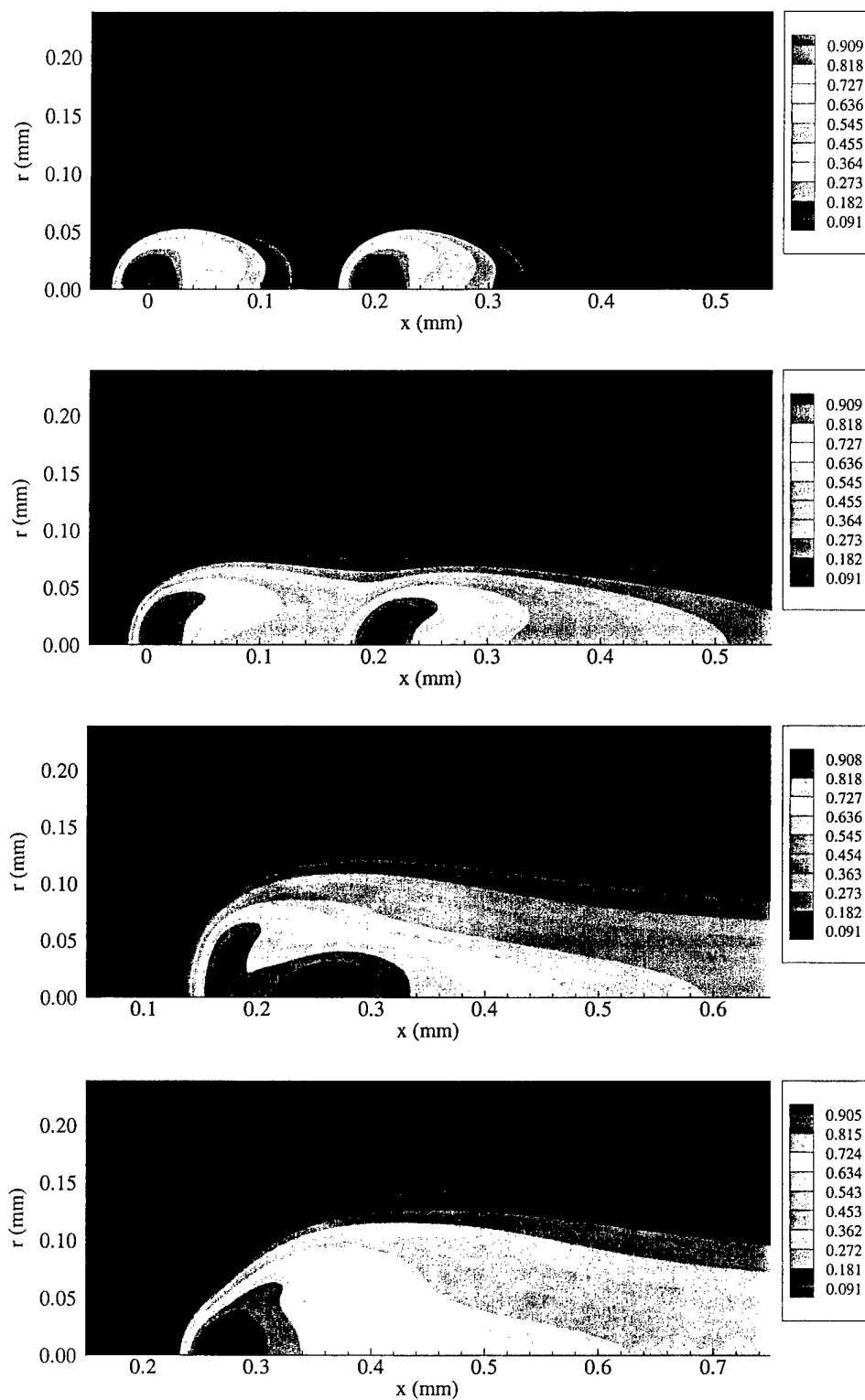


Fig. 6.7. Transient variations of oxygen mass fraction fields at $p=100$ atm, $u=10$ m/s, and H/R ratio of 8 ($t=15, 60, 190$, and $225 \mu s$, respectively).

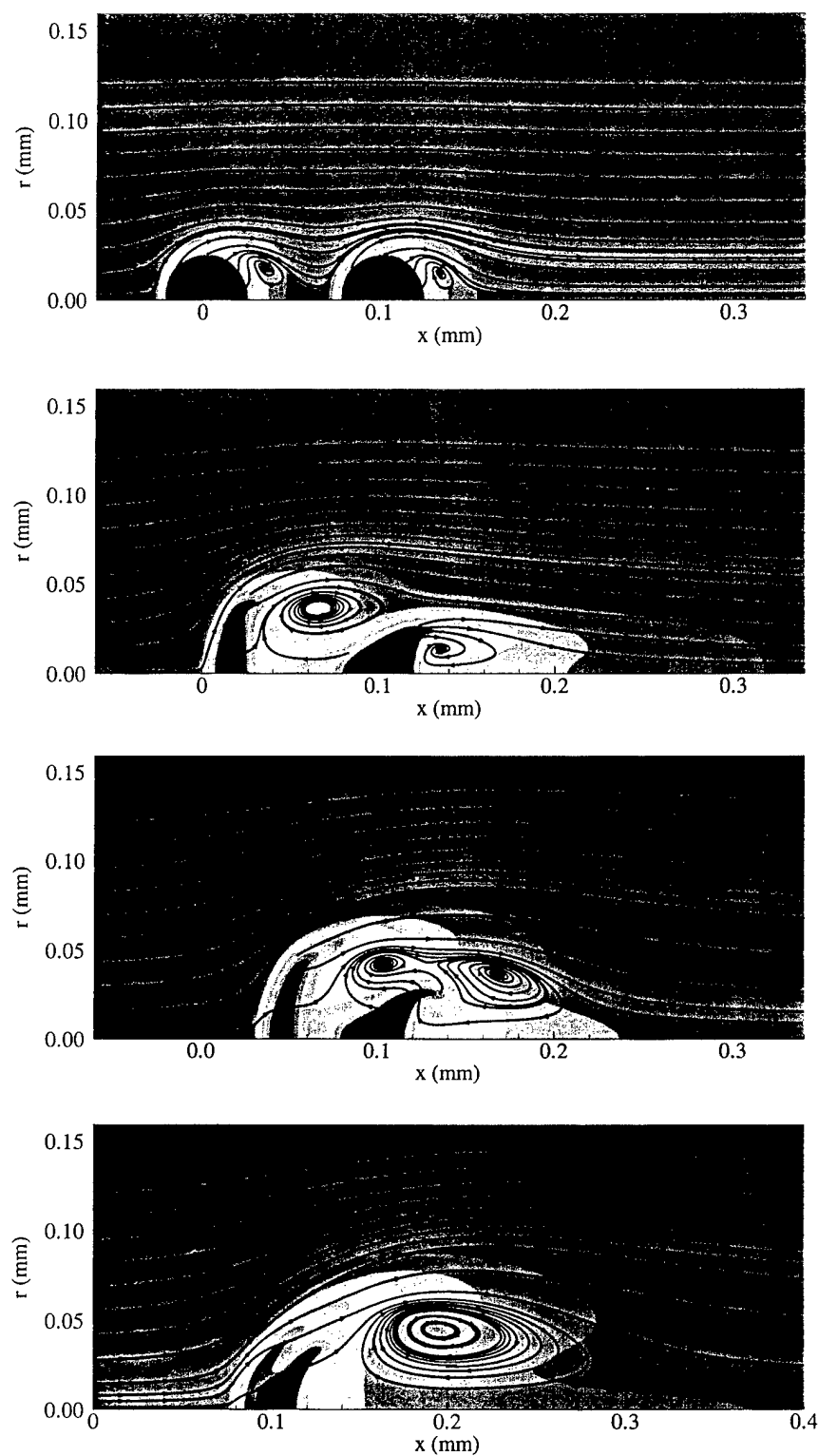


Fig. 6.8. Transient variations of flow fields at $p=100$ atm, $u=20$ m/s, and H/R ratio of 4 ($t=5, 40, 65, 85$ μ s, respectively).

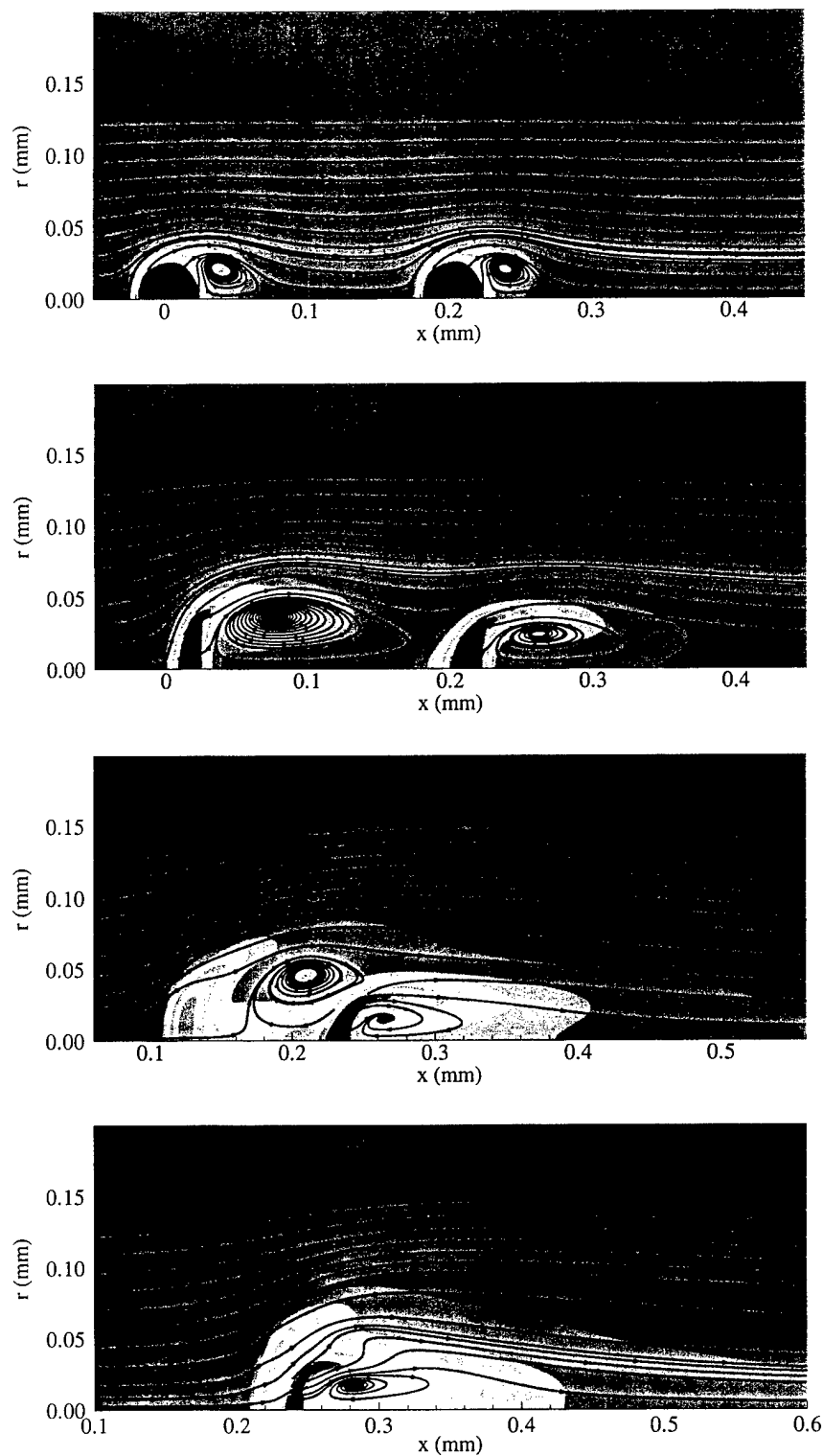


Fig. 6.9. Transient variations of flow fields at $p=100$ atm, $u=20$ m/s, and H/R ratio of 8 ($t=8, 40, 90, 110$ μ s, respectively).

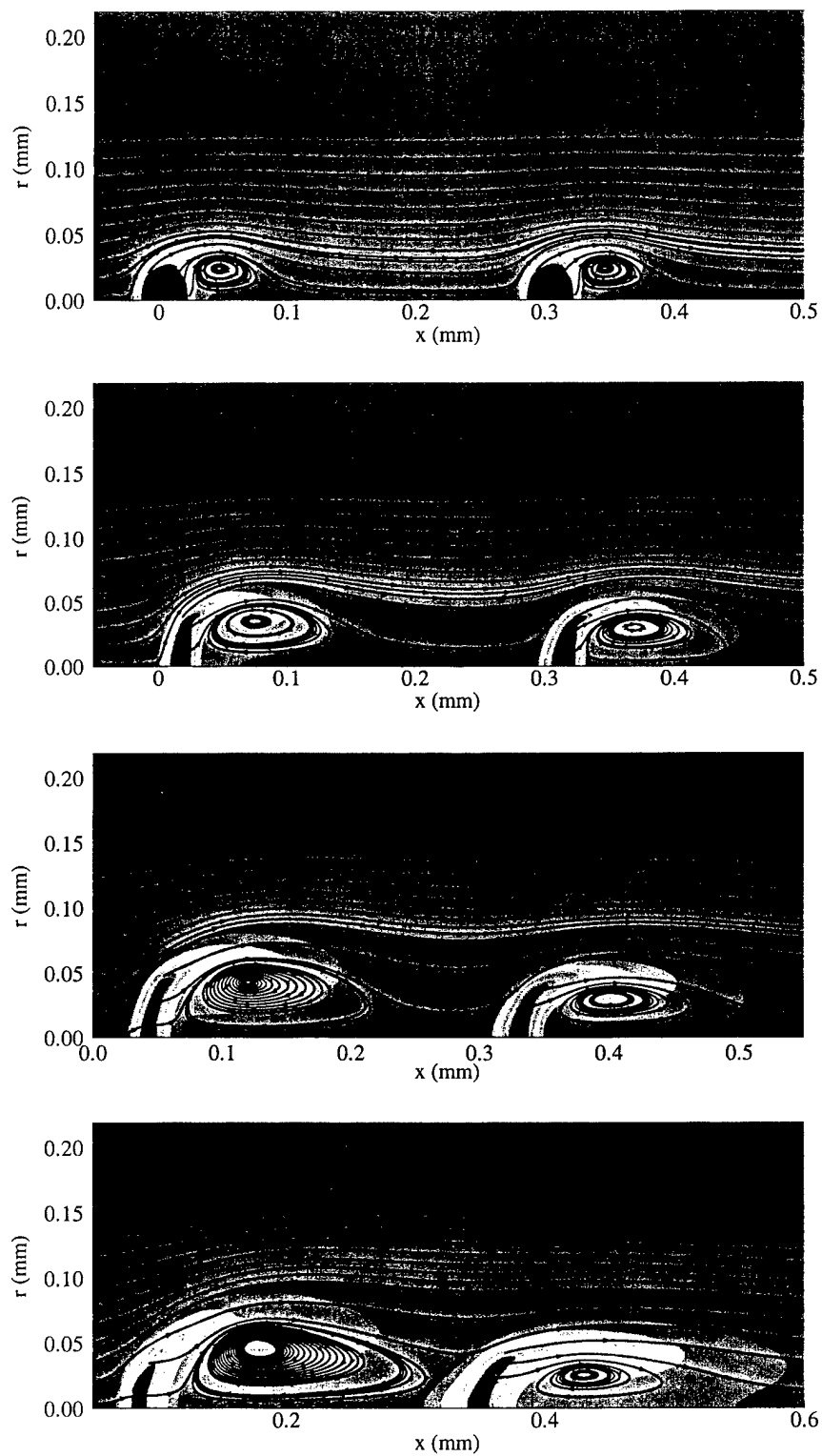


Fig. 6.10. Transient variations of flow fields at $p=100$ atm, $u=20\text{m/s}$, and H/R ratio of 12 ($t=15, 40, 60, 80 \mu\text{s}$, respectively).

Chapter 7

CONCLUSIONS AND RECOMMENDATIONS

A systematic numerical investigation of supercritical droplet vaporization and droplet interactions has been conducted based on the transient conservation equations of mass, momentum, energy, and species. A unified treatment of real fluid behavior was developed, which is capable of treating fluid states over the entire thermodynamic regime, ranging from dense liquid to dilute gas. Fundamental thermodynamic theories were applied for the derivations of thermodynamic relationships, which naturally take pressure effects and thermodynamic non-ideality into account. A preconditioning scheme with the dual time-stepping integration technique was further used to make the numerical algorithm capable of solving small Mach-number fluid flows. In the current research work, a modified Soave-Redlich-Kwong (SRK) equation of state was utilized for evaluating all the thermodynamic correlations, which was then incorporated into the numerical scheme to enhance its efficiency and robustness. The state-of-the-art techniques were employed to estimate the transport properties, and full account was taken for the effect of transport anomaly at the transcritical region. The extended corresponding states one-fluid model combined with the Benedict-Webb-Rubin (BWR) equation of state was implemented to predict the viscosity and thermal conductivity of the mixtures, while the pressure effect on binary mass diffusivity was corrected by the Takahashi method.

A linear correlation relating mass vaporization rate with the difference of chemical potentials in both liquid and gaseous phases, which is based on Onsager's irreversible thermodynamic theory, was incorporated into the unified preconditioning

numerical algorithm to study droplet vaporization in a quiescent environment in Chapter 3. The oxygen-hydrogen system was examined under both sub- and super-critical conditions. Droplet cluster behavior in the inner region of a droplet cluster was explored by assuming an isolated and impermeable bubble surrounding each droplet. Studies were focused on the pressure and temperature effects on droplet interactions. Results demonstrate that pressure has a strong effect on droplet interactions, but the temperature effect is minor, especially at high pressures. With the increase of pressure, the effect of droplet interactions on droplet lifetime decreases. The effects of pressures and temperatures on hydrogen density play a decisive role in determining droplet interactions by ultimately influencing the temperature and mass fraction gradients at the droplet surface. At the later stage of the vaporization process, the lower gradient of oxygen mass fraction at the droplet surface causes more oxygen accumulation, which results in lower thermal conductivity of the mixture and consequently slower heat transfer rate into the liquid droplet. This factor dominates at the later stage of the droplet vaporization process.

An oxygen droplet vaporization in forced-convection hydrogen environments was studied in Chapter 5, where the droplet was assumed to reach the critical mixing state immediately after being injected into the combustion chamber. The effects of the Reynolds number and pressure on droplet deformations, flow field developments, droplet lifetimes, and droplet dynamics were thoroughly examined. A dimensionless parameter, $We^{1/2}/Oh$, which represents the ratio of aerodynamic and viscous forces, was found to be the major factor determining the droplet deformations under supercritical conditions. Both Reynolds number and pressure perform their effects by changing this parameter,

$$We^{1/2}/Oh = Re \frac{\mu_s}{\mu_d} \sqrt{\frac{\rho_d}{\rho_s}} \quad (7.1)$$

At a given pressure, a droplet evaporates more rapidly at a higher Reynolds number, while the droplet lifetime is significantly shortened at a lower pressure and a given Reynolds number. A relationship was established to accurately calculate droplet lifetimes,

$$\frac{t}{t_0} = \frac{1}{1 + 0.1549 Re^{1.26} p_R^{-1.58}} \quad (15 < Re < 240, 2 < p_R < 8) \quad (7.2)$$

A linear relationship was reasonably assumed for droplet velocity, and the linear velocity coefficient b was found to be proportional to $Re^{1.76} p_R^{-1.164}$. Droplet positions calculated from this linear relationship agree well with those directly from numerical computations.

$$b = 12 Re^{1.76} p_R^{-1.164} \quad (15 < Re < 240, 2 < p_R < 8) \quad (7.3)$$

The drag coefficient in the supercritical vaporization case always decreases with time ($\sim \left(\frac{m}{m_0}\right)^{1/3}$) as a result of the weak Reynolds number reduction. At a given Reynolds number, the drag coefficient decreases slightly with the increase of pressure.

Droplet interactions in convective environments were examined in Chapter 6, where studies were focused on two droplets moving in tandem. The goal is to identify the influences from the immediate neighboring droplet on droplet deformations, lifetimes, and trajectories. Deformations of the two droplets display distinct characteristics. The leading droplet confronting strong incoming flow expands perpendicular to the flow direction, while the trailing droplet deforms mainly along the flow direction. Based on

the definition of the droplet surface at an isothermal line of oxygen critical temperature (154.6K), there is no droplet collision observed for all the cases studied herein. However, a forward bag break-up of the leading droplet was found when the two droplets were initially positioned closely at a H/R ratio of 4 and a pressure of 100 atm. According to mass fraction fields, droplet collisions do happen at two initial H/R ratios of 4 and 8. The existence of the trailing droplet produces only slight effects on the lifetimes and trajectories of the leading droplets, while the lifetimes of the trailing droplet are strongly elongated. Forward movement was observed for the trailing droplet at a H/R ratio of 4 and a pressure of 100atm. Increase in pressure weakens droplet interactions, and this conclusion was consistently verified in the studies of temperature fields, flow fields, droplet lifetimes, and droplet trajectories.

Results in this research work enhance the fundamental physical understanding of droplet vaporization and cluster behavior at both sub- and super-critical conditions. The correlations regarding droplet lifetimes and droplet dynamics can be applied directly into the spray combustion modeling.

In the current research work, combustion phenomenon was not included due to computational time. In the future studies, the numerical code is expected to be parallelized to take advantage of the most advanced computational technique, which renders detailed studies of combustion and flame around droplets feasible.

With the increased computational efficiency, this computational algorithm can be further extended for three-dimensional calculations. Droplet interactions with two droplets moving side by side can be studied in detail to complement our basic understanding of this most common droplet interacting phenomenon. In addition, the

computational algorithm can also be used to study three-dimensional supercritical spray and mixing layer, which display features distinct from the low-pressure counterparts based on the current limited experimental results.

The greatest challenge is to study hydrocarbon fuel droplet vaporization in supercritical convective environments, since the droplet is expected to spend sufficiently long time in subcritical regions. Here a high-pressure phase-changing problem with strong surface deformation and possible droplet break-up has to be treated. The internal phase-changing boundary conditions are too complicated for the current surface tracking numerical schemes to handle, as presented in Chapter 2. The success in this area will depend mainly on the future researches on phase-changing physics and the development of the simple and reliable phase-changing correlations.

REFERENCES

- Annamalai, K., and Ryan, W. (1992), Interactive Processes in Gasification and Combustion. Part I: Liquid Drop Arrays and Clouds, *Progress in Energy and Combustion Science*, 18, 221-295.
- Bellan, J. (2000), Supercritical (and Subcritical) Fluid Behavior and Modeling: Drops, Streams, Shear and Mixing Layers, Jets, and Spray, *Progress in Energy and Combustion Science*, 26, 329-366.
- Bellan, J., and Cuffel, R. (1983), A Theory of Nondilute Spray Evaporation Based upon Multiple Drop Interactions, *Combustion and Flame*, 51, 55-67.
- Bellan, J., and Harstad, K. (1987), The Details of the Convective Evaporation of Dense and Dilute Clusters of Drops, *International Journal of Heat and Mass Transfer*, 30(6), 1083-1093.
- Bird, R. B., Stewart, W. E., and Lightfoot, E. N. (1960), *Transport Phenomena*, John Wiley & Sons, Inc., New York-London.
- Briley, W. R., and McDonald, H. (1977), Solution of the Multidimensional Compressible Navier-Stokes Equations by a Generalized Implicit Method, *Journal of Computational Physics*, 24, 372-397.
- Brzustowski, T. A. (1965), Chemical and Physical Limits on Vapor-Phase Diffusion Flames of Drops, *Canadian Journal of Chemical Engineering*, 43, 30-36.
- Buelow, P. E. O. (1995), *Convergence Enhancement of Euler and Navier-Stokes Algorithms*, Ph.D. Dissertation, The Pennsylvania State University, Pennsylvania.
- Callen, H. B. (1985), *Thermodynamics and An Introduction to Thermostatistics*, 2nd Edition, John Wiley & Sons, New York.
- Chervinski, A. (1969), Supercritical Burning of Liquid Droplets in Stagnant Environment, *AIAA Journal*, 7(9), 1815-1817.
- Chiang, C. H. (1990), *Isolated and Interacting, Vaporizing Fuel Droplets: Field Calculation with Variable Properties*, Ph.D. Dissertation, University of California, Irvine, California.
- Chiang, C. H., Raju, M. S., Sirignano, W. A. (1992), Numerical Analysis of Convecting, Vaporizing Fuel Droplet with Variable Properties, *International Journal of Heat and Mass Transfer*, 35(5), 1307-1324.

- Choi, Y. H., and Merkle, C. L. (1993), The Application of Preconditioning in Viscous Flows, *Journal of Computational Physics*, 105, 207-223.
- Curtis, E. W., and Farrel, P. V. (1992), A Numerical Study of High-Pressure Droplet Vaporization, *Combustion and Flame*, 90, 85-102.
- Dandy, D. S., and Leal, L. G. (1986), Boundary-Layer Separation from a Smooth Slip Surface, *Physics Fluids*, 29(5), 1360-1366.
- Daou, J., and Rogg, B. (1998), Convective Burning of Gaseous Fuel Pockets and Supercritical Droplets, *Combustion and Flame*, 115, 145-157.
- Delplanque, J. P., and Sirignano, W. A. (1993), Numerical Study of the Transient Vaporization of an Oxygen Droplet at Sub- and Super-Critical Conditions, *International Journal of Heat and Mass Transfer*, 36(2), 303-314.
- Deng, Z. T., and Jeng, S. (1992), Numerical Simulation of Droplet Deformation in Convective Flows, *AIAA Journal*, 30(5), 1290-1297.
- Deng, Z. T., Litchford, R., Jeng, S., and Jeng, S. M. (1992), Two Dimensional Simulations of Droplet Evaporation and Deformation at High Pressure, *AIAA /SAE/ASME/ASEE, 28th Joint Propulsion Conference and Exhibit*, Nashville, TN, AIAA 92-3122.
- Douglas, J., Gunn, J. E. (1964), A General Formulation of Alternating Direction Method, Part I. Parabolic and Hyperbolic Problems, *Numerische Mathematik*, 6, 428-453.
- Ely, J. F., Hanley, H. J. (1981), Prediction of Transport Properties. 1. Viscosity of Fluids and Mixtures, *Industrial and Engineering Chemistry Fundamentals*, 20, 323-332.
- Ely, J. F., Hanley, H. J. (1983), Prediction of Transport Properties. 2. Thermal Conductivity of Pure Fluids and Mixtures, *Industrial and Engineering Chemistry Fundamentals*, 22, 90-97.
- Faeth, G. M., Dominics, D. P., Tulpinsky, J. F., and Olson, D. R. (1969), Supercritical Bipropellant Droplet Combustion, *Twelfth Symposium (International) on Combustion*, The Combustion Institute, 9-18.
- Godsave, G. A. E. (1953), Studies of the Combustion of Drops in a Fuel Spray: The Burning of Single Drops of Fuel, *Fourth Symposium (International) on Combustion*, The Combustion Institute, 818-830.
- Graboski, M. S., Daubert, T. E. (1978), A Modified Soave Equation of State for Phase Equilibrium Calculation, 1. Hydrocarbon Systems, *Industrial and Engineering Chemistry Process Design and Development*, 17(4), 443-448.

- Graboski, M. S., Daubert, T. E. (1978), A Modified Soave Equation of State for Phase Equilibrium Calculation, 2. Systems Containing CO₂, H₂S, N₂, and CO, *Industrial and Engineering Chemistry Process Design and Development*, 17(4), 448-454.
- Graboski, M. S., and Daubert, T. E. (1979), A Modified Soave Equation of State for Phase Equilibrium Calculations, 3. Systems Containing Hydrogen, *Industrial and Engineering Chemistry Process Design and Development*, 18(2), 300-305.
- Haldenwang, P., Nicoli, C., and Daou, J. (1996), High Pressure Vaporization of LOX Droplet Crossing the Critical Conditions, *International Journal of Heat and Mass Transfer*, 39(16), 3453-3464.
- Harlow, F. H., Welch, J. E. (1965), Numerical Calculation of Time-Dependent Viscous Incompressible Flow of Fluid with Free Surface, *Physics Fluids*, 8, 2182-2189.
- Harstad, K., and Bellan, J. (1998), Interactions of Fluid Oxygen Drops in Fluid Hydrogen at Rocket Chamber Pressures, *International Journal of Heat and Mass Transfer*, 41, 3551-3558.
- Harstad, K., and Bellan, J. (1998), Isolated Fluid Oxygen Drop Behavior in Fluid Hydrogen at Rocket Chamber Pressures, *International Journal of Heat and Mass Transfer*, 41, 3537-3550.
- Harstad, K., and Bellan, J. (1999), A Validated All-Pressure Fluid Drop Model & Lewis Number Effects for a Binary Mixture, *35th AIAA/ASME/SAE/ASEE Joint Propulsion Conference and Exhibit*, June 20-24, Los Angeles, California.
- Haywood, R. J., Nafziger, R., and Renksizbulut, M. (1989), A Detailed Examination of Gas and Liquid Phase Transient Processes in Convective Droplet Evaporation, *Journal of Heat Transfer*, 111, 495-502.
- Hinze, J. O. (1955) Fundamentals of the Hydrodynamic Mechanism of Splitting in Dispersion Processes, *A.I.Ch.E. Journal*, 1(3), 289-295.
- Hirt, C. W., Amsden, A. A., and Cook, J. L. (1974), An Arbitrary Lagrangian-Eulerian Computing Method for All Flow Speeds, *Journal of Computational Physics*, 14, 227-253.
- Hirt, C. W., Nichols, B. D. (1981), Volume of Fluid (VOF) Method for the Dynamics of Free Boundaries, *Journal of Computational Physics*, 39, 201-225.
- Hsiang, L. P., and Faeth, G. M. (1992), Near-Limit Drop Deformation and Secondary Breakup, *International Journal of Multiphase Flow*, 18(5), 635-652.
- Hsiao, G. C., Yang, V., and Shuen, J. S. (1995), Supercritical Vaporization and Dynamics of Liquid Oxygen (LOX) Droplet in Hydrogen Stream, *33rd Aerospace Sciences Meeting and Exhibit*, Jan. 9-12, Reno, NV.

Hsieh, K. C., Shuen, J. S., and Yang, V. (1991), Droplet Vaporization in High-Pressure Environments I: Near Critical Conditions, *Combustion Science and Technology*, 76, 111-132.

Hsieh, S. Y., and Yang, V. (1997), A Preconditioning Flux-Difference Scheme for Chemically Reacting Flows at All Mach Numbers, *International Journal of Computational Fluid Dynamics*, 8, 31-49.

Jacobsen, R. T., and Stewart, R. B. (1973), Thermodynamic Properties of Nitrogen including Liquid and Vapor Phase from 63K to 2000K with Pressure to 10,000bar, *Journal of Physical and Chemical Reference Data*, 2(4), 757-922.

Jia, H., and Gogos, G. (1993), High Pressure Droplet Vaporization; Effects of Liquid-Phase Gas Solubility, *International Journal of Heat and Mass Transfer*, 36, 4419-4431.

Jiang, T. L., and Chiang, W. T. (1994), Effects of Multiple Droplet Interaction on Droplet Vaporization in Subcritical and Supercritical Pressure Environments, *Combustion and Flame*, 97, 17-34.

Jiang, T. L., and Chiang, W. T. (1996), Transient Heating and Vaporization of a Cool Dense Cloud of Droplets in Hot Supercritical Surroundings, *International Journal of Heat and Mass Transfer*, 39(5), 1023-1031.

Jin, J. D., and Borman, G. L. (1985), A Model for Multicomponent Droplet Vaporization at High Ambient Pressures, *SAE Paper 850264*.

Johnson, T. A., and Patel, V. C. (1999) Flow past a Sphere up to a Reynolds number of 300, *Journal of Fluid Mechanics*, 378, 19-70.

Jorgenson, P., and Turkel, E. (1993) Central Difference TVD Schemes for Time Dependent and Steady State problems, *Journal of Computational Physics*, 107, 297-308.

Kadota, T., and Hiroyasu, H. (1976), Evaporation of a Single Droplet at Elevated Pressures and Temperatures, *Bulletin of the JSME*, 19(138), 1515-1521.

Kaltz, T. L., Long, L. N., Micci, M. M., and Little, J. K. (1998), Supercritical Vaporization of Liquid Oxygen Droplets using Molecular Dynamics, *Combustion Science and Technology*, 163(1-6), 279-301

Keizer, J. (1987), *Statistical Thermodynamics of Nonequilibrium Processes*, Springer-Verlag, New York.

Lafon, P. (1995), *Modélisation et Simulation Numérique de L'Evaporation et de la Combustion de Gouttes à Haute Pression*, Ph.D Thesis, à L'Université D'Orléans.

- Lafon, P., Yang, V., and Habiballah, M. (1995), Pressure-Coupled Vaporization and Combustion Responses of Liquid Oxygen (LOX) Droplets in Supercritical Hydrogen Environments, *AIAA Paper 95-2432*
- Leal, L. G. (1989), Vorticity Transport and Wake Structure for Bluff Bodies at Finite Reynolds Number, *Physics Fluids A*, 1(1), 124-131.
- Lee, H. S., Fernandez-Pello, A. C., Corcos, G. M., and Oppenheim, A. K. (1990), A Mixing and Deformation Mechanism for a Supercritical Fuel Droplet, *Combustion and Flame*, 81, 50-58.
- Litchford, R. J., and Jeng, S. M. (1990), Lox Vaporization in High-Pressure, Hydrogen-Rich Gas, *AIAA/SAE/ASME/ASEE Twenty-sixth Joint Propulsion Conference*, Orlando, FL, AIAA 90-2191.
- Manrique, J. A., and Borman, G. L. (1969), Calculations of Steady State Droplet Vaporization at High Ambient Pressures, *International Journal of Heat and Mass Transfer*, 12, 1081-1095.
- Matlosz, R. L., Leipziger, S., and Torda, T. P. (1972), Investigation of Liquid Droplet Evaporation in a High Temperature and High Pressure Environment, *International Journal of Heat and Mass Transfer*, 15, 831-852.
- McCreath, C. G., and Chigier, N. A. (1973), Liquid Spray Burning in a Wake of a Stabilizer Disc, *Fourteenth Symposium (International) on Combustion*, The Combustion Institute, 1355-1363.
- Morin, C. (1999), *Studies on the Influence of Pressure and Temperature on the Vaporization of Hydrocarbon Droplets*, Ph.D. Thesis, Centre National de la Recherche Scientifique, Orléans, France.
- Nakamura, I. (1976), Steady Wake behind a Sphere, *The Physics of Fluids*, 19(1), 5-8.
- Nomura, H., Ujiie, Y., Rath, H. J., Sato, J., and Kono, M. (1996), Experimental Study on High Pressure Droplet Evaporation using Microgravity Conditions, *Twenty-sixth Symposium (International) on Combustion*, The Combustion Institute, 1267-1273.
- Patnaik, G. (1986), *A Numerical Solution of Droplet Vaporization with Convection*, Ph.D. Dissertation, Carnegie Mellon University, Pittsburgh, Pennsylvania.
- Pilch, M., and Erdman, C. A. (1987) Use of Breakup Time Data and Velocity History Data to Predict the Maximum Size of Stable Fragments for Acceleration-Induced Breakup of a Liquid Drop, *International Journal of Multiphase Flow*, 13(6), 741-757.
- Polymeropoulos, C. E., and Peskin, R. L. (1972), Combustion of Fuel Vapor in a Hot Stagnant Oxidizing Environment, *Combustion Science and Technology*, 5, 165-174.

Poettmann, F. H., and Katz, D. L. (1945), Phase Behavior of Binary Carbon Dioxide-Paraffin Systems, *Industrial and Engineering Chemistry*, 37(9), 847-850.

Raju, M. S., and Sirignano, W. S. (1990), Interaction between two Vaporizing Droplets in an Intermediate Reynolds Number Flow, *Physics of Fluids A*, 2(10), 1780-1796.

Ranger, A. A., and Nicholls, J. A. (1969) Aerodynamic Shattering of Liquid Drops, *AIAA Journal*, 7(2), 285-290.

Reid, R. C., Prausnitz, J. M., and Poling, B. E. (1987), *The Properties of Gases & Liquids*, Fourth Edition, McGraw-Hill Book Company.

Rosner, D. E. (1967), On Liquid Droplet Combustion at High Pressures, *AIAA Journal*, 5(1), 163-166.

Rosner, D. E., and Chang, W. S. (1973), Transient Evaporation and Combustion of a Fuel Droplet Near Its Critical temperature, *Combustion Science and Technology*, 7, 145-158.

Sanchez-Tarifa, C., Crespo, A., and Fraga, E. (1972), A Theoretical Model for the Combustion of Droplets in Supercritical Conditions and Gas Pockets, *Astron. Acta*, 17, 685-692.

Sato, J. (1993), Studies on Droplet Evaporation and Combustion in High Pressures, *31st Aerospace Sciences Meeting*, Jan. 11-14, Reno, NV, AIAA 93-0813.

Sato, J., Tsue, M., Niwa, M., and Kono, M. (1990), Effects of Natural Convection on High-Pressure Droplet Combustion, *Combustion and Flame*, 82, 142-150.

Schneider, G. E., and Zedan, M. (1981), A Modified Strongly Implicit Procedure for the Numerical Solution of Field Problems, *Numerical Heat Transfer*, 4(1), 1-19.

Shuen, J. S., Chen, K. H., and Choi, Y. (1993), A Coupled Implicit Method for Chemical Non-Equilibrium Flows at All Speeds, *Journal of Computational Physics*, 106, 306-318.

Shuen, J. S., Yang, V., and Hsiao, C. C. (1992), Combustion of Liquid-Fuel Droplet in Supercritical Conditions, *Combustion and Flame*, 89, 299-319.

Sirignano, W. A., and delplanque, J. P. (1999), Transcritical Vaporization of Liquid Fuels and Propellants, *Journal of Propulsion and Power*, 15(6), 896-902.

Spalding, D. B. (1959), Theory of Particle Combustion at High Pressures, *ARS Journal*, 29, 828-835.

Stiel, L. E., and Thodos, G. (1964), The Thermal Conductivity of Nonpolar Substances in the Dense Gaseous and Liquid Regions, *AIChE Journal*, 10, 26-30.

Sussman, M., Smereka, P., and Osher, S. (1994), A Level Set Approach for Computing Solutions to Incompressible Two-Phase Flow, *Journal of Computational Physics*, 114, 146-159.

Swanson, R. C., and Turkel, E. (1992), On Central-Difference and Upwind Schemes, *Journal of Computational Physics*, 101, 292-306.

Takahashi, S. (1974), Preparation of a Generalized Chart for the Diffusion Coefficients of Gases at High Pressures, *Journal of Chemical Engineering (Japan)*, 7(6), 417-420.

Tishkoff, J. M. (1979), A Model for the Effect of Droplet Interactions on Vaporization, *International Journal of Heat and Mass Transfer*, 22, 1407-1415

Tryggvason, G., Unverdi, S. O. (1990), Computation of Three-Dimensional Rayleigh-Taylor Instability, *Physics Fluids A*, 2(5), 656-659

Udaykumar, H. S. (1994), *A Mixed Eulerian-Lagrangian Approach for the Simulation of Interfacial Phenomena in Solidification Processing*, Ph.D. Dissertation, University of Florida, Gainesville, Florida.

Umemura, A. (1986), Supercritical Liquid Fuel Combustion, *Twenty-first Symposium (International) on Combustion*, The Combustion Institute, 463-471.

Umemura, A., and shimada, Y. (1996), Characteristics of Supercritical Droplet Gasification, *Twenty-sixth Symposium (International) on Combustion*, The combustion Institute, 1621-1628.

Unverdi, S. O., Tryggvason, G. (1992), A Front-Tracking Method for Viscous, Incompressible, Multi-Fluid Flows, *Journal of Computational Physics*, 100, 25-37.

Vielle, B., Chauveau, C., and Chesneau, X., Odeide, A., and Gökalp, I. (1996), High Pressure Droplet Burning Experiments in Microgravity, *Twenty-sixth Symposium (international) on Combustion*, The Combustion Institute, 1259-1265.

Voller, V. R., Prakash, C. (1987), A Fixed Grid Numerical Modelling Methodology for Convection-Diffusion Mushy Region Phase-Change Problems, *International Journal of Heat and Mass Transfer*, 30(8), 1709-1719.

Welch, S. W. J. (1993), *Local Two-Phase Flow Simulations Including Interface Tracking with Mass Transfer*, Ph.D. Dissertation, University of Colorado, Boulder, Colorado.

Welch, S. W. J. (1995), Local Simulation of Two-Phase Flows Including Interface Tracking with Mass Transfer, *Journal of Computational Physics*, 121, 142-154.

Wieber, P. R. (1963), Calculated Temperature History of Vaporizing Droplets to the Critical Point, *AIAA Journal*, 1(12), 2764-2770.

Wierzba, A., and Takayama, K. (1988), Experimental Investigation of the Aerodynamic Breakup of Liquid Drops, *AIAA Journal*, 26(11), 1329-1335.

Yang, V. (2000), Modeling of Supercritical Vaporization, Mixing, and Combustion processes in Liquid-Fueled Propulsion Systems, *Proceeding of Combustion Institute*, Vol. 28

Yang, V., Lin, N. N., and Shuen, J. S. (1994), Vaporization of Liquid Oxygen (LOX) Droplets in Supercritical Hydrogen Environments, *Combustion Science and Technology*, 97, 247-270.

Yuen, M. C., and Chen, L. W. (1976), On Drag of Evaporating Liquid Droplets, *Combustion Science and Technology*, 14, 147-154.

Zung, J. T. (1967), Evaporation Rate and Lifetimes of Clouds and Sprays in Air-The Cellular Model, *Journal of Chemical Physics*, 46, 2064-2070.

Appendix A

THERMODYNAMIC RELATIONSHIPS

Based on the Soave-Redlich-Kwong equation of state, the following derivative expressions, which are used extensively in the following thermodynamic relationships, can be directly derived as

$$\left(\frac{\partial p}{\partial T}\right)_{\rho_j} = \frac{\rho R_u}{(M_w - b\rho)} - \frac{1}{M_w} \left[\frac{\partial}{\partial T} (a\alpha) \right]_{\rho, Y_j} \frac{\rho^2}{(M_w + b\rho)} \quad (\text{A1})$$

$$\left(\frac{\partial p}{\partial \rho}\right)_{T, Y_j} = \frac{M_w R_u T}{(M_w - b\rho)^2} - \frac{a\alpha}{M_w} \frac{\rho(2M_w + b\rho)}{(M_w + b\rho)^2} \quad (\text{A2})$$

$$\begin{aligned} \left(\frac{\partial p}{\partial \rho_i}\right)_{T, \rho_{j \neq i}} &= \frac{M_w R_u T}{M_{wi} (M_w - b\rho)^2} [M_w + \rho(b_i - b)] \\ &\quad - \frac{2\rho \sum_j x_j a_{ij} \alpha_{ij}}{M_{wi} (M_w + b\rho)} + \frac{a\alpha \rho^2 b_i}{M_{wi} (M_w + b\rho)^2} \end{aligned} \quad (\text{A3})$$

where the indexes $i, j = 1 \cdots N$, and the derivative $\frac{\partial}{\partial T} (a\alpha)$ is given in Appendix B.

It should be noted that, according to thermodynamics, these derivatives could be derived based on any equation of state.

The partial density internal energy of species i \tilde{e}_i will then be derived. We first need to find the expression for the internal energy e . From the fundamental thermodynamic theory, we have

$$e(T, \rho) = e_0(T) + \int_0^\rho \left[\frac{P}{\rho^2} - \frac{T}{\rho^2} \left(\frac{\partial p}{\partial T} \right)_\rho \right] d\rho \quad (\text{A4})$$

where the subscript 0 indicates a reference ideal state at a low pressure.

Utilizing SRK equation of state and the partial derivative relation (A1), Eq. (A4) is integrated, which leads to the following relationship:

$$e(T, \rho) = e_0(T) + \frac{T^2}{bM_w} \left(\frac{\partial a\alpha/T}{\partial T} \right)_{\rho, Y_j} \ln \left(1 + \frac{b\rho}{M_w} \right) \quad (\text{A5})$$

where the partial derivative $\frac{\partial a\alpha/T}{\partial T}$ is also presented in Appendix B.

According to the definition for the partial density property, the partial density internal energy \tilde{e}_i can be expressed as

$$\begin{aligned} \tilde{e}_i = e_{i,0} + \frac{2}{bM_{wi}} \left[\sum_j x_j \left(T \frac{\partial}{\partial T} (a_{ij}\alpha_{ij}) - a_{ij}\alpha_{ij} \right) \right] \ln \left(1 + \frac{b\rho}{M_w} \right) \\ + \frac{b_i}{bM_{wi}} \left[T \frac{\partial}{\partial T} (a\alpha) - a\alpha \right] \left[\frac{\rho}{M_w + b\rho} - \frac{1}{b} \ln \left(1 + \frac{b\rho}{M_w} \right) \right] \end{aligned} \quad (\text{A6})$$

In Addition, utilizing Eq. (A6), the internal energy of a mixture can be related to the partial density internal energy as

$$e = \sum_i Y_i \tilde{e}_i - \frac{1}{M_w} \left[T \frac{\partial}{\partial T} (a\alpha) - a\alpha \right] \frac{\rho}{M_w + b\rho} \quad (\text{A7})$$

Based on thermodynamics,

$$\rho h = \rho e + p \quad (\text{A8})$$

Following the definition for the partial density property, the following expression can be found by taking derivative of the partial density of species i to both sides of the Eq. (A8), and keeping temperature and all the other partial densities constant:

$$\left(\frac{\partial \rho h}{\partial \rho_i} \right)_{T, \rho_{j \neq i}} = \left(\frac{\partial \rho e}{\partial \rho_i} \right)_{T, \rho_{j \neq i}} + \left(\frac{\partial p}{\partial \rho_i} \right)_{T, \rho_{j \neq i}} \quad (\text{A9a})$$

It is recognized that Eq. (A9a) is equivalent to

$$\tilde{h}_i = \tilde{e}_i + \left(\frac{\partial p}{\partial \rho_i} \right)_{T, \rho_{j \neq i}} \quad (\text{A9b})$$

The following thermodynamic expression exists, which relates a partial density property to a partial mass property:

$$\tilde{\phi}_i = \bar{\phi}_i + \rho \left(\frac{\partial \phi}{\partial p} \right)_{T, Y_j} \left(\frac{\partial p}{\partial \rho_i} \right)_{T, \rho_{j \neq i}} \quad (\text{A9c})$$

where the parameter ϕ refers to any proper intensive thermodynamic property, such as enthalpy, and internal energy.

Substituting Eq. (A9c) into Eq. (A9b), and taking use of the fundamental enthalpy expression, which can be found in any thermodynamics textbook, the following relation concerning the partial mass enthalpy \bar{h}_i can be further derived:

$$\bar{h}_i = \tilde{e}_i + \frac{T \left(\frac{\partial p}{\partial T} \right)_{\rho_j}}{\rho \left(\frac{\partial p}{\partial \rho} \right)_{T, Y_j}} \left(\frac{\partial p}{\partial \rho_i} \right)_{T, \rho_{j \neq i}} \quad (\text{A10})$$

Next, we begin to derive the expressions for the constant volume and the constant pressure heat capacities based on the SRK equation of state.

The definition of constant volume heat capacity is

$$C_v = \left(\frac{\partial e}{\partial T} \right)_{\rho, Y_j} \quad (\text{A11a})$$

Utilizing Eq. (A5), it is straightforward to find

$$C_v = C_{v,0} + \frac{T}{bM_w} \frac{\partial^2}{\partial T^2} (a\alpha) \ln \left(1 + \frac{b\rho}{M_w} \right) \quad (\text{A11b})$$

where the derivative $\frac{\partial^2}{\partial T^2}(a\alpha)$ is given in Appendix B.

Following fundamental thermodynamic relationships, the constant-pressure heat capacity can be expressed as

$$C_p = C_v + \frac{T}{\rho^2} \left(\frac{\partial p}{\partial T} \right)_{\rho_j}^2 \bigg/ \left(\frac{\partial p}{\partial \rho} \right)_{T, Y_j} \quad (\text{A12})$$

In order to find the thermodynamic relationships regarding chemical potential, the partial density and partial mass entropy have to be derived first,

$$s(T, \rho) = s_0(T, \rho_0) - \int_{\rho_0}^{\rho} \left[\frac{1}{\rho^2} \left(\frac{\partial p}{\partial T} \right)_{\rho} \right] d\rho \quad (\text{A13})$$

Based on the definition of partial density entropy, it is found

$$\begin{aligned} \tilde{S}_i = & \int_{T_{ref}}^T C_{pi,0} \frac{dT}{T} - \frac{R_u}{M_{wi}} (1 + \ln x_i) - \frac{R_u}{M_{wi}} \ln \frac{\rho \frac{R_u}{M_w} T}{p_{ref}} + \frac{R_u}{M_{wi}} \ln \left(1 - \frac{b\rho}{M_w} \right) \\ & - R_u \frac{b_i}{M_{wi}} \frac{\rho}{M_w - b\rho} + \frac{b_i}{M_{wi}} \frac{1}{b^2} \frac{\partial(a\alpha)}{\partial T} \left[\frac{b\rho}{M_w + b\rho} - \ln \left(1 + \frac{b\rho}{M_w} \right) \right] \\ & + \frac{2}{bM_{wi}} \left[\sum_j x_j \frac{\partial}{\partial T} (a_{ij} \alpha_{ij}) \right] \ln \left(1 + \frac{b\rho}{M_w} \right) \end{aligned} \quad (\text{A14})$$

The partial mass entropy can be further related to the partial density entropy as

$$\bar{S}_i = \tilde{S}_i + \left(\frac{\partial p}{\partial T} \right)_{\rho, Y_i} \bar{V}_i \quad (\text{A15})$$

where the partial mass volume is

$$\bar{V}_i = \frac{1}{\rho} \left(\frac{\partial p}{\partial \rho_i} \right)_{T, \rho_{j \neq i}} \bigg/ \left(\frac{\partial p}{\partial \rho} \right)_{T, Y_j} \quad (\text{A16})$$

The chemical potential of species i can be calculated as

$$\mu_i = \tilde{f}_i = \tilde{e}_i - T\tilde{s}_i \quad (\text{A17})$$

Finally, the partial derivatives regarding chemical potential can be expressed as

$$\left(\frac{\partial \mu_i}{\partial p} \right)_{T, Y_j} = \bar{V}_i \quad (\text{A18})$$

$$\left(\frac{\partial \mu_i}{\partial T} \right)_{T, Y_j} = -\bar{S}_i \quad (\text{A19})$$

$$\begin{aligned} \left(\frac{\partial \mu_i}{\partial Y_j} \right)_{T, p, Y_k \neq j} &= \frac{b_i}{M_{wi}} \frac{b_j}{M_{wj}} \frac{a\alpha}{b^2} (M_w \rho) \left[\frac{3b\rho + 2M_w}{(M_w + b\rho)^2} \right] - \bar{V}_i \bar{V}_j \rho^2 \left(\frac{\partial p}{\partial \rho} \right)_{T, Y_j} \\ &\quad - \frac{2 \left(b_i \sum_l x_l a_{jl} \alpha_{jl} + b_j \sum_l x_l a_{il} \alpha_{il} \right)}{M_{wi} M_{wj}} \frac{M_w \rho}{b(M_w + b\rho)} \\ &\quad + \frac{2M_w \ln(1 + b\rho/M_w)}{b^2} \frac{1}{M_{wi} M_{wj}} \left[b_i \sum_l x_l a_{jl} \alpha_{jl} + b_j \sum_l x_l a_{il} \alpha_{il} - \frac{b_i b_j}{b} a\alpha - b a_{ij} \alpha_{ij} \right] \\ &\quad + R_u T M_w \frac{1}{(M_w - b\rho)^2} \frac{[M_w + \rho(b_i - b)][M_w + \rho(b_j - b)]}{M_{wi} M_{wj}} \\ &\quad + R_u T M_w \frac{1}{M_{wi} M_{wj}} \left(\frac{\delta_{ij}}{x_i} - 1 \right) \end{aligned} \quad (\text{A20})$$

Appendix B

DERIVATIVE EXPRESSIONS IN SOAVE-REDLICH-KWONG EQUATION OF STATE

In the Soave-Redlich-Kwong (SRK) equation of state, the terms $a\alpha$ and $\alpha_{ij}a_{ij}$ are functions of temperature. The derivatives of these terms to temperature are derived as

$$\frac{\partial a\alpha}{\partial T} = \sum_{i=1}^N \sum_{j=1}^N x_i x_j \sqrt{a_i a_j} \frac{\partial \sqrt{\alpha_i \alpha_j}}{\partial T} \quad (\text{B1a})$$

where

$$\frac{\partial \sqrt{\alpha_i \alpha_j}}{\partial T} = \frac{1}{2} \left(\frac{\alpha_i}{\alpha_j} \right)^{\frac{1}{2}} \frac{\partial \alpha_j}{\partial T} + \frac{1}{2} \left(\frac{\alpha_j}{\alpha_i} \right)^{\frac{1}{2}} \frac{\partial \alpha_i}{\partial T} \quad (\text{B1b})$$

$$\frac{\partial \alpha_i}{\partial T} = -\frac{S_i}{\sqrt{T T_{c,i}}} \left[1 + S_i \left(1 - \sqrt{\frac{T}{T_{c,i}}} \right) \right] \quad (\text{B1c})$$

$$\frac{\partial \alpha_{ij} a_{ij}}{\partial T} = \sqrt{a_i a_j} \frac{\partial \sqrt{\alpha_i \alpha_j}}{\partial T} \quad (\text{B2})$$

The second derivatives of parameter $a\alpha$ to temperature is

$$\frac{\partial^2 a\alpha}{\partial T^2} = \sum_{i=1}^N \sum_{j=1}^N x_i x_j \sqrt{a_i a_j} \frac{\partial^2 \sqrt{\alpha_i \alpha_j}}{\partial T^2} \quad (\text{B3a})$$

where

$$\begin{aligned}
\frac{\partial^2 \sqrt{\alpha_i \alpha_j}}{\partial T^2} = & \frac{1}{2} \left(\frac{1}{\alpha_i \alpha_j} \right)^{\frac{1}{2}} \frac{\partial \alpha_i}{\partial T} \frac{\partial \alpha_j}{\partial T} - \frac{1}{4} \left(\frac{\alpha_i}{\alpha_j^3} \right)^{\frac{1}{2}} \left(\frac{\partial \alpha_j}{\partial T} \right)^2 - \frac{1}{4} \left(\frac{\alpha_j}{\alpha_i^3} \right)^{\frac{1}{2}} \left(\frac{\partial \alpha_i}{\partial T} \right)^2 \\
& + \frac{1}{2} \left(\frac{\alpha_i}{\alpha_j} \right)^{\frac{1}{2}} \frac{\partial^2 \alpha_j}{\partial T^2} + \frac{1}{2} \left(\frac{\alpha_j}{\alpha_i} \right)^{\frac{1}{2}} \frac{\partial^2 \alpha_i}{\partial T^2}
\end{aligned} \tag{B3b}$$

$$\frac{\partial^2 \alpha_i}{\partial T^2} = \frac{1}{2} \frac{S_i^2}{T T_{c,i}} + \frac{1}{2} \frac{S_i}{\sqrt{T^3 T_{c,i}}} \left[1 + S_i \left(1 - \sqrt{\frac{T}{T_{c,i}}} \right) \right] \tag{B3c}$$

The variable α_i for species H_2, α_{H_2} , is treated differently since hydrogen is a quantum gas. The derivatives of this variable are

$$\frac{\partial \alpha_{H_2}}{\partial T} = -\alpha_{H_2} \left[0.30228 \frac{1}{T_{c,i}} \right] \tag{B4}$$

$$\frac{\partial^2 \alpha_{H_2}}{\partial T^2} = \alpha_{H_2} \left[0.30228 \frac{1}{T_{c,i}} \right]^2 \tag{B5}$$

Appendix C

NUMERICAL JACOBIANS IN PRECONDITIONING SCHEME

Jacobian T is derived as

$$\begin{bmatrix}
 -\frac{A_p}{A_\rho} & 0 & 0 & \frac{1}{A_\rho} & -\frac{A_{Y1}}{A_\rho} & \dots & -\frac{A_{Y_{N-1}}}{A_\rho} \\
 -u_x \frac{A_p}{A_\rho} & \rho & 0 & \frac{u_x}{A_\rho} & -u_x \frac{A_{Y1}}{A_\rho} & \dots & -u_x \frac{A_{Y_{N-1}}}{A_\rho} \\
 -u_r \frac{A_p}{A_\rho} & 0 & \rho & \frac{u_r}{A_\rho} & -u_r \frac{A_{Y1}}{A_\rho} & \dots & -u_r \frac{A_{Y_{N-1}}}{A_\rho} \\
 \begin{bmatrix} -h_t \frac{A_p}{A_\rho} \\ -1 \end{bmatrix} & \rho u_x & \rho u_r & \begin{bmatrix} \rho + \frac{h_t}{A_\rho} \end{bmatrix} & -h_t \frac{A_{Y1}}{A_\rho} & \dots & -h_t \frac{A_{Y_{N-1}}}{A_\rho} \\
 -Y_1 \frac{A_p}{A_\rho} & 0 & 0 & \frac{Y_1}{A_\rho} & \begin{bmatrix} -Y_1 \frac{A_{Y1}}{A_\rho} \\ +\rho \end{bmatrix} & \dots & -Y_1 \frac{A_{Y_{N-1}}}{A_\rho} \\
 \vdots & \vdots & \vdots & \vdots & \vdots & \ddots & \vdots \\
 -Y_{N-1} \frac{A_p}{A_\rho} & 0 & 0 & \frac{Y_{N-1}}{A_\rho} & -Y_{N-1} \frac{A_{Y1}}{A_\rho} & \dots & \begin{bmatrix} -Y_{N-1} \frac{A_{Y_{N-1}}}{A_\rho} \\ +\rho \end{bmatrix}
 \end{bmatrix}
 \tag{C1}$$

Jacobian B is

$$\begin{bmatrix}
 -u_r \frac{A_p}{A_\rho} & 0 & \rho & \frac{u_r}{A_\rho} & -u_r \frac{A_{Y1}}{A_\rho} & \cdots & -u_r \frac{A_{Y_{N-1}}}{A_\rho} \\
 -u_x u_r \frac{A_p}{A_\rho} & \rho u_r & \rho u_x & \frac{u_x u_r}{A_\rho} & -u_x u_r \frac{A_{Y1}}{A_\rho} & \cdots & -u_x u_r \frac{A_{Y_{N-1}}}{A_\rho} \\
 -u_r^2 \frac{A_p}{A_\rho} + 1 & 0 & 2\rho u_r & \frac{u_r^2}{A_\rho} & -u_r^2 \frac{A_{Y1}}{A_\rho} & \cdots & -u_r^2 \frac{A_{Y_{N-1}}}{A_\rho} \\
 -u_r h_t \frac{A_p}{A_\rho} & \rho u_x u_r & \begin{bmatrix} \rho u_r^2 \\ + \rho h_t \end{bmatrix} & \begin{bmatrix} \rho u_r + \\ \frac{u_r h_t}{A_\rho} \end{bmatrix} & -u_r h_t \frac{A_{Y1}}{A_\rho} & \cdots & -u_r h_t \frac{A_{Y_{N-1}}}{A_\rho} \\
 -u_r Y_1 \frac{A_p}{A_\rho} & 0 & \rho Y_1 & \frac{u_r Y_1}{A_\rho} & \begin{bmatrix} -u_r Y_1 \frac{A_{Y1}}{A_\rho} \\ + \rho u_r \end{bmatrix} & \cdots & -u_r Y_1 \frac{A_{Y_{N-1}}}{A_\rho} \\
 \vdots & \vdots & \vdots & \vdots & \vdots & \ddots & \vdots \\
 -u_r Y_{N-1} \frac{A_p}{A_\rho} & 0 & \rho Y_{N-1} & \frac{u_r Y_{N-1}}{A_\rho} & -u_r Y_{N-1} \frac{A_{Y1}}{A_\rho} & \cdots & \begin{bmatrix} -u_r Y_{N-1} \frac{A_{Y_{N-1}}}{A_\rho} \\ + \rho u_r \end{bmatrix}
 \end{bmatrix}$$

(C2)

Jacobian \hat{R}_{xx} is expressed as

$$\hat{R}_{xx} = R_{xx} \frac{\partial Q_v}{\partial \hat{Q}} = R_{xx} \cdot R \quad (C3)$$

where Jacobian R is

$$R = \begin{bmatrix}
 1 & 0 & 0 & 0 & 0 & \cdots & 0 \\
 0 & 1 & 0 & 0 & 0 & \cdots & 0 \\
 0 & 0 & 1 & 0 & 0 & \cdots & 0 \\
 -\frac{B_p}{B_T} & 0 & 0 & \frac{1}{B_T} & -\frac{B_{Y1}}{B_T} & \cdots & -\frac{B_{Y_{N-1}}}{B_T} \\
 0 & 0 & 0 & 0 & 1 & \cdots & 0 \\
 \vdots & \vdots & \vdots & \vdots & \vdots & \ddots & \vdots \\
 0 & 0 & 0 & 0 & 0 & \cdots & 1
 \end{bmatrix} \quad (C4)$$

In Jacobian D , only those terms related to axisymmetric case are given. The combustion terms can be found in Shuen et al. (1990).

$$D = D_1 - \frac{2}{3} \frac{\partial D_2}{\partial x} - \frac{2}{3} \frac{\partial D_3}{\partial r} + \frac{2}{3} \mu \frac{\partial D_4}{\partial x} \quad (C5)$$

where

$$D_1 = \begin{bmatrix} 0 & 0 & 0 & 0 & 0 & \dots & 0 \\ 0 & 0 & 0 & 0 & 0 & \dots & 0 \\ 1 & 0 & \left[-\frac{4}{3} \frac{\mu}{r} - \frac{2}{3} \frac{\partial \mu}{\partial r} \right] & 0 & 0 & \dots & 0 \\ 0 & 0 & 0 & 0 & 0 & \dots & 0 \\ 0 & 0 & 0 & 0 & 0 & \dots & 0 \\ \vdots & \vdots & \vdots & \vdots & \vdots & \ddots & \vdots \\ 0 & 0 & 0 & 0 & 0 & \dots & 0 \end{bmatrix} \quad (C6)$$

$$D_2 = \begin{bmatrix} 0 & 0 & 0 & 0 & 0 & \dots & 0 \\ 0 & 0 & \mu & 0 & 0 & \dots & 0 \\ 0 & 0 & 0 & 0 & 0 & \dots & 0 \\ 0 & \mu u_r & \mu u_x & 0 & 0 & \dots & 0 \\ 0 & 0 & 0 & 0 & 0 & \dots & 0 \\ \vdots & \vdots & \vdots & \vdots & \vdots & \ddots & \vdots \\ 0 & 0 & 0 & 0 & 0 & \dots & 0 \end{bmatrix} \quad (C7)$$

$$D_3 = \begin{bmatrix} 0 & 0 & 0 & 0 & 0 & \dots & 0 \\ 0 & 0 & 0 & 0 & 0 & \dots & 0 \\ 0 & 0 & 0 & 0 & 0 & \dots & 0 \\ 0 & 0 & 2\mu u_r & 0 & 0 & \dots & 0 \\ 0 & 0 & 0 & 0 & 0 & \dots & 0 \\ \vdots & \vdots & \vdots & \vdots & \vdots & \ddots & \vdots \\ 0 & 0 & 0 & 0 & 0 & \dots & 0 \end{bmatrix} \quad (C8)$$

and,

$$D_4 = \begin{bmatrix} 0 & 0 & 0 & 0 & 0 & \cdots & 0 \\ 0 & 0 & 0 & 0 & 0 & \cdots & 0 \\ 0 & 1 & 0 & 0 & 0 & \cdots & 0 \\ 0 & 0 & 0 & 0 & 0 & \cdots & 0 \\ 0 & 0 & 0 & 0 & 0 & \cdots & 0 \\ \vdots & \vdots & \vdots & \vdots & \vdots & \ddots & \vdots \\ 0 & 0 & 0 & 0 & 0 & \cdots & 0 \end{bmatrix} \quad (\text{C9})$$

Appendix D

NUMERICAL MODEL VALIDATION

D1. Validation of Equation of State

In this research work, the modified Soave-Redlich-Kwong (SRK) equation of state is used for calculating all the thermodynamic relationships, and the Benedict-Webb-Rubin (BWR) equation of state is used for evaluating the transport properties, including thermal conductivity and viscosity. Figure D1 presents the relative errors associated with these equations of state for calculating the density of oxygen. The results from the BWR equation of state show excellent agreement with experimental data. Since the coefficients of BWR equation of state are currently only available for several pure substances, the SRK equation of state is used for calculating thermodynamic relationships. Figure D1 indicates that the relative error associated with SRK equation of state is only about 10%, which is better than that of the Peng-Robinson (PR) equation of state.

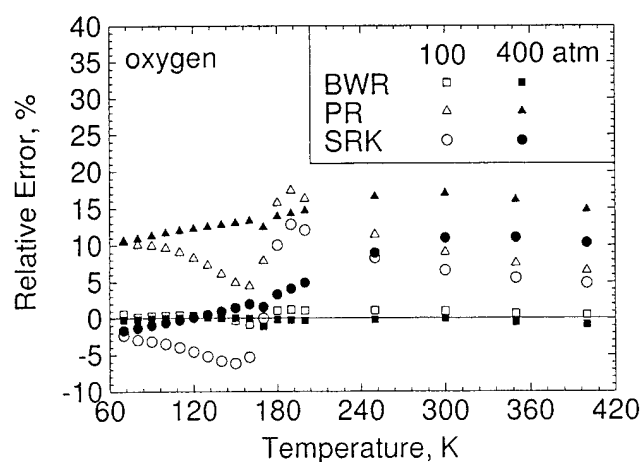


Figure D1 Relative errors associated with SRK and BWR equations of state for calculating the density of oxygen. From Yang (2000). Used with permission.

D2. Calculation of Thermodynamic Phase Equilibrium

Figure D2 presents the thermodynamic states of the n-pentane and carbon dioxide system at phase equilibrium, which are calculated based on the modified Soave-Redlich-Kwong equation of state. The results are compared with the available experimental data (Poettmann and Katz 1945) at two temperatures of 366.7 K and 394.4 K. Figure D2 clearly illustrates the pressure-dependent dissolution of gaseous carbon dioxide into liquid n-pentane. The computational results present excellent agreement with experimental data for the gas-phase equilibrium compositions, but deviate slightly from the liquid-phase experimental data. This is mainly caused by the lack of appropriate experimental data for the binary interaction coefficients in the SRK equation of state. It may also be attributed to the relative errors of the SRK equation of state for estimating liquid density.

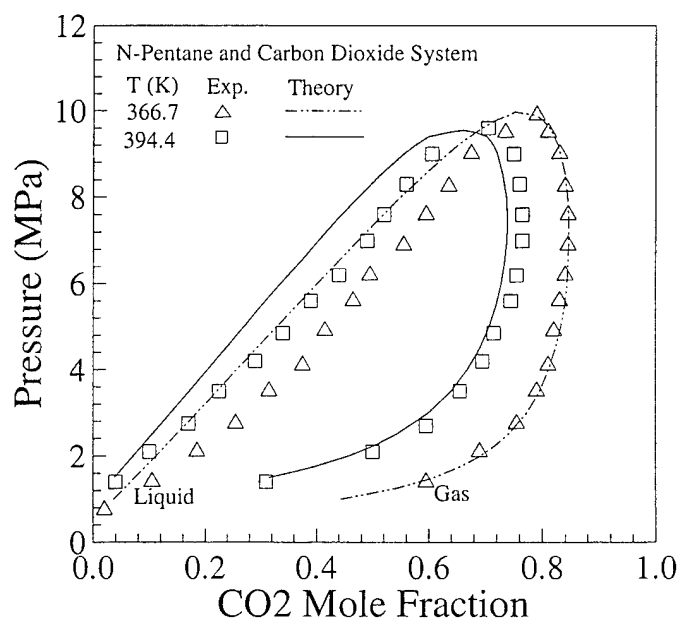


Figure D2 Comparison of computational and experimental results for high-pressure phase equilibrium, n-pentane/carbon dioxide system.

D3. Validation of Numerical Model

The numerical model of single droplet vaporization in a quiescent environment, which is developed in Chapter 2, is validated here by comparing numerical results with experimental data. Since an assumption of non-gravity is used in the development of the numerical model to avoid natural-convection effect, only the experimental data obtained under microgravity conditions can be used for comparison. The most recent experimental results of Nomura et al. (1996) are chosen for model validation. During the experiment, one n-heptane droplet was suspended in a nitrogen environment. The initial droplet diameter was 0.6-0.8 mm, and pressure ranged from 0.1 to 5.0 Mpa. The microgravity conditions were achieved using 5-m and 110-m drop tower and parabolic flights, which reduced the gravity level to the order of 10^{-2} - $10^{-3}g$. The temporal variation of droplet diameter was measured with a computer-aided image analysis system. Before we compare the numerical and experimental results, the following factors, which may cause discrepancies between the results, should be emphasized. First, there were inevitable experimental errors associated with the image analysis system, which were not reported. Second, the experiments were conducted for a suspended droplet, but the numerical computation is conducted for a floating droplet. Recent estimates of Morin (1999) indicate that the effect of suspension fiber on the droplet vaporization rate increases with the increase of pressure and temperature, and with the decrease of droplet size. Finally, the results of Vielli et al. (1996) demonstrate that the microgravity conditions obtained in the drop tower and parabolic flight experiments can not completely avoid the buoyancy effect on droplet vaporization rate, which increases with the increase of pressure.

Figure D3 presents the temporal variations of the dimensionless droplet diameter at a pressure of 0.5 Mpa, and two ambient temperatures of 660 and 750 K, respectively. Reasonably good agreement has been reached for both cases. At the beginning of the vaporization process, both the experimental and computational results illustrate droplet expansion, which is caused mainly by sudden heating of the droplet. Figure D4 compares the numerical and experimental results at a pressure of 2 Mpa and an ambient temperature of 660 K. Excellent agreement is reached in the early stage of the vaporization process, but the difference grows during the vaporization process. This phenomenon is consistent with the conclusions of Morin (1999) and Vielli et al. (1996). The reasonably good agreement of the droplet vaporization rate between the numerical and experimental results validates the numerical model developed in this research work.

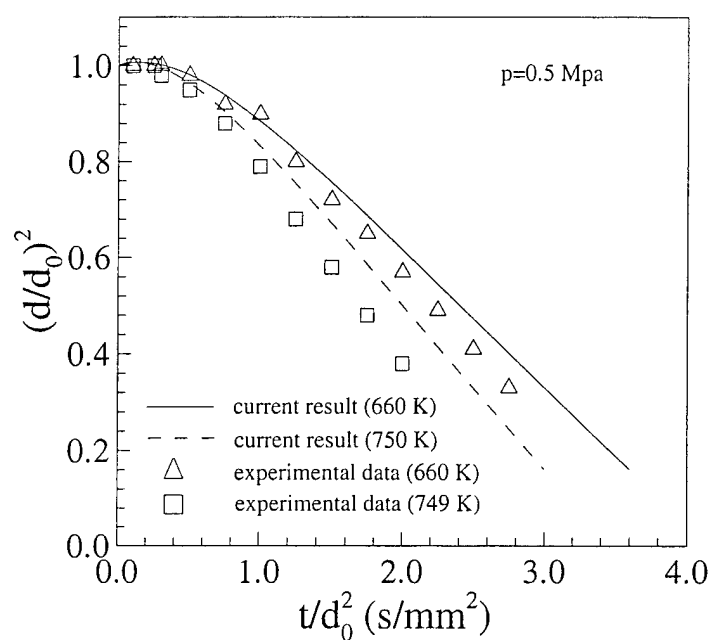


Fig. D3 Comparisons of numerical and experimental results of n-heptane droplet vaporization in nitrogen environments at pressure of 0.5 Mpa and two ambient temperatures of 660 and 750 K.

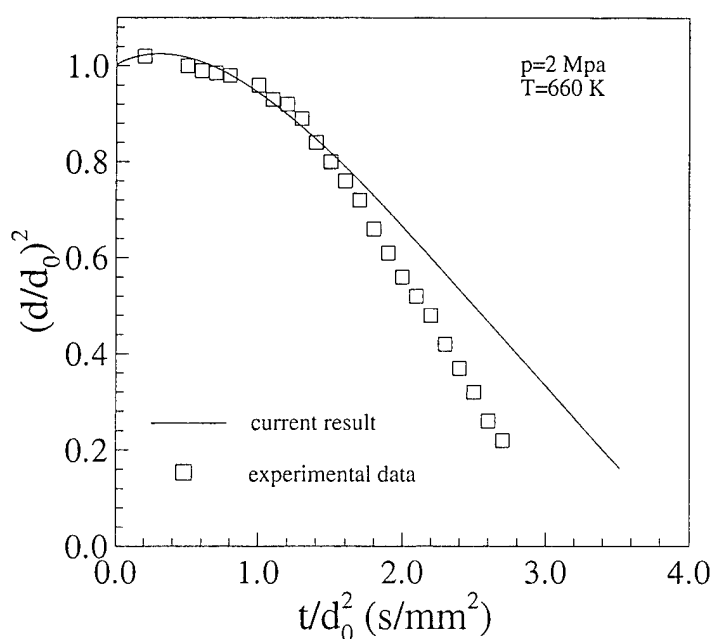


Fig. D4 Comparison of numerical and experimental results of n-heptane droplet vaporization in nitrogen environment at pressure of 2 Mpa and ambient temperature of 660 K.